Characterising water properties of perfluorinated sulfonic acid membranes using terahertz time-domain spectroscopy

George Albert Harry France

Submitted for the degree of Doctor of Philosophy

April 2025

School of Engineering

Lancaster University

Copyright

Copyright © 2025 George France. All rights reserved.

The copyright of this dissertation rests with the author. Copies either whole or in part may not be made without written consent from the author.

Declaration

I declare that this thesis was composed by myself, that the work contained within is my own except where stated otherwise. The work has not been submitted for any other degree, parts of this work have been published as journal and conference publications as later listed. Due references have been appropriately provided for all supporting literature and resources.

George France

Acknowledgements

I am most grateful to have had the opportunity to work with, and receive support from many knowledgeable academics from both the scientific and the social science communities.

I would lie to express my sincere gratitude to Dr Hungyen Lin. As my primary supervisor he has pushed me to become a better researcher and guided me towards the knowledge and expertise to pursue this PhD in the previously unknown to me, field of terahertz spectroscopy. I would also like to thank Dr Richard Dawson for his kindness, support and expertise in electrochemistry, and in fuel cell and electrolyser technologies. I wish you further success in your endeavours at Lina Energy. Dr Gaurav Gupta, thank you for taking on the role of my secondary supervisor from Dr Ricard Dawson and assisting me in area of electrochemistry. Thank you to Riccardo Degl'Innocenti for his patience and allowing me to use his terahertz spectrometer which was crucial for this project.

To Prof Monika Büscher, thank you for many thought-provoking discussions and opening my eyes to many new perspectives from the social sciences viewpoint. I wish you happiness in your retirement. I would also like to thank Prof Richard Harper for taking on Monika's role as co-supervisor and providing some much-needed support and guidance.

The Materials Social Futures (MSF) program was a great introduction to the social sciences and interdisciplinary collaboration. It has enabled me to broaden my understanding and perspectives in the complexities of energy futures, giving me a more rounded, although somewhat pessimistic view of technology. I would particularly like to thank Prof Richard Harper and Prof Rob Short for establishing and directing such an innovative and informative program. I thoroughly enjoyed our many discussions and lively debates.

During my PhD I have been fortunate to have had the opportunity to work with industrial collaborators at the National Physical Laboratory and Johnson Matthey. I would particularly like to thank Andy Wain and Sam Gnaniah from the National Physical Laboratory, and Massimo Peruffo from Johnson Matthey for their fruitful discussions, expertise and assistance.

I would like to thank master's students Mathew Benfield and Maria Sanchez for their assistance in creating the humidity chamber which has been essential for this work. It was a pleasure to supervise you, and I wish you the best for the future. To my fellow PhD colleagues: Decio Alves De Lima, Jordan Frow, Shreenivasan Kiritharan and Mozhdeh Mohammadpour, thank you for the valued discussions, expertise and feedback.

To the Material Social Futures program cohorts including Jonathan Hall, Dom Savage, Eszter Molnar, Philip Bond, Maria Pantsidou and many others, thank you for the great discussions, fond memories and friendships. I wish you all the best in your future endeavours.

I would also like to acknowledge the engineering support staff at Lancaster, particularly Jessica Fisher, Dr Ashley Jones, Jonathan Gates, Vincent Da Costa and Janet Wood for their support throughout my PhD.

On a sentimental note, I would like to thank my friends and family for their continued encouragement and support. You have truly made my Lancaster experience, and I will always treasure the many fond memories of our times together.

Abstract

Perfluorinated sulfonic acid ionomers (PFSAs) are synthetic polymers used in electrochemical devices such as fuel cells and electrolysers due to their low operating temperatures, high proton conductivity, chemical/mechanical stability and low reactant crossover. Membrane performance is highly dependent upon water content due to the role of water in proton conduction mechanisms such as the Grotthus hopping and vehicle mechanisms. Terahertz time-domain spectroscopy (THz-TDS) is an emerging technique which has previously shown sensitivity to the reorientation dynamics of water molecules within thick Nafion 117 PFSAs at a hydrated state and ambient conditions. It is challenging to make comparisons and utilise this information due to the different environments in which additional sample measurements, complimentary experiments and other techniques are performed. This approach is also limited to thicker membranes and not suitable to more industrially relevant thin membranes. This work therefore aims to address these issues and asses the techniques applicability for studying additional water properties within PFSAs. Therefore, in this work a humidity-controlled environment was developed in which THz-TDS measurements could be acquired to extract both water uptake and water states. This work found that the relative proportion of bulk water which is associated with proton conduction increases with higher water contents and relative humidities. Differences in these states between membranes have been observed providing additional material insight which could be utilised for membrane optimisation. Utilising this controlled environment, this work also demonstrates that THz-TDS has the ability to contactlessly study transient water diffusivity and hygral swelling of PFSAs.

Contents

List of tables

List of figures

List of Abbreviations and Acronyms

Abbreviation	Meaning
COM	Communication port
DI	Deionised
DSC	Differential scanning calorimetry
DSC-TGA	Differential scanning calorimetry with thermogravimetric analysis
DVS	Dynamic vapor sorption
EM	Electromagnetic
EMT	Effective medium theory
ePTFE	Expanded polytetrafluoroethylene
EW	Equivalent weight
FTIR	Fourier transform infrared
GDL	Gas diffusion layer
GRG	Generalised reduced gradient
HOR	Hydrogen oxidation reaction
IEC	Ion exchange capacity
LLL	Landau, Lifshitz, Looyenga
LSC PFSA	Long side chain perfluorinated sulfonic acid
MEA	Membrane electrode assembly
NPL	National Physical Laboratory
ORR	Oxygen reduction reaction
PEEK	Polyether ether ketone
PEM	Proton exchange/polymer electrolyte membrane
PES	Polysulfone
PFG-NMR	Pulsed field gradient nuclear magnetic resonance
PFSA	Perfluorinated sulfonic acid
PSSA	Polystyrene
PTFE	Polytetrafluoroethylene
QENS	Quasi-elastic neutron scattering
RH	Relative humidity

RHE	Reversible hydrogen electrode
SAXS	Small angle x-ray scattering
sPEEK	Sulfonated polyether ether ketone
sPI	Polyimide
SSC PFSAs	Short side chain perfluorinated sulfonic acid
THz	Terahertz
THz-TDS	Terahertz time domain spectroscopy
TPX	Polymethylpentene
WU	Water uptake

Original contributions

The following publications were achieved during this PhD. The author was previously known as George Albert Harry Ludlam as listed in these published works and refers to the same author.

Journal publications

- D. F. Alves-Lima, X. Li, B. Coulson, E. Nesling, **G. A. H. Ludlam**, R. Degl'Innocenti, R. Dawson, M. Peruffo, H. Lin," Evaluation of water states in thin proton exchange membrane manufacturing using terahertz time-domain spectroscopy", Journal of Membrane Science, 647, 120329, 2022, doi: 10.1016/j.memsci.2022.120329
- **G. A. H. Ludlam**, S. J. P. Gnaniah, R. Degl'Innocenti, G. Gupta, A. J. Wain, H. Lin," Measurement of Water Uptake and States in Nafion Membranes Using Humidity-Controlled Terahertz Time-Domain Spectroscopy", ACS Sustainable Chemistry & Engineering, 12, 20, 2024, doi: 10.1021/acssuschemeng.4c01820
- **G. A. H. France**, M. Mohammadpour, R. Degl'Innocenti, M. Peruffo, H. Lin, "Probing water properties in perfluorinated sulfonic-acid membranes with humidity-controlled terahertz time-domain spectroscopy", IEEE Transactions on Terahertz Science and Technology, 15, 2025, doi: 10.1109/TTHZ.2025.3594070

Conference publications

- **G. A. H. Ludlam**, D. F. Alves de Lima, X. Li, B. Coulson, E. Nesling, R. Degl'Innocenti, R. Dawson, M. Peruffo, H. Lin," Extracting water states in thin proton-exchange membranes using terahertz time-domain spectroscopy", H2FC Supergen Research Conference, St Andrews, United Kingdom, 2022
- **G. A. H. Ludlam**, D. F. Alves de Lima, X. Li, B. Coulson, E. Nesling, R. Degl'Innocenti, R. Dawson, M. Peruffo, H. Lin," Quantification of water states in thin proton exchange membrane manufacturing using terahertz time-domain spectroscopy", 47th International Conference on Infrared, Millimeter and Terahertz Waves (IRMMW-THz), Delft, Netherlands, 2022, pp. 1-2, doi: 10.1109/IRMMW-THz50927.2022.9895912
- **G. A. H. Ludlam**, R. Degl'Innocenti, G. Gupta, H. Lin," Quantifying humidity dependent water states of Nafion 117 membranes using terahertz time-domain spectroscopy", Optica Sensing Congress 2023, Technical Digest Series, Munich, Germany, 2023, doi: 10.1364/AIS.2023.JW2A.33
- **G. A. H. Ludlam**, D. F. Alves de Lima, X. Li, B. Coulson, E. Nesling, R. Degl'Innocenti, R. Dawson, M. Peruffo, H. Lin," Probing molecular water states of fuel cell membranes using terahertz time-domain spectroscopy", Electrochemistry Northwest, Manchester, United Kingdom, 2023
- **G. A. H. Ludlam**, S. J. P. Gnaniah, R. Degl'Innocenti, G. Gupta, A. J. Wain, H. Lin," Water states measurement in proton-exchange membranes using humidity-controlled terahertz time-domain spectroscopy", 49th International Conference on Infrared, Millimeter and Terahertz Waves (IRMMW-THz), Perth, Australia, 2024, pp. 1-2, doi: 10.1109/IRMMW-THz60956.2024.10697715

- **G. A. H. Ludlam**, S. J. P. Gnaniah, R. Degl'Innocenti, G. Gupta, A. J. Wain, H. Lin," Humidity-controlled terahertz pulsed spectroscopy for characterizing water uptake in thin proton-exchange membranes", 49th International Conference on Infrared, Millimeter and Terahertz Waves (IRMMW-THz), Perth, Australia, 2024, pp. 1-2, doi: 10.1109/IRMMW-THz60956.2024.10697715
- **G. A. H. Ludlam**, S. J. P. Gnaniah, R. Degl'Innocenti, G. Gupta, A. J. Wain, H. Lin," Quantification of humidity dependant water uptake and states in Nafion membranes using terahertz time-domain spectroscopy", Electrochem 2024, Manchester, United Kingdom, 2024
- M. Mohammadpour, **G. A. H. Ludlam**, M. Peruffo ,H. Lin," Sensing Water in Catalyst Coated Membranes with Terahertz Time-Domain Spectroscopy", Electrochem 2024, Manchester, United Kingdom, 2024

1 Introduction

Clean and efficient energy conversions are required to reduce emissions of harmful chemicals such as carbon dioxide and limit our impact upon our natural environment, while maintaining our current way of life which is heavily reliant upon easy access to energy. Hydrogen fuel cells and electrolyzers are electrochemical devices for clean energy conversions between electrical and chemical energy. Crucial to the functionality of these devices are ion exchange membranes. Proton exchange membranes are considered to be one of the most promising ion exchange membrane technologies due to their high electrochemical performance and mechanical-chemical stability at low operating temperatures of less than 120°C. Water is integral to the high proton conductivity of these membranes as protons are transported through water in the phase separated nanostructure. This thesis therefore aims to explore the properties of this water in these membranes which are critical for high performance. Fuel cells and electrolysers are only one part of hydrogen transformations. Therefore, this introductory chapter explores our interactions with energy, hydrogens role in green energy transitions and some of the technologies key to utilising this important chemical.

1.1 Humans and energy

Advancements in the extraction, transformation and use of energy has been pivotal for human advancement, allowing us to achieve things otherwise impossible. Today energy is ubiquitous in our everyday lives and powers our heating, transportation, manufacturing, entertainment, lighting, cooking, refrigeration and many other applications. Energy has become readily available and often delivered directly to our devices and appliances. This energy comes in many forms such as chemical, mechanical, nuclear, gravitational and thermal however, since we learned to harness electrical energy in the 1800s, electricity has revolutionised our lives and become our most prevalent form of energy. Whilst many uses of energy can be seen, many sources and products of energy remain hidden to its users. In particular, in the objects we use daily, and the energy used in the refining, manufacturing and transportation required to deliver a product to its customer. A concept known as embodied energy which is often significantly greater than any energy used during a products useful lifetime. As access to large quantities of energy has become widespread and many uses of energy have become obscured, humans have become disconnected and have lost a true understanding of our energy and the vast quantities we are responsible for. The power output of our human bodies has been vastly exceeded and replaced with a low personal cost in the form of economic expense.

Traditionally our energy has predominantly originated from chemical energy through the combustion of hydrocarbons from wood to coal, oil and natural gas to produce heat, mechanical energy and electricity. The non-renewable nature and environmental impact of burning fossil fuels has become a prevalent concern and as such we have realised a need to produce renewable energy from other sources such as wind, solar, hydro, biomass, geothermal and tidal. However, these have specific geographic requirements, require vast areas of land and or large initial energy costs which limit their adoption. The power output of many of these is also unreliable, relying on natural phenomena and cannot be varied to meet changing demands, as such the need for storing energy has become a great challenge with fossil fuels currently used to compensate for times of insufficient energy output and insufficient storage. Many of these technologies require rare materials in limited supply which also limits their adoption and whilst reducing the production of carbon dioxide, these technologies may produce other environmental contaminants. Renewables technologies may provide a solution to our problem, but should we also be making greater attempts to reduce our personal energy consumption?

1.2 Hydrogen

Hydrogen is the most abundant element in the universe and hydrogen gas is the most gravimetrically energy dense chemical known with no carbon dioxide produced when burned making it an ideal fuel. However, hydrogen gas is rarely found naturally and is therefore a secondary energy source, as such it is often to as an energy vector rather than energy source. Fortunately, hydrogen is a simple molecule allowing us to produce it in many ways from primary energy sources through hydrocarbon reforming and water electrolysis, as such hydrogen has no geopolitical reliance and therefore promises the potential of energy independence. Hydrogen can also be produced as a by-product of industrial chemical processes such as chlorine production however as the hydrogen is a by-product, these are limited in their use.

1.2.1 Hydrogen production

Whilst reforming of hydrocarbons and water electrolysis are the two methods typically used to produce hydrogen commercially, the source of primary energy can come in various forms for both. To reflect this hydrogen is often given a colour to describe how it is made. The spectrum of these methods is known as the hydrogen rainbow. Hydrogen from water electrolysis using renewable electricity is known as green hydrogen, however this category can include wind, tidal, geothermal, hydro and solar which has also been assigned the colour yellow. Electrolysis of water using nuclear energy is not considered green hydrogen and has been assigned pink, purple or red. Steam reforming is a process in which natural gas can be converted into hydrogen and carbon dioxide. When carbon capture and storage is used this is referred to as blue hydrogen whereas grey is given when carbon capture is not used. Hydrogen can be produced from methane using liquid catalysts such as liquid metal or salts or thermal plasma [1] in a process called methane pyrolysis which produces solid carbon rather than carbon dioxide which is much easier to store and can be utilised as a useful product, furthermore this can be a carbon negative process if biomethane is used. Coal gasification is a method of producing hydrogen and carbon dioxide from coal. Coal is separated into brown and black coal with black coal being older and containing less water. The hydrogen produced from these are assigned the same colours. These methods are summarised in Table 1.1

Table 1.1 - Hydrogen rainbow.

Colour	Primary input	Method
Green	Wind, solar, hydro, tidal, geothermal	Electrolysis
Yellow	Solar	Electrolysis
Pink, purple or red	Nuclear	Electrolysis
Blue	Natural gas	Steam reforming with carbon capture and storage
Grey	Natural gas	Steam reforming
Turquoise	Methane	Pyrolysis
Brown	Brown coal	Gasification
Black	Black coal	Gasification

Despite hydrogens clean image and many possible clean methods of production, most of global hydrogen production is not low emission as in 2022 of the 95Mt of hydrogen produced, 62% was produced from natural gas without carbon capture and storage, 21% from coal which was mainly located in China, 16% as a by-product, 0.6% from fossil fuels using carbon capture and storage 0.5% from Oil and only 0.1% from electricity [2]. A large reason for this is historical as these are mature industrial processes which have reduced costs and established supply chains. Another reason is efficiency as we don't currently have plenty of excess renewable energy, therefore increased load due to electrolysis would require more fossil fuels to be burnt. Converting fossil fuels directly to hydrogen is more efficient and therefore currently utilised. Clearly hydrogen is not as clean as many may think and whilst hydrogen can be carbon neutral it is important to be aware of our current emissions due to hydrogen production.

1.2.2 Hydrogen applications

Hydrogen has many uses both industrially and domestically due to its ability to produce heat and electricity but also as a chemical feedstock. The main domestic uses for hydrogen are transportation and heating. Whilst electric vehicles have been gaining popularity in recent years these are typically powered by batteries in battery electric vehicles (BEVs) and hybrid vehicles. Hydrogen can be used in vehicles through fuel cells producing electricity or internal combustion engines. Whilst batteries are very efficient compared with electrolyzers and fuel

cells they have poor energy density and therefore these vehicles are typically much heavier, particularly for long range vehicles and therefore require more output energy. Due to hydrogens low density and the low weight of fuel cells and internal combustion engines, creating efficient long-range vehicles is possible without the drawbacks of BEVs such as increased tyre wear and long recharging/refilling times. The applicability of these technologies to transportation can vary as batteries are generally limited to personal transportation due to the high weight. This is of particular issue for trucks and lorries which have weight restrictions to which the batteries contribute limiting their capacity. These vehicles are generally used over long distances and therefore the range and recharging times also limit their use which is not an issue for hydrogen powered vehicles. Hydrogen fuel cells are particularly attractive for forklifts used in refrigerated warehouses as batteries struggle with cold temperatures and combustion engines produce carbon dioxide and carbon monoxide in the enclosed space which can be deadly.

Both battery and fuel cell electric vehicles face concerns over resource acquisition mainly due to lithium for batteries and platinum for fuel cells. These metals are rare and not always economically viable to extract making mass adoption challenging and costs high. Heating using hydrogen is a promising domestic use as some existing infrastructure can be utilised. Currently some hydrogen is blended with natural gas used in heating however only in small quantities as existing infrastructure and boilers can't handle high hydrogen content. To improve the efficiency of boilers combined heat and power systems can also be used, these are high temperature fuel cells which produce electricity but also make use of the waste heat to reach very high efficiencies and can operate with both natural gas and hydrogen.

Hydrogen has been used as a chemical feedstock industrially for many decades for many products such as Ammonia through the Haber-Bosch process, which is vital in producing fertiliser, other uses include oil refining, production of many products and precursors such as hydrogen peroxide and hydrogenised oils. As these industries have traditionally used hydrogen derived from fossil fuels there exists a large opportunity for decarbonisation through the use of carbon free hydrogen [3]. Many other industrial uses of hydrogen are possible and emerging processes are being considered or trailed such as hydrogens use as a strong reducing agent in metal production, in particular steel which traditionally uses coke and has a high carbon footprint [4]. Synthetic fuels produced from hydrogen and carbon dioxide are also being considered, these provide the advantage of utilising existing infrastructure and don't require new vehicles or equipment, of particular interest is aircraft which has limited clean alternatives [5].

Clearly there are many existing and potential uses for hydrogen but hydrogen cannot be used to decarbonise every domestic and industrial source of carbon dioxide. Hydrogen does provide a good solution to some problems but many other technologies provide alternative solutions which may be superior.

Electrical power grids are important consideration in green and pink hydrogen adoption as electrolysers place additional demand upon new and existing infrastructure. Renewable energy is generally unreliable and highly dependent upon the weather, nuclear provides a stable output but its power output is invariable and therefore cannot compensate for changes in renewable outputs or changes in electric demand such as low demand overnight. Currently fossil fuels are used in grid balancing due to their rapid controllable output. Therefore, for full adoption of nuclear and renewable energy without periods of rolling blackouts due to excessive demand, energy storage is required. Through the use of electrolysers, hydrogen storage and fuel cells, hydrogen could be used as a way to store electrical energy. Unfortunately, the overall efficiency is poor at 30-42% [6–8] and therefore this makes hydrogen unsuitable for large scale storage. Other technologies are available such as pumped hydroelectric storage and batteries. Hydroelectric is a proven technology with a high efficiency of 70-80% [9,10] however due to the need for two reservoirs located close to each other at different altitudes, there are a limited and diminishing number of suitable locations [9]. Battery's for grid storage don't require specific geography, can be designed according to demands and are efficient at 76-81% [11,12] however, whilst lithium-ion batteries have been demonstrated at scale, they are expensive and use increasingly rare materials. As such other battery technologies are being considered such as molten salt, sodium ion, sodium sulphur, iron-air, lithium iron phosphate and many redox flow batteries in which chemicals are stored separately, these are highly configurable and have lower capital costs [13–17]. Lithium ion is well known and utilised due to its high energy density. As grid storage is stationary the weight is less of a concern making other technologies more attractive due to their low material cost and high availability [13]. Whilst hydrogen does not provide an efficient solution to grid storage it can be utilised to balance the grid through variable production and delayed consumption in which the hydrogen output is varied to utilise power when the grid is producing an excess and reduced production in periods of high electrical demand. Whilst energy is required to store hydrogen this would be an approximately 90% efficient process for compressed gas storage [18]. This is also a potential solution for seasonal storage as electricity demand and production change seasonally.

1.2.3 Limitations to hydrogen adoption

Fuel cells were first invented in 1838 by Sir William Grove and in 1932 Francis Thomas Bacon developed the first practical hydrogen-oxygen fuel cell which were further developed for the Apollo program in the 1960s due to the high efficiency and already present hydrogen and oxygen on board, the water produced could also be used. The technology has been around for decades so why are we not using more hydrogen?

One reason is its perceived safety compared to alternatives, this is partially due to its inherent properties such as its ability to leak due to its small molecular size. It can even penetrate through solid metal in a process called hydrogen embrittlement where hydrogen infuses with the metal and weakens it. Hydrogen also has wide flammability limits of 4-75% and detonation limits of 16-59% in air at room temperature [19]. Due to its density, hydrogen is also stored at high pressures. Historically hydrogen has also been associated with explosions such as the Hindenburg disaster and space shuttle challenger. Despite its dangerous properties hydrogen has been in used safely in industry for decades [20] so is hydrogen more dangerous than alternatives? As hydrogen is a gas it can dissipate before any fire occurs particularly with its very low density, if hydrogen leaking from a hole in a tank catches fire, a flame can be produced but is unlikely to spread unlike a flammable liquid which can pool underneath devices such as vehicles and set the entire vehicle on fire. As no carbon monoxide or smoke is produced when hydrogen burns it is also unlikely to cause poisoning but could reduce oxygen levels. Batteries are also considered safe but when cell failure occurs such as in a vehicle accident, cascade cell failure can occur which consumes the whole battery and is extremely difficult to put out. Additionally, the familiarity of a danger can lessen the perceived danger or risk such as the daily use of highly flammable petrol in cars, as such people can be hesitant to try less known technologies with high perceived danger. Often unforeseen dangers can be more risky due to inadequate safety measures such as sugar which is not often considered explosive but sugar dust is explosive and in 2008 caused an explosion at the Georgia Imperial sugar refinery destroying the entire processing plant [21]. High perceived danger can additionally make technology safer due to overbuilding of safety features, an example of this is nuclear power which has one of the least deaths caused per MWh of electricity produced, significantly lower than fossil fuels, biomass and hydropower [22]. Toyota even shot their hydrogen fuel tanks in order to prove its safety with a 50-calibre armour piercing round required to penetrate it and only a small hole was produced [23], this is in contrast to petrol fuel tanks which are significantly weaker.

Adoption is also limited by hydrogens overall efficiency as electrolysers, compressors (storage), transportation and fuel cells all have associated energy losses making it often undesirable for static applications although factors such as weight are often not considered such as high battery weight when comparing transport.

One of the major reasons for low adoption rates is cost as hydrogen technologies have both high capital and operating costs. Infrastructure costs are high [24], partially as they can't use existing infrastructure unlike other technologies such as electric vehicles, the cost of new infrastructure is also high partially due to the high pressure and its tendency to leak. Many important components are expensive requiring highly specialised expensive materials such as platinum group metal nano catalysts such as Platinum, iridium and ruthenium. Platinum group metals are very rare minerals with only 200 tonnes of platinum produced globally in 2023 of which 37 tonnes was from recycling [25]. Iridium and ruthenium are even more scarce with 7 and 28.7 tonnes produced respectively in 2023 [25]. As such lots of research has focussed on reducing required platinum group metal loadings or finding effective replacements which are often less efficient [26] or require specific membranes such as with anion exchange membranes. Platinum group metal mining is difficult due to its rarity and low concentration, it is also a by-product of nickel and copper mining however this is not enough to satisfy demand. South Africa is the largest producer of platinum with 69% of the global mining supply [25] and as such its supply is highly dependent.

Currently 44% of platinum is used in automative industries for catalytic converters, other uses include jewellery 18%, industrial 38% and 0.6% investment in 2023 [25]. Currently approximately 1.5 g of platinum is used per catalytic converter [27], the Toyota Mirai is reported to have 30g of platinum per vehicle [28] efforts to reduce platinum loadings are expected to reduce this and a lower limited has been suggested at 6g [29]. This increase in content per vehicle from internal combustion with catalytic converters to fuel cell electric vehicles is significant and even at the lower limit, we don't currently have enough platinum supply to transition all vehicles to a hydrogen fuel cells, as such platinum group metals remain a significant material cost and barrier for mass adoption with catalysts accounting for 61% of fuel cell stack component cost [30].

Another reason for the high cost is the low demand which limits component producers, hydrogen production and automakers, making them unable to attain economies of scale which inflate costs and limits investment due to uncertain returns on investment.

Fuel cell and electrolyser durability is a significant issue which also limits adoption as the U.S. Department of energy has set targets of 30,000 hours for heavy duty transport whereas durability was only 10,000 hours in 2023 [30]. Many fuel cells components degrade due to the harsh operating conditions they are exposed to with multiple major failure modes in the catalyst layer, gas diffusion layer, bipolar plate, gasket and most severely within the membrane [31]. Whilst durability can be principally monitored through fuel cell voltage [31], low durability limits application and increases overall costs.

1.2.4 The future of the hydrogen economy

Hydrogen technologies are highly entangled within multiple political, environmental, social, technological, legislative and economic factors with significant investments required. The transition to hydrogen has been slow and is still uncertain although existing hydrogen applications in industry are expected to transition towards carbon free hydrogen rather than fossil fuel derived hydrogen. Other emerging industrial applications such as green steel are expected increase hydrogen demand as the most mature alternative proposed for steel decarbonisation [4]. These applications are of high density and therefore don't require the significant infrastructure required for domestic applications. Whilst hydrogen provides a solution for the decarbonisation of transportation, high costs, a lack of infrastructure and alternatives such as battery electric vehicles which have been gaining significant traction will likely limit adoption. These factors provide uncertainty to the future of hydrogen powered vehicles and could vary based on the type of vehicle. Hydrogen for heating is also uncertain with efficient electric heating alternatives such as heat pumps being widely available and use existing infrastructure.

Currently hydrogen is predominantly produced from fossil fuels, however production is likely going to transition towards electrolyser-based production from a range of diverse renewable electrical sources such as wind, solar and nuclear [32]. The electrolyser technology to be used is uncertain and may vary. The future of perfluorinated sulfonic acid (PFSA) membranes currently used in PEM technologies is uncertain with current plans by the EU to ban perfluoroalkyl and polyfluoroalkyl substances (PFAS) [33] as they are non-degradable in the environment due to their chemical stability. Alternative hydrocarbon membranes are being developed, however they currently lack the chemical stability for the required durability. It is possible that PFSAs may receive an exemption for fuel cells and electrolysers due to their use in green technologies and chemical stability is a required property for fuel cell and electrolyser

membranes although this is still uncertain. Other technologies such as anion exchange membranes and solid oxide provide an alternative and don't require platinum group metal catalysts but have additional considerations such as poisoning, stability [34] or high temperatures which limit their applicability.

1.3 PEM fuel cells and electrolysers

Water electrolysis is a key technology for clean hydrogen production as shown in Table 1.1 where electrolysis is used to convert water and electrical energy derived from a variety of clean energy sources into hydrogen and an oxygen by-product. Whilst hydrogen can be produced from hydrocarbon feedstocks, these technologies utilise non-renewable fossil fuels and produce carbon dioxide. As non-renewable hydrogen is currently more economic than clean renewable hydrogen [35], efforts must be made to reduce cost through more efficient devices made at reduced cost and a longer expected lifetime. Fuel cells enable compact and efficient transformation of hydrogen chemical energy into electrical energy. These devices share many components and materials such as the membrane. Proton exchange/polymer electrolyte membranes (PEM) are crucial components of PEM fuel cell and electrolysers. These membranes contribute to a significant loss in device efficiency and are susceptible to degradation mechanisms [36] which limit the lifetime of the membrane and expensive incorporated catalyst which then need replacing. The electrochemical and mechanical properties of these membranes are highly dependent upon water content where greater performance is observed under high levels of hydration. Therefore, optimisation of the efficiency and durability of these membranes under their intended operating conditions is key to reducing costs and accelerate adoption. Additionally, within fuel cells excess water buildup blocks gas flow and can result in cell flooding therefore optimisation is required to achieve high performance and understanding water distribution mechanisms in all relevant components is crucial.

1.4 Terahertz radiation

Terahertz radiation are electromagnetic waves occupying a frequency range of 0.1-10THz and wavelengths of 3mm to 30μm. This band lies between microwave and far infrared waves and is also known as the terahertz gap due to the gap between electrical (lower frequencies) and optical (higher frequency) regimes which presents challenges in its generation, detection and manipulation. At the lower frequencies of microwaves/millimetre waves, efficient generation

is possible through vacuum tubes and solid-state devices [37]. Higher frequency far infrared can be generated through a number of techniques such as molecular gas lasers [38]. Unfortunately, these well-developed technologies could not be applied to terahertz radiation creating the terahertz gap [39]. Developments in terahertz generation, detection and manipulation have resulted in more effective devices and as such interest has increased, particularly with the rise in commercially availability systems [40]. As terahertz radiation is strongly absorbed by liquid water but penetrates many dielectric materials such as polymers and biological materials, it is an attractive technique for studying liquid water contents within hydrophilic and terahertz transparent materials. Terahertz is also sensitive to the reorientational dynamics of water and therefore presents an interesting approach for probing water properties and interactions with hydrophilic molecules.

1.5 Objectives

The aim of this dissertation was to investigate the properties of water within ion exchange membranes using terahertz time-domain spectroscopy (THz-TDS). Water is crucial for the effective electrochemical performance of these membranes which are sensitive to their exposure to water in the liquid and vapor (humidity) phases. Previous studies have studied thick Nafion 117 membranes prehydrated and measured in ambient conditions. Thinner more industrially relevant membranes dry and hydrate rapidly under different humidity environments making this approach unsuitable. Only a limited amount of information can be obtained due to the difficulty comparing results of different water uptakes and humidity environments. Initially Nafion 177 membranes were hydrated in containers containing water or saturated salt solutions to equilibrate to a desired relative humidity. Membranes were then measured in the ambient uncontrolled environment. To further explore water properties, a relative humidity-controlled environment was designed and implemented to enable THz-TDS transmission measurements of membranes under steady state conditions. This humidity-controlled chamber was later equipped with a motorised stage which enabled gathering sample and reference measurements without the need to open the chamber and move the sample. This motorised stage facilitated obtaining continuous measurements without significant changes to the humidity which were required for transient diffusion studies and dimensional stability measurements of PFSAs which have not previously been studied using THz-TDS. This work has utilised this chamber to investigate the applicability of the technique for characterising water content, water states, diffusion and swelling of perfluorinated sulfonic acid ionomer membranes within a humidity-controlled environment.

1.6 Outline

- Chapter 1 has introduced hydrogen, its properties and its role as an energy vector for decarbonisation of the worlds energy. The chapter outlines some of the applications, production methods, advantages and disadvantages of hydrogen technologies and the role of fuel cells and electrolysers in a hydrogen economy. Hydrogen and the many associated hydrogen technologies are highly complex and entangled, therefore there are many factors and considerations which were not covered within this chapter or were only discussed briefly. This was an attempt to outline many of the significant Technological, Economic and Social aspects whereas less attention was given to

Political, Legal, and Environmental factors. The chapter also introduces PEM fuel cells, electrolysers and terahertz radiation.

- Chapter 2 is the literature review, and the aim of this chapter is to provide an overview of fuel cells, their associated electrochemical reactions, components, sources of energy loss and the role of water in PFSA ionomer membranes. Whilst the focus of this chapter was on PEM fuel cells, many of the concepts, theories and understandings can be applied to other fuel cell technologies and electrolysers which share the many of same specialised materials and components. The chapter also summarises transient water diffusion modelling and techniques for characterising water states within PFSAs. Terahertz radiation is introduced and pulse generation and detection using photoconductive antennas is summarised. Methods of THz-TDS data processing, wave modelling and material characterisation are also given.
- Chapter 3 outlines the materials and methods used throughout this thesis. This includes membrane preparation, the design of the relative humidity-controlled chamber, THz-TDS experimental procedures, data acquisition and analysis. Methods used for complimentary techniques such as differential scanning calorimetry, thermogravimetric analysis and dynamic vapor sorption are also given. The methods and models used to describe transient water diffusion have also been described.
- Chapter 4 presents the results of steady state water uptakes and molecular water states. These results have been compared to other techniques for validation and comparison. Dynamic vapor sorption is a gravimetric technique used to study water uptake in a controlled environment and therefore, literature values and an obtained measurement were compared to THz water uptake values. THz water states were compared with freezable and non-freezable water as well as HOH bending vibration of water molecules associated with SO_3^- groups from FTIR.
- Chapter 5 presents the results of the THz study of transient diffusion and compares the fittings and results with complimentary dynamic vapor sorption measurements. The results of the study of thickness swelling with THz-TDS have also been presented. Thickness has been validated using complimentary confocal laser microscopy and micrometre measurements. A dimensional stability study was then conducted to explore changes in thickness due to repeated changes in humidity.
- Chapter 6 summarises and concludes the work whilst also discussing some practical limitations and suggesting methods for further improvement.

2 Literature review

Water is integral to the electrochemical and mechanical properties of perfluorinated sulfonic acid (PFSA) ionomer membranes which are vital in the operation of a number of electrochemical devices such as fuel cells and electrolysers. Numerous techniques have been utilised for the characterisation of water which is situated within the phase separated nanodomains of the PFSA ionomer. Terahertz offers an attractive approach for water characterisation as it is sensitive to molecular reorientation dynamics. This chapter will cover the basics of fuel cell concepts, components and operation to highlight the vital role of PFSA membranes and the different nature and properties of water such as diffusion and membrane swelling. A number of water quantification and characterisation techniques will be reviewed. In particular, the techniques of terahertz time domain spectroscopy (THz-TDS) will be covered including a basic understanding of terahertz time domain spectrometers and methods used to extract information from acquired waveforms. The nature of membrane water diffusion will also be covered including a number of models and techniques which can be used to extract water diffusivity from transient water uptake measurements. The purpose of this chapter is to establish a foundation for the experimental methodologies and techniques used throughout this thesis and provide a background for contextualisation, understanding and interpretation of results.

2.1 Fuel cells

Fuel cells are electrochemical devices which convert chemical energy from fuel and oxygen directly into electrical energy. Unlike some other electrochemical devices such as self-contained batteries, fuel cells don't contain all the reactants internally and require a constant supply of fuel and oxidiser, similar to a redox flow battery. This process has a high efficiency when compared to internal combustion engines. Hydrogen is often used to power these devices as water is the only product whereas carbon dioxide and carbon monoxide are produced when hydrocarbons are used. A wide variety of fuel cells have been developed and operate with a variety of fuels, oxidisers, electrolytes, catalysts and at different operating temperatures, efficiencies, power densities and sensitivity to impurities. In general fuel cells are characterised based on their electrolyte which determines their effective operating conditions and other material choices. A summary of common fuel cell variants is shown in Table 2.1 [41,42].

Table 2.1 - Comparison of fuel cell technologies.

Electrolyte	Exchange ion	Operating temperature	Fuels
Proton exchange /polymer electrolyte	H^+	<120°C	Hydrogen, methanol
Alkaline	OH^-	<100°C	Hydrogen
Phosphoric acid	H^+	150 - 200°C	Hydrogen, natural gas
Molten carbonate	CO_3^{2-}	600 - 700°C	Hydrogen, natural gas
Solid oxide	O^{2-}	500 - 1000°C	Hydrogen, natural gas
Anion exchange membrane	OH^-	50 - 80°C	Hydrogen, methanol

This work is going to focus on proton exchange/polymer electrolyte membranes (PEM). These membranes are used in low temperature fuel cells which exhibit sustained operation with high current density, low weight, compactness, the potential for low cost and volume, long stack life, fast start-ups and suitability for discontinuous operation [43]. Due to their inherent properties PEM fuel cells demonstrate promise for portable, automotive and stationary applications [44].

2.1.1 Electrochemical reactions

In a typical chemical reaction electrons are transferred from the orbitals of one species to another resulting in the formation of a new bond. In electrochemical reactions the reaction is split into two half-cell reactions where electrons are first transferred to an external circuit in the first half-cell reaction and then transferred to the species in the second half cell. For this to occur an ion must be transferred through an ion conducting medium (electrolyte). These two half-cell reactions form a redox pair which combine to produce an overall reaction. Each half cell reaction has an electrical potential which is compared to a reversible hydrogen electrode (RHE) and the difference between these give a potential difference which gives the open circuit potential. In the case of hydrogen PEM fuel cells with its proton exchange membrane, the half-cell reactions are known as the hydrogen oxidation reaction (HOR) and the oxygen reduction reaction (ORR). The HOR occurs at the anode which is usually coated in a platinum catalyst and is supplied with hydrogen which is oxidised to form protons and electrons with a standard potential (E^0 vs RHE) of 0V by definition:

$$H_2 \rightarrow 2H^+ + 2e^- \tag{2.1}$$

Whilst the electron travels through the external circuit providing the electrical energy output, the protons travel through the proton exchange membrane. At the cathode which is usually coated with a platinum catalyst, the protons and electrons reduce the oxygen in the ORR reaction to form water with a standard potential (E^0 vs RHE) of 1.23V [45]:

$$O_2 + 4H^+ + 4e^- \rightarrow 2H_2O \tag{2.2}$$

The ORR reaction has much slower reaction kinetics than the HOR reaction [46] and represents a significant loss for cell efficiency. Two HOR reactions must occur for each ORR and these half-cell reactions form an overall reaction with a standard potential of 1.23V:

$$2H_2 + O_2 \rightarrow 2H_2O \tag{2.3}$$

This overall reaction is equivalent to exothermic hydrogen combustion however, instead of releasing the energy as heat, some of this energy has been captured as electrical energy. The standard potential (E^0) is the open circuit potential at standard heat, pressure and concentration (25°C, 1atm or 1M) for an ideal cell. Under non-standard conditions the open circuit potential will change. The open circuit potential of an ideal cell under standard partial pressures and concentrations can be calculated from the Gibbs free energy as shown in Equation 2.4

$$E_T = -\frac{\Delta G_T}{nF} = -\frac{\Delta H_T - T\Delta S_T}{nF} \quad (2.4)$$

Where E_T is the standard cell potential at a given temperature, ΔG_T is the Gibbs free energy change, n is the number of electrons in the reaction (in this case 4), F is Faraday's constant (96485 C/mol), ΔH_T is the enthalpy of reaction and T is the temperature in kelvin. Changes in the concentration of the reaction species will also impact the potential according to the Nernst equation:

$$E = E_T + \frac{RT}{4F} ln\left(\frac{{P_{H_2}}^2 P_{O_2}}{{P_{H_2O}}^2}\right) \quad (2.5)$$

Where E is the open circuit potential for an ideal cell and is known as the reversible voltage, R is the ideal gas constant (8.314Jmol^{-1}K^{-1}), P_i is the partial pressure of the species i. When using these two equations the ideal open circuit potential can be calculated for any operating conditions.

When using electrolytes with different exchange ions the half-cell reactions change as seen in Table 2.2.

Table 2.2 - Half-cell reactions for different exchange ions.

Exchange ion	Anode reaction	Cathode reaction
H^+	$H_2 \rightarrow 2H^+ + 2e^-$	$O_2 + 4H^+ + 4e^- \rightarrow 2H_2O$
OH^-	$H_2 + 2OH^- \rightarrow 2H_2O + 2e^-$	$O_2 + 2H_2O + 4e^- \rightarrow 4OH^-$
CO_3^{2-}	${CO_3}^{2-} + H_2 \rightarrow H_2O + CO_2 + 2e^-$	$O_2 + 2CO_2 + 4e^- \rightarrow 2{CO_3}^{2-}$
O^{2-}	$H_2 + O^{2-} \rightarrow H_2O + 2e^-$	$O_2 + 4e^- \rightarrow O^{2-}$

The overall reaction and the Nernst equation for all these half-cell reaction pairs is the same. As each half cell reaction and their operating conditions are different, the reaction mechanisms are also different and require different catalysts for optimum performance.

2.1.2 PEMFC components

PEM fuel cells are made of multiple layers as seen in Figure 2.1 which work together to form the cell and are held together by compression with gasket layers used to form seals and stop any gas leakage.

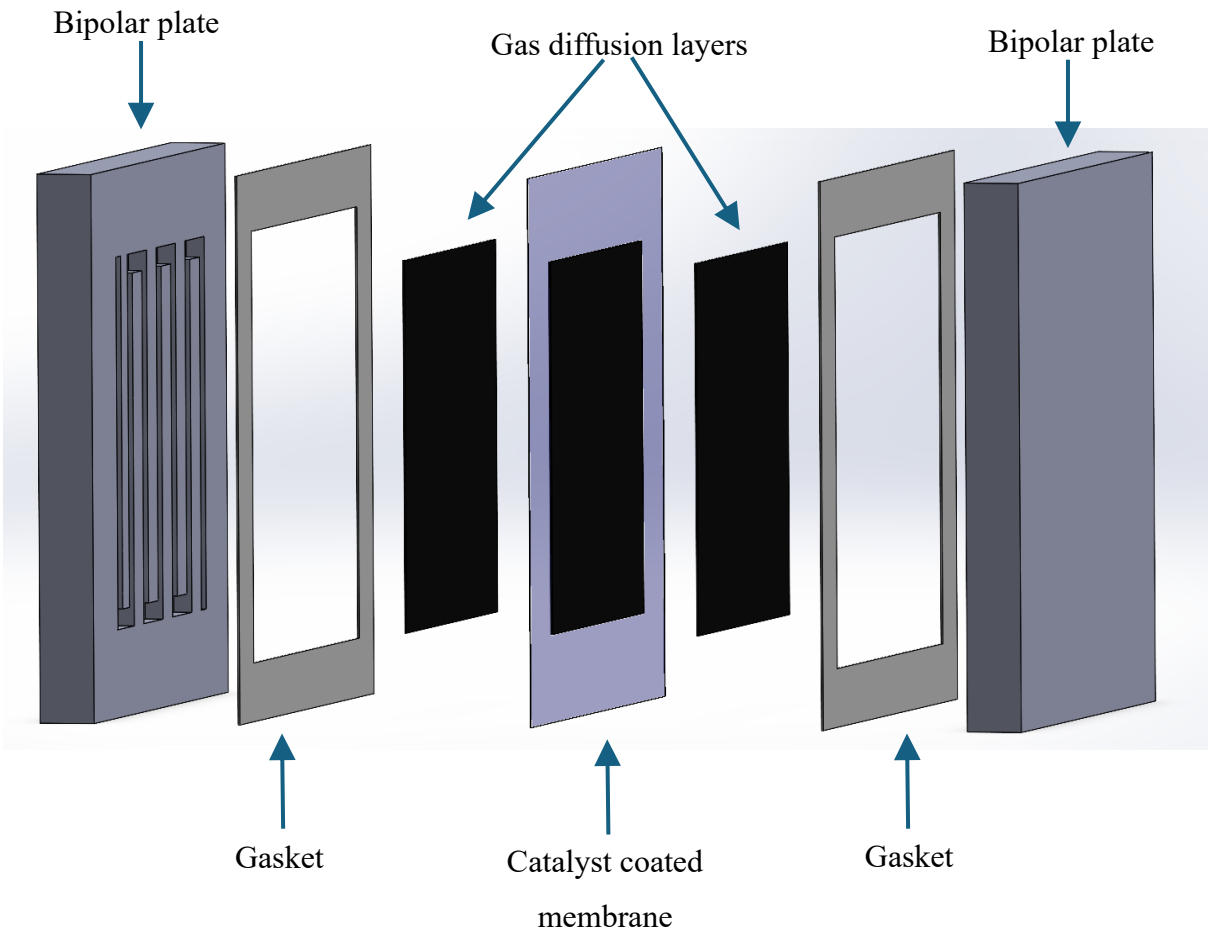

Figure 2.1 – PEM fuel cell components.

Proton exchange membrane

At the centre of the cell lies the proton exchange membrane which is designed to selectively conduct protons (H^+) and water between the anode and cathode. The membrane must also prevent ohmic shorting (electron transport) and gas crossover which both reduce the fuel cell performance and can cause damage to the membrane. This damage is in the form of membrane thinning and pinhole formation through local heat generation which then exacerbates gas crossover [47,48].

Catalyst layer

The electrochemically active catalyst layer is fixed to the membrane and together they form the membrane electrode assembly (MEA). Typically, the catalyst is an activated carbon supported platinum nano catalyst often referred as platinum black or Pt/C. Due to the sluggish ORR reaction at the cathode higher platinum loadings of 0.3-0.5$mg_{Pt}cm^{-2}$ are required compared to the HOR reaction at the anode at <0.05 $mg_{Pt}cm^{-2}$ [49]. Due to the high loading on the cathode substantial effort has been dedicated to reducing loadings to 0.1 $mg_{Pt}cm^{-2}$ or even

lower [50,51]. Activated carbon is used to support the platinum due to its low cost, porosity, high surface area and high electronic conductivity [52]. A polymeric binder which is made of the same material as proton exchange membranes is also used to bind the Pt/C to the membrane [49] and conduct the protons and water to and from the electrodes. Whilst plenty of research into platinum free catalysts have been conducted due to platinum's high cost and scarcity it remains the go to material for PEM fuel cells due to its superior performance and durability [53].

Gas diffusion layer

The gas diffusion layer (GDL) is designed to allow water as well as reactant and product gases to pass through it to and from the catalyst layer. The GDL also conducts electrons from the catalyst layer and provide mechanical support for the MEA. This 100-400µm layer [54,55] is made from carbon paper or a woven carbon fabric which may have a hydrophobic PTFE coating to avoid water chocking the pores and effectively remove water from the catalyst [54,56]. A carbon-based material is used as it is stable in acidic conditions, has good electronic conductivity and elastic behaviour under compression [57]. Due to their greater flexibility and ability to withstand higher compression woven fabrics are preferred [54].

Bipolar plate/current collector

The bipolar plate is the outer layer of the cell and provides flow channels for evenly delivering the fuel and oxidants to the electrodes through the GDL. The bipolar plate is also required to remove any water and exhaust gas from the cell, additionally the bipolar plate is required to collect the generated current [58]. The bipolar plates are made from either graphite or metals such as stainless steel, titanium, and a number of titanium alloys [59] as they need to be impermeable, durable, corrosion resistant and a good conductor of electricity and heat [60]. The configuration of the bipolar plate such as the plate size, anode and cathode flow field configuration, thickness and coolant flow fields must be optimised for the active area, intended application and operating conditions [58]. Optimising the flow field is a key factor in determining cell power [61] and many configurations exist such as parallel, coiled, single serpentine, multiple serpentine, interdigitated, wave parallel and 3D fine mesh [59,62,63] with the main considerations being pressure drop, even fluid distribution and efficient liquid water drainage [59,60,64]. In a single cell only a one-sided plate is used but for multiple cells the bipolar plate has flow control on both sides of the plate [62].

2.1.3 Fuel cell stack

A single cell is usually insufficient to supply the required power and therefore a series of cells are connected in a stack with single bipolar plates acting as an anode and a cathode for adjacent cells [65]. Due to this, the cells are connected in series [66,67] to produce higher voltages whereas current is determined by cell active area and cell current density.

2.1.4 Energy loss

The reversible voltage is the expected potential for an idea cell however, in reality the measured potential is lower due to losses which occur at or within the various cell components, under increasing current densities these losses increase resulting in lower cell voltage as seen in Figure 2.2.

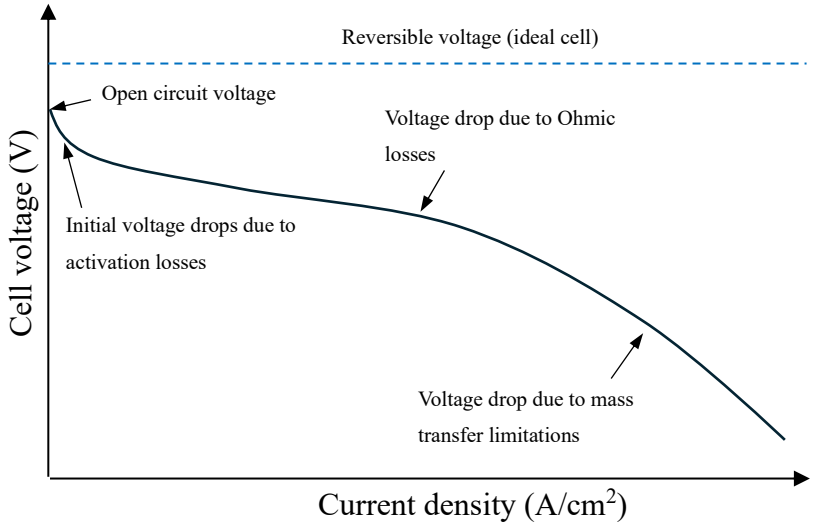

Figure 2.2 - Polarisation curve.

Losses at open circuit voltage

There are losses even for the open circuit potential (no current), this is due to fuel crossover, internal short circuits and mixed currents. Fuel crossover occurs due the diffusion of hydrogen across the membrane from the anode to the cathode [68,69]. Gases such as oxygen and nitrogen also diffuse across the membrane however, their diffusive fluxes are several orders of magnitude lower than hydrogen [68] and as such are often ignored. Internal short circuits are caused by the flow of electrons through the membrane instead of the external circuit [68,70,71]. Membranes are designed to be impermeable to gases and electrical insulators to minimise these effects which are more significant in thinner membranes however, compromises have to be made to optimise performance. Mixed currents result from PtO partially covering the surface

of the Pt catalyst and therefore a mixed potential is formed with the O_2/H_2O cathodic half reaction and the Pt/PtO anodic half reaction causing a potential drop compared to a pure platinum catalyst [68]. The effects of fuel crossover, internal short circuits and mixed currents are substantial at low current densities however, at high current densities these are insignificant [68].

Activation losses

Activation polarisation (η_{act}) is the voltage overpotential required to overcome the activation energy of the electrochemical reaction at the surface of the catalyst and can be described by the Butler-Volmer equation:

$$i = i_0 \left[\exp\left(\frac{a_a nF}{RT}\eta_{act}\right) - \exp\left(\frac{-a_c nF}{RT}\eta_{act}\right)\right] \tag{2.6}$$

Where i is the current density, i_0 is the current exchange density, a_a and $a_c$are the anodic and cathodic charge transfer coefficients respectively, n is the number of electrons transferred in the rate limiting step. At low overpotentials the Butler-Volmer equation simplifies and rearranges to form the Tafel equation [72]:

$$\eta_{act} = -ln\frac{RT}{a_c nF} log\left(\frac{i}{i_0}\right) \tag{2.7}$$

A plot of η_{act} vs log (i) gives a linear relationship with slope of $-ln\frac{RT}{a_c nF}$ which is known as the Tafel slope and an extrapolated intercept of i_0. This logarithmic response can be seen in the initial voltage drop in the polarisation curve seen in Figure 2.2.

Ohmic losses

Ohmic loss (η_{ohmic}) is the potential loss resulting from resistance to electron and ionic flow [73]. Resistance to electron flow comes from the electronically conductive components such as the catalyst layer, gas diffusion layer, current collector and interconnects as well as the contact resistance at the interface of these components. The largest source of ohmic loss is the resistance to ion flow through the membrane [74] which varies with the operating conditions of the cell. The Ohmic loss can be expressed as a sum of these resistances and is dependent upon the current as shown in Equation 2.8 [73]:

$$\eta_{ohmic} = IR_{ohmic} = I(R_{elec} + R_{ionic} + R_{contact}) \tag{2.8}$$

Where R_{ohmic} is the total Ohmic resistance, R_{elec}, R_{ionic} and $R_{contact}$ are the resistances due to electronic, ionic and contact resistance respectively.

The resistance for both the electronic and ionic can be determined from the conductivity of the material (σ), its length in the direction of charge flow (L) and the cross-sectional area of the conductor (A) as shown in Equation 2.9

$$R = \frac{L}{\sigma A} \tag{2.9}$$

The cell current (I) can be calculated from the current density and the cell area (A_{cell}) as shown in Equation 2.10

$$I = iA_{cell} \tag{2.10}$$

Hence the total ohmic loss can be expressed as shown in Equation 2.11

$$\begin{aligned} \eta_{ohmic} &= iA_{cell}R_{ohmic} \\ &= iA_{cell}\left(\sum\left(\frac{L_{elec}}{\sigma_{elec}A_{elec}}\right) + \frac{L_{memb}}{\sigma_{memb}A_{memb}} + R_{contact}\right) \end{aligned} \tag{2.11}$$

Where subscripts $elec$ and $memb$ refer to the electronic conductors and membrane respectively. This shows that the ohmic loss is linearly proportional to current density [75] which can be seen in the polarisation curve shown in Figure 2.2.

Concentration loss

At high current densities the mass transfer of reactants to the catalyst surface becomes insufficient and the concentration of reactants decreases. As the current density increases the limit of mass transfer is reached and concentration at the catalyst reaches 0. At this point a potential difference of 0 is obtained, the current density at this point is known as the limiting current density (i_L) and this region is known as the concentration region [76]. Assuming that the diffusion follows Fickian behaviour through the porous layers it is possible to determine the concentration of reactants and products at the catalyst surface through the flux across a concentration gradient from the bulk concentration in the flow channel and assuming no accumulation (steady state). Inserting these concentrations into the Nernst equation and using the definition of the limiting current density it is possible to determine the concentration loss as shown in Equation 2.12

$$\eta_{conc,Nernst} = \frac{RT}{nF} ln \frac{i_L}{i_L - i} \tag{2.12}$$

A limiting current density can be determined for both the anode and cathode however for fuel cells mass transfer limitations for oxygen are typically much more severe and so the anode is ignored [77]. The resistance to mass transfer consists of three parts: molecular diffusion resistance, Knudsen diffusion resistance and local transport resistance. Molecular diffusion resistance and Knudsen diffusion resistance mainly depend on the geometry of the gas diffusion layers and catalyst layers, specifically the thickness, porosity and pore size [78]. Local transport represents the impedance to gas permeation from the ionomer thin film to the Pt surface [78].

Whilst this method covers the potential loss due to diffusion, mass transfer can be limited by a drop in the concentration within the flow channels, this could be due to flooding or insufficient gas feed flow.

Overall losses

Although each loss in potential has its own dominating region of the polarisation curve, each contribution is always present and so the potential must be calculated from all 3 contributions as shown in Equation 2.13

$$E_{cell} = E_{OCV} - \eta_{act} - \eta_{ohmic} - \eta_{conc,Nernst} \tag{2.13}$$

Where E_{cell} is the cell potential. Understanding the relationship of current density and potential difference is essential. Optimisation should be targeted for a desired outcome for example if a cell is designed to operate at low current densities or occasionally operate at high peak current densities, reducing the concentration loss may not result in the desired improved performance. However, if a cell is required to operate at high current densities, then reducing concentration loss may result in the most significant performance gains. Reduction in cell efficiency is not the only factor for optimisation as cost, durability and operating conditions are also important. An example would be membrane thickness as thinner membranes are desirable for reduced ohmic loss, but thinner membranes are more susceptible to degradation. Another example would be the use of platinum free catalysts which are more affordable but less effective, for devices used infrequently however this reduction may be more acceptable. Operating cells at high current densities is also desirable for reducing the required cell area and hence reduced volume, weight and production cost therefore, it is often important to optimise all aspects of efficiency loss. Understanding these relationships is useful for understanding which contributions are most significant. The membrane is an important factor in this optimisation as it is a significant source of cell potential loss but also prone to degradation and sensitive to changes in hydration.

2.2 Proton exchange membranes

Proton exchange membranes are designed to transport protons and water between the electrodes whilst preventing electron transport and gas crossover. However, they must maintain these properties throughout their lifetime which is targeted at 25,000 hours by the U.S. Department of Energy[79] at a voltage drop of <10% for fuel cell electric vehicles [79][80]. Membranes are subject to both mechanical and chemical degradation during fuel cell operation which leads to increased gas crossover and membrane resistance [81]. These effects are most significant in thin membranes which have reduced membrane resistance and hence better performance.

2.2.1 Materials

Proton exchange membranes are made of either a pure polymer or a composite where materials are embedded into a polymer matrix. These ionic polymers are known as ionomers as they consist of electrically neutral repeating units and ionised units [82] which are bonded to the polymer backbone. The most common class of ionomer used in PEMFCs are perfluorinated sulfonic acid (PFSA) ionomers, these fluoropolymers are synthetic polymers synthesised through the copolymerisation of functionalised monomers [83]. Other ionomers exist such as sulfonated polystyrene (PSSA), sulfonated polyether ether ketone (sPEEK), polysulfone (PES), polyimide (sPI) and various others [84–86], have been developed as alternatives, these were developed due to the high cost, environmental concerns due to recycling difficulty, high fuel permeability, and loss of ionic conductivity at elevated temperatures in PFSAs [85]. Despite this PFSAs have continued to dominate the PEMFC market due to their remarkable ion conductivity and chemical-mechanical stability [87].

PFSA ionomers consist of a semicrystalline, chemically inert, and hydrophobic polytetrafluoroethylene (PTFE) backbone with perfluorovinyl ether branched chain side groups terminated with hydrophilic sulfonate groups [86–89]. PFSAs achieve their high proton conductivities through their interaction with water and achieve the highest conductivities at high humidities.

Mechanical degradation occurs due to non-uniform mechanical stresses [80]. Stress occurs due to the swelling and shrinking of the membrane due to changes in hydration, particularly at high humidities [81]. Under current load the water content of the cathode is higher due to electroosmotic drag and water generation causing greater strain and stress at the cathode side

of the membrane [81]. Localised stresses caused by particles, non-uniform cell conditions, vibrations and uneven clamping stress accelerates mechanical degradation [81].

Chemical degradation of the main chain and side chain occurs due to chemical attack mainly from hydroxide radicals (•OH) [87]. Peroxide radicals formed at the anode through oxygen permeation and at the cathode, as a by-product of the ORR reaction which is accelerated by the presence of metal ions such as Fe^{2+} and Cu^{2+} which catalyse peroxide decomposition [81,87]. These radicals attack both the main PTFE chain by attacking vulnerable H containing end groups producing HF and CO_2 from the CF_2 unit [87,90]. This process shortens the backbone and can cut off the whole side chain in a process referred to as chain unzipping [87,90]. This degradation can be monitored through the fluoride release [87]. The radicals also attack the side chains with multiple degradation mechanisms proposed through attacks to the sulfonate groups and ether linkages [87,90–95].

The first PFSA was Nafion which was developed and commercialised by DuPont in the mid 1960s for a Genal Electric fuel cell designed for NASA spacecraft missions [86,96]. Nafion has continued to dominate in literature studies despite a verity of alternative PFSAs such as 3M, Aquivion (formerly known as Dow SSC), GORE, Flemion [87] and Fumasep. Differences in the side chemical structure of some these ionomers can be seen in Figure 2.3.

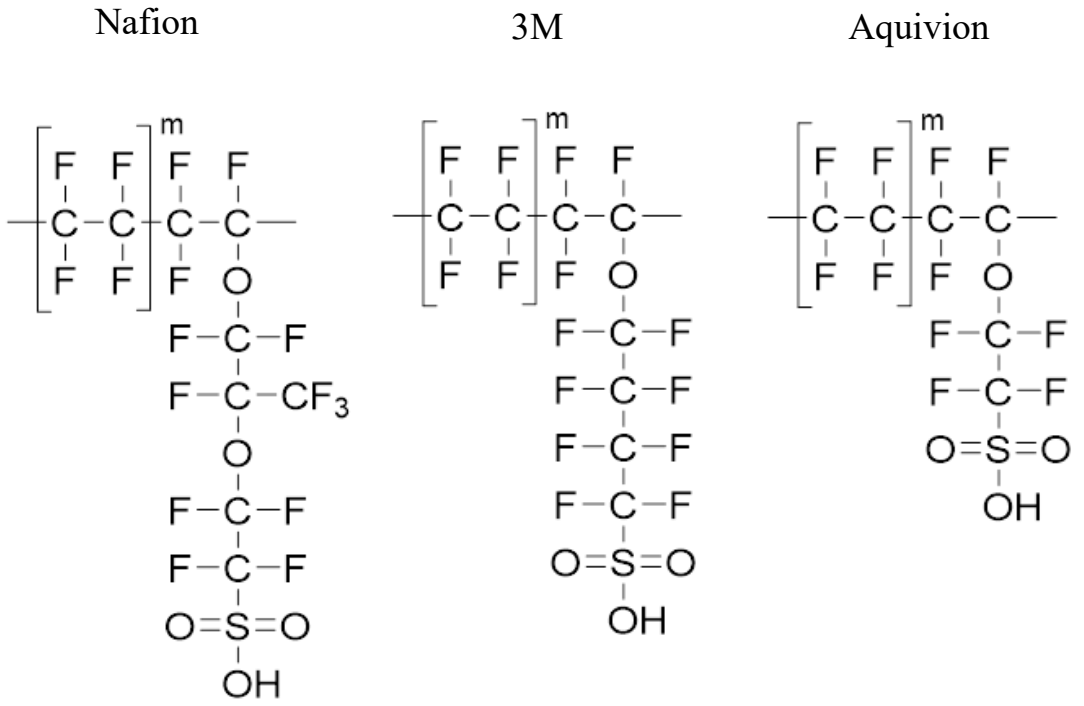

Figure 2.3 - Chemical structure of Nafion, 3M and Aquivion.

The ratio of backbone PTFE groups to side chain groups is an important factor in membrane development as it effects nanostructure, water uptake, swelling, conductivity, crystallinity, glass transition temperature and durability [87]. This property is characterised by the equivalent weight (EW) which is the weight of polymer per mole of sulfonate groups and can be calculated via $EW = 100m + MW_{side\ chain}$ [87], where m is the ratio of backbone PTFE groups to side chain groups as shown in Figure 2.3. This is assuming no other material is present in the membrane such as an additive. Ion exchange capacity (IEC) is a measure of the functional group within the membrane to undergo the displacement of ions. For PFSAs the sulfonate group is the functional group which dissociates under hydration to SO_3^- and H^+, the H^+ is free and can sometime be displaced with a positive metal ion such as Na+. IEC is inversely proportional to the equivalent weight and can be determined experimentally, conversion can be done via $EW = \frac{1000}{IEC}$.

Due to the size of the side chain, Nafion is denoted as a long side chain PFSA (LSC PFSA) whereas the 3M and Aquivion shown in Figure 2.3 are denoted as short side chain PFSAs (SSC PFSAs). SSC PFSAs generally have a lower EW and exhibit increased conductivity [97] possibly due them having better developed channels [98] with smaller but more widespread ionic domains [87,99]. SSC PFSAs also exhibit greater mechanical stability due to an increase in crystallinity [87,100] and greater resistance to chemical degradation due a reduced number of vulnerable ether linkages [100,101].

2.2.2 Water interactions

One of the most important factors affecting the performance and properties of PFSA membranes is its sorption behaviour as water affects their phase separated morphology [87] which determines their transport and mechanical properties. As such understanding the non-linear water uptake at different humidities and temperatures, water diffusion and the impact of water upon the phase separated morphology is important for subsequent understanding of macroscopic properties such as proton conductivity and water transport. Water uptake is generally determined through gravimetric measurements where a water uptake is compared to the mass of the dry membrane ($g_{water}/g_{dry\ membrane}$) and is often given as a percentage. The water uptake can also be expressed as molar fraction of water to sulfonic acid groups and is given the notation "λ". λ can be determined from the water mass uptake (WU) and equivalent weight using Equation 2.14

$$\lambda = WU\frac{EW}{M_{H_2O}} \tag{2.14}$$

Where M_{H_2O} is the molecular weight of water (18.02g/mol). Water sorption into the phase separated nanostructure is a complex process in which wate occupies domains of mostly 1-3nm although larger domains of >5nm have also been reported [87]. SSC PFSA ionomers have been found to have more dispersed smaller domains which leads to better connectivity compared with LSC PFSA ionomers [102–105] although smaller differences in the clusters are seen higher water contents [104]. The shape of these domains are usually assumed to be spherical, cylindrical or lamella. With increasing hydration these water domains swell increasing in size and begin to form connections between adjacent domains to create interconnected channels of water. This is described by the cluster network model proposed by Gierke, Hsu and co-workers [87,106,107], which proposes an evolution from spherical to rod like domains and is represented in Figure 2.4.

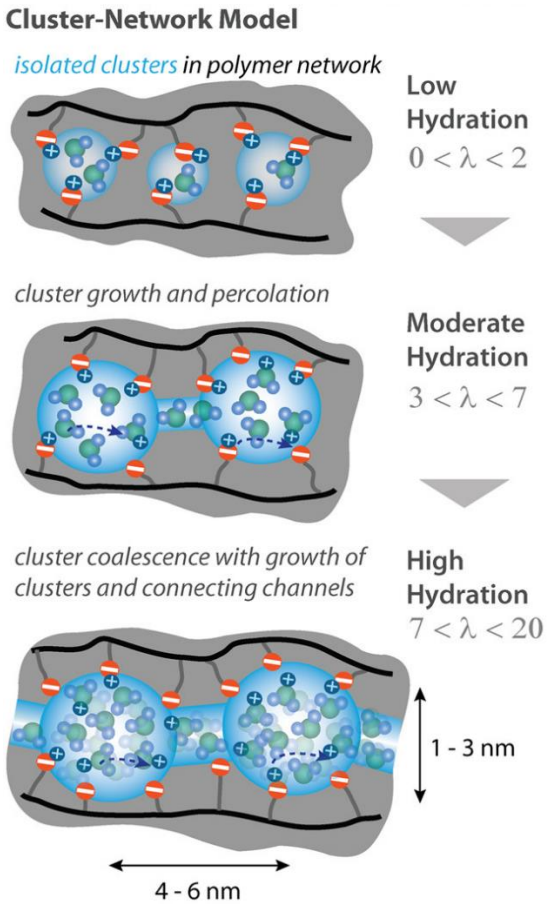

Figure 2.4 - Water cluster model of the phase separated morphology of PFSAs taken from [63].

Whilst assumptions have been made and used in molecular modelling, determining the exact shape, distribution and connectivity of these domains remains a challenge particularly across

different water contents [87]. Water within these domains interacts with the PFSA ionomer through hydrogen bonding interactions, particularly the sulfonic acid of the hydrophilic side chain. The strength of the interactions between the PFTE backbone and side chain with water does vary based in the chemical structure of the PFSA, particularly the side chain [87,102,108,109] and the crystallinity of the membrane which decreases the water domain spacing [87].

Nanoswelling of the water domains in order to accommodate more water causes the membrane to swell macroscopically increasing in volume. As membranes require dimensional stability [110] understanding the anisotropic nature of swelling and shrinking is vital. There are a number of factors which impact the swelling properties of PFSAs including water uptake, thermal history, reinforcement, previous stress, confinement, compression, degradation, PFSA chemistry and hygral fatigue [87,111]. As stress can cause elastic deformation (temporary) and plastic deformation (permanent) [87]. Understanding swelling induced stress and other sources of stress in membranes is vital in managing mechanical degradation. The increase in volume is 3 dimensional however, swelling and shrinking can be anisotropic with differences typically observed for the in-plane and thickness directions [112] as shown in Figure 2.5 where it can be seen that most studies only obtain a dry and hydrated measurement. Non reinforced membranes such as Nafion 212 typically exhibit an almost isotropic behaviour whereas reinforced membranes such as Nafion XL exhibit significant swelling anisotropy [112,113]. Membranes that have been mechanically reinforced with materials such as ePTFE provide in-plane support and hence reduce the in-plane swelling unfortunately, the swelling in the thickness direction increases as the total volume swelling is comparable to non-reinforced membranes to resulting in swelling anisotropy [87,112]. In-plane swelling is a bigger concern as membranes are confined in a fuel cell stack by frames and plates which increases the in-plane stress leading to fatigue and creep eventually causing crack formation [111], in-plane swelling can also lead to separation of the MEA components [113]. Membranes are typically under compression in the thickness direction which doesn’t cause induced damage, but significant swelling can impact cell compression [113].

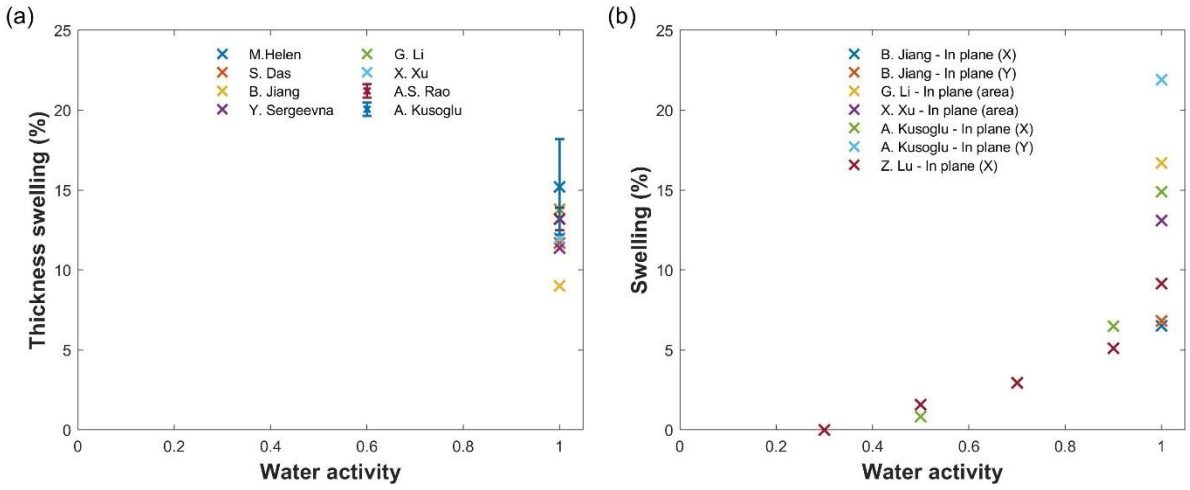

Figure 2.5 - Swelling of Nafion from literature in the thickness (a) and inplane (b) directions [114–122].

During hydration from a dry PFSA the first water molecules form a strong hydrogen bond ionising and binding to the sulfonic acid group forming hydronium ions (H_3O^+). From λ=1-2 water molecules continue to form strong hydrogen bonds around the sulfonic acid group forming a stable hydration shell allowing the hydronium ion to become dissociated and form more complex hydrated hydronium ions of $H_5O_2^+$, $H_7O_3^+$ and $H_9O_4^+$with the proportion of larger ions increasing with hydration across the whole sorption process [123]. These strongly hydrogen bonded water molecules surround the sulfonic acid group are termed strongly bound water and require elevated temperatures of 120°C for removal with some even persisting up to 200°C [87,124,125]. Additional water molecules enhance the phase separation and begin to form hydrophilic ion rich domains which can begin to form an interconnected network of clusters. These water molecules begin to form hydrogen bonds with the strongly hydrogen bonded water molecules in a second hydration shell rather than the sulfonic acid group. At λ=5-6 the percolation threshold is reached [126] and the clusters can be considered to be an interconnected network. At λ>6 further growth of the domains promotes a more bulk-like water region [87] in which water form weak temporary hydrogen bonds which have an average lifetime of ~1ps [127–129] and can freely move exhibiting more liquid like properties with reorganisation of the hydrogen bonding network, this water is known as bulk water.

2.2.3 Proton and water transport

The transport of water and protons are highly coupled with protons conducting through the water. The nature of the water and its interaction with the sulfonic acid group are important factors in the proton conducting mechanisms, impacting dynamics across a wide range of time and length scales [87]. Proton transport generally occurs through two mechanisms, the first is

the vehicular mechanism in which protonated water complexes translate. The second mechanism is the Grotthuss hopping mechanism where a series of proton transfer reactions take place between molecules of water through the temporary formation of protonated water complexes, an example is shown in Figure 2.6.

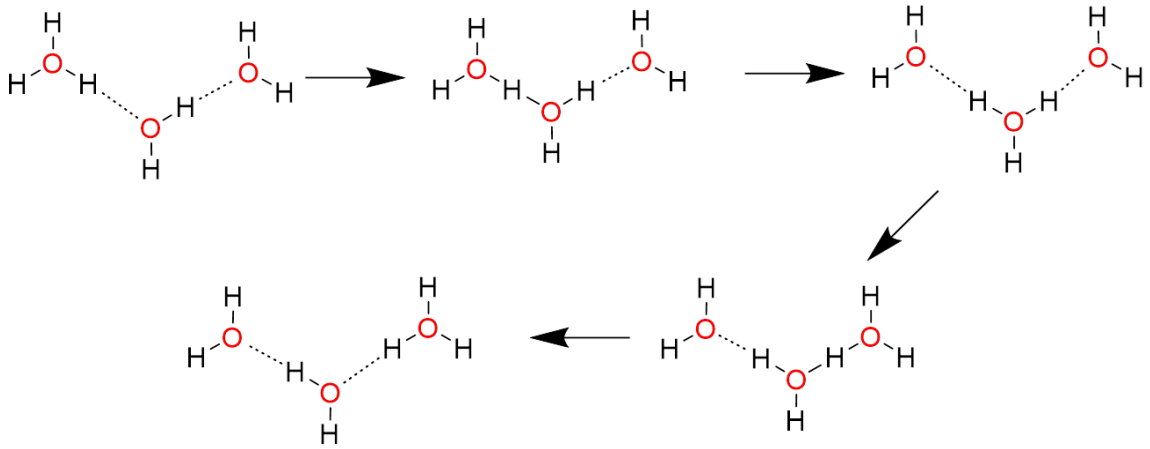

Figure 2.6 - Illustration of Grotthuss hopping mechanism.

Due to the nature of the Grotthuss hopping mechanism, the proton that is initially dissociated is not transported through the whole membrane. In low humidities the vehicle mechanism dominates however, effective Grotthuss hopping is possible in more hydrated conditions and requires a fast reorientation compared with the translation for the vehicle mechanism resulting in much faster conductivity [87]. As the Grotthuss hopping mechanism requires rapid reorientation, the mechanism primarily occurs in bulk-like water where weak hydrogen bonds are temporary and reorientation is fastest. This results in fast proton transfers every 1.9-0.5ps on average with faster hops occurring in more hydrated PFSAs [123]. It is therefore important to understand both the reorientational motion of water and the translational movement of water in the conduction mechanisms for PFSA membranes.

Whilst highly hydrated membranes are desirable due to their high performance, a build-up of excess water can cause flooding which limits the transport of reactants to the catalyst layers. Maintaining membrane hydration in fuel cells without causing flooding can be challenging. Water is generated at the cathode through the oxygen reduction reaction, water is also introduced and extracted though the humidified inlet and outlet gas streams respectively. The distribution of water varies within fuel cells and therefore understanding water transport dynamics is key for optimum design and operation of PEM fuel cells.

Due to the electric field across the membrane during operation, water is pulled towards the cathode [130] in a process known as electroosmotic drag. This opposes the diffusion of water

which typically is assumed from the cathode to the anode [130]. When a pressure drop is observed across the membrane water is also transported due to hydraulic permeability and is related to a chemical-potential driving force [87].

2.2.4 Water diffusion

Many techniques have been used to study the diffusion of water in PFSA membranes including, dynamic vapor sorption (DVS) [131–133], pulsed field gradient nuclear magnetic resonance (PFG-NMR) [134–137], Fourier transform infrared (FTIR) spectroscopy, steady state monitoring of water permeation between two water activities, radiotracer and quasi-elastic neutron scattering (QENS) [138,139]. These different techniques work at different length scales and as a result measured values can vary by orders of magnitude (10^{-8}-10^{-5}) with higher diffusivity measured at smaller time and length scales, which is due to the different water transport mechanisms being probed [140].

QENS has the shortest time and length scale (~10ps, ~0.15nm) [139] and as such it probes diffusion on the molecular scale and has the highest reported diffusion at ~10^{-5} cm^2/s [138,139], NMR also has a short time and length scale (~1-100ms, a few μm) [134–137] and as a result has higher reported diffusivity at ~10^{-6} cm^2/s [134–136,141,142] than other techniques which take macroscale measurements with reported diffusivities of ~10^{-7} - 10^{-8} cm^2/s. Macroscale steady state is quantified through the measurement of the diffusive flux (rate of transfer of a diffusing species through a cross section) over a membrane with a concentration gradient maintained by different environmental conditions on each side of the membrane.

Transient diffusion tracks the diffusion of water over time as a change in the environmental condition occurs. The diffusivities obtained from this method are generally lower than steady state measurements. This difference is due to some delay in the change to the environmental condition, polymer relaxations and swelling [143–146] due to structural changes in response to the change in water uptake [147]. To extract water diffusivity from these techniques, models must be applied and as such assumptions have to be made. Many different variations and approaches have been used with differing assumptions and experimental geometries. As these different techniques probe different aspects of water diffusion due to their different time and length scales, procedures and driving forces, an understanding of each approach, its limitations, variables and membrane morphology is needed.

Reported diffusivities from steady state [148–152], transient [131–133,152,153], NMR [135,142,154–157] and QENS [138,139] measurements can be seen in Figure 2.7. The plot

demonstrates the variability in the value of diffusion coefficients from different methods and also within the same technique, in particular the steady state and transient measurements. Different techniques shown varying trends in extracted diffusivities. For instance, transient measurements show a decrease in diffusivity at around λ>5, in contrast to the plateau seen from other techniques. Both the steady state and transient measurements exhibit a peak at λ = 2-4 and λ =3 respectively. This peak is sharper from steady state measurements, and is likely due to the water content range caused by the step change of transient measurements. In addition, the location of the peak varies, however this likely due to differences in the measurement of water content such as differences in residual water content as the peak location of humidity dependant data is the same as seen in Figure 5.13.

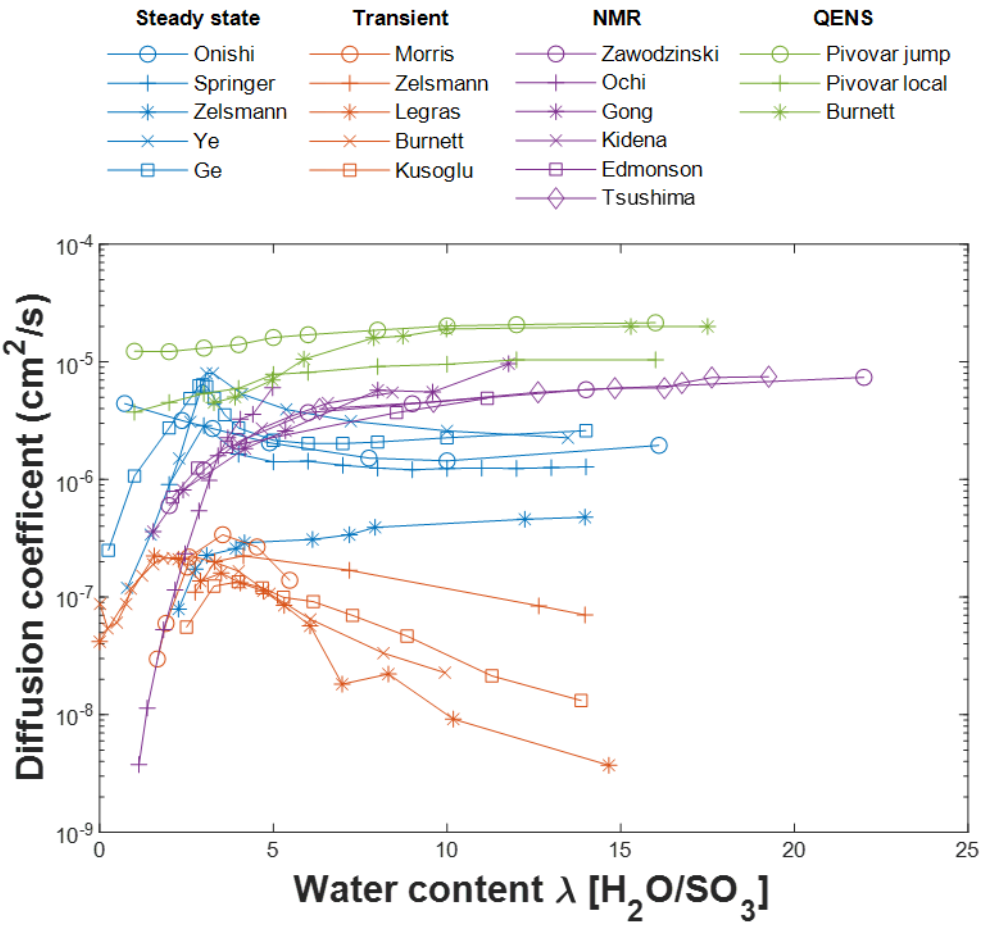

Figure 2.7 - Reported water diffusivity in steady state, transient, NMR and QENS [131–133,135,138,139,142,148–152,152–157].

Terahertz has previously been used to study the diffusion of water in polymers [158]. However, this study was for thicker films with longer experimental times (days) using water submersion. As the work shown in chapter 4 demonstrates THz-TDS can be used to measure water uptake

in a controlled environment, it should be possible to replicate the work of DVS in measuring transient water diffusion in PFSA films at different humidities.

2.2.5 Membrane postprocessing and additives

There are many inherent factors which influence the performance of PFSA membranes such as the equivalent weight, side chain length and chemical structure of the PFSA ionomer. There are also a number of techniques used to further improve membrane performance, in particular the longevity of the membrane by increasing the chemical and mechanical stability. It is well known that membranes are sensitive to temperature and membrane properties are influenced by thermal history. When testing membranes, it has become common practice to remove all thermal history through boiling membranes in peroxide, sulfuric acid and then water, these remove thermal history whilst cleaning, reactivating and inducing hydration respectively. Other heat treatment processes such as thermal annealing can also be used selectively impact membrane properties such as increasing crystallinity. These heat-treatments have been shown to alter a number of properties such as water uptake [159–164], proton conductivity [112,163–165], diffusivity [163,166], mechanical properties [160–164], phase separated nanostructure [160,162–165,167,168], density [169], permeability [170,171] and thermal stability [166].

The method of membrane manufacturing can also impact performance which are generally extrusion or dispersion cast. Extruded membranes have higher water uptake with better conductivity and mechanical properties [171,172]. However, dispersion cast membranes can be used to create thinner membranes and also allows reinforcements or additives to be incorporated. The properties of dispersion cast membranes, in particular their mechanical nature is highly dependent upon the solvent used and casting conditions such as temperature [86,173,174].

The incorporation of reinforcements such as expended PFTE and additives such as CeO_2 [175], SiO_2 [176], TiO_2 [177], ZrO_2 [179], clays [180], carbon nanotubes [181] and zeolites [182] into PFSA membranes can also improve their performance. Reinforcements are used to reduce in-plane swelling and reducing mechanical stress but have greater thickness swelling [87]. Additives such as CeO_2 are used as radical scavengers reducing chemical degradation from peroxide radicals and inorganic fillers are used to improve water retention capacity particularly at low humidities, selectivity, mechanical properties and thermal stability[87].

Improving the mechanical and chemical stability of PFSAs generally decreases the proton conductivity of the membrane however, more resilient membranes can be made thinner and

therefore reduce the membrane resistance. Membrane optimisation is a complex process with many interlinked factors and trade-offs which generally impact stability and/or electrochemical performance which must be optimised for the requirements of the desired application.

2.3 Modelling diffusion

In order to extract the diffusivity of a membrane using transient or steady state measurements, certain assumptions must be made about the nature of the diffusion taking place. This section will explore the approaches taken in modelling transient diffusivity however, many of the concepts can also be applied to steady state diffusivity.

2.3.1 Theoretical underpinnings and governing processes

As membranes are thin plane sheets, the diffusion of water can be considered to be one dimensional with the assumption that diffusion through the edges is negligible. Much like many other polymer systems [158,183] the diffusion kinetics of PFSA membranes follows Fickian behaviour [87,145,146,184] in which the diffusive flux (rate of transfer of a diffusing species through a cross section) is directly proportional to the concentration gradient of the diffusing species. This can be derived from random molecular motions and is shown in Equation 2.15

$$J = -D\frac{dC_w}{dx} \tag{2.15}$$

Where J is the diffusion flux, C_w is the water concentration, D is the diffusion coefficient and x is the distance from the centre of the membrane plane. Ficks first law can be used to calculate the diffusivity from the water flux determined in steady state diffusivity measurements. Using Ficks first law it is also possible to derive the change in concentration as a function of time through the conservation of mass and is shown in Equation 2.16, this is known as Fick's second law and can be used for determining diffusivity in transient measurements.

$$\frac{\partial C_w}{\partial t} = D(C_w)\frac{\partial^2 C_w}{\partial x^2} \tag{2.16}$$

Where t is the time elapsed and $D(C_w)$ is the diffusivity at a given water content. This equation can be solved to determine the rate of sorption or desorption when the initial distribution and boundary conditions are known. Whilst it is possible to solve this problem, some assumptions must be made such as instantaneous change to RH, the initial water distribution is uniform, diffusivity is constant over the RH range and constant surface concentration, meaning that interfacial diffusion is neglected. These can be expressed using Equations 2.17 - 2.19

$$C_w = C_0, \qquad -\frac{l}{2} < x < \frac{l}{2}, \qquad t = 0 \tag{2.17}$$

$$C_w = C_1, \qquad x = \pm\frac{l}{2}, \qquad t \geq 0 \tag{2.18}$$

$$\frac{\partial C_w}{\partial t} = D\,\frac{\partial^2 C_w}{\partial x^2} \tag{2.19}$$

Where C_0 is the initial water concentration, C_1 is the water concentration at an infinite time and l is the membrane thickness. Problems such as this are known as initial value problems or Cauchy problems as the system is described by a differential equation and the initial conditions are known. A solution must satisfy both the differential equation and all initial values. A solution to this problem was determined using Laplace transforms and was presented by Crank [147] shown in Equation 2.20.

$$\frac{C - C_0}{C_1 - C_0} = \frac{M_t}{M_\infty} = 1 - \frac{8}{\pi^2}\sum_{n=0}^{\infty}\frac{1}{(2n+1)^2}\exp\left(-\frac{D(2n+1)^2\pi^2 t}{l^2}\right) \tag{2.20}$$

Where M_t and M_∞ are the increase in water uptake from the initial water uptake at t=0 to a time t and an infinite duration (steady state) respectively. Whilst this solution satisfies the set conditions it is important to note its limitations due to the assumptions made.

2.3.2 Interfacial resistance

Constant concentration at the membrane interface has been assumed however, in reality the change in humidity is not instantaneous and there are mass transfer limitations within the water vapor close to the membrane surface as shown in Figure 2.8.

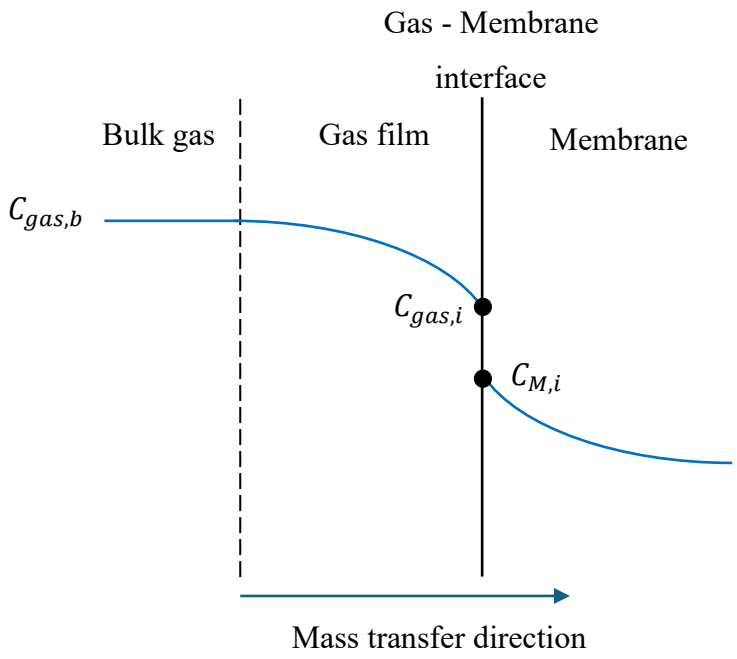

Figure 2.8 - Illustration of interfacial mass transfer.

Where $C_{gas,b}$ is the concentration of water in the bulk gas phase, $C_{gas,i}$ is the concentration of water vapor at the membrane interface and $C_{M,i}$ is the concentration of liquid water at the membrane interface. As the mass transfer of water vapor is complex due to various factors such as air flow, temperature and environment geometry this factor is typically determined experimentally. The boundary condition can be described through the water flux at the interface as shown in Equation 2.21 [131].

$$D\frac{dC_w}{dx} = k_m(C_\infty - C_0), \qquad t \geq 0 \tag{2.21}$$

Where k_m is the mass transport coefficient which is inversely proportional to the interfacial resistance. A solution to Fickian diffusion with this boundary condition is shown in Equation 2.22 [131].

$$\frac{M_t}{M_\infty} = 1 - \sum_{n=0}^{\infty} \frac{8\sin^2(\beta_n/2)}{{\beta_n}^2 + \beta_n \sin(\beta_n)} \exp\left(-{\beta_n}^2 \frac{Dt}{l^2}\right) \tag{2.22}$$

Where β_n are the positive roots of the Equation 2.23.

$$\beta_n \tan(\beta_n/2) = Bi \tag{2.23}$$

Bi is the dimensionless Biot number which represents the ratio of the characteristic time for diffusion through the bulk membrane ($\tau_{diffusion}$) and mass transport to the membrane interface

($\tau_{interface}$). It therefore can be used to determine which process dominates such as when water transport is solely limited by diffusion in the membrane i.e $\tau_{diffusion} \ll \tau_{interface}$ the Biot number approaches 0 and the equation simplifies to the solution presented by crank [147]. Using this equation, it is possible to fit both the Biot number and diffusivity from the transient water uptake.

2.3.3 Humidity response

As changes in humidity are not instantaneous the RH response can also lead to some delay. To account for this, the interfacial concentration at the membrane interface can sometimes be described by an exponential approach to an equilibrium as shown in Equation 2.24.

$$C_w = C_1\left(1 - exp\left(-\frac{t}{\tau_s}\right)\right), \qquad x = \pm\frac{l}{2}, \qquad t \geq 0 \tag{2.24}$$

Where τ_s is the time constant for obtaining equilibrium saturation at the film surface and can be used to represent an instrumental parameter such as the change in humidity. Using this new boundary condition, it is possible to derive a time dependant equation for Fickian diffusion as shown in Equation 2.25.

$$\frac{M_t}{M_\infty} = 1 - \exp\left(-\frac{t}{\tau_s}\right)\left(\frac{4\tau_s D}{l^2}\right)^{\frac{1}{2}} tan\left(\frac{l^2}{4\tau_s D}\right)^{\frac{1}{2}}$$
$$\frac{8}{\pi^2}\sum_{n=0}^{\infty}\frac{\exp\left(-\frac{D(2n+1)^2\pi^2 t}{l^2}\right)}{(2n+1)^2\left(1-\left((2n+1)^2\frac{\tau_s D\pi^2}{l^2}\right)\right)} \tag{2.25}$$

2.3.4 Simple exponential model

If multiple diffusivities or time dependant process exist within the measurement system, the analysis can become very complex and therefore selecting the right model for a given experiment can be challenging as the model must describe all significant factors. An empirical approach can therefore be used such as a simple exponential model shown by Equation 2.26 which has the capability to capture multiple time dependant processes.

$$\frac{M_t}{M_\infty} = \left(1 - \sum_m A_m \exp\left(-\frac{t}{\tau_m}\right)\right) \text{ with } \sum_{m=1} A_m = 1 \tag{2.26}$$

Where A_m is an arbitrary constant and τ_m is a time constant for the process m.

2.3.5 Finite element analysis

Whilst the simple exponential model can incorporate many time dependant processes, it is limited due to requirement of the processes to follow the exponential behaviour. Finite element analysis is a technique for solving differential equations and is typically applied to heat transfer, fluid flow, mass transport and structural analysis as it can be applied to multiple spatial dimensions. Applying this technique in the study of membrane diffusion provides an approach which can incorporate many processes which aren't required to be exponential however, each process requires a satisfactory model or additional data for incorporation. This technique works by discretisation of the system into nodes of smaller simpler parts called finite elements which can be calculated using approximations and the surrounding nodes. These finite elements can be explicit where the system variable is calculated at a later time by extrapolation from the current variable or implicit where the variable is calculated from the current and later variables. Finite elements are created through tessellation, as the diffusion can be considered one dimensional this tessellation is simple and takes a square grid pattern in the thickness and time directions as illustrated in Figure 2.9.

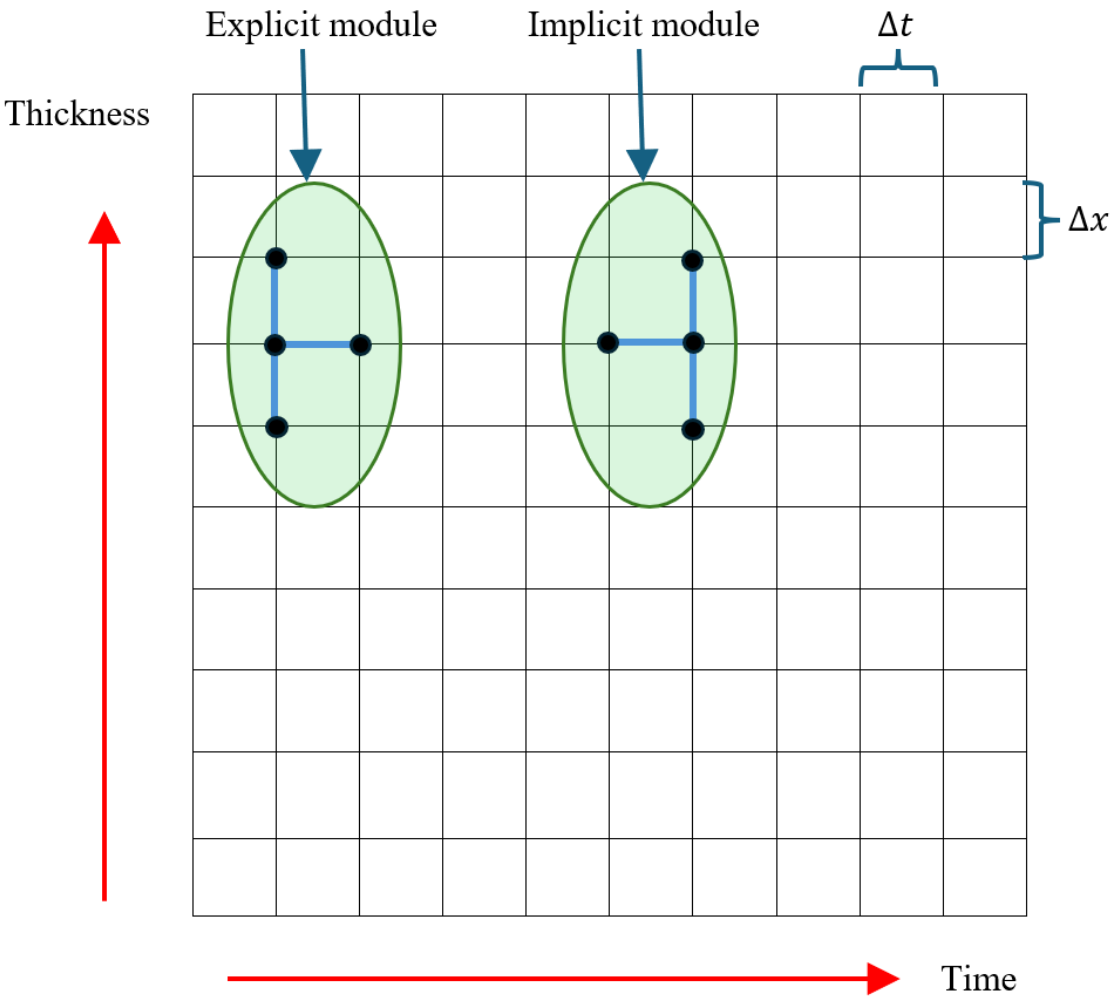

Figure 2.9 - Tessellation grid for finite element modelling of diffusion in the thickness direction.

An explicit module based around an interior node n_0 can be created as shown in Figure 2.10 where Δx and Δt are the step size for the thickness and time dimensions respectively. Finite element analysis is an approximation and the error decreases with reduced step size however, this also increases the computational cost.

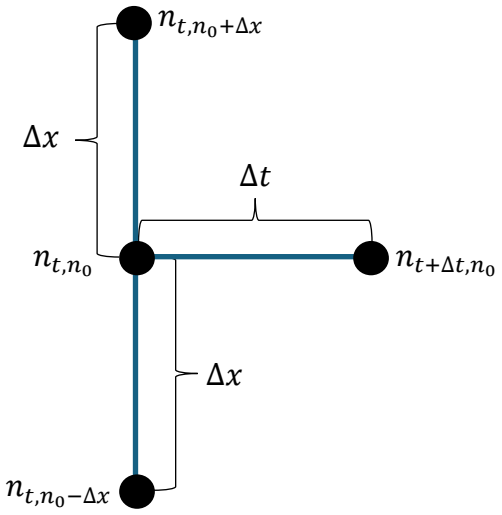

Figure 2.10 – 4 node interior explicit module for finite element analysis.

Using our expression for $\frac{dC_w}{dt}$ and $\frac{\partial^2 C_w}{\partial x^2}$ from Equation 2.16 we can first expand a Taylor series from node n_{t,n_0} to $n_{t+\Delta t,n_0}$ commencing with the t direction to form an expression for the rate of concentration change as shown by Equation 2.27.

$$\frac{C_{t+\Delta t,n_0} - C_{t,n_0}}{\Delta t} = \frac{dC_w}{dt}_{n_0} + \mathcal{O}\frac{\Delta t^2}{2} \tag{2.27}$$

This is known as the forward difference approximation where the truncation error $\left(\mathcal{O}\frac{\Delta t^2}{2}\right)$ is second order. The second order spacial derivative can be calculated using a Taylor series in the x direction as shown by Equation 2.28.

$$\frac{C_{t,n_0+\Delta x} - 2C_{t,n_0} + C_{t,n_0-\Delta x}}{\Delta x^2} = \frac{d^2 C_w}{dx^2}_{n_0} + \mathcal{O}\frac{\Delta x^4}{12} \tag{2.28}$$

This is the central difference approximation for the second derivative with a fourth order truncation error $\left(\mathcal{O}\frac{\Delta x^4}{12}\right)$ and substitution of Equation 2.27 and 2.28 into Ficks law Equation 2.16 yields Equation 2.29.

$$\frac{C_{t,n_0+\Delta x} - 2C_{t,n_0} + C_{t,n_0-\Delta x}}{\Delta x^2} = \frac{1}{D}\frac{C_{t+\Delta t,n_0} - C_{t,n_0}}{\Delta t} + \mathcal{O}\frac{\Delta t^2}{2} + \mathcal{O}\frac{\Delta x^4}{12} \tag{2.29}$$

This can be rearranged to obtain Equation 2.30.

$$C_{t+\Delta t,n_0} = \frac{D\Delta t C_{t,n_0+\Delta x} + (\Delta x^2 - 2D\Delta t)C_{t,n_0} + D\Delta t C_{t,n_0-\Delta x}}{\Delta x^2} \tag{2.30}$$

Where $\frac{D\Delta t}{\Delta x^2}$ is known as the Fourier number. This explicit method is known as Eulers method and requires $\frac{D\Delta t}{\Delta x^2} < \frac{1}{2}$ to be stable and converge. This allows all nodes ($n_{t+\Delta t,n_0}$) to be determined based on the previous time points of $n_{t,n_0-\Delta x}$, n_{t,n_0} and $n_{t,n_0+\Delta x}$ beginning from t=0 if the diffusivity, initial distribution and boundary conditions are known. Implicit methods also exist, these are based around implicit modules such as the one shown in Figure 2.9 and are more stable, not needing to follow the Fourier number limit. However, they require a number of simultaneous equations to be solved which generally involves inverting many a tridiagonal matrices. To use both explicit or implicit finite element methods, the boundary conditions must be defined and are typically characterised as Dirichlet or Neumann. For a Dirichlet boundary, the value of the function i.e. concentration is specified whereas for a Neumann boundary the normal derivative is specified at the boundary.

2.3.6 Impact of temperature and pressure

In steady state and transient diffusion studies conducted at various temperatures it has been observed that the rate water diffusivity in both sorption and desorption increases with temperature [131,132,151]. This is generally represented by an Arrhenius equation as shown by Equation [131].

$$D(T) \propto \exp\left(-\frac{E_a}{RT}\right) \tag{2.31}$$

Where E_a is the activation energy for water diffusion, R is the ideal gas constant and T is temperature. Due to this effect, temperature is generally maintained throughout an experiment. The reported activation energies are 20-30 kJ/mol [143,185,186] for sorption experiments whereas values of 12-28kJ/mol [135,137,157,187,188] are reported from NMR measurements. Higher values also reported at 33-44kJ/mol [187,188] for subzero temperatures which is likely due to water freezing [188] and represents the activation energy of non-freezing water diffusion [187]. The rate of water diffusion reported by NMR also decreases with pressure [189,190]. Understanding the effects of both temperature and pressure are important as fuel cells and electrolysers can be operated under a variety of different operating conditions.

2.4 Probing water states

The unique nanomorphology of PFSA gives rise to a variety of environments where water can exist, thus resulting in multiple different water states governed by a combination of geometric factors and intermolecular interactions. As water plays a vital role in the proton conductivity of PFSAs through the Grotthuss and vehicle mechanisms, understanding the nature and properties of water within the nanodomains is critical in understanding membrane performance. Many techniques have been used to characterise membrane hydration such as small angle X-ray scattering spectroscopy [105,190,191], neutron scattering and imaging [192–196] nuclear magnetic resonance [136,197–199], microwave dielectric relaxation spectroscopy [200,201], Fourier transform infrared spectroscopy (FTIR) [202–206], dynamic vapor sorption (DVS) [208,209], differential scanning calorimetry (DSC) [210–217] and Raman spectroscopy [218–221]. These techniques have been used to study different aspects of membrane hydration such as structure [106,191,192,197,205,222–225], diffusion [137,198,208,209,218,224,225] and proton conduction [106,199,202–204,211–213]. Water properties and states characterised by these techniques typically share descriptive similarities such as water which is strongly bound to the sulfonate group through hydrogen bonds. However, each technique with the exception of dielectric spectroscopy and terahertz time domain spectroscopy probe different physical phenomenon, therefore both differences and similarities in the descriptions, definitions and boundaries between acquired states can be expected.

Dynamic vapor sorption (DVS) is a gravimetric technique most commonly used for measuring water content as a function of relative humidity. Adsorption isotherms are created by plotting the relative weight of water to the weight of the dry material, usually as a percentage. This curve is known as an adsorption isotherm where isotherm refers to constant temperature. The shape of an adsorption isotherm can be described through models which can be empirical or theoretical and based upon an assumption of an equilibrium of the adsorbent at the adsorption surface. For example, the Langmuir isotherm is derived based on a fixed number of absorption sites situated in a single surface layer or BET with multiple layers. The absorption isotherm of PFSAs are nonlinear and can exhibit hysteresis between the sorption and desorption. A number of models have been used to describe the shape of the isotherms including the BET, GAB, Flory-Huggins, Feng's, Polynomial and Park's models [87,208,209,226,227]. The park model is interesting as it is comprised of three different models, each of which describes different sorption behaviours attributed to different types of water. The first model is Langmuir's model

and describes the initial shape of the isotherm below ~20% RH. The second model is Henrys law which is a linear model, and the shape can often be observed in the middle of the isotherm. The shape of the third isotherm can be observed at high humidities of greater than ~60% RH and follows a water clustering model. These models can be combined through addition to create the park model with 3 water populations each described by a model. Specific absorbed water (W_{SA}) is described by Langmuirs model and represents strongly bound water with little mobility, nonspecific absorbed water (U_{NSA}) is described by Henry's law and has the highest mobility, clustered water (W_C) is described by the water clustering model and represents water which forms through water aggregation [208,209]. By fitting a sorption isotherm to the Park model it is possible to determine these water populations as shown in Figure 2.11. It should be noted that the quantity of specific absorbed water can vary significantly as residual water remains at 0% RH which is not measured but would contribute exclusively towards the Langmuir portion of the model. Whilst this model does not probe different properties of water it does provide some indication of the nature of water and its interaction with the PFSA ionomer.

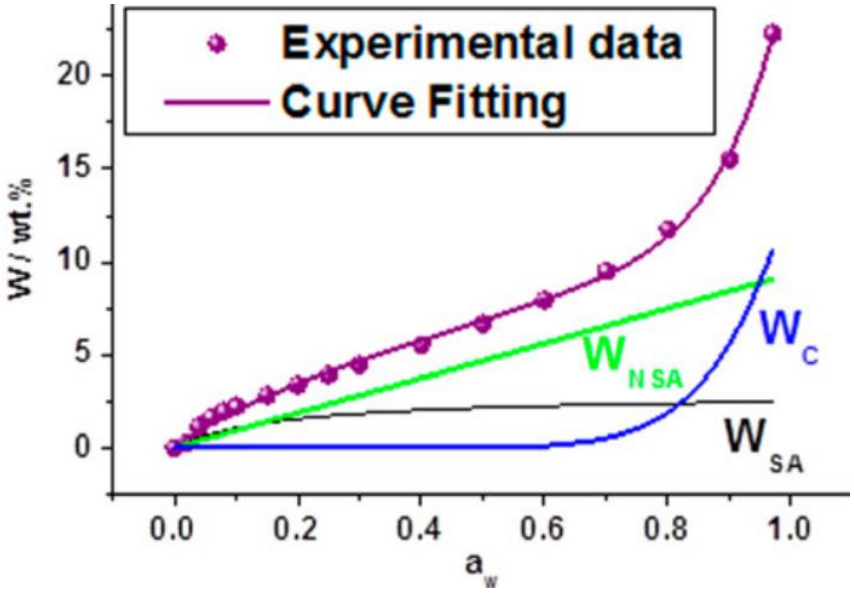

Figure 2.11 - Example Park model fitting of Nafion membrane taken from [208].

Fourier transform infrared (FTIR) spectroscopy has been used extensively to study PFSA ionomers as the ~4000-400cm^{-1} range contains many absorption bands which have been identified as corresponding to many different components of Nafion and water such as CF2 stretching, SO stretching, CF stretching, COC stretching, and HOH bending vibrations [203,206,228,229]. The two main bands corresponding to water are the OH stretching band located at 4000-2700cm^{-1} and the HOH bending located at 2000-1400cm^{-1} [203,228,229].

Within each band multiple overlapping peaks have been observed corresponding to water molecules associated with different species. Of particular interest for this work is the peak located at 1630cm^{-1} which has been assigned to HOH bending vibration of water molecules associated with SO_3^- groups [203,228,229], this peak is particularly interesting as Kunimatsu et al [203] demonstrated that this peak increases linearly with conductivity. Within the same HOH bending band, an asymmetric peak located at 1740-1710 has been assigned to protonated water molecules (hydronium, Zundel and Eigen) [203,207,228,229], this peak appears to be interesting as theses ions play a significant role in the Grotthuss hopping mechanism however the peak intensity quickly plateaus at low membrane hydration [203], this is consistent with molecular dynamic simulations where protons almost fully dissociate at λ=3 [123,230]. These two peaks overlap and need to be deconvoluted through a curve fitting using Gaussian components with two required to account for the asymmetry of the 1740-1710 peak [203], this process can lead to some uncertainty.

Typically, when water is cooled to 0°C at 1 atm it freezes, however water confined within PFSAs exhibit different freezing properties. A portion of water does freeze however a range of supressed freezing points can be observed down to -30°C [215,217], this water is known as freezable water. The remaining water does not freeze and is known as nonfreezable water, this is due to the water being immobilised by the strong hydrogen bonds which form in hydration shells due to the close proximity of the sulfonate group. Nonfrezing water occurs as the water molecules cannot reorient themselves and pack into a crystal lattice [212]. Although immobile, studies have suggested that this strongly bound water can still conduct protons and PFSAs have been shown to demonstrate proton conductivity at subzero temperatures where freezable water will have frozen [213,231,232]. Freezable water is not strongly hydrogen bonded around the sulfonate group and is thought to exist in the centre of ionic channels. It is only weakly hydrogen bonded to the surrounding water molecules as with bulk water and therefore can reorient to pack into a crystal lattice. Differential scanning calorimetry has previously been used to characterise water within PFSAs and other ion conducting polymer membranes [210,212,214–217], this technique measures the heat flow required to heat or cool a sample. When no phase change occurs heat flow is generally attributed to the heat capacity of the material however when a change in phase occurs such as melting or freezing, a significant peak is observed as a phase change is highly exothermic or endothermic. By quantifying the peak area of this phase change it is possible to determine the heat required for the phase change, as the enthalpy of water freezing/melting is known it is possible to determine the amount of water

that freezes or melts during the process. The quantity of nonfreezable water can be determined by subtracting the freezable water from the total water content of the material which can be determined using the enthalpy of water vaporisation or though gravimetric techniques such as differential scanning calorimetry with thermogravimetric analysis (DSC-TGA) to probe water vaporisation. Therefore, this technique is capable of characterising samples according to the quantities of freezable and nonfreezable water.

Solid state ^{1}H nuclear magnetic resonance (NMR) is a technique which can probe spin-lattice relaxation times (T_1) which is known as a thermal relaxation. ^{1}H NMR also probes spin-spin relaxation times (T_2) which are related to the reorientation of the nucleus with respect to the applied magnetic field and is always shorter than T_1. Three types of water have been detected in Nafion through peak deconvolution with different T_2 relaxation times. These types of water have been named as bulk or free water with the longest T_2 relaxation time, loosely bound with an intermediate T_2 relaxation time and tightly bound with the shortest T_2 relaxation time [215,216,233]. There is some difficulty deconvoluting the T_2 peaks as in some studies the peaks of the loosely and tightly bound water could not be distinguished, and some difficulty was also experienced fitting the bulk water [215,216,233].

Microwave dielectric relaxation spectroscopy is a technique used to probe the dielectric properties of a material as a property of frequency. Dielectrics are materials which do not possess free electrons and so are electrical insulators. When an electric field is applied, instead of conducting electrons, the material is polarised in which polar molecules reorient to align with the applied field. These materials are characterised by their complex relative permittivity, where the real part is related to stored energy whereas the imaginary part is related to energy dissipation. Two types of water within PFSAs and other material systems have been shown to follows Debye relaxations in the microwave regime [201,234]. The first of these relaxations is attributed to the dynamics of bulklike water which has little interaction from the polymer and as such the relaxation is centred around 18GHz in good agreement with liquid/bulk water across all levels of hydration [201]. The second relaxation is known as loosely bound or irrotational water and is attributed to water that is loosely bound to both the polymer and the strongly bound water which surrounds the hydrophilic sulfonate group [200,234]. The relaxation of loosely bound water is not observed in liquid/bulk water and exhibits a faster reorientation at higher levels of hydration although always slower than bulklike water [200].

Small angle x-ray scattering (SAXS) has been deployed in the study of PFSA ionomers as it is able to probe morphological features of the phase separated nanostructure and structural

information such as the crystallinity of the semi-crystalline PFSA under different levels of hydration. SAXS is capable of probing the size and shape of the 2-3nm thick hydrophobic domains which separate the 0.5-4nm water cluster domains which swell under increasing hydration [86]. Although SAXS cannot probe the properties of water, measuring the size and shape of water domains is useful in understanding the results of water state measurements and performance metrics such as proton conductivity, permeability, macroscopic swelling and diffusivity of PFSAs.

2.5 Terahertz sensing

Terahertz radiation is a part electromagnetic (EM) spectrum which occupies the frequency range of 0.1-10THz (1THz = 1012 Hz) and wavelengths of 0.03-3mm, it is also known as sub-millimetre radiation. This places Terahertz between the microwave and infrared regions of the spectrum. The terahertz region is also known as the terahertz gap, which refers to the gap in traditional technologies used to generate EM waves and as such remained almost inaccessible for most of the 20th century [39]. At lower frequencies lies the electronic regime where radio waves and microwaves can be generated at high power densities through oscillating electronics such as vacuum tubes used in magnetrons for devices such as microwave ovens and are typically high power. High-speed solid-state devices such as field effect transistors and IMPATT diodes also generate microwaves but are typically lower power [36]. At higher frequencies lies the optical regime where infrared, visible, ultraviolet and x-rays can be found. Infrared can be generated in a number of ways such as quantum cascade, gas, chemical or free electron lasers [37]. Within the terahertz regime these established technologies fail [38] and as such a different approach is needed. As with microwaves and infrared, at these frequencies the radiation is non-ionising and THz systems are typically low energy at a few milliwatts [235] and hence do not present a risk of eye injuries. Since the late 90s and during the 2000s, THz technologies have reached commercialization with systems available from a handful of companies [39,236]. Large and difficult to operate homemade laboratory systems have evolved into highly integrated, easier to operate, more reliable commercial systems with excellent performance [39].

2.5.1 Terahertz generation and detection

The vast majority of THz measurements and studies have been performed using terahertz time domain spectroscopy (THz-TDS) [237]. This technique utilises very short picosecond pulses

which are measured in the time domain and frequency domain data is then extracted. Photoconductive antennas are the most commonly used devices used to generate and detect terahertz pulses used in terahertz time domain spectrometers [238,239] although other alternatives do exist. When an electron changes its velocity EM radiation is emitted [238] and this concept is at the heart of terahertz wave generation within photoconductive antennas. The change in electron velocity occurs in the form of a short current change in the picosecond range resulting in an electric field which generates the THz pulse, this occurs within a semiconductor material of the antenna which is most commonly made from GaAs [238–240] and InGaAs [239,241]. The picosecond current change occurs between two electrical contacts under a DC voltage, the gap between these contacts is typically 5 to 50μm although emitters upto 2mm have been used for higher power devices [239]. The semiconductor is undoped and exists between these contacts with a high electrical resistivity which resists conduction between the contacts. This causes a charge to be stored between the contacts acting as a capacitor. Key to the timing of the entire system is a laser capable of generating very short pulses of less than 100 femtoseconds [239], a Ti-sapphire laser is most commonly used as it is capable of producing the shortest pulse length of less than 10fs which is desirable for high terahertz bandwidth [239]. This laser is split into two beams, one of which is known as the pump beam and is focused between at the semiconductor in the gap between the metal contacts as shown in Figure 2.12. The beam has enough photon energy to excite the electrons in the semiconductor from the valence band into the conduction band increasing the semiconductors conductivity [238,239]. The applied potential bias and photoinduced conductivity results in a rapid current flow between the metal contacts which is limited by the stored charge [238]. This current is known as the photocurrent which is approximately proportional to the optical intensity and applied bias [239]. The photocurrent produces a THz pulse which is typically 1-2ps in duration which is one to two orders of magnitude longer than the probe pulse [239]. The generated THz pulse is typically collected from the back of the antenna and focused towards the detector.

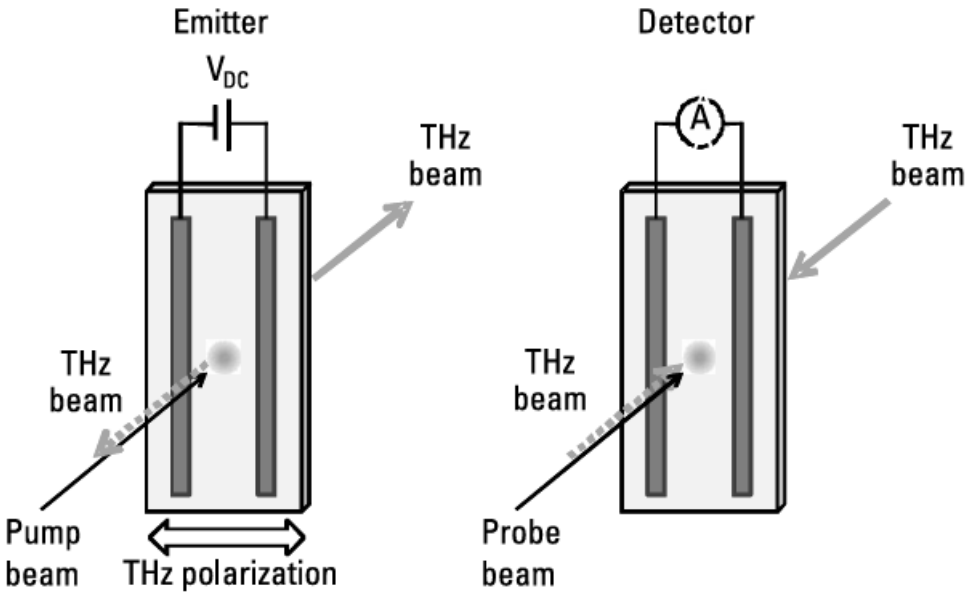

Figure 2.12 - Schematic of photoconductive emitter and detector taken from [239].

The detector works similarly to the emitter as shown in Figure 2.12 although no bias is applied, instead the photocurrent is generated by the electric field of the incident terahertz pulse. The induced photoconductivity is generated by the same laser as the emitter, which was split into two, this pulse is known as the probe beam. The induced photocurrent is typically 0.01-1 nA [239] and is proportional to the electric field strength of the terahertz pulse and photoconductivity. The photocurrent must therefore be selectively amplified using a lock-in amplifier which amplifies the signal within a given reference frequency to remove the noisy background [238]. This signal is then filtered to obtain the DC component of interest. As the detector only detects the electric field amplitude during illumination with the probe pulse, only a small fraction of the THz pulse is detected. As this is repeatable, by varying the delay of probe pulse through a delay line, the whole THz pulse can be probed within the time domain, this is typically achieved by increasing the path length of the probe beam. Generated EM pulses are polarised parallel to the flow of charge carriers. Due to the directionality of the electron movement from the photocurrent between the metal contacts, the generated and detected THz pulses are highly polarised allowing for polarisation sensitive measurements to be obtained. The bandwidth produced by photoconductive antennas is typically 4-5THz although higher bandwidths up to 20THz have been demonstrated [239].

2.5.2 THz wave propagation

Refractive index and permittivity are important material parameters that can be extracted from THz-TDS and are used significantly to characterise the properties of materials. These properties are inherently linked and the complex permittivity of a material can be calculated from its complex refractive index as shown

$$\hat{\varepsilon}_r = \hat{n}^2 \tag{2.32}$$

Where the ε_r is the relative permittivity and n is the refractive index, the hat notation denotes that these are complex quantities with real and imaginary parts as shown in Equations 2.33 and 2.34.

$$\hat{n} = n - i\kappa \tag{2.33}$$

$$\hat{\varepsilon}_r = \varepsilon' - i\varepsilon'' \tag{2.34}$$

The complex refractive index is made up of the refractive index n which denotes the relative speed of light through the material and the extinction coefficient κ which indicates the attenuation of light as it propagates through the material. The real part of the complex relative permittivity, ε' is related to stored energy whereas the imaginary relative permittivity, ε'' is related to energy dissipation. The real and imaginary permittivity's can also be determined from the refractive index and extinction coefficient (κ) as shown

$$\varepsilon' = n^2 - \kappa^2 \tag{2.35}$$

$$\varepsilon'' = 2n\kappa \tag{2.36}$$

Inversely the refractive index and extinction coefficient can also be determined from the complex permittivity as shown.

$$n = \left(\frac{\sqrt{\varepsilon'^2 + \varepsilon''^2} + \varepsilon'}{2} \right)^{1/2} \tag{2.37}$$

$$\kappa = \left(\frac{\sqrt{\varepsilon'^2 + \varepsilon''^2} - \varepsilon'}{2} \right)^{1/2} \tag{2.38}$$

When light reaches the interface of a dielectric material the EM wave is either reflected or transmitted as shown in Figure 2.13.

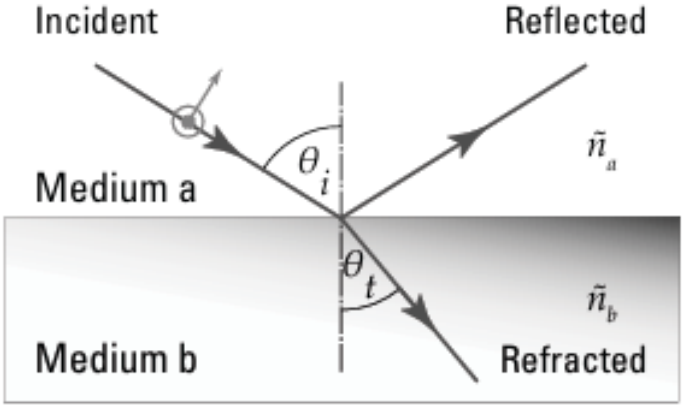

Figure 2.13 - Transmitted and reflected wave at a dielectric interface taken from [239].

The angle of reflected light is the same as the incident wave relative to the perpendicular of the surface at the point of reflection. The transmitted light refracts, and the angle of the refraction (θ_t) can be determined from the refractive index of the incident medium (n_a) and refracted medium (n_b) as described by Snells law:

$$\theta_t = \sin^{-1}\left(\frac{n_a}{n_b}\sin\theta_i\right) \tag{2.39}$$

As light is reflection or transmitted at the interface of two dielectric materials a change to the amplitude and phase of the incident wave occurs, these are described by Fresnels equations. When the electric field is polarised perpendicular to the plane of incidence the Fresnel transmission coefficient, τ_σ and the Fresnel reflection coefficient, ρ_σ can be determined for a wave propagating from medium a to medium b using the complex refractive indexes of the materials as shown:

$$\tau_\sigma = \frac{2\hat{n}_a\cos\theta_i}{\hat{n}_a\cos\theta_i + \hat{n}_b\cos\theta_t} \tag{2.40}$$

$$\rho_\sigma = \frac{\hat{n}_a\cos\theta_i - \hat{n}_b\cos\theta_t}{\hat{n}_a\cos\theta_i + \hat{n}_b\cos\theta_t} \tag{2.41}$$

When the polarisation is parallel to the plane of incidence the Fresnel transmission coefficient, τ_π and the Fresnel reflection coefficient, ρ_π can also be determined as shown:

$$\tau_\pi = \frac{2\hat{n}_a\cos\theta_i}{\hat{n}_a\cos\theta_t + \hat{n}_b\cos\theta_i} \tag{2.42}$$

$$\rho_\pi = \frac{\hat{n}_a \cos\theta_t - \hat{n}_b \cos\theta_i}{\hat{n}_a \cos\theta_t + \hat{n}_b \cos\theta_i} \tag{2.43}$$

When the angle of incidence is normal to the interface the angles of incidence and refraction are 0° and therefore the Fresnel coefficients can be simplified as follows:

$$\tau_\sigma = \tau_\pi = \frac{2\hat{n}_a}{\hat{n}_a + \hat{n}_b} \tag{2.44}$$

$$\rho_\sigma = \rho_\pi = \frac{\hat{n}_a - \hat{n}_b}{\hat{n}_a + \hat{n}_b} \tag{2.45}$$

When a wave propagates from medium b to medium a, the transmission coefficient ρ' and reflection coefficient τ' can be determined as follows:

$$\rho' = -\rho \tag{2.46}$$

$$\tau' = \frac{1 - \rho^2}{\tau} \tag{2.47}$$

When an EM wave incidents a dielectric slab a fraction is transmitted whilst the other fraction is reflected, the transmitted fraction then propagates through the material. The propagation of the wave through medium b can be described by multiplying the incident electric field of the traversing wave by $\exp\left(-i\hat{n}_b \frac{\omega l_\theta}{c}\right)$ where ω is the angular frequency which can be calculated from frequency f using $\omega = 2\pi f$, c is the speed of light in a vacuum and l_θ is the propagation distance which can be calculated using $l_\theta = l/\cos\theta_t$, where l is the thickness of the material. The wave then reaches an internal interface and either reflects or transmits, the reflected waves again traverse the material to another interface and this process can repeat multiple times. This means the incident wave is split into multiple waves with different amplitude and phases which are transmitted and reflected from the material as shown in Figure 2.14.

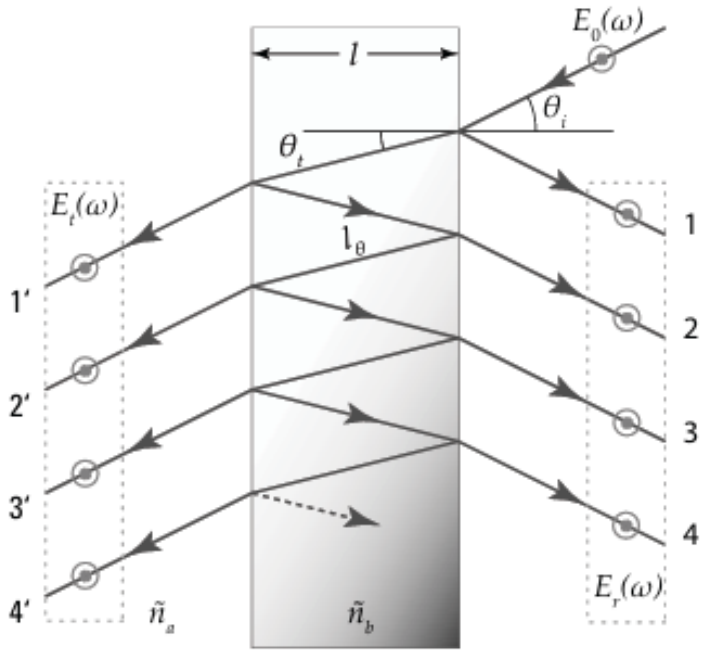

Figure 2.14 - Wave propagation paths through a dielectric slab taken from [239].

Each wave can be modelled by following the beam path and multiplying the electric field of the incident wave $E_o(\omega)$ by the Fresnel transmission and reflection coefficients and the propagation term for each transmission, reflection and propagation that occurs as shown in Table 2.3. It should be noted that many more reflections can occur but are decreasingly significant as each reflection and propagation causes a decrease in the resulting waves magnitude.

Table 2.3 - Multiplication factors for wave propagations across a dielectric slab.

Reflection	Multiplication factor	Transmission	Multiplication factor
1	ρ	$1'$	$\tau\tau'\exp\left(-i\hat{n}_b\frac{\omega l_\theta}{c}\right)$
2	$\tau\tau'\rho'\exp\left(-2i\hat{n}_b\frac{\omega l_\theta}{c}\right)$	$2'$	$\tau\tau'\rho'^2\exp\left(-3i\hat{n}_b\frac{\omega l_\theta}{c}\right)$
3	$\tau\tau'\rho'^3\exp\left(-4i\hat{n}_b\frac{\omega l_\theta}{c}\right)$	$3'$	$\tau\tau'\rho'^4\exp\left(-5i\hat{n}_b\frac{\omega l_\theta}{c}\right)$
4	$\tau\tau'\rho'^5\exp\left(-6i\hat{n}_b\frac{\omega l_\theta}{c}\right)$	$4'$	$\tau\tau'\rho'^6\exp\left(-7i\hat{n}_b\frac{\omega l_\theta}{c}\right)$

When the incident wave is normal to the dielectric interface, these multiple waves will be superimposed as the paths overlap causing constructive and destructive interference in the resulting transmitted wave $E_t(\omega)$ and the reflected wave $E_r(\omega)$. The interaction of these waves

is known as the Fabry-Pérot effect which produces an interference effect. These multiple waves can be expressed as an infinite sum and used to determine the total transmitted wave as shown by Equation 2.48 [239].

$$E_t(\omega) = E_o(\omega)\tau\tau' \exp\left(-i\hat{n}_b \frac{\omega l_\theta}{c}\right)\left[1 + \sum_{m=0}^{\infty}\left(\rho'^2 \exp\left(-2i\hat{n}_b \frac{\omega l_\theta}{c}\right)\right)^m\right] \quad (2.48)$$

This can be simplified separated into the primary wave and the waves of the Fabry-Pérot effect represented by $FP(\omega)$ as shown

$$E_t(\omega) = E_o(\omega)\tau\tau' \exp\left(-i\hat{n}_b \frac{\omega l_\theta}{c}\right) FP(\omega) \quad (2.49)$$

Where

$$FP(\omega) = 1 + \sum_{m=0}^{\infty}\left(\rho'^2 \exp\left(-2i\hat{n}_b \frac{\omega l_\theta}{c}\right)\right)^m \quad (2.50)$$

This infinite sum can be simplified to reduce the computations required as shown [239]

$$FP(\omega) = \left(1 - \rho'^2 \exp\left(-2i\hat{n}_b \frac{\omega l_\theta}{c}\right)\right)^{-1} \quad (2.51)$$

For reflection the same approach can be used although the reflection at the initial interface is separated from the rest of the terms as shown.

$$E_t(\omega) = \rho E_o + E_o(\omega)\tau\tau'\rho' \exp\left(-2i\hat{n}_b \frac{\omega l_\theta}{c}\right) FP(\omega) \quad (2.52)$$

It should be noted that $FP(\omega)$ is the same for both transmission and reflection. The difference in phase of the superimposed waves causes the interference pattern of the total transmitted wave. The temporal separation Δt is equal to the duration of the wave propagation as it traverses back and forth within the slab, this can be calculated as shown

$$\Delta t = \frac{2n_g l}{c} \quad (2.53)$$

Where n_g is the group refractive index defined as $n_g = n_b + \omega \partial n_b / \partial \omega$. As expected, the spectral separation increases linearly with material thickness due to the increased path length and also refractive index as the wave velocity is reduced. The Fabry Perot is demonstrated in Figure 2.15.

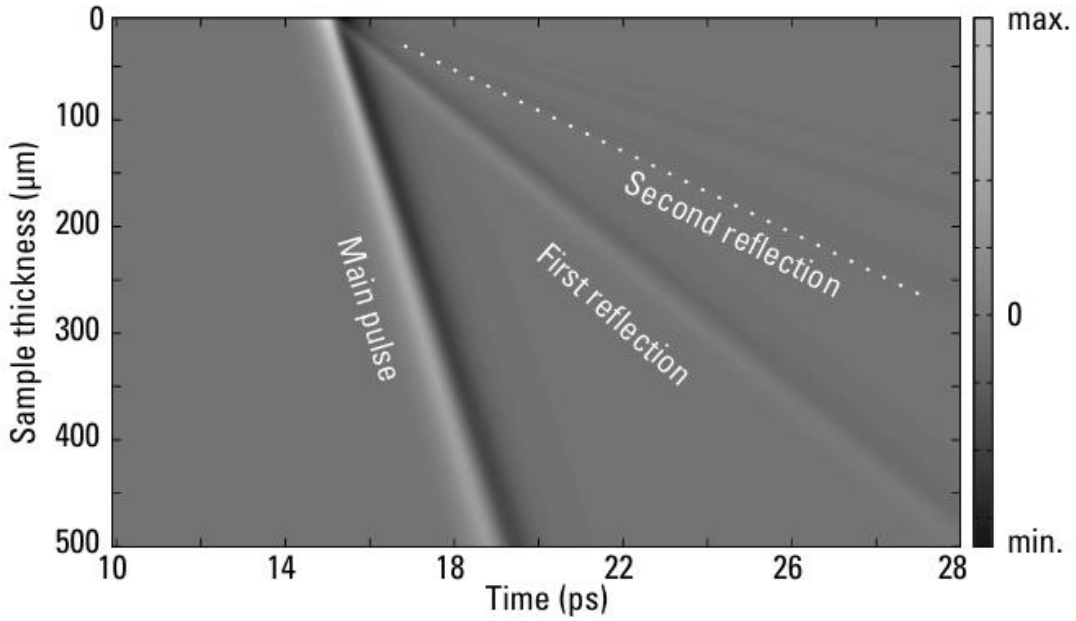

Figure 2.15 - Example of Fabry Perot effect in the time domain with the first two reflections taken from [239].

The temporal separation translates to the frequency separation Δf of the interference pattern where $\Delta f = 1/\Delta t$. In this case the frequency separation decreases and the attenuation increases with increasing thickness, an example of an interference pattern is shown in Figure 2.16

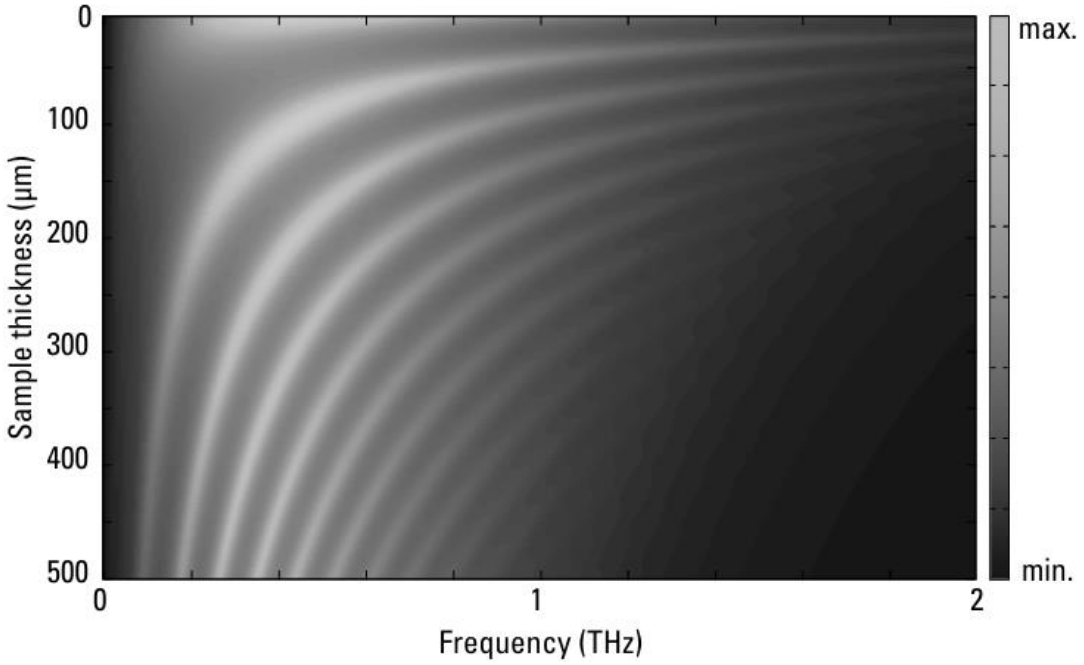

Figure 2.16 - Example of Fabry Perot effect in the frequency domain taken from [239].

This has shown how wave propagation occurs and can be modelled through a single slab however, the same methods can be applied to layered samples using the same propagation terms and the Fresnel transmission and reflection coefficients according to each material and

interface. This adds additional complexity due to an increase in the number of possible wave paths which can be reduced through time gating if some layers are of sufficient thickness.

2.5.3 Data processing and approximated optical parameters

As with any measurement technique, THz-TDS measurements contain random noise. To reduce the random noise, multiple measurements can be obtained and averaged. This is an effective technique when used in the time domain but is ineffective in the frequency domain [242] and can significantly lower the noise floor improving dynamic range [239]. Data is acquired in the time domain, however THz analysis is typically carried out in the frequency domain and therefore must be derived from the time domain data via a Fourier transform to obtain the both the amplitude and phase in the frequency domain. Phases obtained through this method lie within -π and π due to phase wrapping as when a phase is obtained with an absolute value greater than π, the phase jumps to the opposite polarity by 2π. This phase jumping causes phase discontinuities which need to be unwrapped to obtain useful phase information. To achieve this the number of phase discontinuities in the frequency range below the desired frequency are multiplied by 2π and added or subtracted to the wrapped phase. Outside of the reliable part of the spectrum with insufficient signal to noise ratio, the signal noise introduces artificial phase discontinuities. As phase unwrapping begins from the lowest frequencies within this noise, the phase error from this region which is typically below ~0.05-0.1THz propagates to the phases within the reliable part of the spectrum. Therefore, the phases are extrapolated from the reliable part of the spectrum such that the extrapolate phase at 0THz is 0 radians as shown in Figure 2.17.

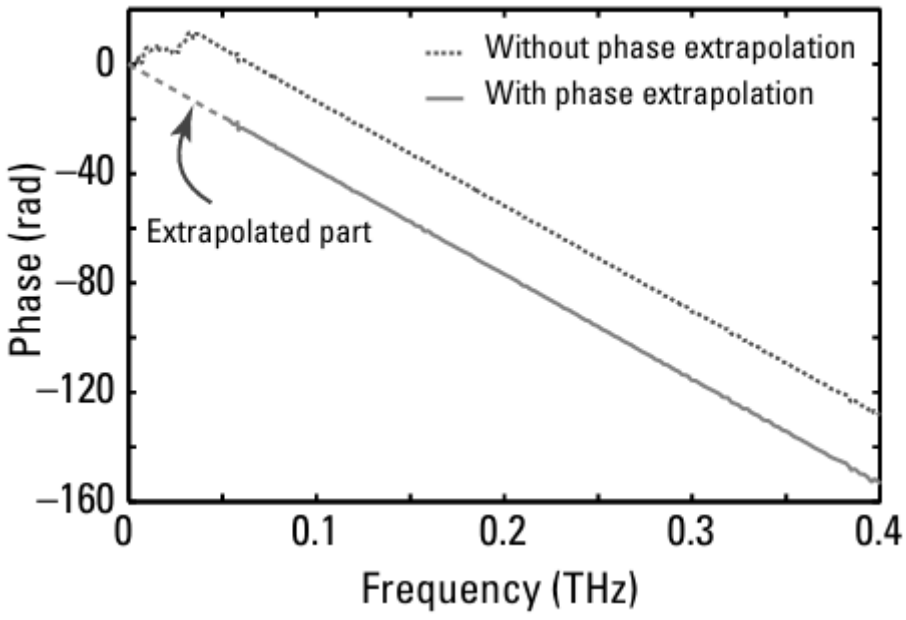

Figure 2.17 - Example of phase unwrapping taken from [239].

For transmission measurements normal to the surface of thick bulk materials where the Fabry Perot reflections are temporarily separated from the main pulse or materials with high terahertz attenuation, a simplification to the wave modelling can be made. In these cases, the transmitted wave $E_{sam}(\omega)$ can be expressed as a function of the incoming wave $E_o(\omega)$ according to Equation 2.54.

$$E_{sam}(\omega) = E_o(\omega)\frac{4\hat{n}_s n_o}{(\hat{n}_s + n_o)^2}\exp\left(-i\hat{n}_s\frac{\omega l}{c}\right) \tag{2.54}$$

Where $\hat{n}_s$ and n_o are the refractive indexes of the sample and free space (typically air) respectively. It should be noted that this is taken from Equation 2.49 and assuming a normal incident wave. Therefore, this approach yields optical parameters which have been approximated assuming that Fabry Perot reflections are temporally separated from the main pulse through time gating (thick samples), but can also be applied for materials with high terahertz attenuation as the magnitude of the Fabry Perot reflections can be assumed to be insignificant. Likewise, the measured reference wave can also be expressed as a function of the incoming wave.

$$E_{ref}(\omega) = E_o(\omega)\exp\left(-in_o\frac{\omega l}{c}\right) \tag{2.55}$$

By rearranging and combining these two expressions it is possible to express the normalised sample spectrum $H(\omega)$ which is known as the as the transfer function as follows:

$$H(\omega) = \frac{E_{sam}(\omega)}{E_{ref}(\omega)} = \frac{4\hat{n}_s n_o}{(\hat{n}_s + n_o)^2}\exp\left(-\kappa_s\frac{\omega l}{c}\right)\exp\left(-i[n_s - n_o]\frac{\omega l}{c}\right) \tag{2.56}$$

The complex refractive index of the Fresnel transmission coefficient, $\frac{4n_s n_o}{(n_s+n_o)^2}$, is also often approximated with the real refractive index as shown in Equation 2.57.

$$H(\omega) = \frac{4n_s n_o}{(n_s + n_o)^2}\exp\left(-\kappa_s\frac{\omega l}{c}\right)\exp\left(-i[n_s - n_o]\frac{\omega l}{c}\right) \tag{2.57}$$

The argument, $\angle H(\omega)$ calculated with phase unwrapping, and logarithm of the magnitude $|H(\omega)|$ of this simplified transfer function can be taken which gives.

$$\angle H(\omega) = -[n_s - n_o]\frac{\omega l}{c} \tag{2.58}$$

$$ln|H(\omega)| = ln\left(\frac{4n_s n_o}{(n_s + n_o)^2}\right) - \kappa_s \frac{\omega l}{c} \tag{2.59}$$

These expressions can be rearranged to yield the refractive index and extinction coefficient of the sample as shown in Equations 2.60 and 2.61.

$$n_s = n_o - \frac{c}{\omega l}\angle H(\omega) \tag{2.60}$$

$$\kappa_s = \frac{c}{\omega l}\left[ln\left(\frac{4n_s n_o}{(n_s + n_o)^2}\right) - ln|H(\omega)|\right] \tag{2.61}$$

Attenuation is also frequently expressed as an absorption coefficient α which can be determined from the extinction coefficient as shown in equation 2.62.

$$\alpha = \frac{2\omega\kappa}{c} \tag{2.62}$$

The SI units for absorption coefficient are m^{-1} but is usually given as cm^{-1}. This approach yields approximated optical constants under the assumption that Fabry Perot effects can be ignored but is a closed form solution, whereas accurate estimation requires iterative approaches [239]. A similar approach can also be taken with reflection measurements where extract optical parameters for each measured frequency.

2.5.4 Parametric methods

Another approach for extracting information are parametric methods which fit data across the whole spectrum. To do this a satisfactory model which adequately describes the materials electromagnetic response must be assumed [243]. As these models describe the frequency dependent response, they can therefore describe the whole spectrum according to only a few model parameters as opposed to many other approaches where the complex refractive index is determined at each data point. These model parameters are used to extract a complex refractive index which can be used in propagation models such as with Equation 2.49 to calculate a modelled transfer function. By minimising the error between the modelled transfer function and the measured transfer function, optical parameters can be extracted [243–250]. This error is commonly known as the objective function in optimisation and expressed as

$$\widehat{H}_{theory}(\omega) - \widehat{H}_{measured}(\omega) \tag{2.63}$$

By using this approach, the challenges of working with multiple possible solutions and the complex relationship of real refractive index and extinction coefficient fitted to both magnitude

and phase can be mitigated [243]. The approach can also be used for a variety of experimental configurations across reflection and transmission measurements. Parametric approaches can be utilised with samples of known thickness but can also be applied to samples with unknown thickness as in some cases thickness can be included as an additional fitting parameter allowing for it to be extracted. As the objective function is nonlinear, suitable optimisations algorithms must be used such as the Nelder-Mead [234,243] and particle swarm [251,252] algorithms. This approach can be very efficient, but if models are unable to adequately describe the electromagnetic response, the method cannot be applied [253].

2.5.5 Material characterisation

Terahertz waves can interact with matter in a variety of ways, due to the low photon energy weak resonances such as rotations and vibrations of molecules [253]. The resulting spectra can exhibit broad absorption peaks, narrow absorption lines with unique spectral signatures known as a fingerprint or materials can be highly transparent, attenuating or reflective. Therefore, the experimental procedure and analysis approach must be selected according to the sample's interactions, properties and geometry.

Terahertz has shown sensitivity to many chemical and structural properties across a wide range of materials and has many different electromagnetic responses to different material categories. The following is a short summary of some applications.

THz has a strong interaction with gaseous polar molecules such as H_2O, N_2, O_2, O_3, CO, SO_2, CH_3CN, etc which have distinct spectral peaks in the regime [254]. Each gas exhibits unique spectral signatures that originate from transitions between rotational quantum levels which can be separated to quantify multiple gases simultaneously [255,256] and hence used for trace gas sensing.

For liquid and solid states, molecule vibrations are coupled with neighbouring ones. In pure crystals vibrations propagate resulting in a strong peak, the quantity of energy for these vibrational modes is called an optical phonon and each pure crystal has a characteristic frequency such as 8.05THz for GaAs at room temperature [253]. Polycrystalline materials such as glass have broader peaks as coherent propagation of the mechanical wave is not possible [253].

Materials containing free charges such as metals are highly reflective to THz waves and their permittivity is often well described by the Drude model which assumes the free charges form a gas which does not interact with the crystal lattice or other free charges [253]:

$$\hat{\varepsilon}(\omega) = \varepsilon_\infty - \frac{{\omega_p}^2}{\omega(\omega + i\Gamma)} \tag{2.64}$$

Where ε_∞ is the infinite dielectric constant, ω_p is the plasma pulsation which depends upon the carrier density and Γ is the damping pulsation which is corresponds to a damping effect linked to the finite electrical conductivity. While the Drude model often well describes conductive materials it does have its limitations and therefore has been modified to better describe material interactions such as the Drude-Smith model which accounts for back scattering of charge carriers [257]. Other models such as the Drude-Lorentz model can be used to describe bound charges.

Polymer materials are transparent or semi-transparent to THz waves even for many optically opaque materials. Therefore, THz has been used extensively to non-destructively study the macroscopic and morphological properties of polymeric materials such thickness determination, detection of defects and crystallinity changes as well as determination of foam densities. These techniques can be applied to pure polymers, polymer composites and adhesives [237]. When used in reflection it has also been demonstrated that THz-TDS can be used to determine the thickness of layered coating such as paints [237]. THz has also shown to be promising in the pharmaceutical sector as many materials are semi-transparent to THz and often possess characteristic spectral signatures, therefore THz has been used to probe chemical compositions in addition to structural information such as tablet coating thickness, porosity and pore size [237].

Liquids containing polar molecules such as water are strongly attenuated whereas non-polar liquids are typically transparent. Charge separation occurs when polar materials interact with an oscillating EM field creating oscillating dipoles due to the applied field. At low frequencies dipole oscillations are unhindered and are able to follow the field amplitude at all times and therefore the material is transparent [128]. However, at higher frequencies dipole motion are hindered resulting in a delayed response to the applied field resulting in absorption [239].At the high frequency limit the field oscillates too quickly for the dipoles to react resulting in a transparent material [128]. The Debye model describes the interaction of the EM wave with polar materials in terms of a response time, τ which is known as the relaxation time [258]:

$$\hat{\varepsilon}(\omega) = \varepsilon_\infty + \frac{\Delta\varepsilon}{1 + i\omega\tau} \tag{2.65}$$

Where $\Delta\varepsilon$ is the dielectric strength of the relaxation and is the difference between the static dielectric constant, ε_s and the i.e. $\Delta\varepsilon = \varepsilon_s - \varepsilon_\infty$. More polar materials have greater dielectric strengths such as water with $\Delta\varepsilon$=78.2 yet nonpolar high resistivity silicon has approximately the same infinite dielectric and static dielectric constants of 11.7 [239], the dielectric strength also increases with concentration. This relaxation is centred about $\omega = 1/\tau$ and is symmetric when plotted with a logarithmic frequency axis as shown by Figure 2.18.

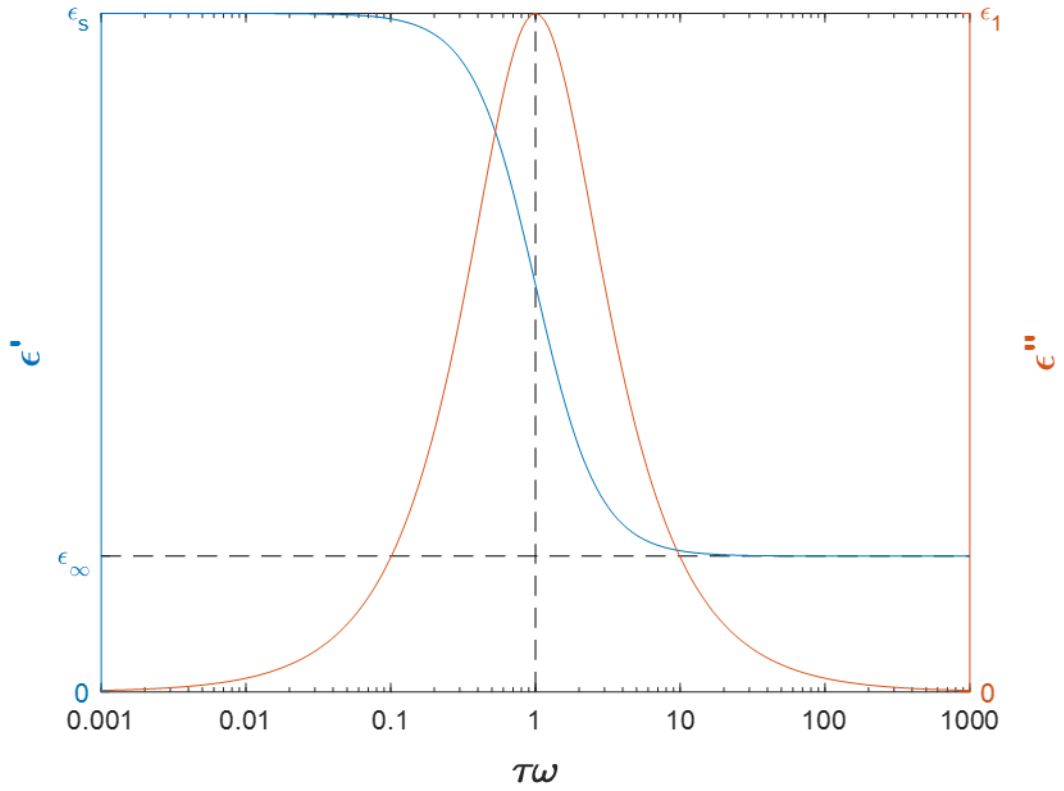

Figure 2.18 - Complex permittivity of Debye model.

THz has therefore emerged as a powerful tool for probing highly polar molecules such as water within a number of material systems including biological and polymer materials [157,233,234,259–263]. This is due to its strong sensitivity with a strong absorption limiting the penetration in water to ~100μm [233].

2.5.6 Water interactions

THz is sensitive to the structure and dynamics of water as it is able to probe the reorientation of molecules at picosecond timescales. Within pure water two distinct relaxation processes occur when exposed to terahertz radiation with a frequency of 0-1THz [264]. Relaxation

processes occur when a system deviates from its equilibrium state due to a change in its environment and then returns to its equilibrium state [265]. In this case water molecules reorient in response to the applied electric field of the terahertz radiation due to an interaction with the water dipoles and then return to their equilibrium state. Pure water has a slow and fast relaxation within the THz regime, the slow relaxation also known as the bulk relaxation. The complex permittivity of these relaxations can be described by the double Debye model as shown in equation 2.66.

$$\hat{\varepsilon}(\omega) = \varepsilon_{\infty} + \frac{\Delta\varepsilon_1}{1 + i\omega\tau_1} + \frac{\Delta\varepsilon_2}{1 + i\omega\tau_2} \tag{2.66}$$

where $\Delta\varepsilon_1$ and $\Delta\varepsilon_2$ are the dielectric strengths of the bulk and free Debye relaxations, τ_1 is the bulk relaxation time and τ_2 is the free relaxation time. It should be noted that THz-TDS and dielectric spectroscopy are complimentary methods which probe the same dielectric properties and therefore, microwave dielectric spectroscopy has been used to probe the dielectric properties water. Due to the frequency ranges studied (0.045-26 GHz), the free relaxation is not detected with the technique but the bulk relaxation can be studied, as it exhibits a resonance at 18GHz or ~8ps at 25°C [266,267].

Microwave dielectric spectroscopy has been applied to hydrated PFSA membranes where it was found that the bulk relaxation time of the confined water matched that of pure water for the 25-45°C measured across all studied levels of hydration [266]. Another state of water was also detected with slower dynamics exhibiting a lower and variable relaxation time attributed to water described as loosely bound [266]. Based upon these results THz-TDS was performed under ambient conditions (40% RH) and fitted to the double Debye model using additional GHz literature data from [266], in this work the double Debye model with bulk and free water relaxations was found to adequately describe the dielectric properties of the membrane [268]. Bound water contributions were not included as this resonance falls outside the THz window as the process is too slow to be observed. It should be noted that performing independent measurements without reliable humidity control is likely to result in physical differences in the membrane properties due to their sensitivity to a number of factors such as humidity and thermal history [86]. THz-TDS was then used to study water properties within lipid membranes [233]. However, instead of using microwave dielectric relaxation data to fit the bulk relaxation, the known relaxation time was assumed constant at 8ps. Additionally, the concentrations of the bulk and free states were determined from the dielectric strengths. Using the total water content (determined from FTIR) was it was then possible to determine the concentration of bound water

[233]. This is because bound is the only water state unaccounted for and can therefore be determined by subtracting the bulk and free water populations from the total water content. This approach was later applied to PFSA and sPEEK membranes although THz-TDS was additionally used to determine the total water content using Beer Lamberts law [234]. Again 3 states were characterised: bound water (strongly hydrogen bonded and predominantly bound to the hydrophilic sulfonate groups) [200,233], bulk water (weakly hydrogen bonded and exhibiting co-operative reorganisation of hydrogen bonds) [233,234] and free water (temporarily not hydrogen bonded) [269]. Additionally bound water can be separated into strongly bound water and loosely bound water which can be described by a Debye relaxation and can be characterised in the microwave regime [200,233] however, it does not appear in the THz regime as the reorientation is too slow to be observed.

When water interacts with other materials, the dielectric response can change and variants to this model exist to describe the deviations due to material interactions although these are typically seen at lower frequencies using techniques such as microwave dielectric relaxation spectroscopy. The Havriliak-Negami is an empirical modification of a single Debye relaxation and is very versatile in describing the relaxation distribution with shape parameters α for materials with asymmetric peak broadening and β for symmetric dielectric peak broadening [270,271] as shown.

$$\hat{\varepsilon}_r(\omega) = \varepsilon_\infty + \frac{\Delta\varepsilon_1}{[1 + (i\omega\tau_1)^{1-\alpha}]^\beta} \tag{2.67}$$

In the limiting case when α=0 and β=1 this simplifies to the Debye equation. Another limiting case is the Cole-Cole equation for symmetric dielectric loss peak broadening [272] where $0 \leq \alpha < 1$ and β=1. Additionally, the Cole-Davidson limiting case can be used for asymmetric dielectric loss peak broadening [273,274] where α=0 and $0 < \beta \leq 1$. Additional Debye relaxations can also be used to describe additional relaxations as with the double debye model [200,233]. In the terahertz regime it has been found that the double Debye model describes the response of the bulk and free relaxations without the need for any of these modifications. In a number of studies, the dielectric strength $\Delta\varepsilon_i$ has been assumed to be proportional to the concentration of the relaxation species [233,234,275] C_i as follows:

$$C_i = K\Delta\varepsilon_i \tag{2.68}$$

Where K is a proportionality factor which contains information about the species polarizability and dipole moment according to the Cavell equation [200,276,277]:

$$K = \frac{2\varepsilon_s + 1}{\varepsilon_s}\frac{k_B T \varepsilon_0}{N_A g \mu^2} \tag{2.69}$$

Where ε_s is the static permittivity, k_B is Boltzmann's constant, T is the temperature, N_A is Avogadro's constant, μ is the molecular dipole and g is the Kirkwood correlation factor. Therefore, the assumption is based on these factors being constant. Unfortunately, there is some evidence that protons can depolarise water due to a structuring effect [276] which could lead to some uncertainty when using this assumption for protonated materials, although it is thought to be insignificant [275].

2.5.7 Effective medium theory (EMT)

Composite materials can often be described by a macroscopic material parameters such as permittivity or refractive index which describes the properties of the bulk material. These materials are often described as system consisting of particles or inclusions embedded within a host material and when particle size is much smaller than the wavelength the effects of scattering are negligible [253,278]. Quasi-static effective medium theories are approaches which relate macroscopic material properties to component properties. For example the Maxwell-Garnet describes the effective permittivity of the composite ($\hat{\varepsilon}_{eff}$) with a particle volume fraction (F_p) as a function of the permittivities of the spherical particles ($\hat{\varepsilon}_p$) and host material ($\hat{\varepsilon}_h$) [253]:

$$\hat{\varepsilon}_{eff} = \hat{\varepsilon}_h \frac{\hat{\varepsilon}_p\left(1 + 2K_p\right) + 2\hat{\varepsilon}_h(1 - K_p)}{\hat{\varepsilon}_p\left(1 - K_p\right) + \hat{\varepsilon}_h(2 + K_p)} \tag{2.70}$$

This model works well for spherical particles with small concentrations. The Polder and van Santen is an extension of Maxwell-Garnet and includes the effect of changing permittivity due depolarisation caused by the presence of other particles and can therefore be used for higher particle concentrations [253,278]. A depolarisation factor can also be calculated based on the particle shape and used to extend the approach to rod and disk shaped particles [278]. Whilst the Polder and van Santen model can describe higher particle concentrations, a high permittivity contracts impacts its validity [278]. The Bruggeman model can be used to describe composites with a large contrast in permittivity however is limited to spherical particles [253,278]:

$$1 - K_P = \frac{\hat{\varepsilon}_p - \hat{\varepsilon}_{eff}}{\hat{\varepsilon}_p - \hat{\varepsilon}_h} \sqrt[3]{\frac{\hat{\varepsilon}_h}{\hat{\varepsilon}_{eff}}} \tag{2.71}$$

Combining the Brugemann with the Polder and van Santen approaches more general forms can be derived [278–280]. These models have all assumed that particles are randomly distributed and therefore within anisotropic materials with disk or rod shaped particles such as in some reinforced composites, the orientation may introduce macroscopic birefringence [278] and therefore is sensitive polarizability of the incident wave. Another approach is the Landau, Lifshitz, Looyenga (LLL) model which does not take particle shape into account and assumes an infinitesimal amount of particles [278]:

$$\sqrt[3]{\hat{\varepsilon}_{eff}} = K_p \sqrt[3]{\hat{\varepsilon}_p} + (1 - K_P) \sqrt[3]{\hat{\varepsilon}_h} \tag{2.72}$$

This method can also be applied to more than two components and is favoured for irregularly shaped particles [278]. Empirical approaches also exist such as power law approaches [253] and simple models such as the complex refractive index model where the complex refractive index is linearly dependent upon volume fraction as shown [278]:

$$\hat{n}_{eff} = K_p \hat{n}_p + (1 - K_P) \hat{n}_h \tag{2.73}$$

Where $\hat{n}_{eff}$, $\hat{n}_p$ and $\hat{n}_h$ are the complex refractive index of the effective medium, particle and host materials respectively. Another approach is the linear absorption mixing model which is similar to the complex refractive index model but only absorption coefficient is considered as shown [281]:

$$\alpha_{eff} = K_p \alpha_p + (1 - K_P) \alpha_h \tag{2.74}$$

Where α_{eff}, α_p and α_h are the absorption coefficient of the effective medium, particle and host materials respectively. As many models exist it is important to select a model which appropriately describes the studied composite. Therefore, factors such as approximate permittivities, volume fraction and particle shape are needed for selecting a model. Required outcome also plays a role as simpler empirical models such as the linear absorption mixing model may be most appropriate for determining particle concentrations.

2.6 Summary

PFSA membranes are one of the many vital components at the heart of electrochemical devices such as PEM fuel cells and electrolysers which may play a critical role in achieving net zero

carbon emission targets. The electrochemical performance and the chemical-mechanical durability of these membranes are critical in achieving long lasting and efficient chemical-electrical energy transformations. The properties of these membranes are tied to their hydration which exhibit increases electrochemical performance at higher relative humidities and temperatures upto their operating temperatures of 80-90°C. Water is fundamental for proton conduction through the phase separated nanomorphology of PFSAs via the vehicle and Grotthuss hopping mechanisms. Therefore, understanding these mechanisms at play and the intrinsic properties of water which enable proton conduction is crucial in the development of membranes with both improved durability and electrochemical performance. To maintain effective hydration, membranes must be exposed to high humidities without causing excess liquid buildup and flooding which restricts gas transport to the electrochemically active catalyst layers. Within the membrane water is transported by diffusion, electroosmotic drag and hydraulic permeability. Water is introduced to the cell at the humidified reactant gas inlets, generated at the fuel cell cathode and evacuated through the gas outlets. Therefore, transport mechanisms must be understood to ensure effective water distribution and understanding of water transport mechanisms within and externally to the membrane are vital for effective cell design and operation. The diffusion of water in transient water uptake measurements is considered to follow Fickian diffusion in which diffusion is proportional to the concentration gradient. A number of models exist to describe the nature of Fickian diffusion through a thin slab and are based upon different assumptions of the membrane interface as well as empirical models. Finite element analysis is also a promising approach to modelling diffusion due to its versatility as additional data can be incorporated rather than assumptions or model fitting and it is also possible to include multiple different factors such as dynamic changes to thickness or relative humidity and interfacial resistance. A number of techniques have been utilised in the characterisation of water content, properties and states including small angle X-ray scattering spectroscopy, neutron scattering and imaging, nuclear magnetic resonance, microwave dielectric relaxation spectroscopy, Fourier transform infrared spectroscopy (FTIR), dynamic vapor sorption (DVS), differential scanning calorimetry (DSC) and Raman spectroscopy. As these techniques probe different physical phenomenon, differences and similarities in the definitions and boundaries between extracted states can be expected. Terahertz time-domain spectroscopy has recently shown sensitivity to the reorientational dynamics of water within PFSA ionomers which follows a double Debye response. An overview of THz pulse generation and detection using photoconductive antennas has been shown and some of the methods used to extract frequency domain data have been given. Modelling of THz wave propagation has

also been shown for extraction of optical material parameters such as complex permittivity and complex refractive index.

3 Methodology

This chapter outlines the materials used and experimental methodology used during the PhD work shown in this dissertation. This includes the preparation of a number of commercially available PFSA ionomer membranes. The preparation of membranes through the control of relative humidity using saturated salt solutions. The hardware and software used to further control humidity through a humidified gas delivery system to allow in situ terahertz measurements inside a relative humidity-controlled chamber. Additionally, the equipment and methods used to obtain and then analyse terahertz time domain spectroscopy data to extract both water uptakes and water states from the PFSA ionomer membranes. The methods and equipment used to characterise the membranes using differential scanning calorimetry, thermogravimetric analysis and dynamic vapor sorption are also outlined. Finally, the fitting of transient water uptake profiles in the study of diffusion using empirical, theoretical and computational analysis models are shown.

3.1 Samples

The PFSA membranes used include different grades of commercial Nafion (117, 211, XL and 212), Aquivion E98-05S and Fumasep F10120-PK (Fuel Cell Store, TX, USA). Nominal thicknesses, ion exchange capacity (IEC), reinforcement and densities are shown in Table 3.1.

Table 3.1 - Properties of membranes studied.

Membrane	Thickness (μm)	Ion exchange capacity (meq/g)	Reinforcement	Density (g/cm^3)
Nafion 117	183	0.9	none	1.94
Nafion 211	25	0.9	none	1.94
Nafion XL	27	0.92 [282]	ePTFE	1.94
Nafion 212	50	0.9	none	1.94
Aquivion E98-05S	50	>1	none	2.1
Fumasep F10120-PK	120-130	0.79	PEEK open mesh	2

The Nafion membranes were selected as they are most prominent within literature for comparison. The selection includes a variety of membrane thicknesses from the previously studied Nafion 117 but also thinner more commercially viable membranes. Nafion XL was additionally selected as it features an ePTFE reinforcements and additives which have been shown to impact water uptake and water states [283]. The Aquivion and Fumasep were selected as they are also PFSAs but have a different chemical structure and IEC such as the Fumaseps with its short side chain and lower IEC. Aquivion E87-05S with a higher IEC of >1.12 meq/g and the same chemical structure as the Aquivion E98-05S was also ordered for comparison however, the membrane has since been discontinued and was not delivered. The Fumasep was additionally selected due to its PEEK open mesh reinforcement and thickness in order to test its dimensional stability.

The ePTFE reinforcement of the Nafion XL is a microstructure whereas the PEEK open mesh reinforcement is more macroscopic allowing for it to be seen by eye as well as under a

microscope as seen in Figure 3.1. The microscope used was a LEXT OLS5000-SAF with a 10x objective lens (MPLFLN10xLEXT). The ePFTE of the Nafion XL could not be seen under a microscope and only surface details could be seen as with the non-reinforced membranes such as the Nafion 117. The strands of the open mesh of Fumasep F10120-PK were measured using the microscope and the strand width was 40µm with a spacing of 220µm.

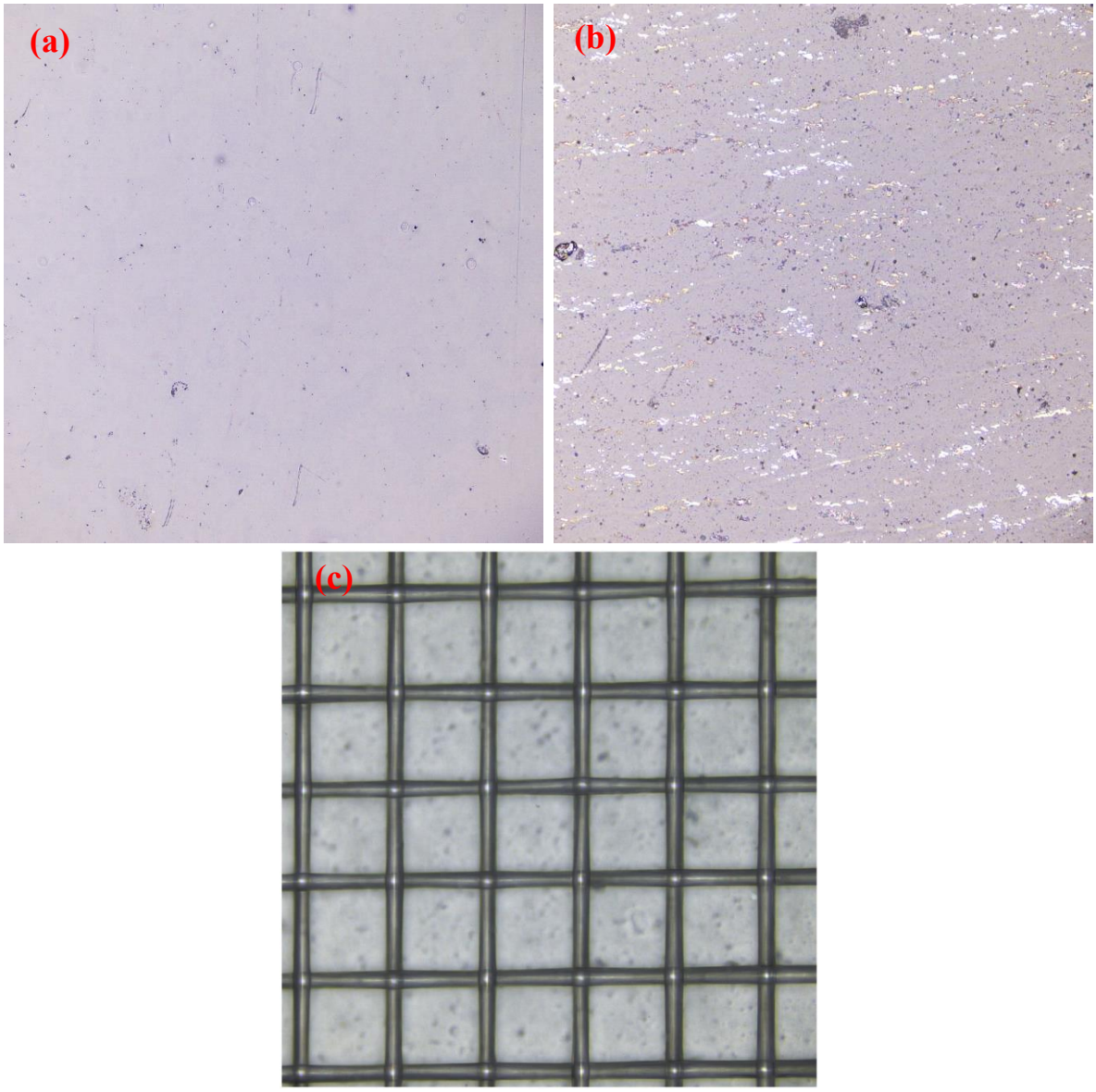

Figure 3.1 - Microscope images of Nafion 117 (a), Nafion XL (b) and Fumasep F10120-PK (c).

Membranes were cut into 3 cm × 3 cm samples and pre-treated by boiling in 3% H_2O_2, submersion in boiling deionised (DI) water, then boiling in 0.5 M H_2SO_4 and finally submersion in DI water at ambient conditions (1 hour for each step). 3 repeats for each type of membrane were prepared for each steady state experiment and only one for diffusion and hygral swelling studies.

Discrete levels of Nafion 117 WU were first achieved by placing the pre-treated membranes in sealed containers containing a beaker of water (24 hours) or a saturated salt solution (48 hours) to reach equilibrium as shown in Figure 3.2, the membrane is not white as depicted but was placed on a white piece of plastic. A humidity sensor was used to ensure the correct humidities were obtained and initial attempts produced higher humidities than expected. It was found that although a saturated solution was obtained, a high excess of solid salt was required. This is likely due to temperature fluctuations and a slower rate of water vapor sorption to desorption as although the equilibrium relative humidities (RHs) have little temperature dependence, the absolute humidity does vary.

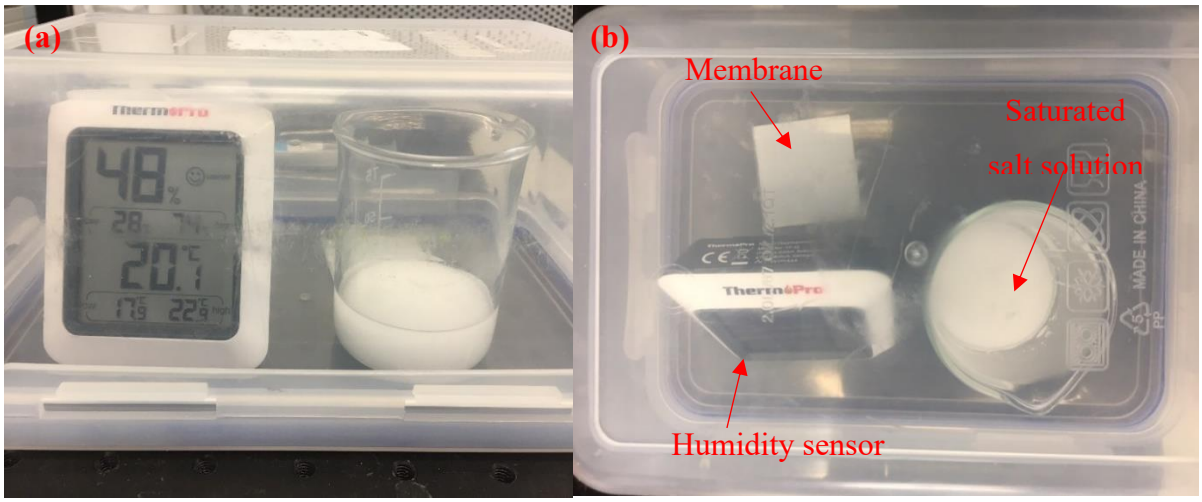

Figure 3.2 - Container used to prepare membranes with saturated salt solutions.

The solutions used and the RH measured using a TP50 hygrometer (ThermoPro, USA) are shown in Table 3.2.

Table 3.2 – Conditions for membrane hydration and the expected WU.

Saturated salt solution	Measured RH (%)	Expected Nafion 117 WU (wt%) [158]
Magnesium chloride	38-40	7.7
Potassium carbonate	47	8.6
Sodium chloride	74-78	13.1
DI water	100	26.0

An oven was also used to obtain dry membrane measurements however it was later found that membranes still contained significant amounts of water and therefore these measurements were not used.

Measurements were performed under ambient conditions and clamped in a sample holder which has a 20x20mm hole as shown in Figure 3.3. As the sample was removed from the sealed container, a deviation from the equilibrium water uptake can be expected.

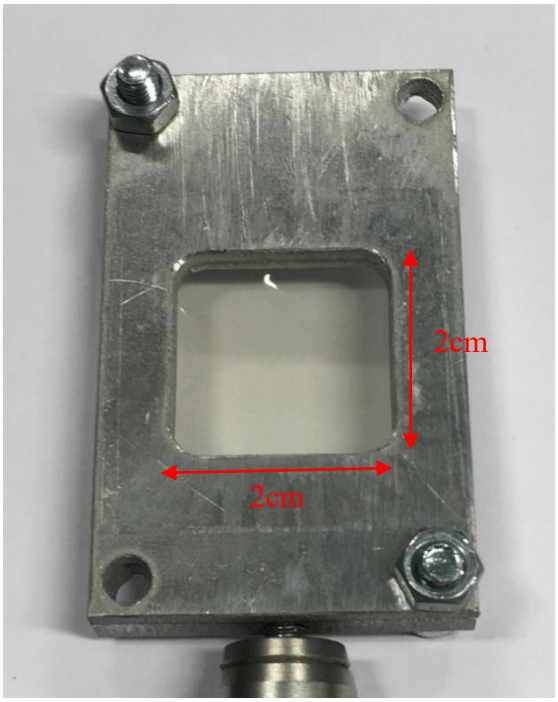

Figure 3.3 - Sample holder containing a sample of Nafion 117.

3.2 Humidity chamber

Membranes require 2 days to reach an equilibrium with the humidity from saturated salt solutions and variations in achieved humidity were observed. In addition, removing samples from the sealed containers to obtain measurements causes a deviation in the membrane water uptake which is no longer in equilibrium. This is a significant issue for thin samples such as Nafion 211 which rapidly changes when exposed to the ambient humidity as demonstrated previously [234,283]. With is in mind, a bespoke humidity chamber was proposed which would allow for measurements to be obtained without removing the sample from the controlled environment.

3.2.1 Humidity chamber design

The bespoke humidity chamber was designed, realised and retrofit to the sample portion of the terahertz beam-path in the THz-TDS setup. This step was necessary to minimise moisture exposure to the terahertz optics and devices to avoid material degradation [260]. In particular, the humidity chamber was positioned within the focused region of the terahertz beam-path as shown in Figure 3.4 and has welded pipes for inlet and outlet airflow, as well as two 80mm diameter z-cut quartz windows of 3mm thickness for terahertz beam propagation [284]. In principle, other highly terahertz transparent window materials could also be used such as high-density polyethylene and high-resistance silicon [239].

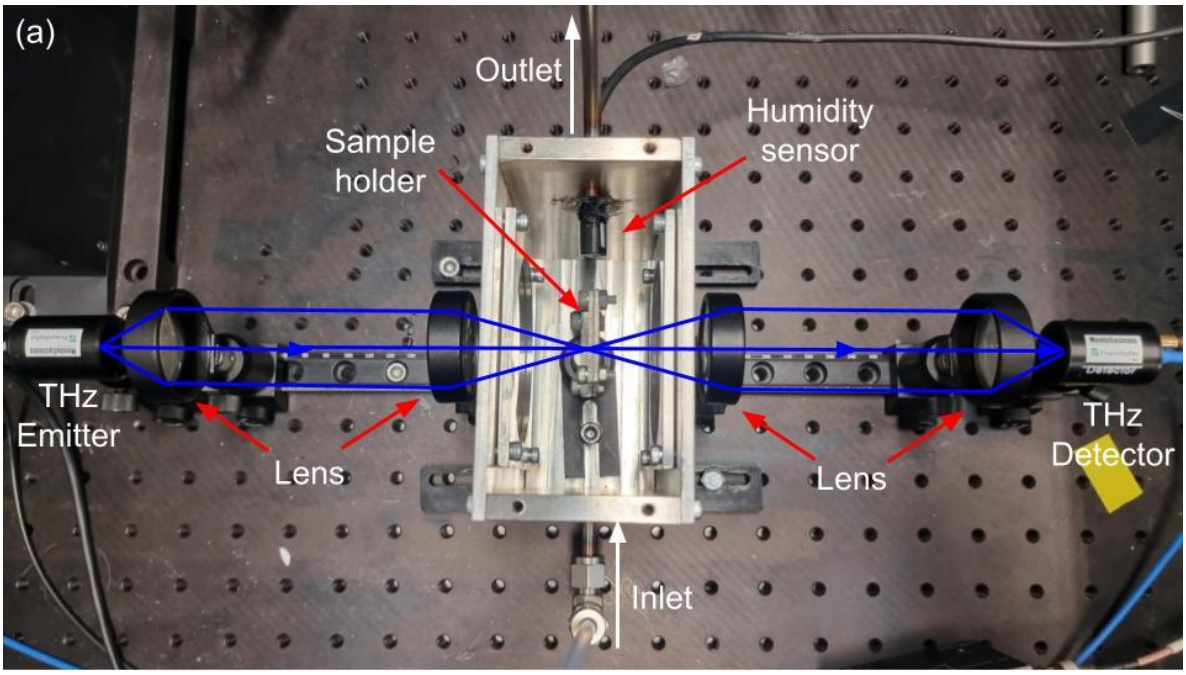

Figure 3.4 – (a) Experimental setup for humidity chamber measurements using THz-TDS shown with chamber lid removed.

The length of the chamber was designed with the windows being 28.5 mm from the sample to avoid etalon reflections within the 100 ps terahertz measurement window. Etalon reflections are reflections between two parallel surfaces and in this case will occur between the windows and close lenses due to their proximity. However, as the materials do not change between the sample and reference measurements, they do not impact the results. These reflections will also occur between the changing sample and windows, but as only 100ps is measured by the THz-TDS these reflections are not captured due to their separation and the finite speed of light. Limiting the measurement window to remove undesirable responses such as etalon reflections is known as time gating and is used to simplify analysis and isolate specific material responses.

The design and dimensions of the chamber with an internal volume of 0.72L are shown in Figure 3.5. This allowed for easy access to the sample holder by removing the top 4 bolts and removing the lid. The sample holder attached to a ½ inch diameter post could easily be placed securely in a post holder without the need to further tighten any bolts.

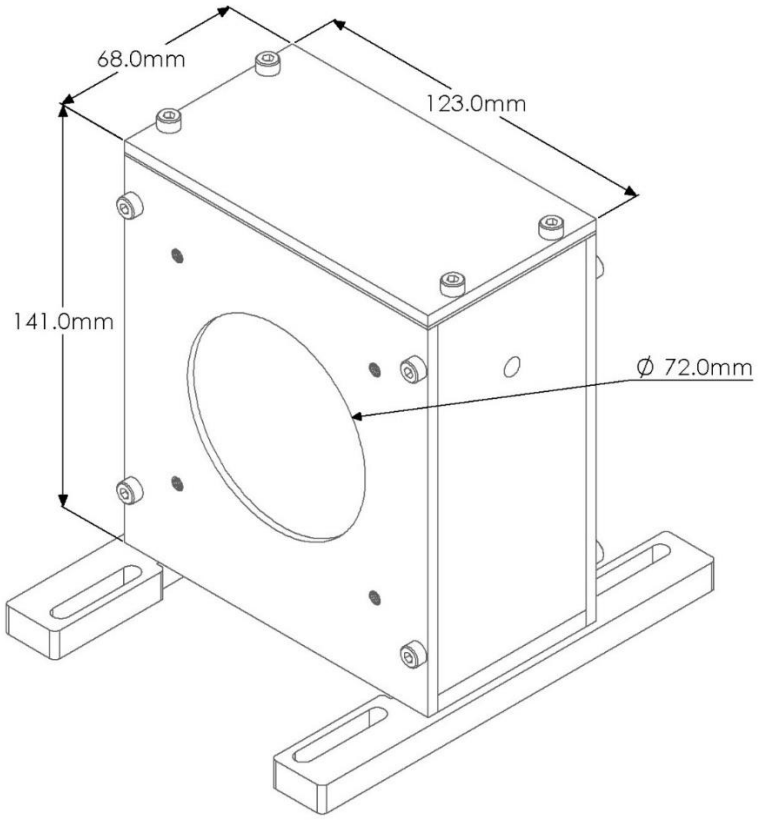

Figure 3.5 - Technical drawing of the chamber in perspective view.

Humidified air was supplied to the chamber via the gas inlet and was prepared externally as seen in Figure 3.6 where dry compressed air was mixed with saturated air, which had been passed through a home-made bubble humidifier.

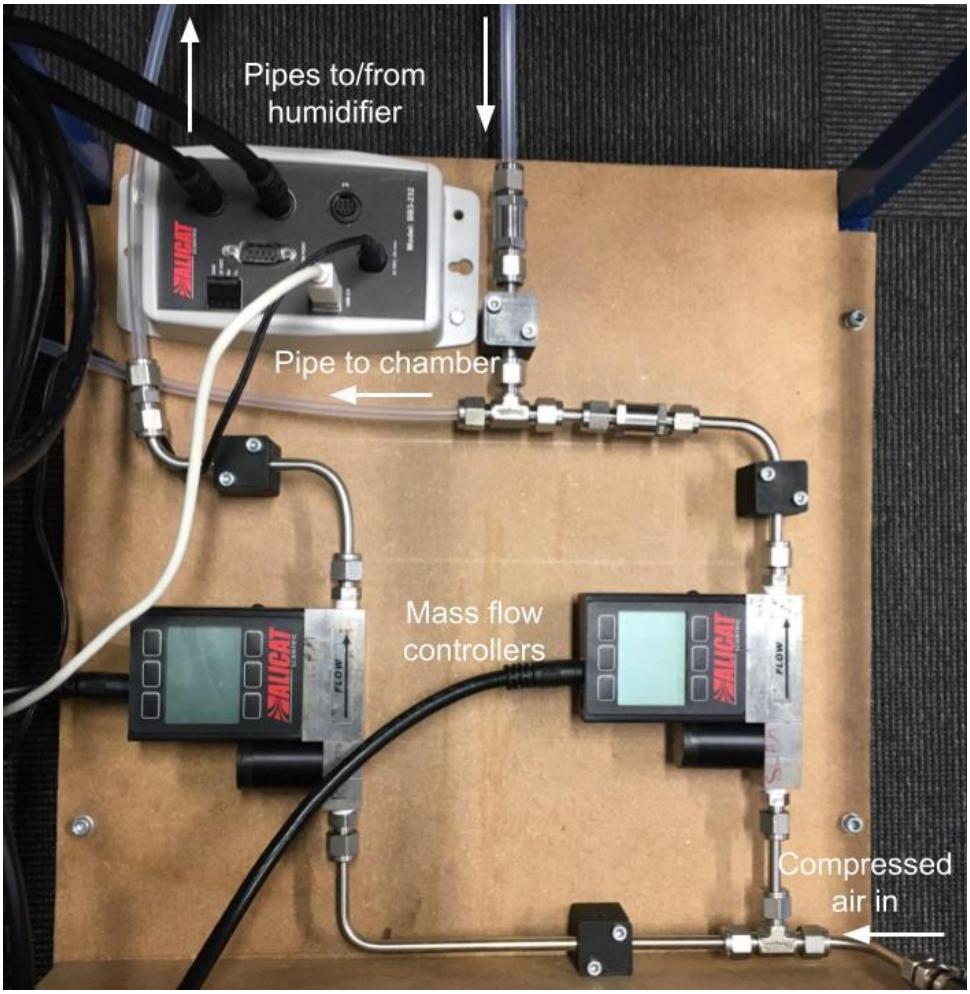

Figure 3.6 - Humidity control pneumatics.

The level of humidification was controlled by changing the flow rates of dry and hydrated air, which were controlled using the two mass flow controllers (Alicat, USA) connected to a PC via a breakout box for flow control networking.

The total gas flow rate was set to 1 standard litre per minute. This was the maximum flow rate for the mass flow controller available, a reduced flow rate would result in a slower response. The humidified gas stream was delivered to the chamber through a connected pipe as seen in the overall system setup shown in Figure 3.7.

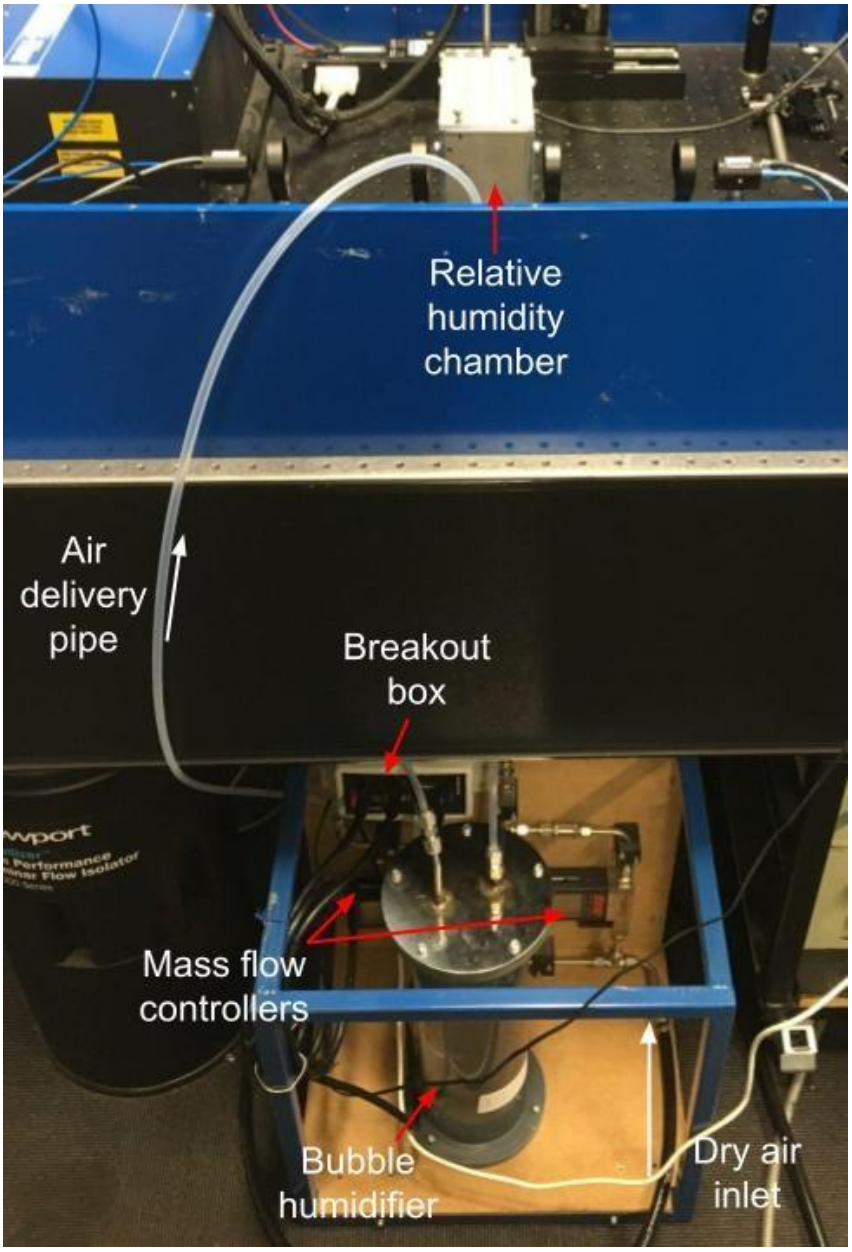

Figure 3.7 - Overview of the system setup.

Humidity was measured inside the chamber as shown in

Figure 3.4 using a T9602 polymer capacitance humidity sensor (Amphenol, USA) with a specified accuracy of ±2% at 20-80% RH and up to ±3.5% at 0-20% and 80-100% RH. The sensor was wired to an Arduino microcontroller which would determine the relative humidity and temperature. As the chamber has a volume of 0.72 L, this results in a residence time of ~43 seconds. The ratio of dry/wet gas was controlled using a PID controller within LabVIEW which was used to control the whole humidity system as shown in Figure 3.8.

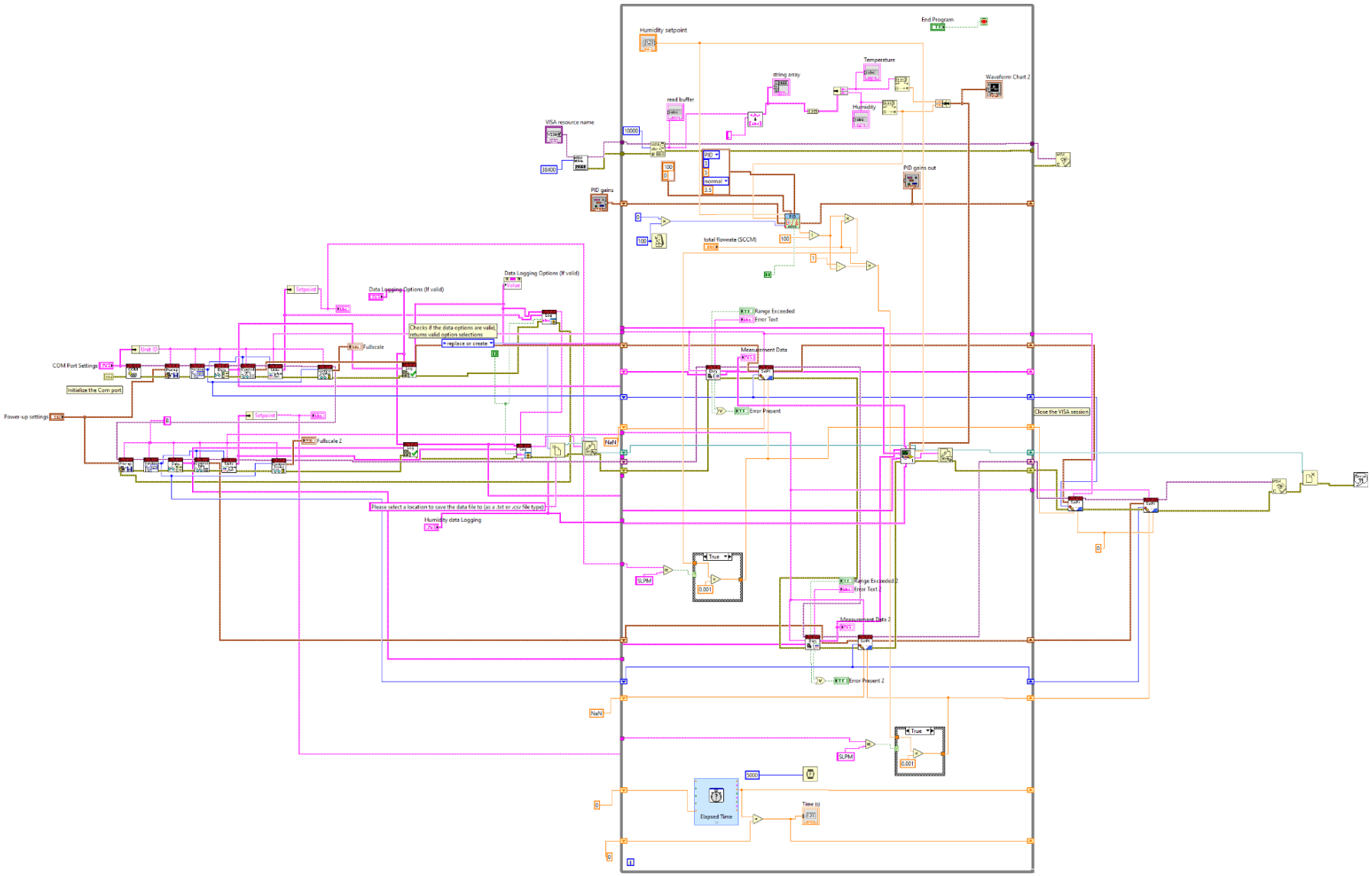

Figure 3.8 - LabVIEW block diagram for humidity control.

A simplified flow diagram for this program can be seen in Figure 3.9. The program must connect to both mass flow controllers and the Arduino through USB connections and the mass flow controller breakout box which is connected to each mass flow controller. The setpoints for the total flow rate and the humidity setpoint are also required. During operation the humidity sensor reading is input into the PID controller which determines the percentage of wet gas required to reach the current setpoint. A resolution of 0.01% RH was used for the sensor readings and although the sensor was not accurate to this degree. 0.1% RH resolution was initially used but insufficient resolution causes control instability. The flow rates are then determined and sent to the mass flow controllers. Data from the mass flow controllers such as actual flow rate and pressure are logged along with the humidity setpoint, humidity sensor reading and a timestamp for comparing to THz measurement timestamps. This is repeated every 5 seconds as the system response is slow and rapidly changing the setpoint of the mass flow controllers over long periods of time can cause burning out the memory (EEPROM) with excessive writes. In the case of a 0% RH setpoint, the flow rates were later overwritten as these are known to be 0% wet gas and the controller would periodically increase slightly due to fluctuations in the sensor reading.

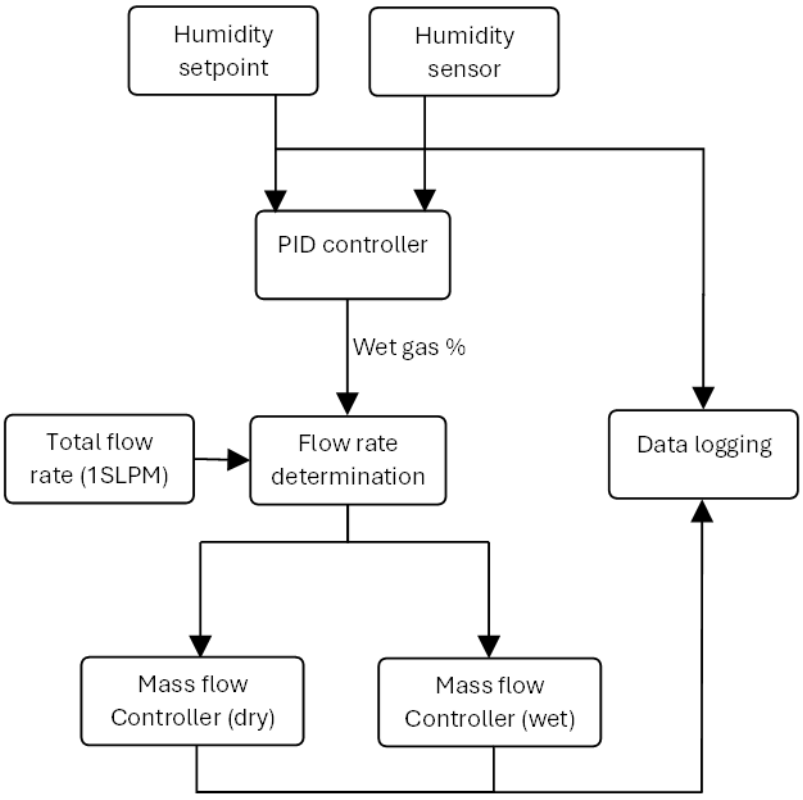

Figure 3.9 - Flow diagram of humidity PID control.

All of this can be controlled though a virtual interface as shown in Figure 3.10. Here the communication ports (COM) can be configured for the Arduino and breakout box as well as setpoints. Data logging options can also be modified. Mass flow controller data is also shown alongside a plot of the humidity and temperature data from the sensor which can be used for monitoring purposes.

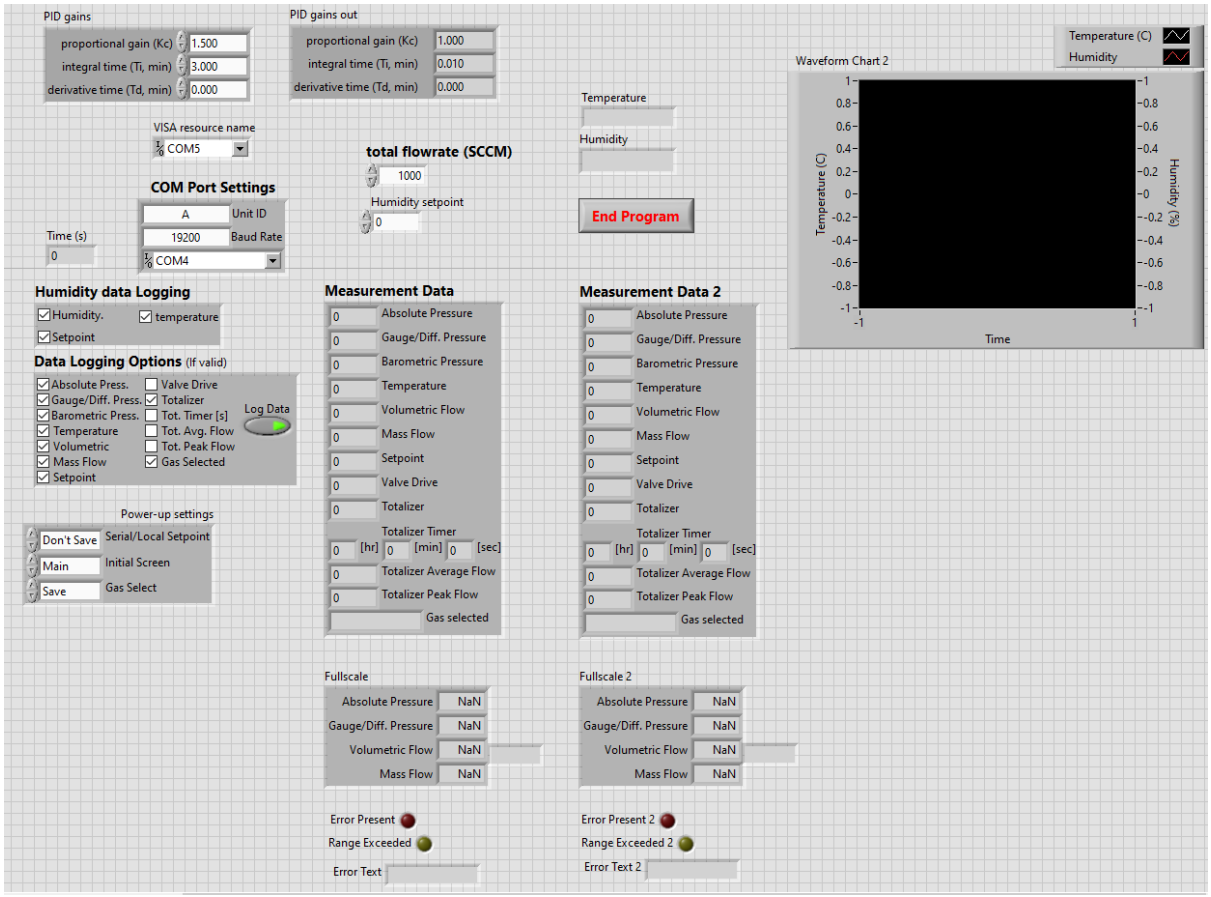

Figure 3.10 - LabVIEW virtual interface for humidity control.

Optimisation of the PID control was achieved through trial and error with a proportional gain of 1.5 and integral time of 3 minutes. No derivative time was used as this caused some instability due to the time delay and also small fluctuations. An automatic PID optimiser was implemented however, this failed to achieve suitable optimisation possibly due to the some sensor delay and slow response. A system benchmark was then performed in sorption followed by desorption in a range of 0-90% RH in 10% intervals with 10 minutes per setpoint excluding 0 and 90% RH which were given 20 minutes as shown in Figure 3.11. Overall, the setpoints are reached within the 10 minutes although further testing revealed that 15-20 minutes was required to stabilise to within ±0.1% of the measured RH. Reaching the 0% and 90% RH setpoints is slower with 0% not reached in the test, this is due to the PID control hitting the 0

and 100% wet gas limits as shown in Figure 3.11. The length of time required to reach 0% RH varied and 3-4 hours were often used to obtain 0% RH measurements. The long time required is likely due to the need to remove all water from the active sections of the gas delivery system and chamber.

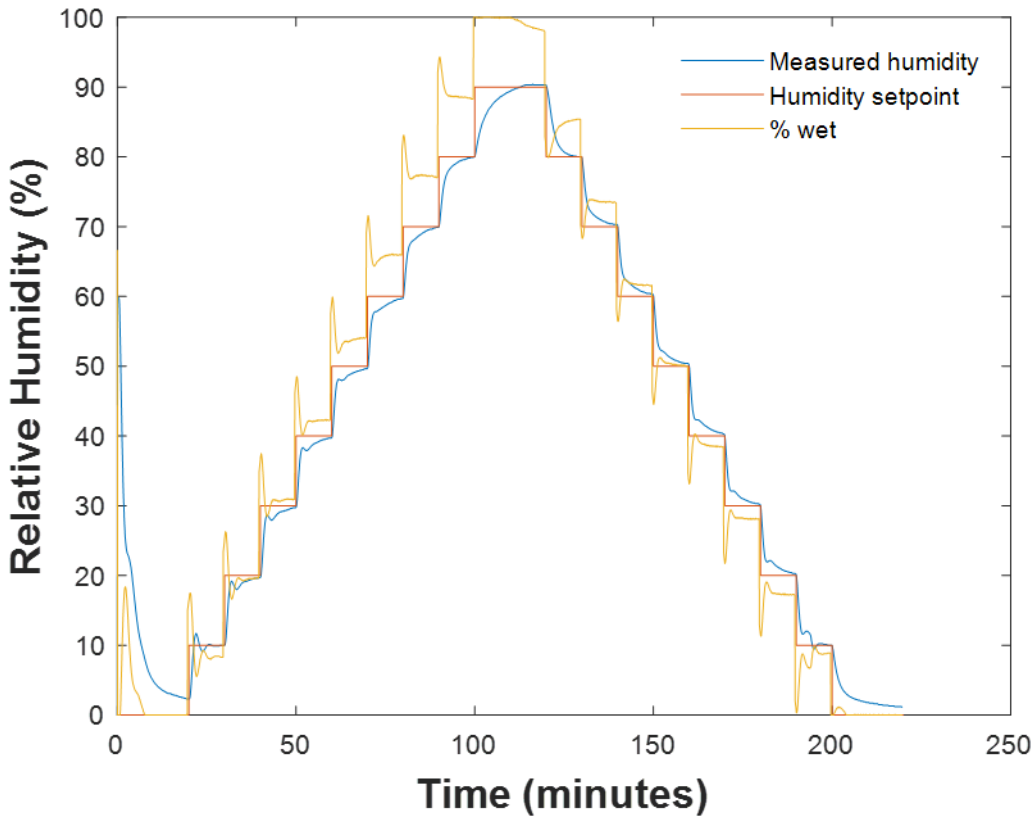

Figure 3.11 - Humidity control system benchmark.

3.2.2 Steady state

In general, based on the RH sensor readings, initially for steady state measurements the chamber was able to operate between ~0-85% RH consistently, above which e.g. at 90% RH set-point, variations were observed. This was due to a lack of temperature control and water build up in one of the one-way valves, this was from water condensation due to temperature changes when the chamber was not in use. Detaching the humidifier when not in use generally resolved this issue and reaching 90% RH became much more consistant. The lack of temperature control is a limitation of this system as it affects membrane WU [86,285] and achievable RH. However, temperature was recorded for all experiments and varied between 20.7 and 25 °C. Steady state measurements were acquired at decreasing measured humidities of 90%, 70%, 50%, 30%, 10% and 0% RH at steady state for 2 hours beginning from a pre-

hydrated state at 100% RH due to 24 hours spent in a container containing DI water as with saturated salt preparation.

3.2.3 Diffusion

The chamber was initially designed for steady state measurements however, it should be noted that the chamber had to be opened to remove the sample from the beam path in order to take reference measurements. As the reference needs to be taken at the same humidity as the sample measurement, the chamber must again reach the same desired humidity setpoint which took 15-20 minutes and even longer for 0% RH. This is due to water absorption lines which can be seen in the terahertz regime and would impact the subsequent analysis but can be removed with a reference at the same humidity. The chamber would then need to be opened to place the sample back into position within the beam path for the next measurement. Removal of the sample may have caused some hysteresis to occur in the first steady state tests where the chamber needed to be opened. In order to take regular measurements over time as required for diffusion measurements, a motorised stage was built to accurately move the sample within the chamber whilst the humidity remained constant as shown in Figure 3.12. Due to taking 100 THz-TDS averages and the movement of the stage, a reference could be taken with each sample measurement every 2 minutes. In principle the whole chamber could be moved rather than the sample as long as the beam still passes through the window and the window has uniform thickness and surface finish with no defects such as scratches. Moving the sample however provides a solution with reduced tolerances requirements. The mechanical stage works by rotating a lead screw with a stepper motor. This is connected to a threaded bracket which pulls or pushes the post holder. The post holder is attached to a dovetail rail carrier which guides the linear motion along the dovetail rail. The stepper motor was powered by an external DC power supply through a CW8060 motor driver which was controlled by a connected Arduino as seen in Figure 3.12. The distance travelled was not set and instead the duration was set to 9.6 seconds, this was configured after the initial stage position was set to ensure the stage did not crash by moving too far but also ensure the sample holder is sufficiently out of the beam path, and the direction was changed to return the sample to its initial position.

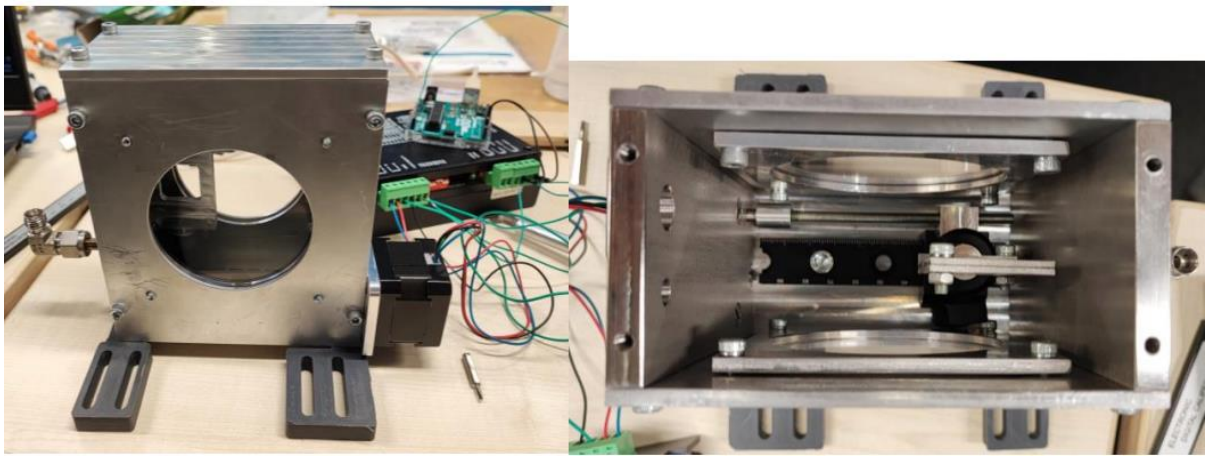

Figure 3.12 - Motorised stage for sample movement with the enclosed chamber.

To measure the diffusion of water using THz-TDS, monitoring of membrane hydration during a change in ambient water activity is required. In these experiments incremental changes of 10% RH were studied for both sorption and desorption in the range of 30-90% RH over a period of 1.5 hours per interval. Membranes were also equilibrated for 1.5 hours at the first setpoint prior to any diffusion measurements and 3 measurements were acquired prior to the change in humidity to account for uncertainty. Due to heat generated by the stage motor the temperature in the chamber would increase. Therefore, reference measurements were only obtained every 10 minutes after the first 20 minutes following a change in relative humidity to limit the heat generated, as such maximum temperature increases were ~4°C as seen and further discussed in Chapter 5. After 20 minutes only small changes to humidity would occur and therefore water absorption lines were no longer a problem. Due to the increased chamber temperature relative to the humidifier, sorption measurements from 80-90% RH were not possible. Desorption from 90-80% RH was possible as only a couple of measurements were taken before the change in humidity.

Nafion 117 was selected for this study due to its thickness which results in a slower change in water content, this gave a greater separation of membrane diffusion response from interfacial and RH response. This also gives better fittings due to the limited rate of data acquisition. The impact of water vapor diffusion at the membrane interface is also reduced. The terahertz data was analysed in the same manner as the steady state measurements.

3.2.4 Hygral swelling and shrinking

To probe the effects of hygral swelling, samples of Nafion 117 and Fumasep F10120-PK were studied. These were selected as they are both thick PFSA membranes with the Nafion 117

featuring no reinforcement and the Fumasep F10120-PK having a PEEK fibre mesh reinforcement. The changes previously observed in a literature study at room temperature were only ~2% of the membranes thickness [110]. Due to the uncertainty of fitting thickness with THz-TDS, these changes would likely not be observed in thin membranes such as the Nafion 211 previously studied [110]. The study found in literature [110] cycled the humidity 6 times between 30 and 90% RH and the change in RH was ramped at a constant rate of 2% per minute followed by a dwell time of 20 minutes. Due to the limitations of the RH system, in this study the humidity was cycled between 10 and 80% RH as these RH could be obtained quickly and consistently. No specific rate of RH change was used and the PID control was immediately changed to the new setpoint. Due to the thicker membranes used, the RH changes occurred every 1.5 hours to ensure that an equilibrium was obtained, and no thickness changes observed were due to a difference in RH or not reaching an equilibrium. To try and increase the impact of hygral swelling, the humidity was cycled 18 times over a period of 3 days. Measurements were obtained each day with two 80% RH and two 10% RH sets of measurements. Cycling continued overnight but no THz measurements were obtained. 5 repeat measurements were obtained for each measurement as there is some uncertainty in the obtained thickness as seen in Chapter 5. Some initial tests with no repeats appeared to show other trends due to this uncertainty. The stage was also used for these measurements which was important as removing the sample from the chamber for a reference measurement would cause the membrane to shrink or swell impacting the study. Unlike the steady state and diffusion studies where the membrane was clamped within a frame, a spacer was also used to ensure the membrane was not constrained. This was done to ensure that hygral swelling and shrinking was responsible for any observed thickness changes rather than the membrane slipping in a frame when under tension from shrinking.

3.2.5 Rapid desorption

FTIR provides an additional method for the characterisation of water within PFSA membranes. In particular Kunimatsu et al [202] demonstrated that there is a correlation between the intensity of the band at 1630 cm^{-1} and proton conductivity. The experiment performed was a desorption of Nafion 211 from a hydrated state using a dry air purge. To compare the data from Kunimatsu et al [202] to THz-TDS, this experimental methodology had to be replicated. Therefore, a Nafion 211 membrane was hydrated to 90% RH for 2 hours to reach an equilibrium, dry air was then used to purge the humidity from the chamber and THz-TDS measurements were obtained every 2 minutes as with the transient diffusion study for 2 hours.

3.3 Terahertz time-domain spectroscopy

Transmission terahertz spectroscopy was performed using a commercial THz-TDS setup (TERA K15, Menlo Systems, Germany) which features polymethylpentene (TPX) lenses for focusing and collimation as shown in Figure 4.3 and Figure 3.13. Nafion 117 hydrated with saturated salt solutions was measured in free space without the humidity chamber present at ambient environmental conditions as seen in Figure 3.13 and for each measurement 100 averages were acquired. A reference measurement was also acquired immediately prior to any measurements to reduce any laser jittering effects

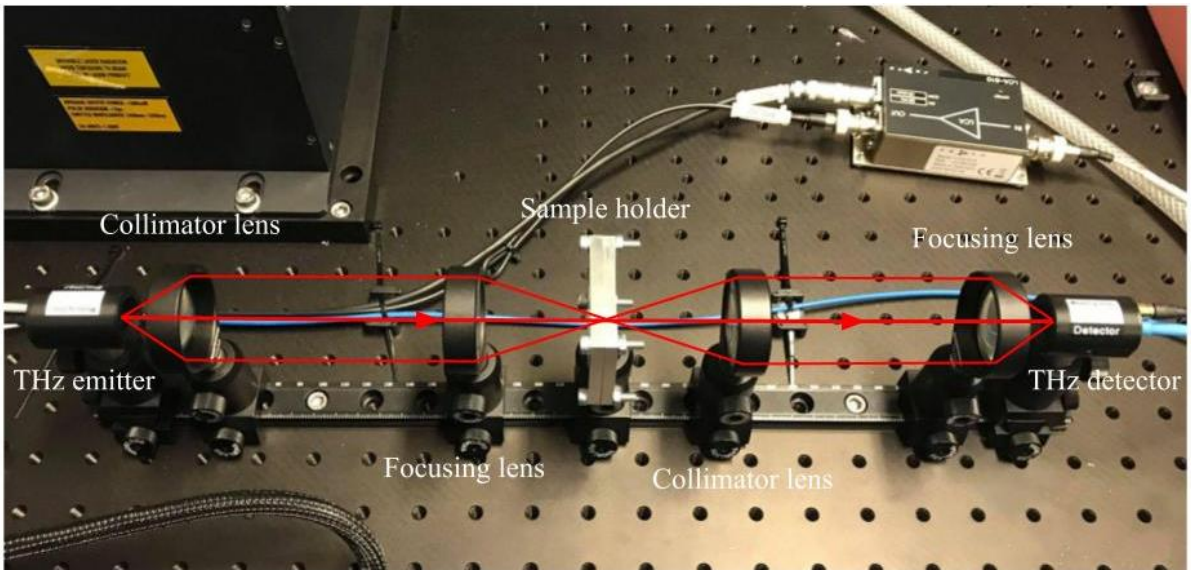

Figure 3.13 - THz-TDS free space experimental setup.

For steady state measurements 500 averages were acquired for a reduction in measurement noise as the membrane was at steady state allowing for a longer measurement time. 100 averages were used for diffusion and hygral swelling studies. All measurements were acquired with a time delay resolution of 33.3fs and a time delay span of 100ps as seen in Figure 3.14.

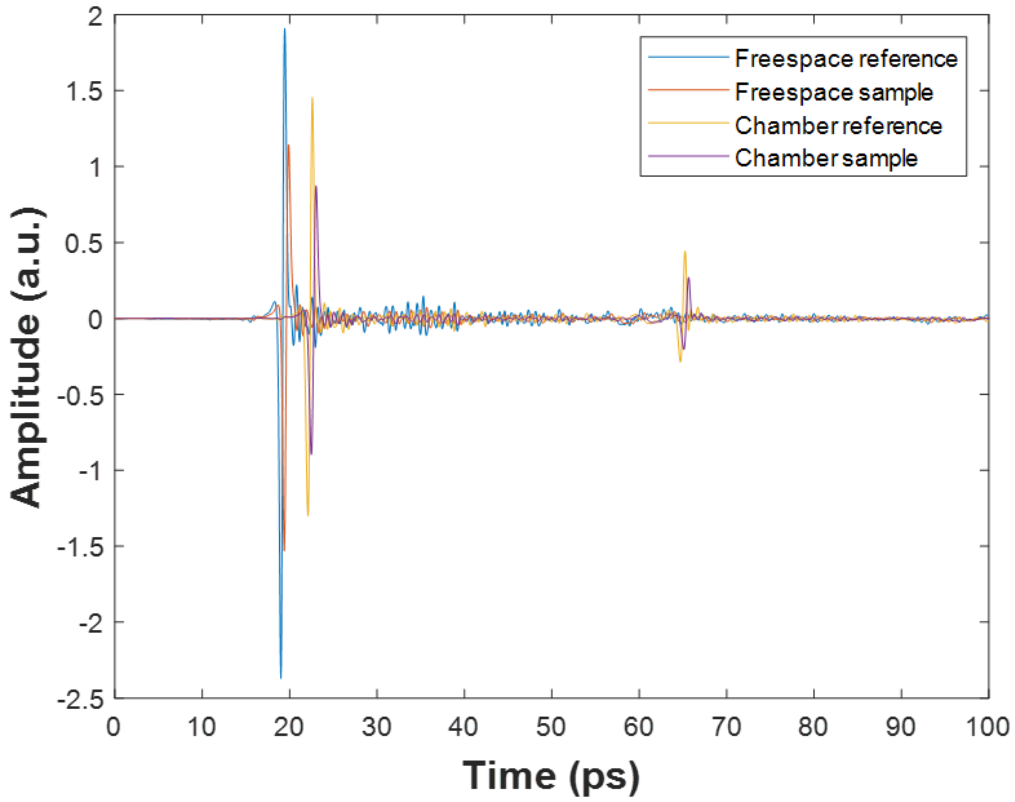

Figure 3.14 - Waveforms for reference and sample measurements of free space and chamber measurements of Nafion 117 under ambient humidity.

Figure 3.14 shows a comparison of the waveforms for the reference and sample measurements of Nafion 117 in free space and with the chamber under the same ambient humidity. It can be seen that the chamber windows have caused the primary pulse to be delayed by approximately 3ps which also has a reduced amplitude. This is due to internal reflections in the windows which also results in a significant secondary pulse ~43ps later from the primary internal reflection, any further reflections are not captured within the 100ps range. Some reduction in amplitude will also be due to minor absorption within the window.

Despite the clear differences in the THz waveforms, the extracted magnitude and phase from the ambient Nafion117 is not impacted. This can be seen in Figure 3.15, demonstrating that the presence of the chamber has negligible effect on the measurement results. Confirming that the design of the chamber is sufficient to avoid reflections between the sample and windows within the 100ps window.

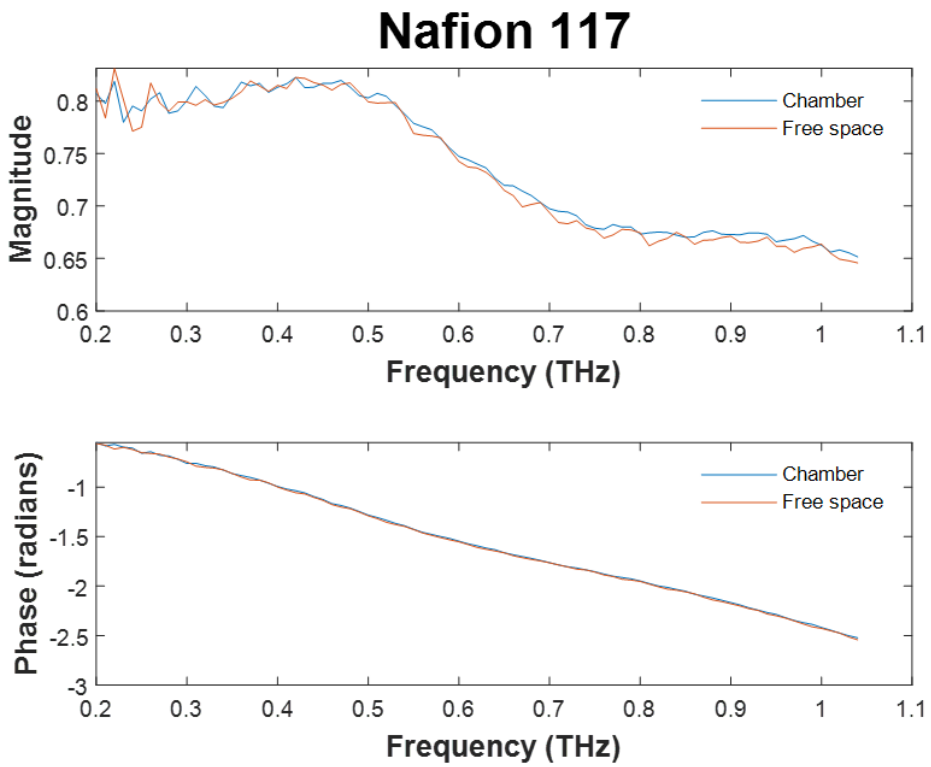

Figure 3.15 - Comparison of chamber and free space membrane magnitude and phase response under ambient conditions.

For chamber measurements, due to the presence of discrete water vapor absorption lines in the terahertz spectral regime [286] which can be seen in Figure 3.16 and the changing humidity, a separate set of reference measurements were acquired at the same humidities as the sample measurement but without the membrane being present. This is necessary to remove water vapor absorption lines, which would otherwise interfere with subsequent data analysis.

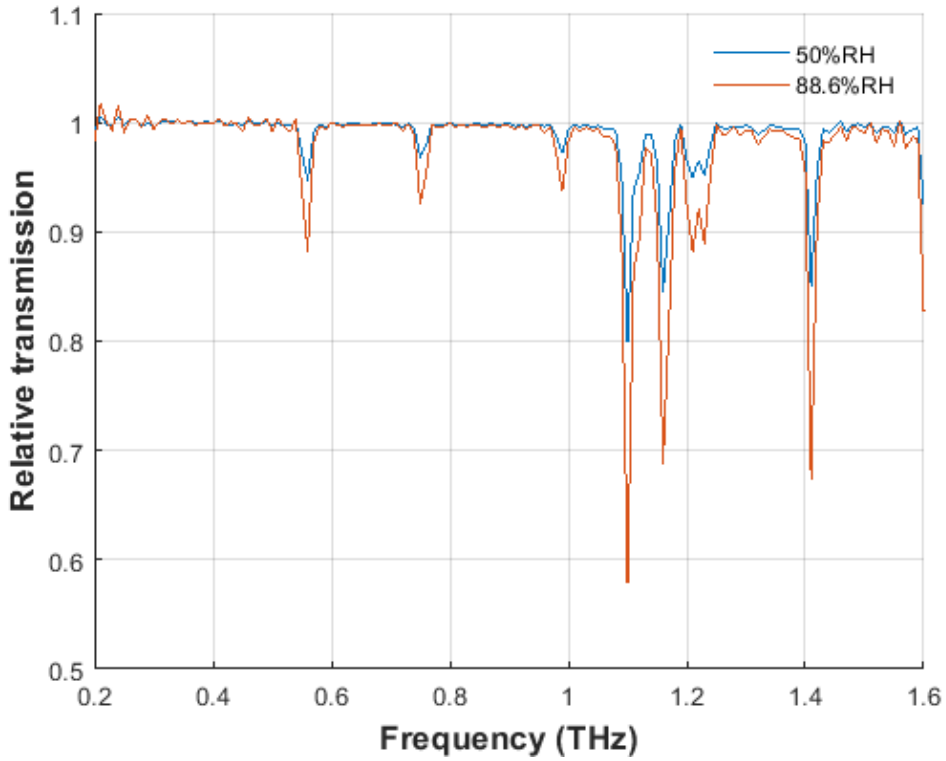

Figure 3.16 - Transmission showing water vapor absorption lines of chamber equilibrated at 50% RH and 88.6% RH, reference measurement used was 0% RH.

3.4 Terahertz data analysis

Prior studies have shown how macroscopic WU can be determined in hydrated membranes where an equivalent model of hydrated membranes is arranged as a dry membrane and a uniform layer of water thickness [234]. As the dielectric properties of membranes at different WUs can be described using effective medium theory, here a simple, linear mixing model is assumed relating the effective frequency dependent absorption and the volume fraction of water in the system [281] as shown in Equation 3.1

$$d_{hyd}(RH)\alpha_{hyd}(\omega, RH) = d_m\alpha_m(\omega) + d_w(RH)\alpha_w(\omega) \tag{3.1}$$

where α is the absorption coefficient, ω is the angular frequency and d is the thickness, subscripts hyd and m refer to hydrated and dry membrane, respectively, while w is the water contribution. By rearranging Equation 3.1, effective water thickness can be determined using Equation 3.2

$$d_w(RH) = \frac{1}{\alpha_w(\omega)}\left(\alpha_{hyd}(\omega, RH)d_{hyd}(RH) - \alpha_m(\omega)d_m\right) \tag{3.2}$$

Absorption coefficients and thicknesses of dry and hydrated membranes are calculated from analysing acquired waveforms using a parameter-based algorithm [283]. In general, this algorithm models the transmitted electromagnetic wave through a dielectric slab with a complex refractive index $\hat{n}_s = n_s(\omega) - ik_s(\omega)$ at a normal angle of incidence in free space using plane-wave approximation shown in Equation 3.3 [283]

$$\frac{\hat{E}_s(\omega)}{\hat{E}_r(\omega)} = \hat{H}(\omega) = \frac{2}{\hat{n}_s + n_0}\frac{2\hat{n}_s}{\hat{n}_s + n_0} exp\left(-i[\hat{n}_s - n_0]\frac{\omega d}{c}\right) FP(\omega) \tag{3.3}$$

where $\hat{E}_s(\omega)$ and $\hat{E}_r(\omega)$ are the Fourier transform of the sample and reference waveforms, respectively, $\hat{H}(\omega)$ is the transfer function, n_0 is the refractive index of air, c is the speed of light in a vacuum, d is the sample thickness. $FP(\omega)$ is the Fabry-Perot from multiple internal reflections given by Equation 3.4

$$FP(\omega) = \frac{1}{\left(1 - \left(\frac{n_0 - \hat{n}_s}{n_0 + \hat{n}_s}\right)^2 exp\left[-2i\hat{n}_s\frac{\omega d}{c}\right]\right)} \tag{3.4}$$

Iterative methods are then used to extract the optical parameters by minimising the error between the modelled transfer function and the measured transfer function [244–250], commonly known as the objective function in optimisation and expressed as

$$\hat{H}_{theory}(\omega) - \hat{H}_{measured}(\omega) \tag{3.5}$$

To ensure the solver can arrive at physical solutions, *a priori* information on the dielectric response of the materials is included, which is valid for hydrated membranes as they are known to follow a double Debye response [200,234,268,283] given by 3.6

$$\hat{\varepsilon}(\omega) = \varepsilon_\infty + \frac{\Delta\varepsilon_1}{1 + i\omega\tau_1} + \frac{\Delta\varepsilon_2}{1 + i\omega\tau_2} \tag{3.6}$$

where ε_∞ is the infinite dielectric constant, $\Delta\varepsilon_1$ and $\Delta\varepsilon_2$ are the dielectric strengths of the bulk and free Debye relaxations, τ_1 is the bulk relaxation time and τ_2 is the free relaxation time. The temperature dependence of the bulk relaxation time of DI water has been extensively studied in literature using both THz-TDS and dielectric spectroscopy, literature values at different temperatures [200,264,287–296] are shown in Figure 3.17. The bulk relaxation time has previously been measured for water within Nafion membranes using dielectric spectroscopy and found to be the same as DI water at all levels of hydration within the 25-45°C range studied [200]. The results show a clear trend for relaxation time with a value of 8ps at 25°C, this value has been used as a constant in fittings as was done previously [234,283].

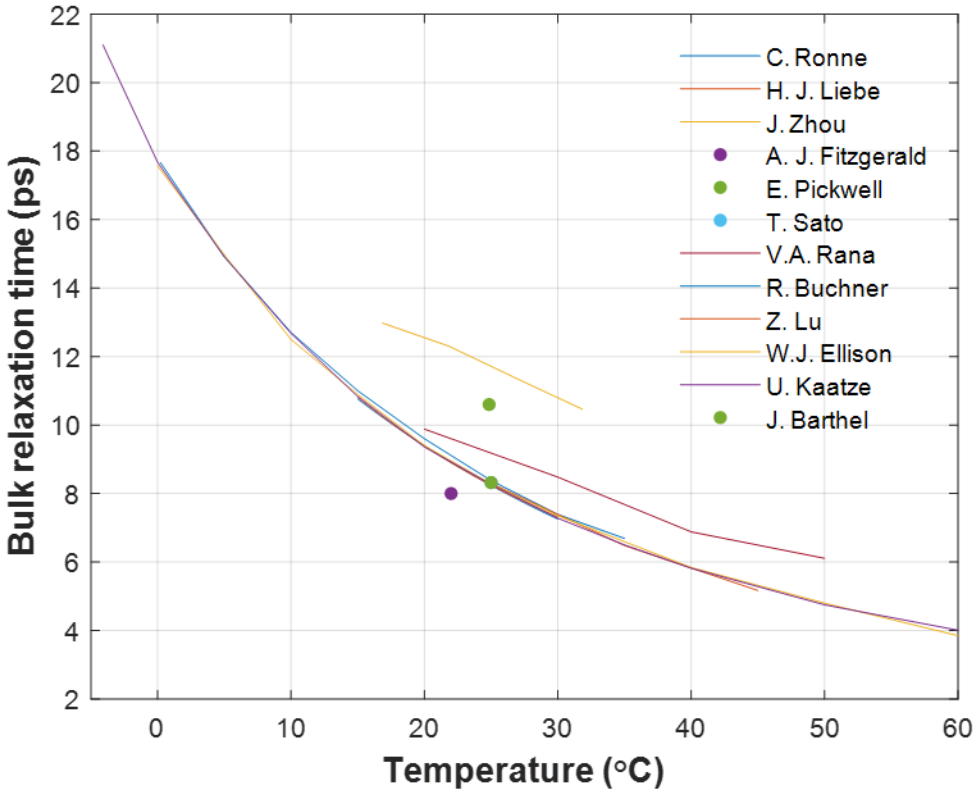

Figure 3.17 - Temperature dependant bulk water relaxation time and dielectric strength in DI water from literature [200,264,287–296].

Bounds of the fitting parameters are shown in

, the thickness range was selected per sample but was approximately ±15-20% of the nominal thickness. A reduction of the upper bound and initial value for the infinite dielectric constant to 2.7 was required for some thinner membranes.

Table 3.3 - Search range of selected fitted variables.

Variable	Lower bound	Initial value	Upper bound
ε_∞	2.2	3	3
$\Delta\varepsilon_1$	0.01	30	30
$\Delta\varepsilon_2$	0.01	2	2
τ_2 (ps)	0.08	0.15	0.4

The complex permittivity and absorption coefficient in turn are related to the complex refractive index using equations 3.7 and 3.8

$$\hat{\varepsilon}(\omega) = \varepsilon'(\omega) - j\varepsilon''(\omega) = {n_s}^2(\omega) - {k_s}^2(\omega) - j\,2n_s(\omega)k_s(\omega) \qquad (3.7)$$

$$\alpha = \frac{2\omega k_s(\omega)}{c} \tag{3.8}$$

Using the absorption coefficient of liquid water [287] together with the optical parameters and thicknesses from the solver, humidity dependent effective water thicknesses and hence WU can be determined using Equations 3.2 and 3.9

$$WU(RH) = \frac{d_w(RH)\rho_w}{d_m\rho_m} \tag{3.9}$$

where ρ_w and ρ_m are the density of water (1 g/cm^3) and Nafion (1.94 g/cm^3 [234]), respectively. Using the extracted dielectric strengths and WU, the proportions of bulk, bound and free water states are then determined using Equations 3.10 - 3.12 [233,234,283]

$$f_{bulk}(RH) = \frac{C_0}{C_{H_2O(RH)}} \frac{\Delta\varepsilon_1(RH)}{\Delta\varepsilon_{1,bulk} + \Delta\varepsilon_{2,bulk}} \tag{3.10}$$

$$f_{free}(RH) = \frac{C_0}{C_{H_2O(RH)}} \frac{\Delta\varepsilon_2(RH)}{\Delta\varepsilon_{1,bulk} + \Delta\varepsilon_{2,bulk}} \tag{3.11}$$

$$f_{bound}(RH) = 1 - f_{bulk}(RH) - f_{free}(RH) \tag{3.12}$$

where $\Delta\varepsilon_{1,bulk}$ and $\Delta\varepsilon_{2,bulk}$ are the dielectric strength of bulk and free water relaxations for pure water, respectively, and C_0 is the concentration of pure water (55.5 mol/L). The density of the hydrated membrane and concentration of water within the membrane can be determined using Equations 3.13 and 3.14 [234,283] where M_w is the molecular weight of water (18 g/mol)

$$\rho_{wm} = \frac{\big(100 + WU(RH)\big)}{\left(\frac{WU(RH)}{\rho_w} + \frac{100}{\rho_m}\right)} \tag{3.13}$$

$$C_{H_2O}(RH) = \frac{WU(RH)\rho_{wm}}{(100 + WU(RH))M_w} \tag{3.14}$$

It should be noted that due to a measurement delay between sample and reference measurements, terahertz pulse drift is likely and hence the resultant phase is corrected by multiplying the transfer function by a phase shift term $\exp(-i\Delta t\omega)$ [297] where Δt corresponds to a small timing change (<15 fs) for selected measurements. Thin membranes are particularly susceptible to pulse shifts compared with their thicker counterparts and as a result thick membranes such as Nafion 117 and Fumasep F10120 require no corrections. In thin membranes outlier phases were corrected according to a number of factors which are based on additional measurements, prior knowledge and experience from fitting thick membrane data

where phase correction is not required. In the case of steady state measurements both the amplitude and phase are approximately evenly spaced in order of humidity with lower amplitudes and phases seen at higher humidities as seen in Figure 4.1. Therefore, phase deviations can be seen through comparisons to the measurements at other humidities such as if the phase crosses the line of other phases or does not appear between adjacent humidity measurements. Given the amount of correction applied can affect the extracted membrane thicknesses, the amount can be validated by comparing the resultant thicknesses against actual thickness obtained using a micrometre measurement taken immediately after each terahertz measurement. In particular, the thickness difference between the two modalities was generally less than 5% for thin membranes. Micrometre measurements were obtained with an RS Pro external digital micrometre with 1um resolution and an accuracy of ±2μm. Measurements were obtained with the membrane placed between two 50μm polypropylene films as the micrometre could grip and stick to the membrane surface causing damage, the micrometre was rezeroed using the polypropylene films before each measurement. Occasionally pulse drift can result in poor quality of transfer function fittings for either amplitude or phase indicating a phase shift is required, this is uncommon but generally occurs with measurements of thin membranes performed at low humidities. A combination of these methods was used to inform phase correction decisions and ensure that any phase corrections were applied appropriately. Additionally, if a combination of these methods still yields some uncertainty for phase correction, comparisons with repeat measurements may provide additional indications for phase deviation. In this case comparison of the amplitude should also be carried out to ensure phase is responsible. These methods for correcting phase to ensure high quality fitting to the measurement for the robust extraction of the parameters, the fitting spectral range is taken up to 1 THz, above which, water vapor absorption becomes increasingly dominant as seen in Figure 3.16. The choice over this spectral range also coincides with the rotational relaxation of water [233,273,298]. All the acquired terahertz measurements were processed using codes developed in Matlab (Mathworks, Inc., MA, USA).

For comparison against DSC data, conversion to respective water contents [H_2O/SO_3] were made using Equations 3.15 - 3.17

$$WC_{total}(RH) = \frac{WU(RH)EW}{100M_w} \tag{3.15}$$

$$WC_{bulk}(RH) = f_{bulk}(RH)WC_{total}(RH) \tag{3.16}$$

$$WC_{bound}(RH) = f_{bound}(RH)WC_{total}(RH) \quad (3.17)$$

where WC is the water content [H_2O/SO_3] and EW is the equivalent weight of Nafion (1100g/mol).

3.5 Differential scanning calorimetry and thermogravimetric analysis

DSC was performed by the National Physical Laboratory (NPL) using a DSC Q2000 instrument (TA Instruments) using a temperature modulation mode. The same Nafion 117 samples were cut into small (2-5 mg) pieces and equilibrated at room temperature for at least 2 h prior to measurement either in DI water or at 85% RH in a humidity chamber. Samples were transferred rapidly into aluminium DSC crucibles with minimal (<1 minute) exposure to the ambient atmosphere before sealing. The DSC cycling programme comprised a negative temperature ramp from 20 °C to -90 °C at 2 °C/min cooling rate, followed by a positive temperature ramp up to 160 °C at 2 °C/min. A temperature modulation amplitude of ± 1 °C every 60 seconds was used to reduce the problem of looping artifacts caused by supercooling effects. The instrument software Universal Analysis (UA) was used for the peak integration analysis of the thermogram shown in Figure 3.18. The mass of freezable water was calculated by integrating the endothermic peak on the heating thermogram associated with ice melting (between -20 °C and 0 °C), and assuming the enthalpy of freezing of water is 314 J/g [211]. The total mass of water was calculated by integrating the broad endothermic peak associated with water evaporation (between 20 °C and 120 °C) and taking the enthalpy of vaporisation of water to be 2258 J/g [299]. For each condition, repeat measurements were performed on at least two samples.

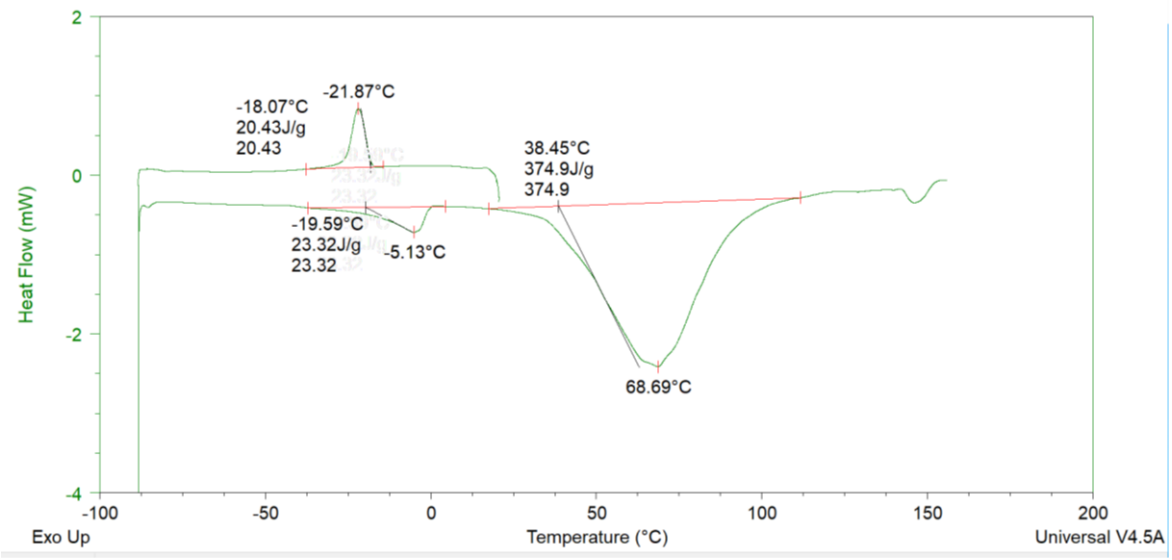

Figure 3.18 - DSC thermogram for a fully hydrated Nafion 117, exhibiting water freezing/melting events (peaking at -22 °C/-5 °C, respectively), and water vaporisation (peaking at 69 °C).

Thermogravimetric analysis (TGA) was performed by the National Physical Laboratory (NPL) using a Q5000 IR instrument (TA Instruments). The Nafion 117 sample was cut into 5 mg pieces and equilibrated at room temperature in DI water for at least 2 h prior to analysis. Samples were dabbed with tissue paper to remove any excess water and transferred rapidly (<30 s transfer time) into aluminium TGA crucibles before sealing. A temperature ramp of 5 °C/min was employed from room temperature up to 200 °C and the mass change at 150 °C was used to calculate the total water content. Repeat measurements were performed on at least two samples.

3.6 Dynamic vapor sorption

DVS measurements were performed by Johnson Matthey using a commercial analyser (Q5000SA, TA Instruments). Approximately 5 to 15 mg of the same sample used for THz-TDS measurements were placed in an open quartz metal coated pan.

As no literature data could be found for Fumasep F10120-PK complimentary DVS measurements were performed. The first step of was heating to 60°C under a dry air purge for 60 minutes to remove as much water as possible. Following this the temperature was set to 21°C for the remainder of the measurement and after 60 minutes the humidity was set to 30% RH for 2 hours to reach an equilibrium. The humidity was then increased in intervals of 10% RH up to 90% RH and then decreased to 30% RH in 10% intervals, the durations of each step change is shown in Table 3.4.

Table 3.4 - Duration of DVS humidity step changes for Fumasep sample.

RH range	Duration (hours)	
	Sorption	Desorption
30-40	2	2
40-50	2.5	2
50-60	2.5	2.5
60-70	3	2.5
70-80	3	3
80-90	4	3

The transient diffusion within Nafion 117 was also replicated with a complimentary DVS measurement. The first step of was heating to 60°C under a dry air purge for 60 minutes to remove as much water as possible. Following this the temperature was set to 20.5°C for the remainder of the measurement and after 60 minutes the humidity was set to 30% RH for 2 hours to reach an equilibrium. To complement the THz diffusivity data a measurement was obtained using DVS using the same experimental procedure with 1.5 hour intervals between RH changes, 90-80% RH was additionally measured. However, the membrane and humidity response were slower and not close to steady state. Therefore, the measurements were extended from 1.5 hours based on the initial results to the durations shown in Table 3.5.

Table 3.5 - Duration of DVS humidity step changes.

RH range	Duration (hours)	
	Sorption	Desorption
30-40	2	2
40-50	2	2
50-60	2.5	2
60-70	2.5	2.5
70-80	3	2.5
80-90	4	3

The DVS measurements performed on samples provided by Johnson Matthey were also first heated to 60°C under a dry air purge for 60 minutes to remove as much water as possible. The temperature was then set to 25°C still under a dry air purge to obtain 0% RH. The humidity

was then increased in 10% RH increments up to 90% RH in sorption and then decreased in 10% RH increments down to 0% RH. Durations for each step are given in Table 3.6.

Table 3.6 - Duration of RH steps used in DVS measurements of samples from Johnson Matthey.

Desired RH	Duration (minutes)	
	Sorption	Desorption
0	60	120
10	30	50
20	30	50
30	30	50
40	30	50
50	30	50
60	40	90
70	50	90
80	90	90
90	210	

Due to the control scheme used the actual RH reached at the end of each step was not necessarily the setpoint such as the 10% RH setpoint which reached 10.4-10.5% RH.

The sorption isotherm can be fitted with Park's multi-mode sorption model [207,300–302] in which the total water uptake (WU_{TOT}) can be expressed as the sum of three sorption mechanisms. Specific absorbed water (WU_{SA}), nonspecific absorbed water (WU_{NSA}) and clustered water (WU_C) as shown in Equation 3.18.

$$WU_{TOT} = WU_{SA} + WU_{NSA} + WU_C \tag{3.18}$$

The water uptake of each sorption mechanism can be modelled as a function of water activity (a_W) according to Equations 3.19 - 3.21 [207]. Where specific absorbed water is the water associated to the mechanisms of Langmuir adsorption at low water activity. Non-specific water is modelled according to Henry's law and clustered water is modelled with a water clustering model and is more prominent at high water activity.

$$WU_{SA} = \frac{a_L K_L a_W}{1 + K_L a_W} \tag{3.19}$$

$$WU_{NSA} = K_W a_W \tag{3.20}$$

$$WU_C = nK_A a_W{}^n \tag{3.21}$$

Where a_L is the specific site capacity, K_L is an affinity constant, K_H is Henry's law coefficient, K_A is the aggregation equilibrium constant and n is the aggregate size. Combing these three models allows Park's model to fit to the total water uptake of sorption isotherms and determine the population of each sorption mechanism. Fittings were achieved through a generalised reduced gradient (GRG) nonlinear solver in Excel. These populations can also be expressed as fractions using Equations 3.29 - 3.31.

$$\theta_{SA} = \frac{W_{SA}}{W_{TOT}} \times 100 \tag{3.22}$$

$$\theta_{NSA} = \frac{W_{NSA}}{W_{TOT}} \times 100 \tag{3.23}$$

$$\theta_C = \frac{W_C}{W_{TOT}} \times 100 \tag{3.24}$$

3.7 Diffusion fitting

In order to extract the diffusivity of water from transient measurements using both THz and THz-TDS, the water diffusion must be modelled and then fit to the experimental data. Whilst many models and approaches exist for calculating the diffusion coefficient from transient water transport measurements based on different assumptions and experimental conditions. When multiple time constants or diffusivities exist within a system, analysis can become very complex. Non-Fickian water diffusion has previously been observed in PFSAs [142–145] and additional factors can impact the sorption rate such as interfacial vapor diffusion [130,303], mechanical polymer relaxations [142–145] and the rate of change in humidity [304]. Due to these complexities, an empirical approach was first taken with a simple exponential model which has the capability to capture multiple time dependant processes as shown in Equation 3.25.

$$\frac{M_t}{M_f} = a\left(1 - \sum_m A_m \exp\left(-\frac{t}{\tau_m}\right)\right) = \frac{M_t}{aM_\infty} \text{ with } \sum_{m=1} A_m = 1 \tag{3.25}$$

Where a is a constant, as the final increase in water uptake measured (M_f) is subject to uncertainty as seen in Chapter 5. Therefore, a fitting will provide a more accurate measurement of the water uptake at an infinite time (M_∞). A_m is an arbitrary constant with and τ_m is a time constant for the process m. This was first used with two processes however, the time constants

were the same suggesting that only one process was present. Literature suggests that polymer relaxation and swelling introduce another time constant. The reason this was not detected is likely due to this process being observed during the first 1-2 minutes [145] and hence with infrequent measurements this was not detected. Following this the model was used with only the water diffusion process.

As only one process was detected, it is also possible to take an analytical approach however, some assumptions must be made such as instantaneous RH change, uniform initial water distribution and constant surface concentration as described by Equations 3.26 and 3.27.

$$C_w = C_0, \qquad -\frac{l}{2} < x < \frac{l}{2}, \qquad t = 0 \tag{3.26}$$

$$C_w = C_1, \qquad x = \pm\frac{l}{2}, \qquad t \geq 0 \tag{3.27}$$

Where C_0 is the initial water concentration, C_∞ is the water concentration at an infinite time and l is the membrane thickness. The assumption of constant surface concentration means that interfacial diffusion is ignored. Constant diffusivity over the RH range must also be assumed A solution to this problem was presented by Crank [146] as shown in Equation 3.28.

$$\frac{C - C_0}{C_\infty - C_0} = \frac{M_t}{M_\infty} = 1 - \frac{8}{\pi^2}\sum_{n=0}^{\infty}\frac{1}{(2n+1)^2}\exp\left(-\frac{D(2n+1)^2\pi^2 t}{l^2}\right) \tag{3.28}$$

The value for M_∞ was taken from the exponential fit and this equation was applied up to n=20, this approximation was found to be satisfactory with an error of <1%. When using this model THz-TDS has a distinct advantage as the membrane thickness is simultaneously determined and does not therefore need to be estimated as with other methods [130] or assumed constant [142].

Variation and additions to this model have previously been used and include interfacial diffusion [130,142–144] and the system response of the humidity change [304]. Through the use of thick membranes, the impact of interfacial diffusion is reduced, as such the expected change in shape [143] was not observed and through the exponential model only one process was found. Whilst the humidity change was not instantaneous, adopting this variable into the model requires fitting the changing humidity to an exponential which does not fit the data due to the PID control in the THz-TDS. The model was used without these additions however, it is important to note assumptions and hence limitations.

For comparison to the terahertz diffusivity measurements, complementary DVS measurements were obtained for comparison. Fitting of the DVS results was similar to the THz data however, the humidity response was slower and while initially appearing to be exponential, when fitting the measured RH to the exponential model, it did not fit as seen in Figure 3.19.

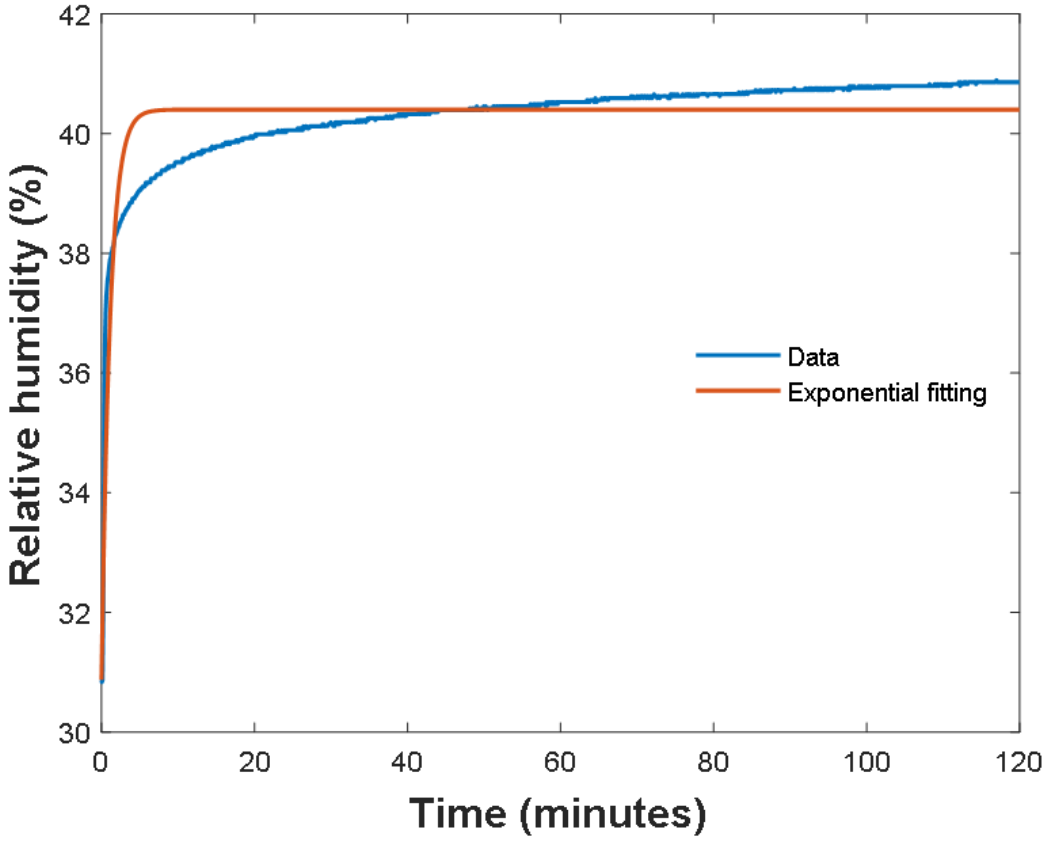

Figure 3.19 - Example fitting of DVS relative humidity using exponential model.

As a result, the theoretical model with an included exponential RH response could also not be used. The RH response was more significant for DVS measurements than the THz, this was likely due to the different control schemes and the gas flow limitations when using a gravimetric technique. RH response therefore had to be included, particularly for higher RH where the response was slowest. Due to this, finite element analysis was proposed as the RH data could be used directly rather fit to a model.

To use finite element analysis all the boundary conditions have to be defined. As this is a symmetric system only half of the membrane needs to be modelled with a boundary at the centre and another at the interface. At the centre of the membrane the value of $C_{t,n_0+\Delta x}$ and $C_{t,n_0-\Delta x}$ should be equal and therefore can be substituted into equation 2.30 resulting in Equation 3.29.

$$C_{t+\Delta t,n_0} = \frac{2D\Delta t C_{t,n_0-\Delta x} + \left(\Delta x^2 - 2D\Delta t C_{t,n_0}\right)}{\Delta x^2}, \qquad x = 0, \qquad t > 0 \qquad (3.29)$$

At the air-membrane interface the normalised RH data can be used as shown in Equation 3.30.

$$C_w = C_0 + (C_\infty - C_0)\frac{RH_t - RH_0}{RH_\infty - RH_0}, \qquad x = \pm\frac{l}{2}, \qquad t \geq 0 \qquad (3.30)$$

Where RH_t, RH_0 and RH_∞ are the relative humidities at time t, t=0 and steady state respectively. This is an approximation as the water concentration is not linearly dependent upon RH however within the 10% RH intervals chosen this should not cause significant error. For larger changes in RH or more nonlinear water uptake regions such as 0-10% RH a fitted nonlinear model would be recommended. As with previous solutions the initial distribution can be assumed to be constant as described by Equation 3.31.

$$C_w = C_0, \qquad -\frac{l}{2} < x < \frac{l}{2}, \qquad t = 0 \qquad (3.31)$$

If an equilibrium is not achieved before the experiment this will not be the case as with the initial DVS measurements using just 1.5 hours per RH step change. Using Eulers method for internal nodes given by Equation 2.30, allows for all nodes to be calculated starting from t=0. To minimise the truncation error a small step size is desired and due to the limitation of the Fourier number, a step size of 0.05 seconds (100 points per RH datapoint) and 50 points in the x direction were chosen. This would satisfy the Fourier number limit up to diffusivities of $3*10^{-7}$ cm^2/s for all thicknesses of Nafion 117. This diffusivity was used as the upper limit when fitting sorption and desorption curves with a minimum of $1*10^{-9}$ cm^2/s. Modelling and fittings were implemented in Matlab using the residual sum of squares for the error function. The error function was minimised using a particle swarm algorithm which is based on golden section search and parabolic interpolation. A block diagram for this method is shown in Figure 3.20.

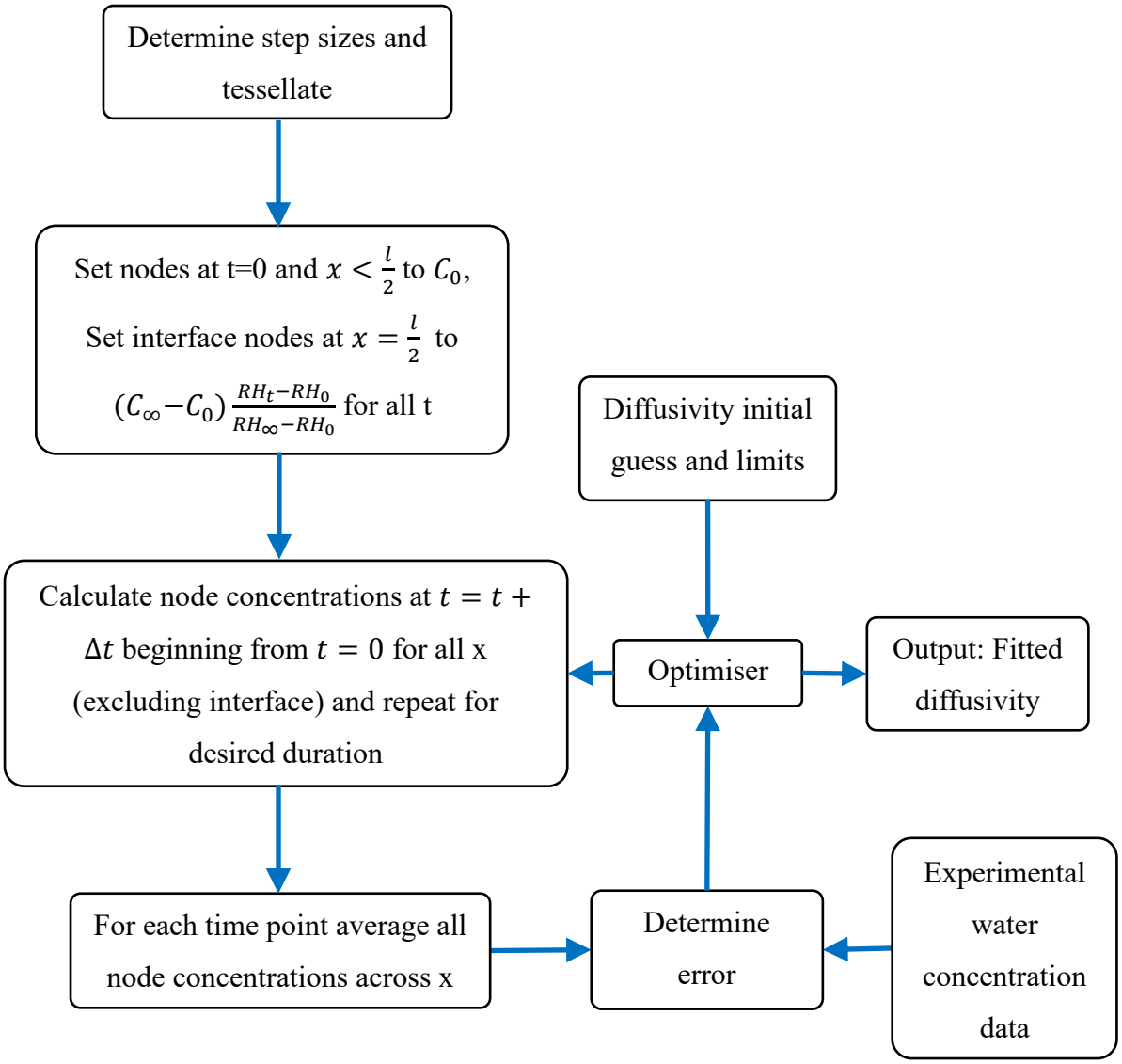

Figure 3.20 - Block diagram for method used to fit diffusivity using finite element analysis.

Validation of the finite element analysis was achieved by comparing the finite element analysis to the theoretical model presented by crank [146] up to n=100. To do this the finite element was modified to include the same interfacial boundary condition as shown in Equation 3.32.

$$C_w = C_1, \qquad x = \pm\frac{l}{2}, \qquad t \geq 0 \tag{3.32}$$

The comparison of the finite element model with the theoretical model is shown in Figure 3.21 using D = 2x10^{-8} cm^2/s. This shows that the finite element model is accurate and can therefore be applied.

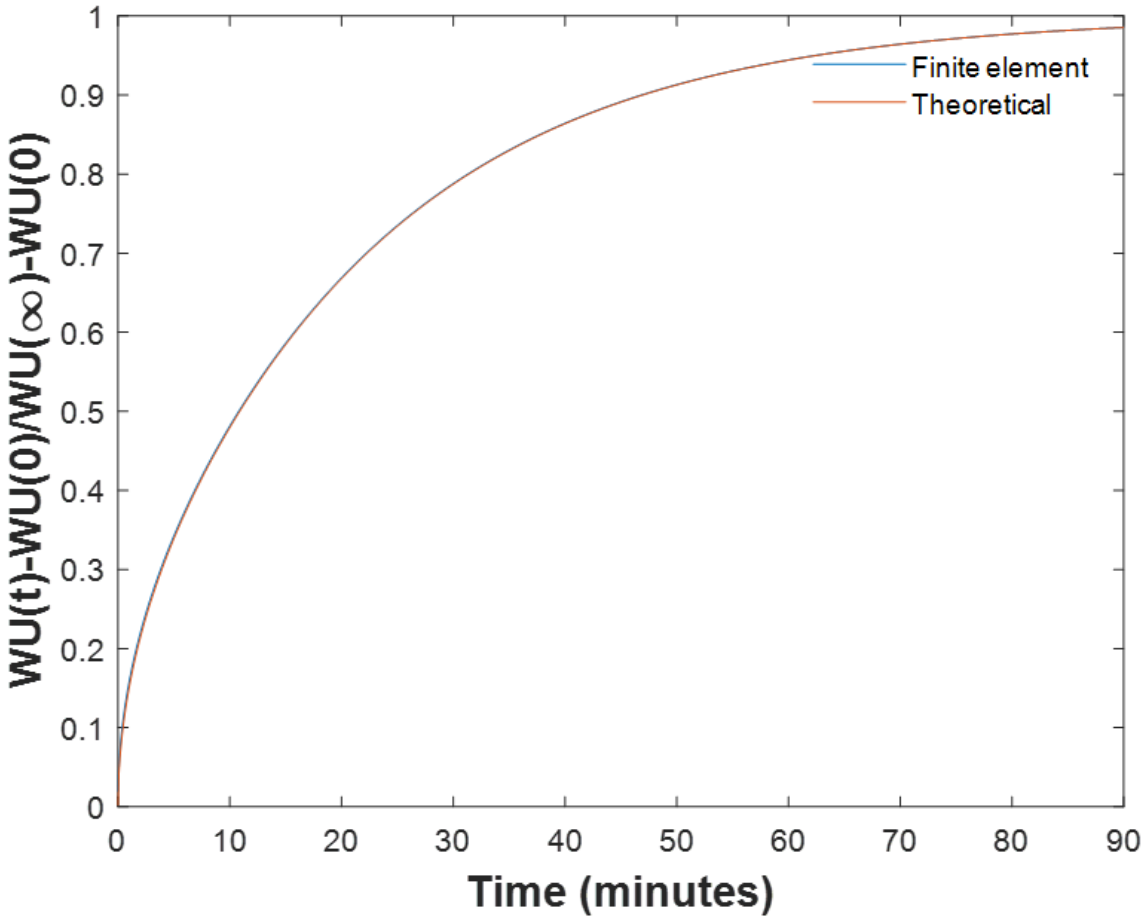

Figure 3.21 - Finite element analysis comparison with theoretical model, D=2x10-8.

Following this, the THz-TDS measurements were also fitted using this approach as it was clear that the RH response could have a significant impact on the fitting and extracted diffusivity. Unfortunately, due to the humidity sensor used, this also introduced additional uncertainty due to the slow sensor response as discussed in chapter 5.

3.8 Summary

In summary this chapter has covered the experimental methodology for all studies presented in his thesis. This includes the samples used and their preparation for THz-TDS testing. The design of a relative humidity-controlled environment for insitu THz testing. This is followed by the integration of a motorised stage to enable a greater range of further studies. The procedures used to characterise membranes in steady state, transient and hygral swelling studies have also been covered. The measurement procedures and subsequent analysis of water uptake and states using THz-TDS was developed. Further techniques used in the characterisation of water within PFSA membranes using differential scanning calorimetry, thermogravimetric analysis and dynamic vapor sorption have also been realised. Finally, the

fitting of transient water uptakes to diffusion models has been achieved. Empirical and theoretical models from literature have been used but found to be dissatisfactory leading to the development of a new approach utilising finite element analysis to include the impact of the humidity response.

4 Results – Steady state

Fuel cells and electrolysers are generally operated under hydrated steady state conditions for optimum performance. Membrane performance is highly dependant upon this level of hydration and may also be operated under reduced humidities, for example under start up conditions and therefore, understanding the role of hydration for cell performance is critical. In this chapter the water uptake and water states in a number of commercially available PFSA membranes have been probed using THz-TDS under steady state conditions using a bespoke humidity-controlled chamber. In addition, THz water states have been compared to water states from other techniques, freezable and non-freezable water using differential scanning calorimetry. Also, the HOH bending vibration of water molecules associated with SO_3^- groups in a band located at 1630 cm^{-1} within the FTIR spectrum. The works shown within have been published [283,305,306] but contains additional information and results.

4.1 Model validation and fittings

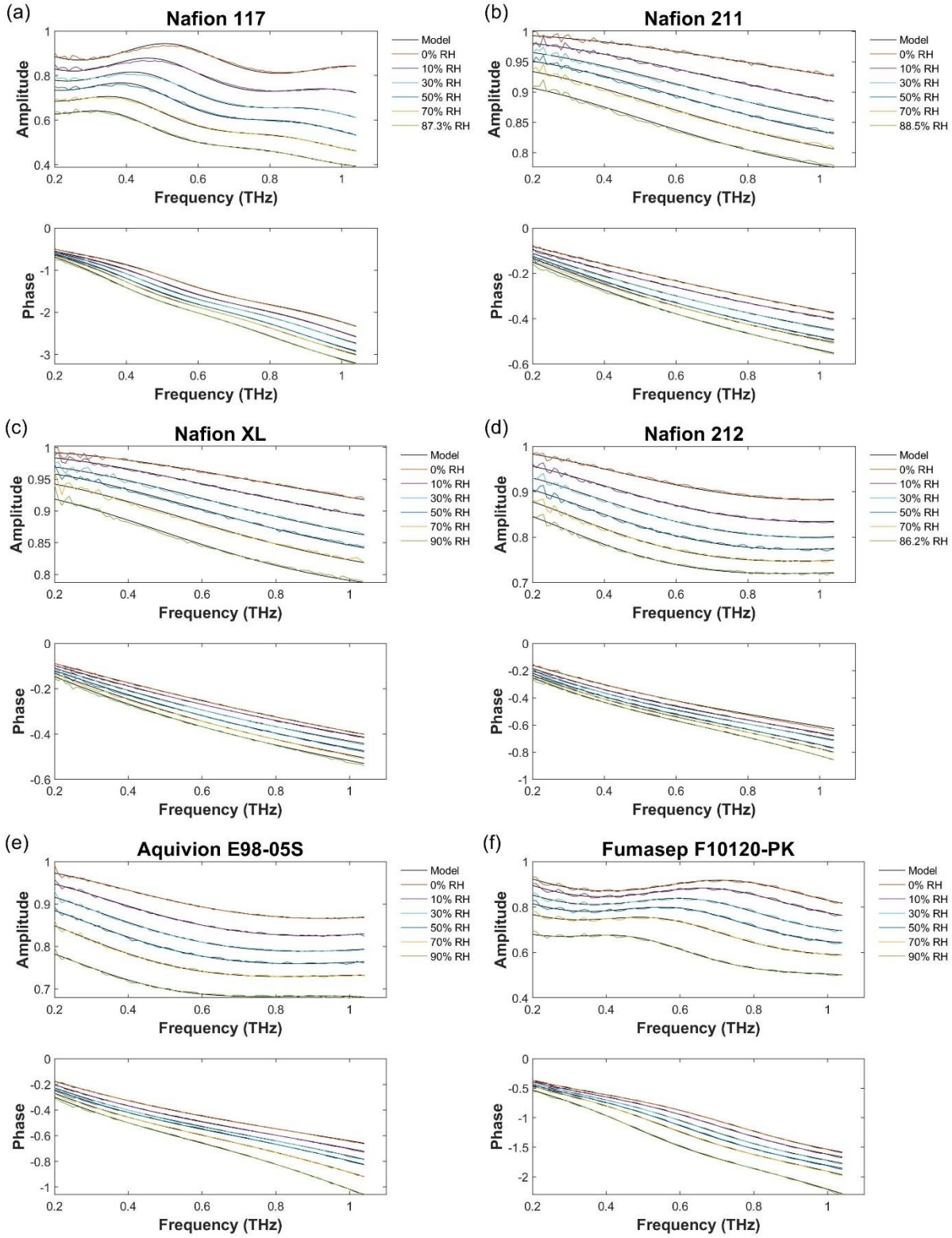

Figure 4.1 – Example measurement and fittings of the complex transfer function for Nafion 117 (a), Nafion 211 (b), Nafion XL (c), Nafion 212 (d), Aquivion E98-05S (e) and Fumasep F10120-PK (f) as function of RH.

Acquired transfer functions and their fittings can be seen in Figure 4.1 for a repeat of each membrane studied, which shows a good quality of fit for both amplitude and phase which decrease for each sample with increasing humidification. It can also be seen that the thicker membranes such as Nafion 117 and Fumasep F10120-PK have significantly more absorption and time delay than thinner membranes such as Nafion 211 and XL.

Given the quality of the fits and a general agreement with the micrometre-measured thicknesses, the response therefore confirms the broad applicability of our data analysis algorithm [283]. It also highlights that this data can be well described by a double Debye response (Equation 3.6) as demonstrated in Table 4.1 for Nafion 117 with τ_1 fixed to the bulk water time constant at 8 ps. Such a value is also observed in pure water in terahertz region [269,287,298,307] as well as hydrated Nafion 117 measured using dielectric spectroscopy [200]. As expected, there is an increase in the dielectric strengths of the bulk and free Debye relaxations with increasing humidification, these correspond to the quantity of bulk and free water which have both been shown to decrease under desorption experiments [234,283]. A decrease in the membrane thickness can also be seen due to the membranes shrinking during the desorption process as the membrane no longer needs to accommodate as many water molecules.

Table 4.1 - Double Debye parameters of Nafion 117.

RH (%)	ε_∞	$\Delta\varepsilon_1$	$\Delta\varepsilon_2$	$\tau_2(ps)$	Thickness (μm)
0	2.41	0.38	0.31	0.078	171.3
10	2.51	2.03	0.45	0.11	175.1
30	2.51	4.02	0.60	0.14	181.2
50	2.58	5.96	0.72	0.15	185.0
70	2.59	8.81	0.81	0.17	190.2
87.3	2.70	12.53	0.94	0.19	194.8

To explore the possible impact of temperature variations on fittings, Nafion 117 fittings were obtained using different bulk dielectric times from 6-10ps representing a range of 15-40°C. Negligible impact was observed for all the fitting parameters with the exception of the bulk dielectric strength as shown in Figure 4.2. Based on Figure 3.17, the relaxation time is expected to vary by a maximum of ~1ps within the measured temperatures across all experiments. Therefore, some small variations to the fitted bulk dielectric strength are expected and may result in some uncertainty.

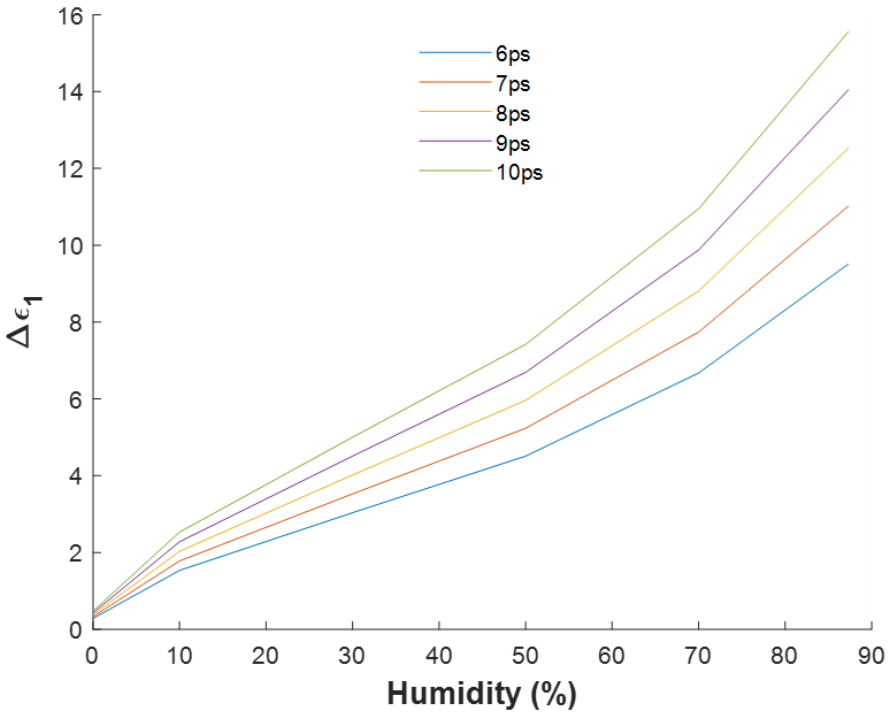

Figure 4.2 - Fitting of 90% RH Nafion 117 bulk dielectric strength as a function of bulk relaxation time.

Figure 4.3 shows examples of the extracted dielectric response for the Nafion, Aquivion and Fumasep membranes at measured RHs of 0%, 10%, 30%, 50%, 70% and 86-90%. As expected, both the real and imaginary components of the complex dielectric permittivity increase with humidity [200].

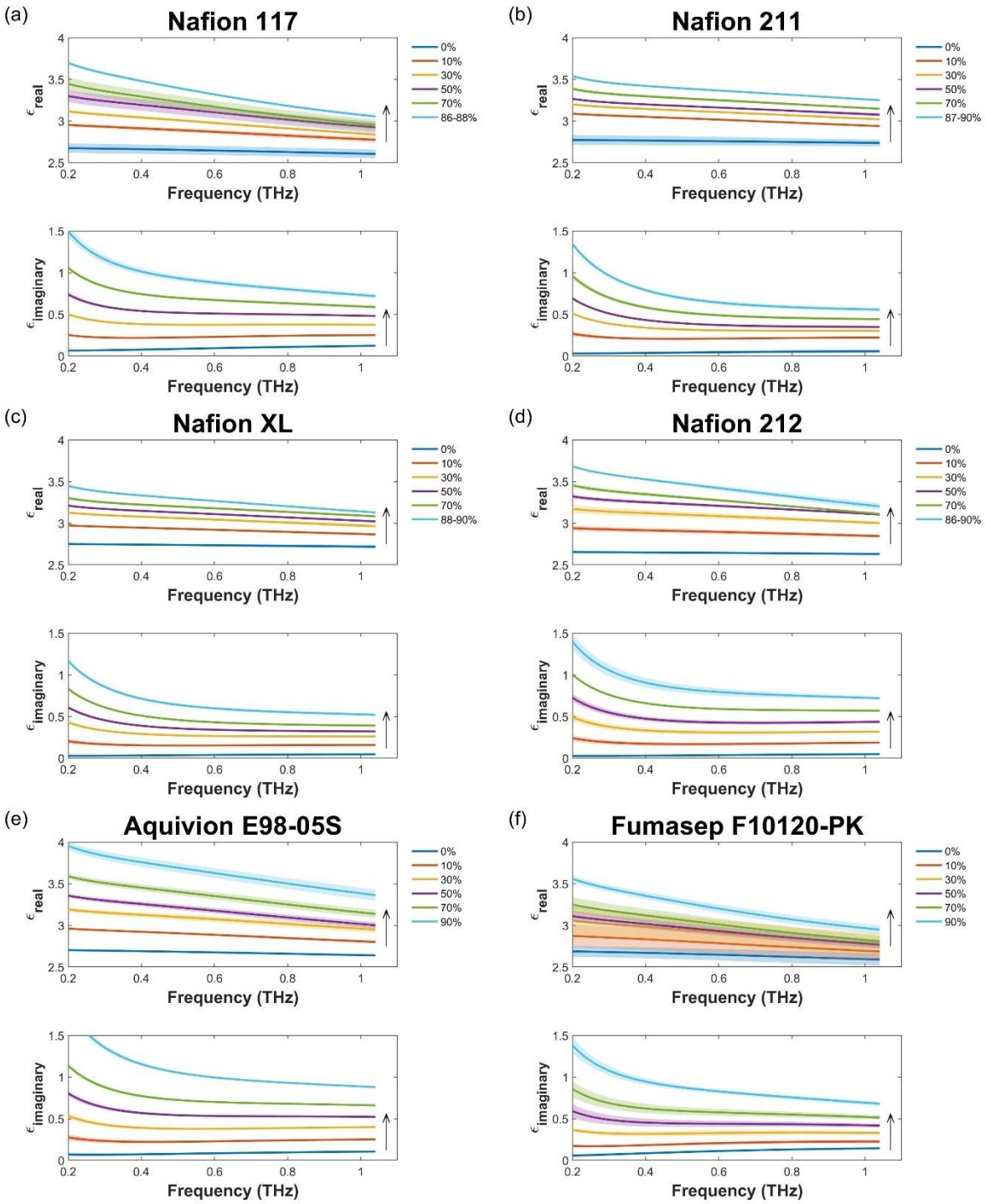

Figure 4.3 – The real and imaginary parts of the complex dielectric permittivity of Nafion 117 (a), Nafion 211 (b), Nafion XL (c), Nafion 212 (d), Aquivion E98-05S (e) and Fumasep F10120-PK (f) at different RHs.

These results therefore confirm that these hydrated membranes contain water molecules with reorientation dynamics similar to bulk water molecules [200,234,283]. The data obtained in the current study for Nafion 117 is additionally consistent with data at RHs controlled using salt solutions where our measurements are also in agreement with prior work that used cuvettes shown in Figure 4.4 [272,308], which extends down to sub-GHz frequencies. Small differences

could possibly be due to variations in how the membranes have been pre-treated and their thermal history.

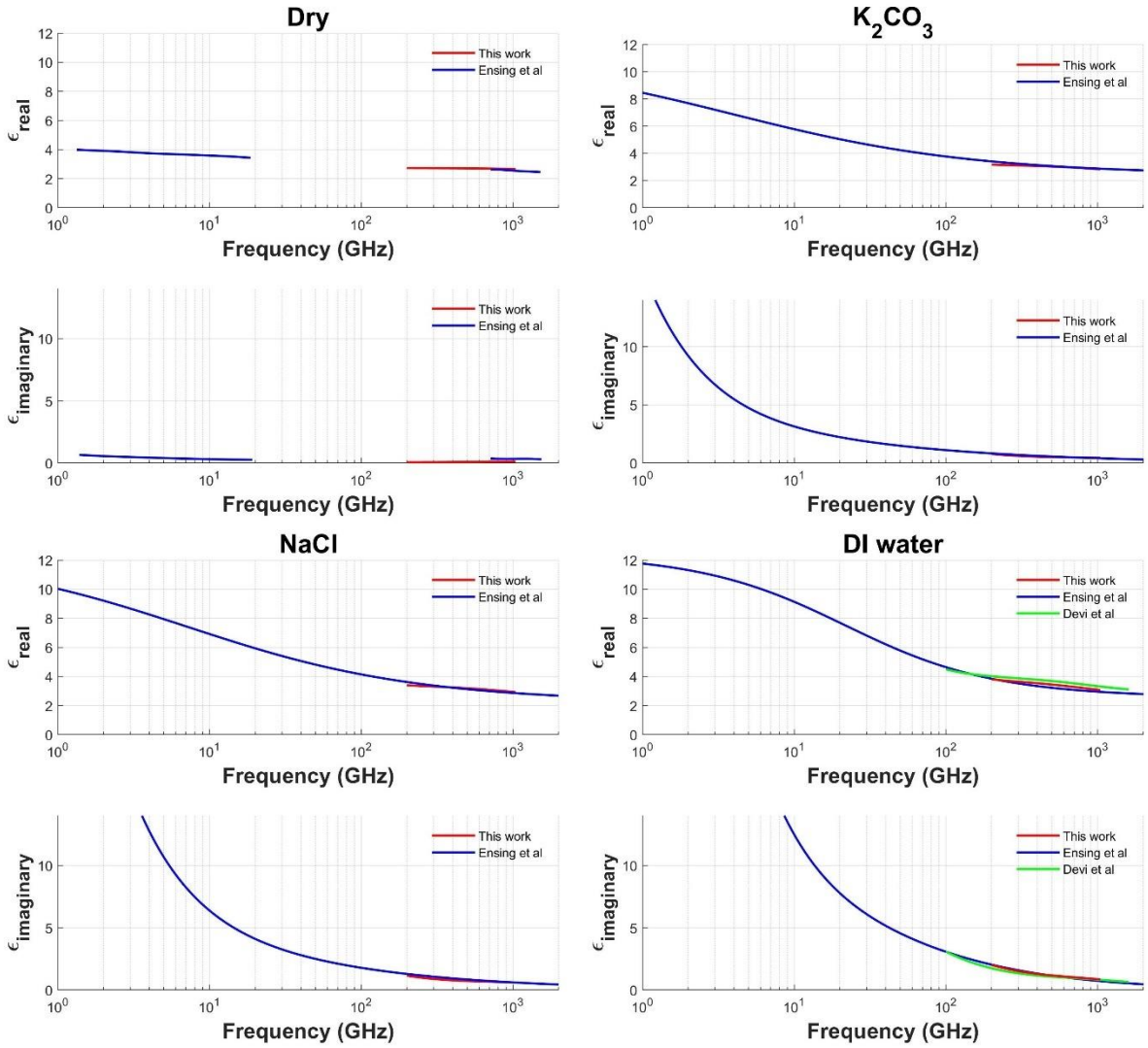

Figure 4.4 - Fitted permittivity comparison of Nafion 117 hydrated using saturated salts with literature [272,308].

4.2 Water uptakes

Using the extracted thicknesses and optical parameters of the hydrated membranes, effective water thicknesses were determined using Equations 3.2 and 3.9 to produce humidity dependent WU as shown in Figure 4.5. These results are compared against literature values acquired using gravimetric based DVS [86,96,111,154,155,158,226,309–313], where a general agreement between the nonlinear uptake profile is observed for the different Nafion membranes and the Aquivion E98-05S with small differences between the absolute WU values. No WU literature values were found for Fumasep F10120-PK for comparison however DVS measurements were obtained for comparison.

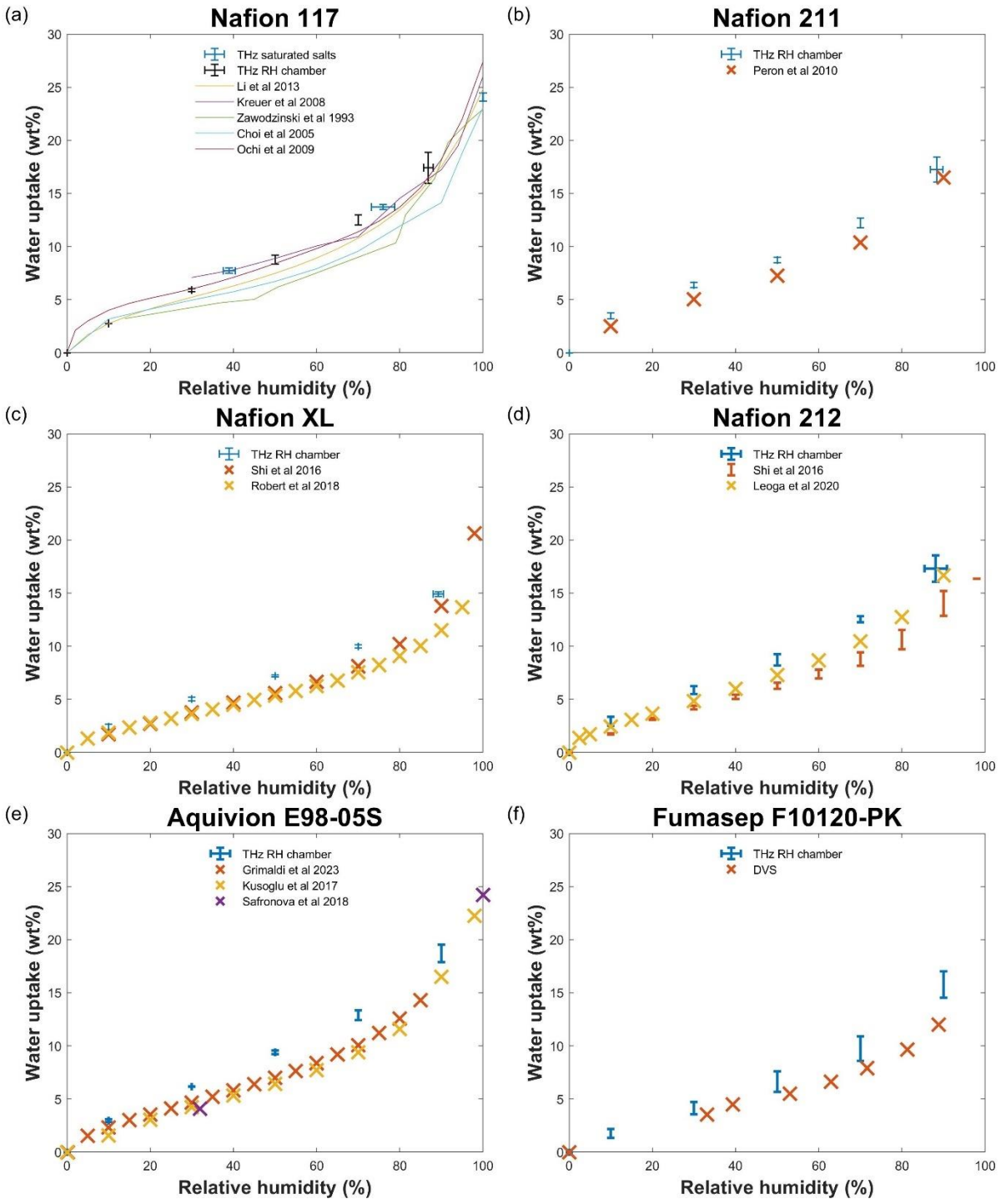

Figure 4.5 – Isotherms of Nafion 117 (a), Nafion 211 (b), Nafion XL (c), Nafion 212 (d), Aquivion E98-05S (e) and Fumasep F10120-PK (f) from THz-TDS against literature DVS values [86,96,111,154,155,158,226,309–313].

Due to a lack of temperature control in the realised chamber, variations are also be expected. In the case of Nafion XL, these differences are additionally convoluted by the hysteresis [310] where the only accessible literature data is related to sorption instead of desorption [111,311]. The Aquivion E98-05S literature data was also sorption of the extruded ionomer [312] and experimental details were not available for the other values [86,96]. These results therefore

suggest that effective medium theory can be used to estimate the effective water thickness, which reduces to zero at 0% RH resulting in a zero WU in line with DVS measurements where residual water is generally ignored [86,111,161,162,314]. Here the residual water is also calculated which generally requires an elevated temperature for removal [161] as the measured value at 0% RH using equation 3.2 with an assumed dry membrane absorption coefficient of 0. While these are generally in agreement with literature values, our values are slightly lower for Nafion 211 and XL [86,315,316], this is possibly due to some uncertainty or greater water removal but is consistent with the small offset observed for the results seen in Figure 4.5. In general, the Fumasep F10120-PK is close to the DVS results with the biggest difference seen for 90% RH where the DVS is measured in sorption and an equilibrium has not been reached as seen in Figure 4.6.

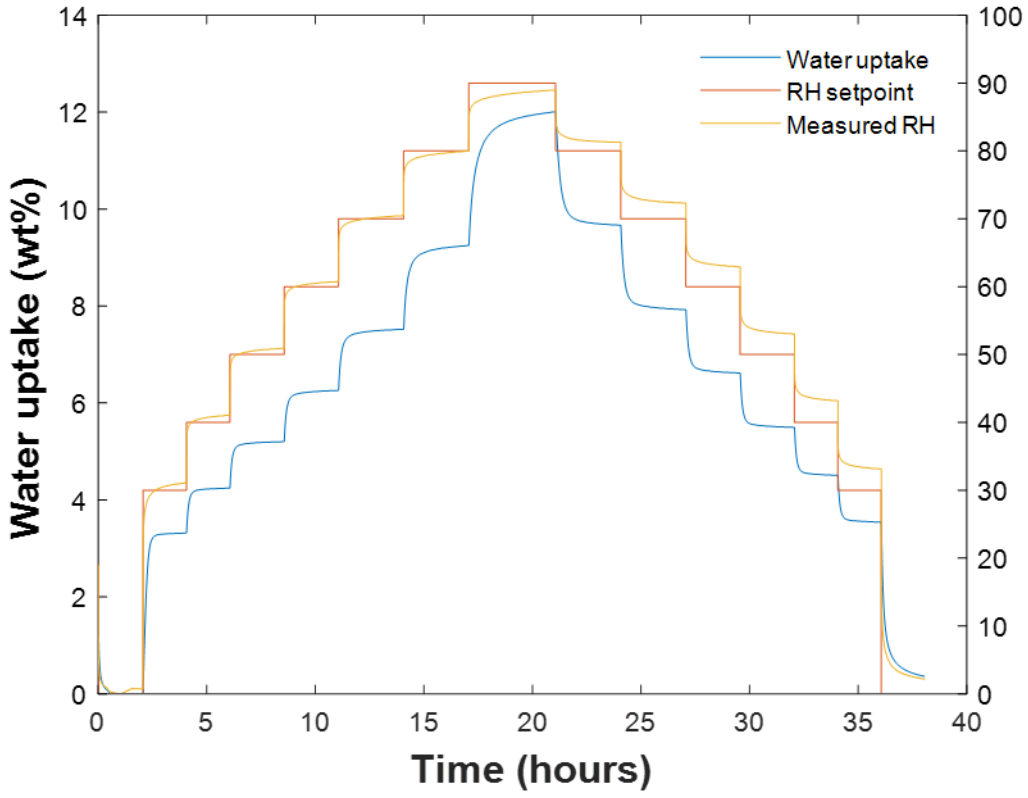

Figure 4.6 - DVS water uptake and relative humidity profile for Fumasep F10120-PK.

Figure 4.7 shows the comparison of water uptake for the membranes tested, in general the values are similar with Nafion 117, Nafion 211, Nafion 212 and Aquivion E98-05S having almost the same water uptakes. As the Aquivion E98-05S has a lower equivalent weight at 980g/mol than the Nafions at 1100g/mol, the water uptake was expected to be higher as water uptake decreases with increasing equivalent weight [86,317,318]. However, the water uptake

is notably lower in the Aquivion ionomer at a given EW and similar values have previously been observed for these membranes [317]. Nafion XL has a lower water uptake than the other Nafion membranes despite being made from a lower equivalent weight PFSA ionomer [319]. This is due to its Cerium additives [319] and the ePTFE reinforcement which is hydrophobic and therefore increases the membranes equivalent weight inside the ePTFE reinforced layer, whilst the non-reinforced surface layers retain the lower equivalent weight [320,321]. The Fumasep generally has a lower water uptake than the Aquivion E98-05S and Nafions 117, 211 and 212, at low humidities the water uptake is lower than Nafion XL but at higher RH is similar and even higher at 90% although within the errorbars. This membrane is reinforced and has the highest equivalent weight therefore, a lower water uptake is expected although its PFSA chemical structure is unknown and this could have an impact as seen with Aquivion and Nafion.

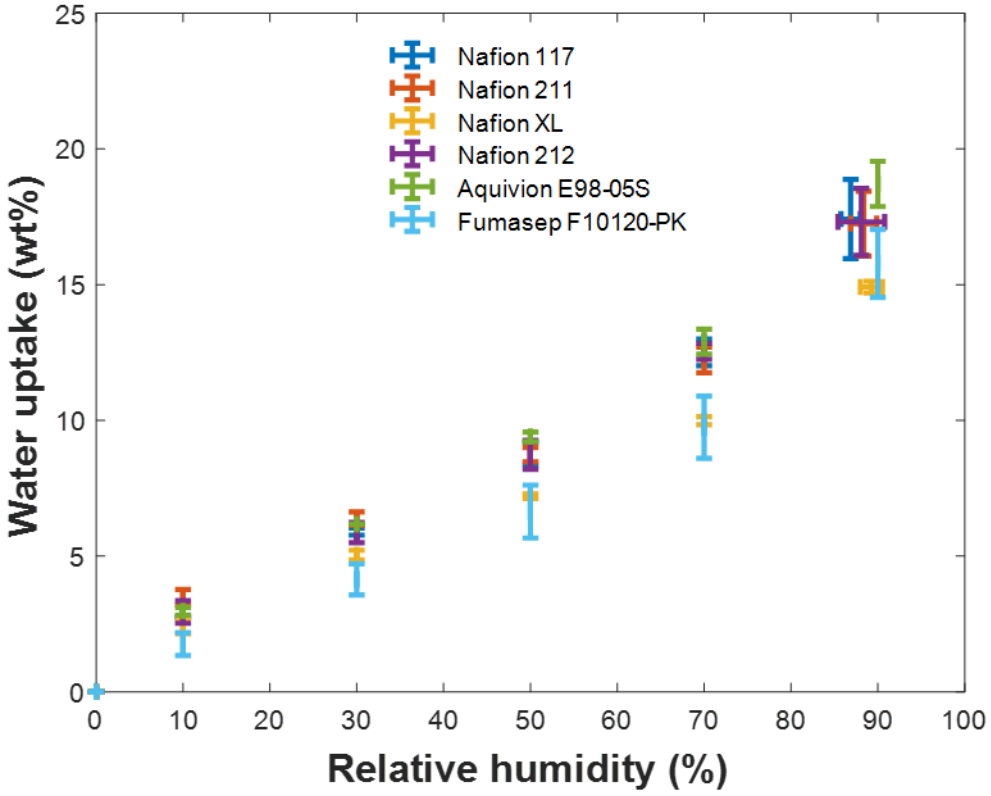

Figure 4.7 - Water uptake comparison of Nafions 117,211, XL, 212, Aquivion E98-05S and Fumasep F10120-PK.

4.3 Water states

Using the extracted model parameters from Equations 3.10-3.12 in a manner similar to previous studies [233,234,283], Figure 4.8 shows the proportion of RH dependent water states in the Nafion, Aquivion and Fumasep membranes. As expected, the relative proportion of bulk water

increases with increasing humidification, while a concomitant decrease in bound water is observed. This behaviour is generally in qualitative agreement with understanding [86] and observations made using other characterisation methods (e.g. DSC [211], dielectric spectroscopy [200]), membrane systems [233] and prior work [283]. In particular, bound water dominates at low RHs and as the water activity in the membrane increases through humidification, the proportion of bound water contribution decreases in exchange for increase in bulk water.

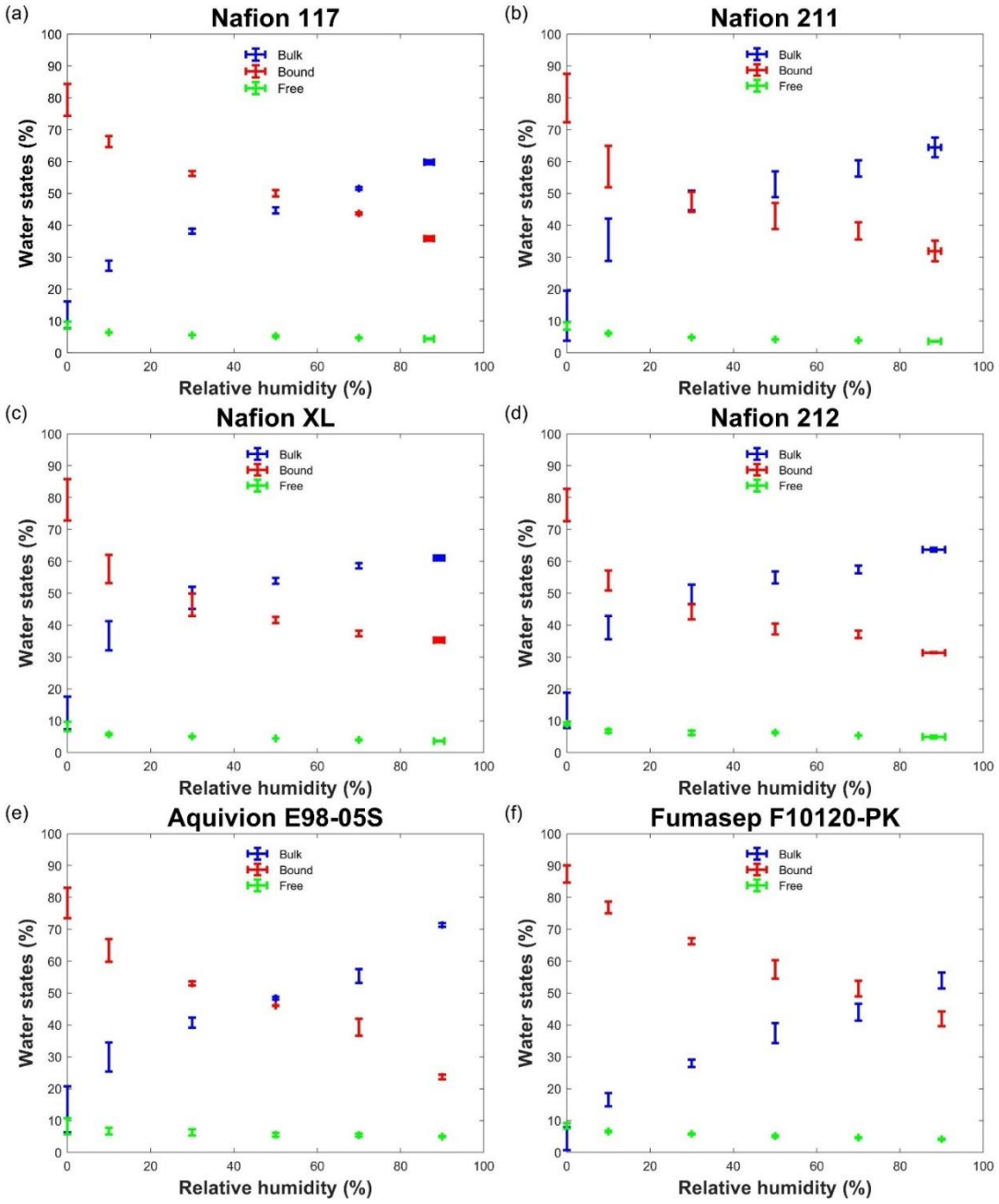

Figure 4.8 - Humidity dependent water states of Nafion 117 (a), Nafion 211 (b), Nafion XL (c), Nafion 212 (d), Aquivion E98-05S (e) and Fumasep F10120-PK (f).

The value of RH at which there is a crossover between bulk and bound water is different for membrane types and thicknesses. Specifically, the crossover points for Nafion 211, XL and 212 occur at ~30-40% RH, lower than the ~60% RH observed for Nafion 117. This may be due to the 117 membranes being extruded as opposed to dispersion casted [322,323]. This results in a membrane with a higher crystallinity [173] which was previously found to decrease the proportion of bulk water [283]. At high RHs, bulk water proportions for Nafion XL and 117 are similar, resulting in similar proton conductivities [111,324], but are ~5-6% lower than Nafion 211 and Nafion 212. The reduction in bulk water within Nafion XL compared to Nafion 211 and 212 suggests that water domains have been disrupted under hydrophobic PTFE reinforcements, thus decreasing the ability of the membranes to accommodate water, consistent with a reduced WU as seen in Figure 4.5 and consequently a reduced proton conductivity [111,325]. Comparing the Aquivion to the Nafion membranes it was found that the fraction of bulk water is lower than the Nafion 211 and XL at low humidities but higher than Nafion 117, yet at higher humidities the Aquivion membrane has the highest fraction of bulk water. This is likely due to the different ionomer used which has a shorter side chain and a higher ion exchange capacity at >1meq/g compared to Nafion at 0.9meq/g. The fraction of bulk water in Aquivion was expected to be higher than the Nafions due to the higher ion exchange capacity and proton conductivity [96]. However, this is possibly due to short chain PFSAs such as Aquivion having smaller but more widespread ionic domains [86,98] which form better developed channels [97]. The Fumasep had the lowest proportion of bulk water at all humidities, this is probably due to the lower water uptake and structure of this PFSA which isn't disclosed but has long side chains and the lowest ion exchange capacity at 0.79meq/g, this membrane also has a PEEK open mesh style reinforcement which could impact the water states.

4.4 Differential scanning calorimetry

DSC is routinely used for discriminating and quantifying freezable and non-freezable water content in membrane systems [209,211–216], which can provide an indication of the water states. Therefore, DSC measurements were performed on the same Nafion 117 membrane used in terahertz measurements to compare the distribution of water states derived from these two techniques. Figure 4.9 shows the freezable/non-freezable water content estimated from our DSC measurements against DSC literature values [209,211–214]. Our DSC results are broadly consistent with the trend observed in the literature values, although differences are observed for the fully humidified sample, which exhibited a slightly higher freezable (and lower non-

freezable) water content compared to literature. One possible reason for these differences is that the water evaporation peak was used in the DSC thermogram to estimate the total water content, while it is more common in the literature to calculate this by TGA. A difference may arise because the DSC calculation assumes the enthalpy of water vaporisation to be the same in the membrane as it is for liquid water, which may contribute a significant source of error. To investigate this, TGA was performed on the fully humidified Nafion 117 to estimate the total water content and the associated data points from Figure 4.9. Importantly, the total water estimated by TGA was found to be slightly lower than that estimated by DSC, so this cannot account for the deviation between our non-freezable water calculation and that reported in the literature. Hence, there must be additional experimental factors that are responsible for this discrepancy, and these are discussed further in Section 4.3. Importantly, the use of TGA to estimate the total water introduces considerably more error to the water states information compared to the use of DSC for this purpose, which highlights a potential weakness in using this approach for quantitative analysis.

In order to compare terahertz bulk/bound against DSC freezable/non-freezable water content, terahertz water fractions were converted from Figure 4.8 into their respective water content as described above, where a similarity between the respective trends can be observed consistent with other hydrophilic polymers [263]. Despite this similarity, terahertz generally reports a higher bulk water content than DSC freezable water for a given total water content (Figure 4.9a) possibly due to: 1) bulk water fusion enthalpy being used to estimate freezable water content from DSC as opposed to a lower membrane dependent value [210], which would increase the freezable water content; 2) total water content used to calculate water states from DSC is often independently measured gravimetrically [209,212,213,215], which can introduce considerable uncertainty; 3) differences in the boundary between the water states being probed [263] resulting in some of the non-freezable water being incorrectly categorised as bulk water by the terahertz measurement. The latter difference arises from different physical parameters being measured e.g. water fusion enthalpy by DSC as opposed to bulk water dielectric strengths by terahertz. Water states are likely to change based upon temperature and it is possible that some bulk water can become loosely bound as temperature decreases. Temperature is known to influence the reorientation dynamics of water are impacted shown by changes to the dielectric strength and relaxation times of bulk water with temperature [200,264,287–296] therefore the water states are likely impacted. Whilst there is also some similarity between the trends between non-freezable and bound water (Figure 4.9b), this similarity is less compared

to the freezable/bulk water case. This is possibly due to uncertainties from the independently measured water content, which is additionally convoluted by aforementioned factors that propagates into the respective water content calculation.

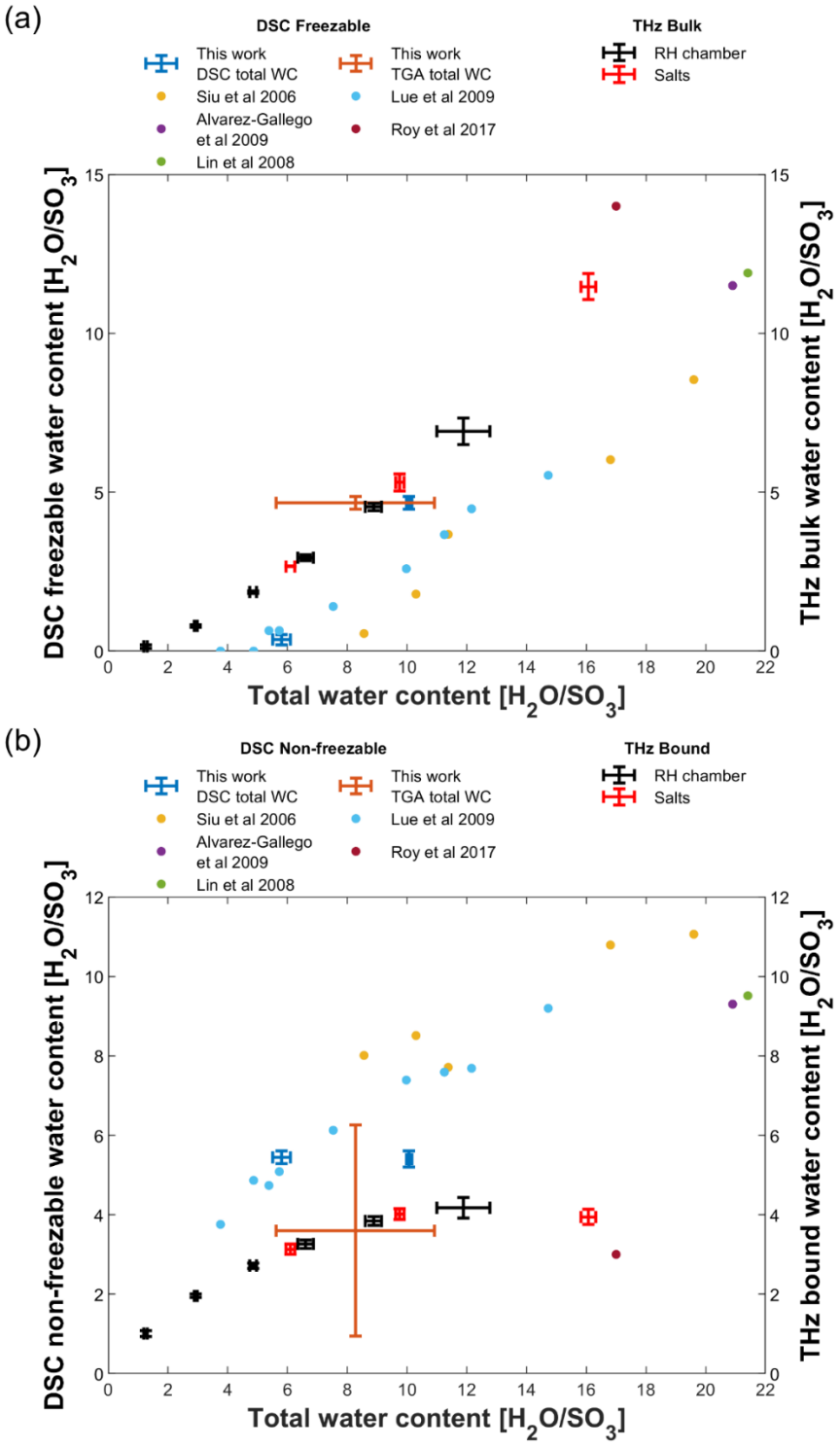

Figure 4.9 – Nafion 117 water states comparison of (a) bulk and (b) bound states against DSC water states [209,211–214].

The use of DSC to quantify freezable water content can be challenging, particularly when attempting this at different, controlled total water contents. For measurements using fully humidified membranes, the water freezing/melting events are easily detectable in the thermograms but, as noted in section 3.5, supercooling effects can lead to crystallisation loops [326] which may compromise the quantification. Such effects can be minimised by employing a slow temperature ramp and/or employing temperature modulated DSC, in which a sinusoidal perturbation is superimposed on the linear temperature ramp. Humidity control is not typically possible using DSC instrumentation, so to perform DSC measurements on membranes at known levels of humidity below saturation is difficult to achieve accurately. In this work the membranes were equilibrated at 85% RH in an environmental chamber, but as soon as the sample is removed from the controlled environment, re-equilibration with the ambient lab conditions will begin instantly. Whilst steps were taken to minimise the ambient exposure time, it is very likely that the actual water content at the point of measurement will have decreased by an unknown amount. The impact of this will depend not only on the thickness of the membrane (thicker membranes are expected to re-equilibrate more slowly than thinner ones), but also the type of crucible used in the DSC measurement (i.e. whether or not it creates an air-tight seal). Furthermore, the water freezing events in the DSC thermograms for the 85% RH samples were very weak, so measurements at lower total water content would be expected to be below the limit of detection (this was confirmed by the absence of any detectable freezing events in membranes equilibrated at ~50% RH). Hence, DSC is limited to a relatively narrow range of total water contents, and even for the samples equilibrated at 85% RH, a considerable uncertainty can be expected (of the order of 20%) associated with the low signal-to-noise and difficulties selecting appropriate baselines for the peak integration.

4.5 Fourier transform infrared spectroscopy

FTIR spectroscopy can provide an alternative means to characterise water in PFSA membranes. In particular, Kunimatsu et al [202] demonstrated that there is a correlation between the intensity of the band at 1630 cm^{-1} (assigned to the HOH bending vibration of water molecules associated with SO_3^- groups) and the membrane proton conductivity. To compare our terahertz measurement against the FTIR data reported by Kunimatsu et al [202], an equivalent experiment was performed in which a 90% RH hydrated Nafion 211 membrane was continuously purged with dry air and the terahertz response was recorded as a function of time during membrane dehydration. Figure 4.10 compares the dielectric strength for bulk relaxation,

which is associated with bulk water (see Equation 6) against the reported area under the 1630 cm^{-1} peak [202]. A correlation can be observed between the two datasets, suggesting that the extracted terahertz bulk relaxation data may serve as a proxy for proton conductivity.

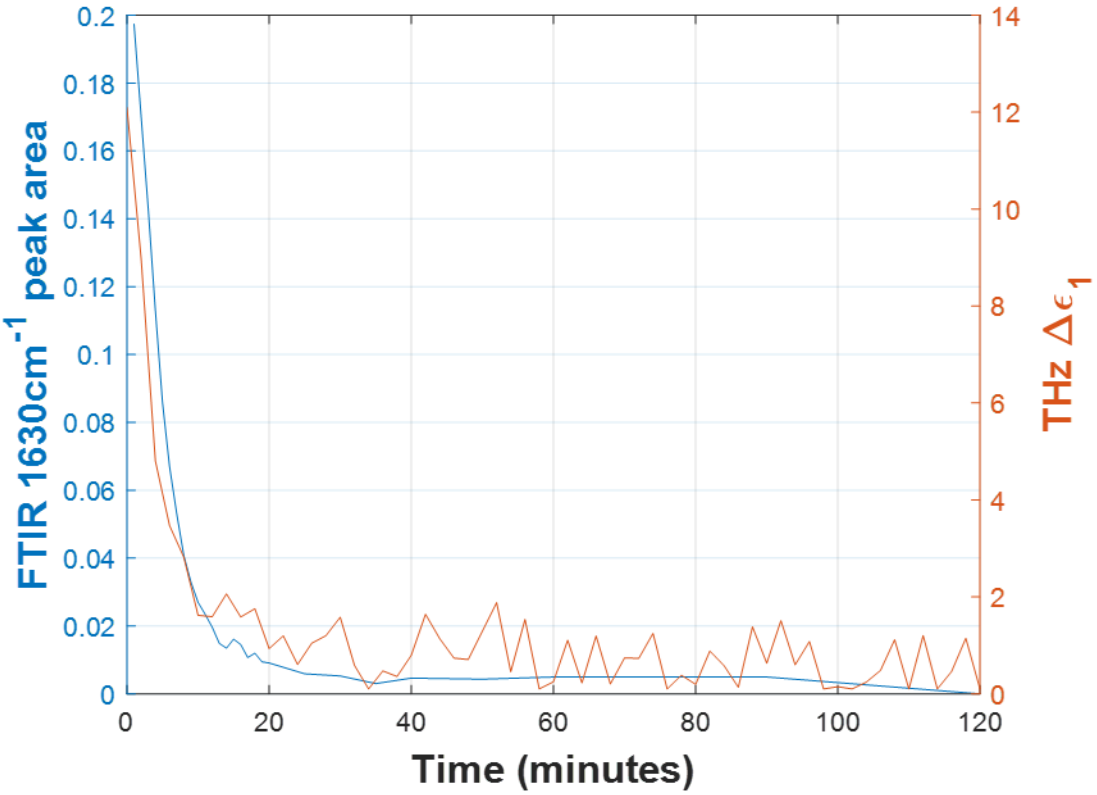

Figure 4.10 - Terahertz bulk dielectric strength for comparison with literature FTIR peak area [202].

In contrast to DSC, humidity control with FTIR during measurement is more straightforward [202] and the measurement is sensitive enough to detect very low amounts of water. The most significant challenge with FTIR, however, lies in the analysis and spectra interpretation as the OH^- stretching and HOH bending IR modes are typically very broad and comprise multiple peaks. Deconvoluting these multi-component bands by peak fitting is therefore challenging and uncertainties arise as to the individual component bands assignment. Moreover, quantitative FTIR spectroscopy is not recommended without appropriate calibration data, as absorbance does not necessarily scale linearly with analyte concentration, particularly in highly concentrated, strongly absorbing media like water [327].

4.6 Dynamic vapor sorption

Sorption isotherms can be fitted with a variety of models including Park's multi-sorption model [207,300–302] which describes the total water uptake as the sum of three sorption mechanisms

giving rise to associated water populations. The water sorption isotherms of PFSA ionomer membranes provided by Johnson Matthey were obtained using dynamic vapor sorption. These isotherms were fitted with Park's multi-mode adsorption model [207] to extract the water populations of specific absorbed water associated to the mechanisms of Langmuir adsorption at low water activity, non-specific adsorption in accordance with Henry's law and clustering at high water activity. The fitted isotherms can be seen in Figure 4.11 where a high quality of fit can be seen.

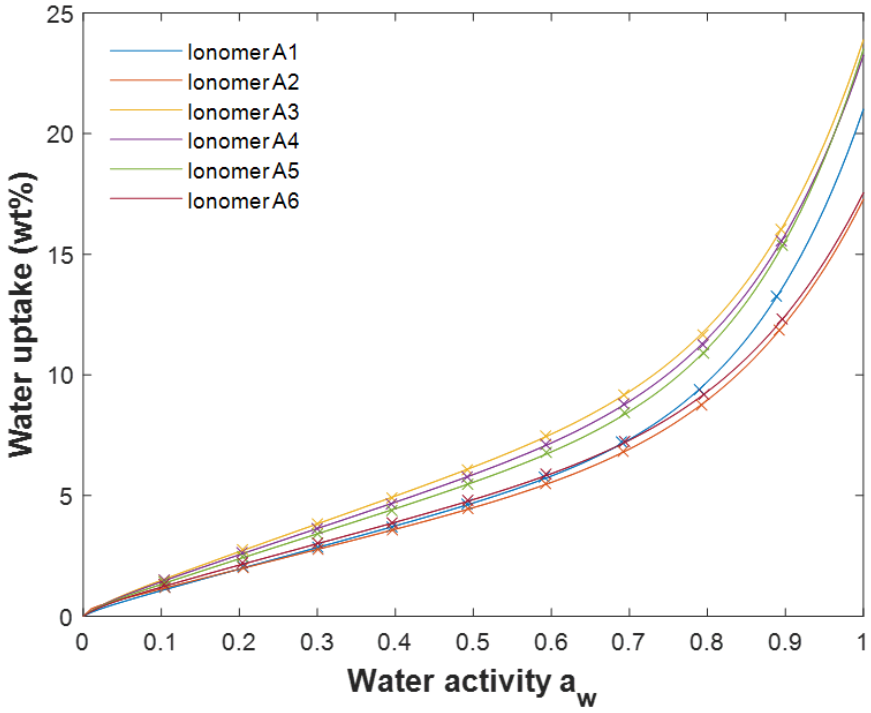

Figure 4.11 - Parks model fitting of sorption isotherms from DVS data of ionomers A1-A6 provided by Johnson Matthey.

The fitting parameters can be used to calculate the relative proportions of each water population as seen in Figure 4.12 where similar trends can be seen for all membranes tested although small differences can be observed such as the population of specific absorbed water present at 0 water activity and non-specific absorbed water at a water activity of 1.

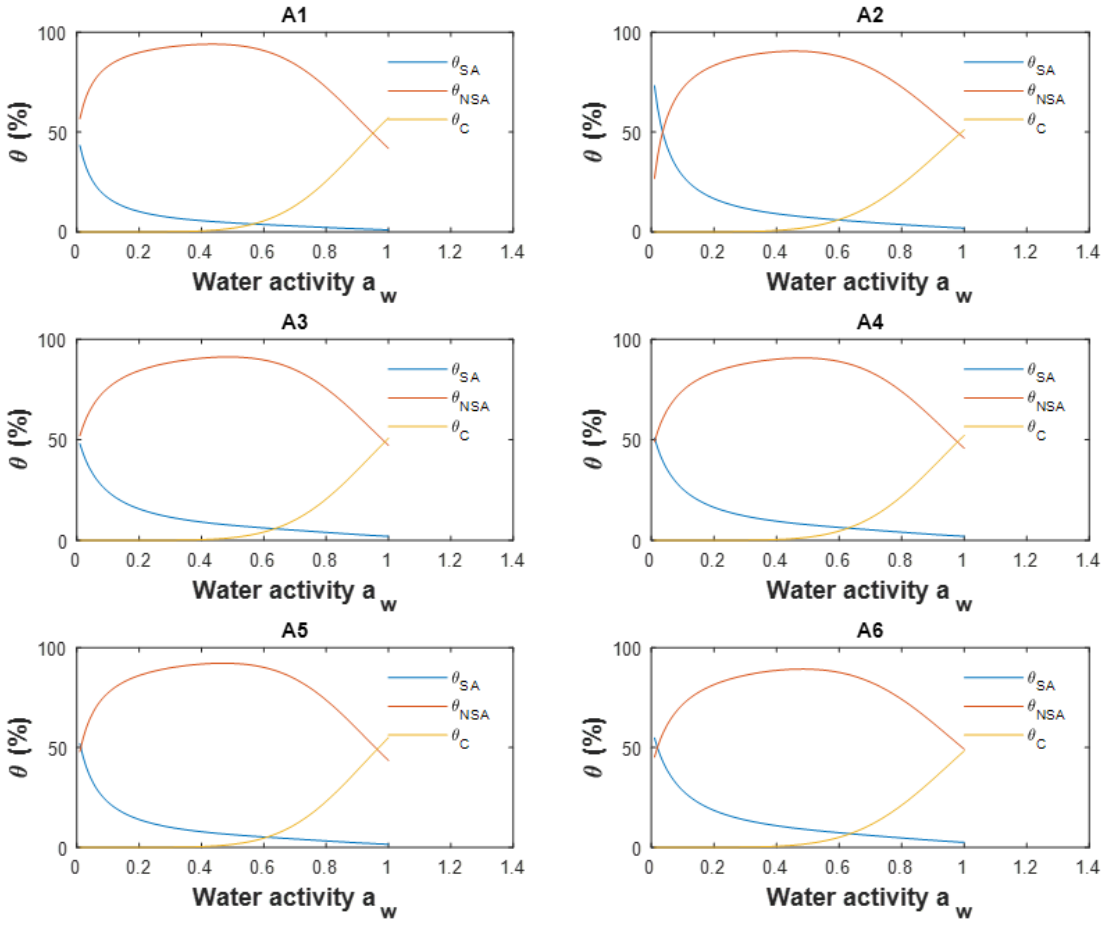

Figure 4.12 - Normalised water content of water associated to the mechanisms of Langmuir adsorption at low water activity θ_{SA}, non-specific adsorption in accordance with Henry's law θ_{NSA} and clustering at high water activity θ_C for Ionomers A1-A6 provided by Johnson Matthey.

As the non-specific adsorbing water corresponds to water with the highest mobility, which has been shown to correlate to non-freezable water [207], Figure 4.13 compares the non-specific adsorbing water against terahertz bulk water fractions previously obtained [283] for the same membranes. These measurements were obtained over a 25-minute duration in the ambient environment (approximately 26 °C and 41% RH) from a hydrated state. For comparison the bulk water fractions at t=0 were compared with an estimated equivalent water activity of ~0.8 and t=25 with water activity ~0.4 for Ionomers A1-A6 where some similarities between the trends can be observed. However, there are some discrepancies, e.g. Ionomer A5 at t =0, Ionomer A1 and A6 at t=25, but these are relatively small compared to the changes at t=0 between Ionomers A1, A2 and A3-A6. These discrepancies could be due to uncertainties associated with membrane water activity, and the fact that single point measurement is taken in THz-TDS as opposed to over an entire membrane by DVS.

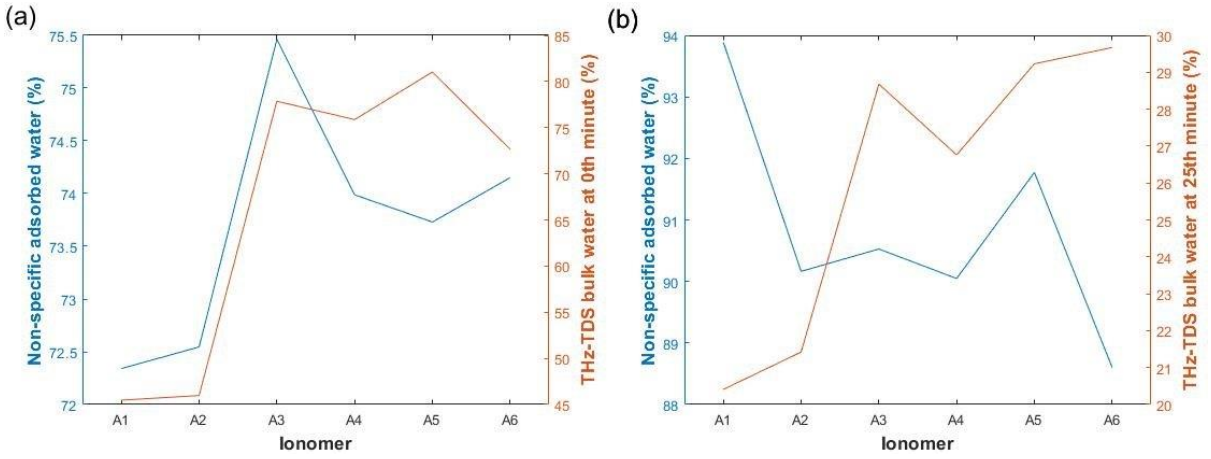

Figure 4.13 - Comparison of non-specific adsorption in accordance with Henry's law extracted from DVS with a_w of 0.8 (a) and 0.4 (b) against bulk water from THz-TDS at the 0th minute (a) and at the 15th minute (b) for Ionomers A1-A6 provided by Johnson Matthey.

4.7 Summary

In this work, the possibility of quantifying water uptake and states inside a variety of Nafion membranes has been demonstrated as well as Aquivion E98-05S and Fumasep F10120 using the proposed humidity-controlled THz-TDS. This has produced WU data consistent with literature DVS values and water state trends are in general agreement with literature DSC and FTIR data. Whilst differences have been observed these are likely due to the different physical phenomenon probed and differences in the water state boundaries. Even though water states within PFSAs have been probed, without a loss of generality, the proposed technique is also applicable to other membranes such anion exchange membranes, where THz-TDS has also demonstrated sensitivity with results consistent with complementary small-angle x-ray and neutron scattering measurements [328]. As an emerging technique, table-top based humidity-controlled THz-TDS can probe samples rapidly and non-destructively under controlled environments thus opening up opportunities for future membrane testing for greater material insights to enable optimisation particularly in performance-stability trade-offs.

5 Results – Diffusion and Hygral swelling

The results of steady state water uptake and water states have been covered in Chapter 4. Whilst membranes spend the majority of their time operating at steady state there are transient periods where hydration is changing. In this chapter the scope of this work is extended to the study of changing membrane properties over time. Firstly, the transient water uptake response has been studied in response to changes in humidity to study membrane water diffusivity. The feasibility to use extracted membrane thickness has also been explored and compared to complimentary methods to allow studies of hygral swelling and dimensional stability. The works of swelling shown within have been published [305] but contains additional information and results.

5.1 THz diffusivity

THz-TDS has demonstrated its capability to quantify steady state water uptake within a humidity-controlled environment. Under transient humidity conditions a membrane experiences a change in water uptake as water diffuses into or out of a membrane. As a motorised stage was added to the humidity-controlled chamber as described in Chapter 3, the capability to obtain measurements every 2 minutes was obtained, and hence transient water uptake studies of diffusion were possible. Ideally for a transient diffusion study the relative humidity exposed to the membrane would change instantaneously as assumed in a many models. In reality some time is required to obtain the new setpoint but should be minimised as much as possible, particularly for thin membranes where a rapid change in water uptake is observed and the change in humidity becomes a more significant factor. Reducing the impact of humidity change and also interfacial resistance are the reasons for studying the thick Nafion 117 membrane throughout this diffusivity study, rather than thin membranes such as Nafion 211. During the steady state experiments, temperature was not controlled and subject to changes in the ambient environment. In this study of diffusion, the temperature was also not controlled however, due to frequent use of the motorised stage an increase from the ambient temperature was observed due to heat generated by the motorised stage as seen in Figure 5.1.

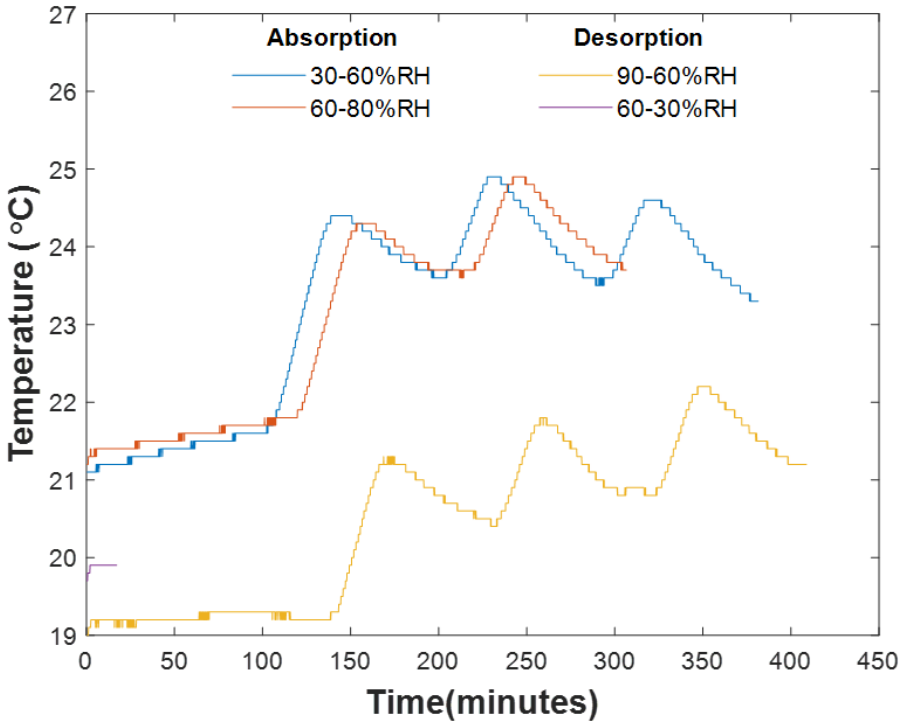

Figure 5.1 - Temperature variations during diffusion experiment.

As references were taken for every measurement during the first 20 minutes a rise in temperature occurred due to the use of the stage, after which a temperature decline can be seen due to a reduction in generated heat as references were then obtained every 10 minutes. Although the temperature rise was only a couple of degrees, this has impacted the humidity response which can be seen in Figure 5.2. Due to this increase in temperature, sorption from 80 to 90% RH was not possible as the humidifier was at a lower ambient temperature than the chamber which now required a higher absolute humidity to reach 90% RH. Additionally, the temperature and humidity were not recorded for the 60 to 30% RH measurements due to a software bug. A repeat was later taken to obtain an RH response for analysis and modelling with finite element analysis. The THz-TDS was no longer available so only RH data was acquired which will lead to some additional uncertainty, the stage was also moved to replicate the heating effect despite not being needed when not obtaining the THz measurements. A repeat for 90-60% RH was also repeated without the THz-TDS to observe the consistency of the RH response and a close match was observed.

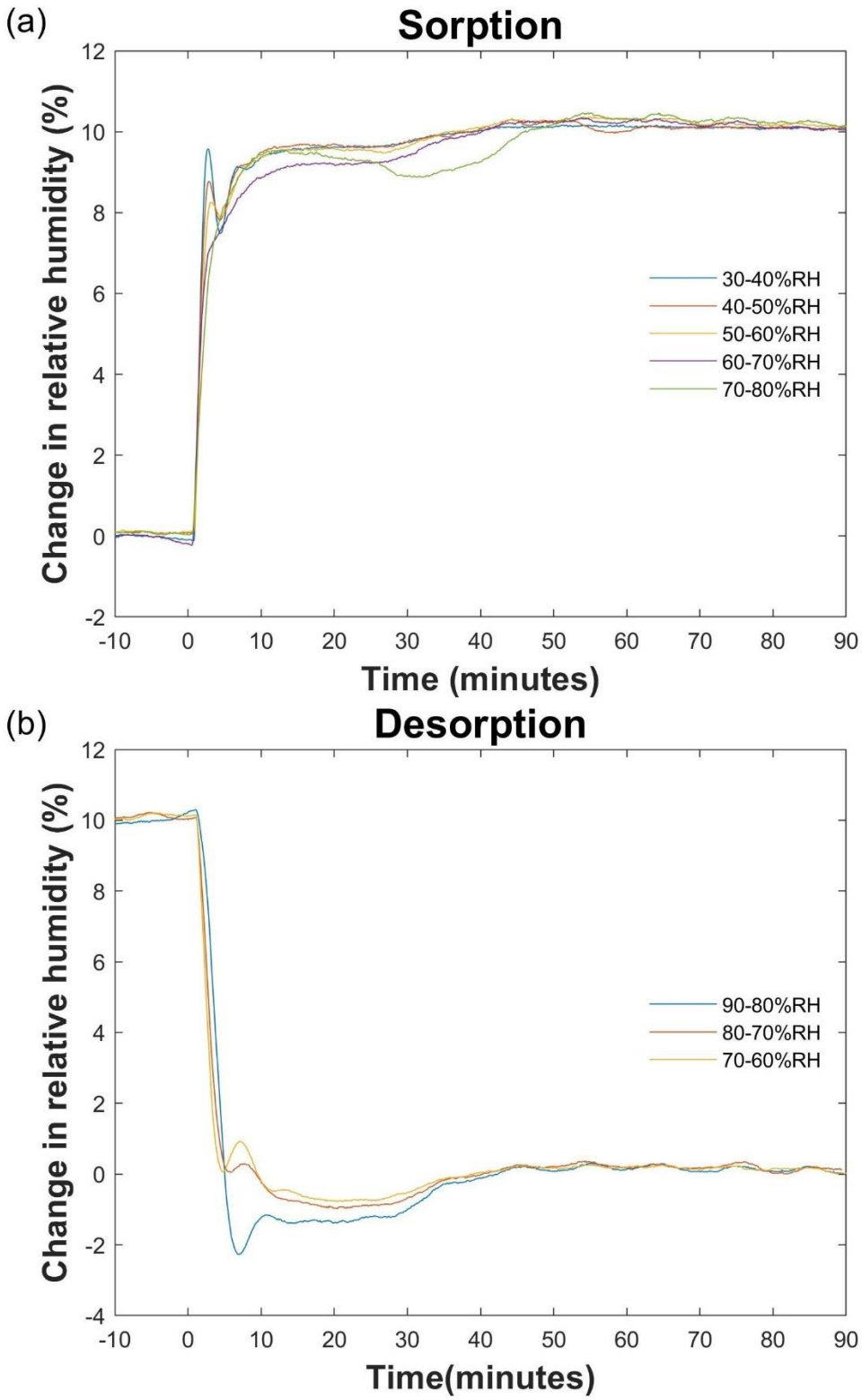

Figure 5.2 - Relative humidity step changes with THz-TDS setup for (a) sorption and (b) desorption.

Variations to the humidity response can be seen for the different RH step changes and a trend in the humidity response can be observed. In general, a small delay of approximately 1 minute is seen is due to some delay in the piping system, software and a humidity response from the sensor which is listed at 29 seconds (T 63%) under 1m/s airflow by the manufacturer, as the air

velocity is lower than 1m/s, the response will likely be slower. The humidity achieved is initially lower than the setpoint for both sorption and desorption at approximately 10-30 minutes as seen in Figure 5.2. This is not observed for steady state measurements where the stage is not used and is likely due to the increasing temperature. Additionally, some oscillation is observed at steady state and is likely due to the decreasing temperature. A dip in the response for 70 to 80% RH can be observed at 20-30 minutes, this was due to the rise in temperature and the dehumidifier not capable of producing a higher humidity due to its lower temperature. Whilst the humidity response is similar for the different step changes it is clear that improvements to the humidity sensor, control algorithm and reducing heat generation could produce a faster and more consistent humidity response.

The acquired waveforms obtained from measurements of Nafion 117 were processed using the same methods as with steady state measurements. The fitted double Debye parameters were acquired as shown in Figure 5.3 where an exponential change in the dielectric strengths of bulk and free water as well as membrane thickness can be seen. The infinite dielectric constant generally remains within 2.4-2.5 for all humidities whereas a small increase from 2.41-2.7 was seen in steady state measurements as shown in Table 4.1. This is possibly due to the sample being free to shrink and contract whereas the sample was clamped in a frame to avoid in-plane shrinking during steady state measurements

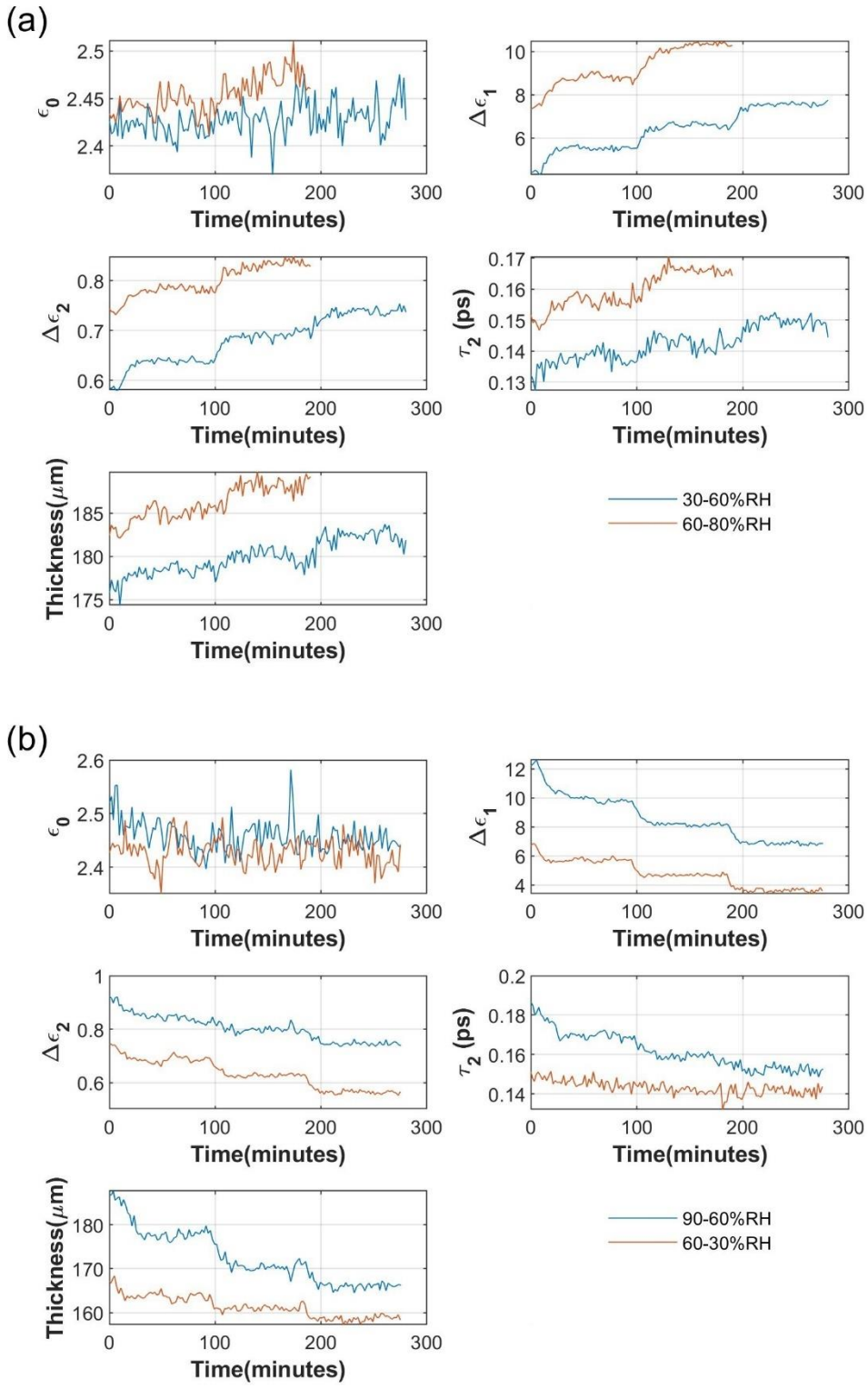

Figure 5.3 - Fitted double Debye parameters for transient water uptake of Nafion 117 under (a) sorption and (b) desorption.

The water uptake can be seen in Figure 5.4 which shows exponential behaviour for both the sorption and desorption in response to the changes in humidity with a rapid initial response followed by steady state as the membrane reaches an equilibrium with the environment. Some

variation to the steady state water uptakes between sorption and desorption can be seen. Water uptake hysteresis can be expected however, some sorption steady state values are higher than desorption which is inconsistent with hysteresis and is likely due to differences in temperature or membrane expansion/contractions. These variations are consistent with the uncertainty between repeat measurements shown in the steady state studies.

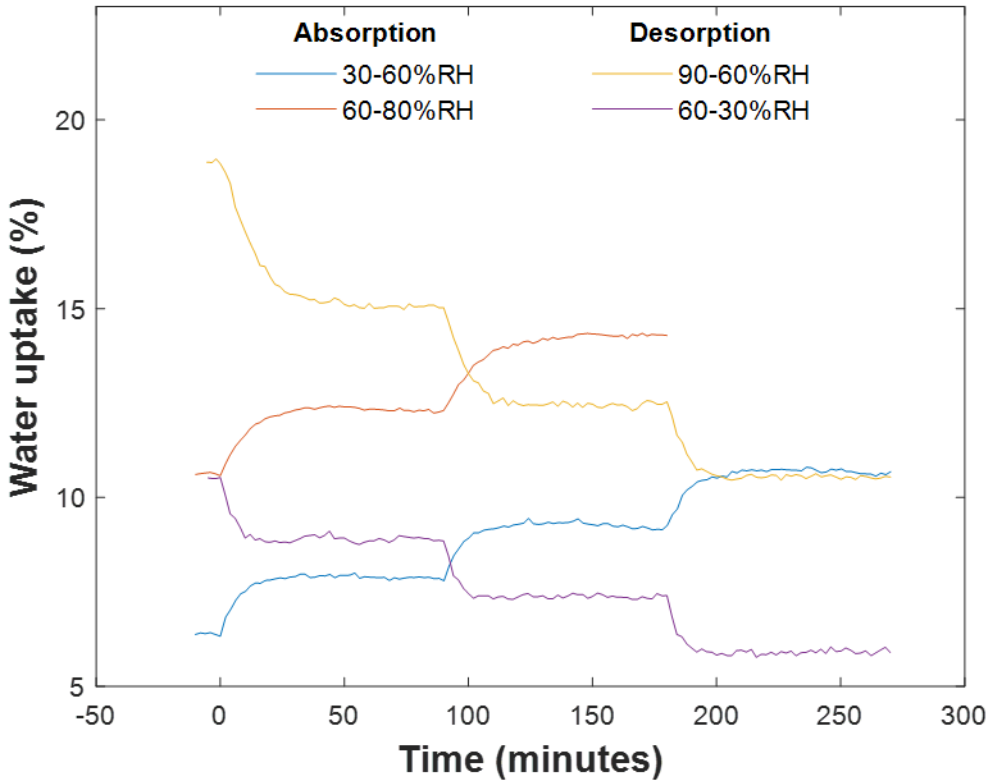

Figure 5.4 - Transient water content measured with THz-TDS.

The water uptake response of the membrane can be fitted to both the exponential and analytical model, with some good fits achieved as demonstrated for sorption between 30 and 40% RH in Figure 5.5. However, the initial rate using the analytical model tends to be too large particularly at high RH as seen in the fit for 70 to 80% RH, this is likely due to the RH response or interfacial resistance. It can be seen that the final value of normalised water uptake at 90 minutes is not 1 which is due to the variations in the steady state water uptake and hence steady state water uptake is fitted when applying the exponential model.

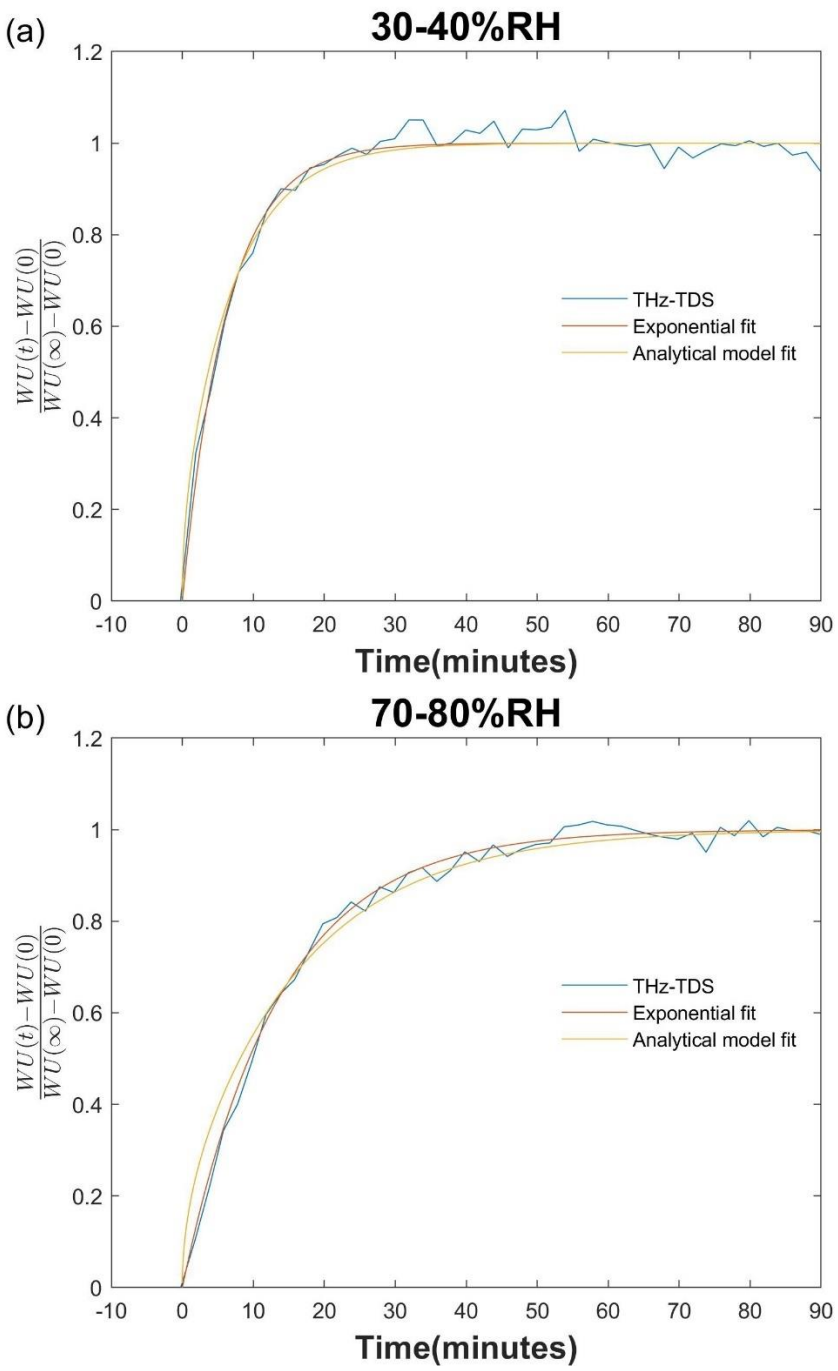

Figure 5.5 - Example fitting for water sorption from (a) 30 to 40% RH and (b) 70-80% RH using exponential and analytical models.

All model fittings with the analytical model are shown in Figure 5.6 and it can be clearly seen that the rate of change in water uptake is slower for membranes at higher humidities. It can also be seen that the rate of change for sorption is slower than desorption and is consistent with prior literature observations for transient water diffusion experiments [142,145].

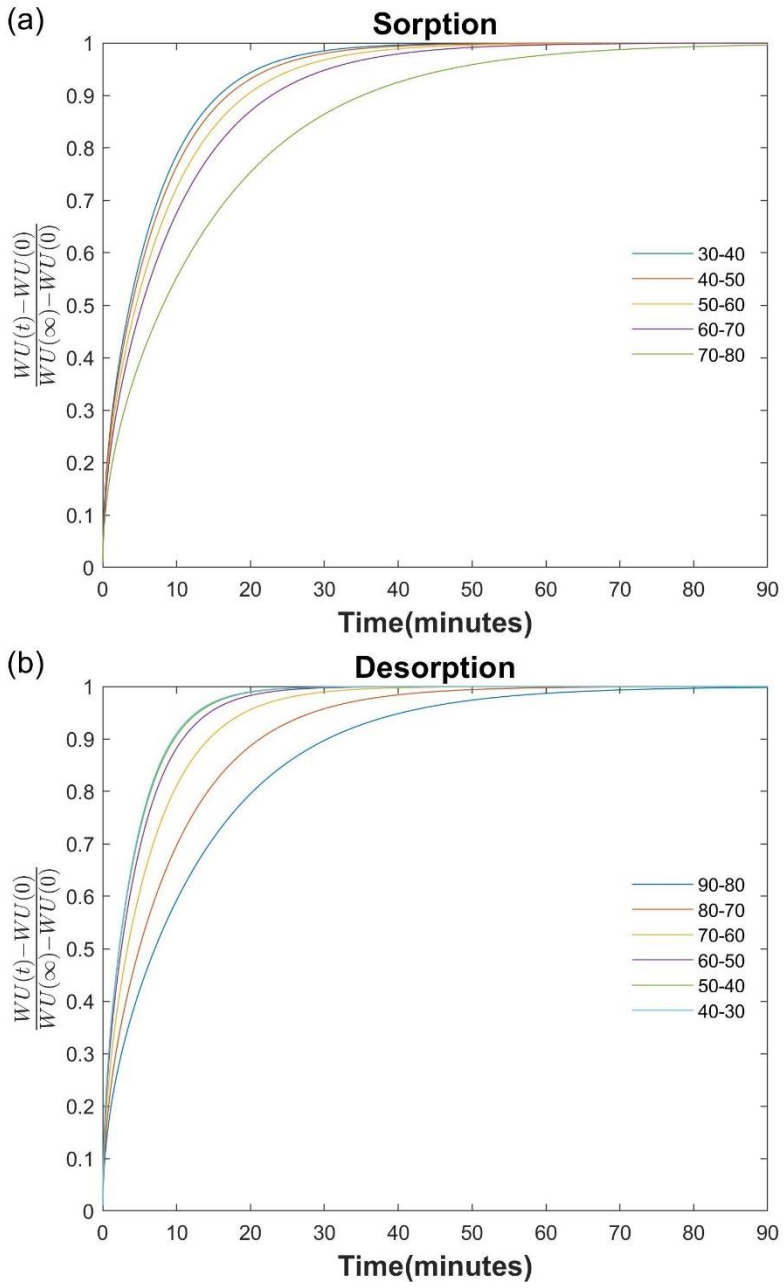

Figure 5.6 - Analytical Model fittings for (a) sorption and (b) desorption.

The RH response is not instantaneous as assumed in the model. Due to the slow response of the RH in the DVS measurements, finite element analysis was used to fit the diffusivity in addition to the analytical solution and a significant difference in the extracted diffusivities was observed. Due to this, finite element analysis was also applied to the THz-TDS data as shown in Figure 5.7. Whilst satisfactory fits with DVS were obtained using finite element analysis and the RH data, the quality of fit to the THz-TDS data was not as good as expected, there are some reasons for this. First the sensor delay and slow response seen in Figure 5.2 as well as the slow decrease in water uptake seen from approximately 50 minutes which is likely due to the change in temperature and possibly sensor response. Temperature is known to impact the relaxation

time of bulk water and was expected to have a minor impact within the temperature range. However, as this study is observing small changes in water uptake within 10% RH intervals, these temperature variations have become more significant. Due to this decrease only the first 60 minutes was fit and the steady state water uptake was fit as an additional parameter. The undershoot of the RH setpoint at 10-30 minutes results in a hump in the fits which is not necessarily observed in the THz-TDs data although it may be hard to see due to some uncertainty in the data.

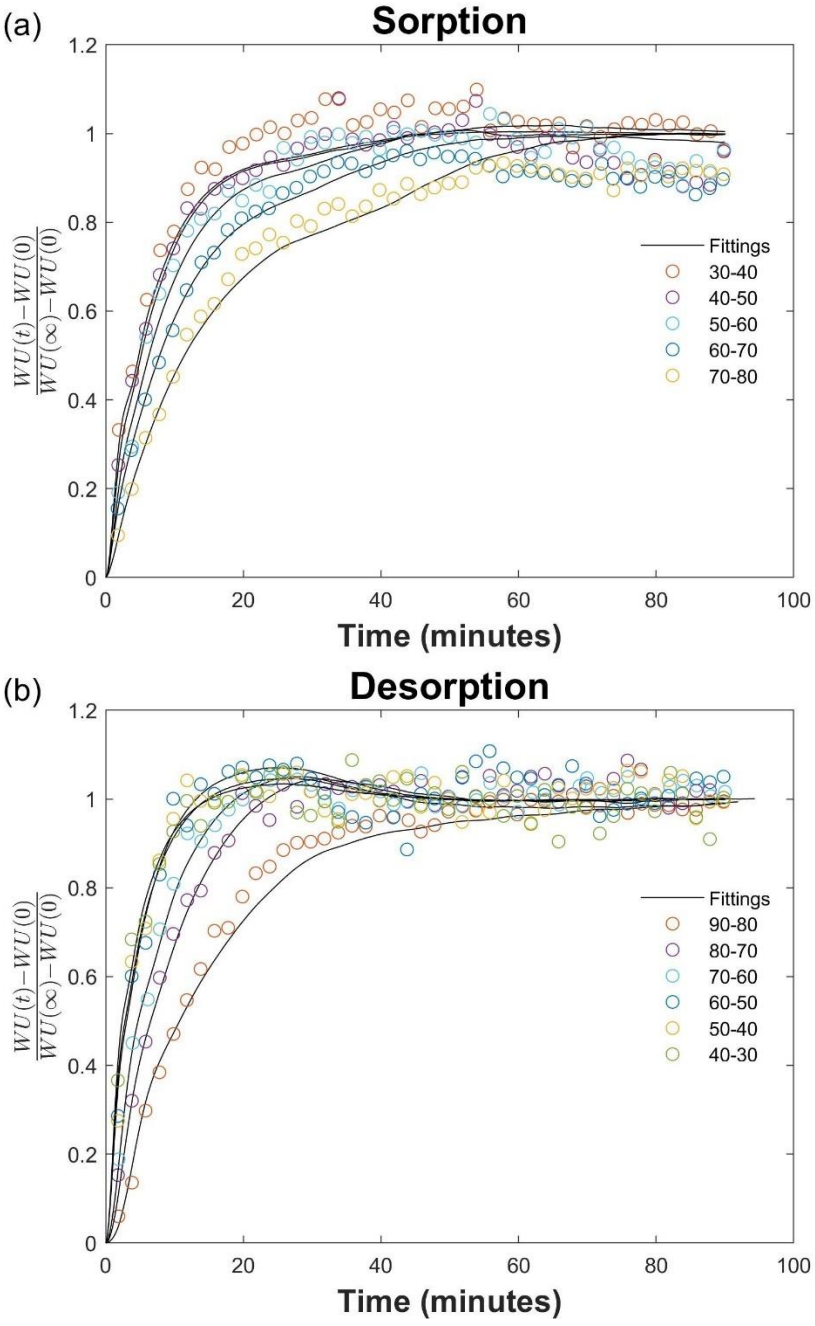

Figure 5.7 - Fittings of THz-TDS diffusion using finite element analysis.

5.2 DVS diffusivity

To complement the THz diffusivity data, a measurement was obtained using DVS using the same experimental procedure with 80-90% RH additionally measured. However, the membrane and humidity response were slower and not close to steady state at 90 minutes. Therefore, the measurements were extended based on the initial results according to Table 3.5 and as shown Figure 5.8. Figure 5.9 shows that the humidity setpoint was not reached, with most reaching higher humidities than the setpoint despite being close to steady state, this is likely due to the method of humidity control which has no feedback.

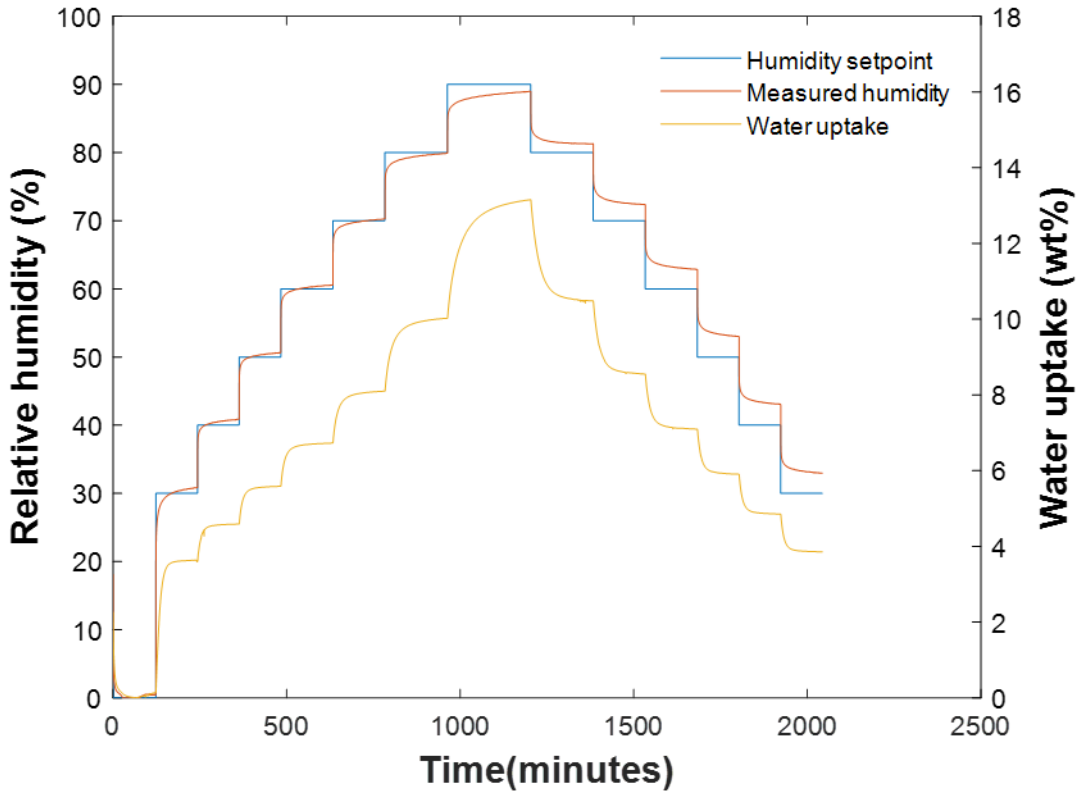

Figure 5.8 - Humidity and water uptake response of DVS measurement.

Figure 5.9 shows the normalised humidity response which shows that the DVS takes longer to reach RH steady state and is the reason for the longer experimental time. A slower response with increasing humidity for sorption can also be seen whilst desorption only has a small deviation in response. The slower diffusion and this slower humidity response are the reason for increased experimental time at higher humidities.

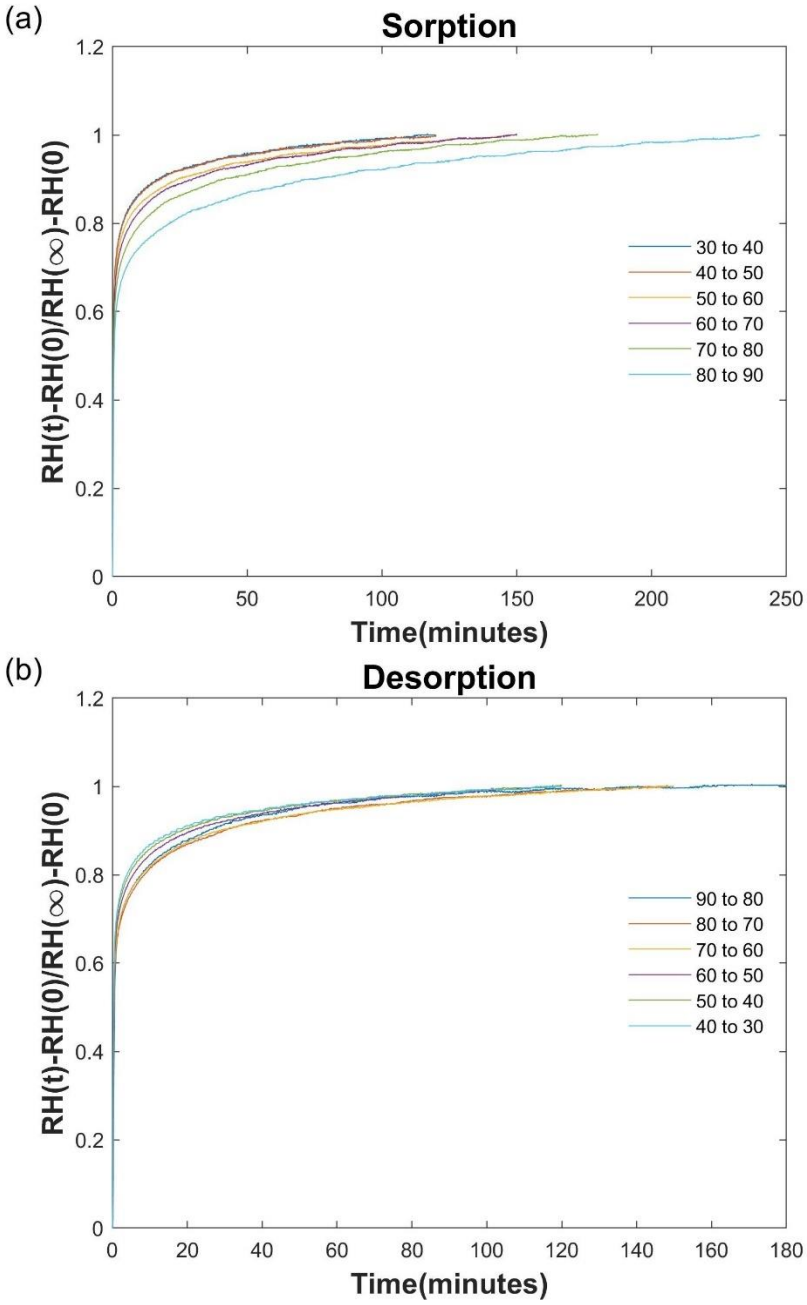

Figure 5.9 – Normalised relative humidity step change response of DVS.

The water uptake response was modelled using finite element analysis with the RH response included. This was important in achieving a good fit as even after 90 minutes when the THz measurements were finished, the humidity is still changing. The data was fit across the whole experiment unlike the THz as the associated issues were not present. As can be seen in Figure 5.10, the rate of change decreases with increased humidity which is consistent with the THz, although this is now partially due to the humidity response during sorption. The desorption rate also appears faster and is consistent with the THz shown in Figure 5.7. The quality of the fittings are better than the THz which is likely due to the fast RH sensor response, temperature

control, reduced water uptake uncertainty and lack of oscillation in the RH due to the PID control.

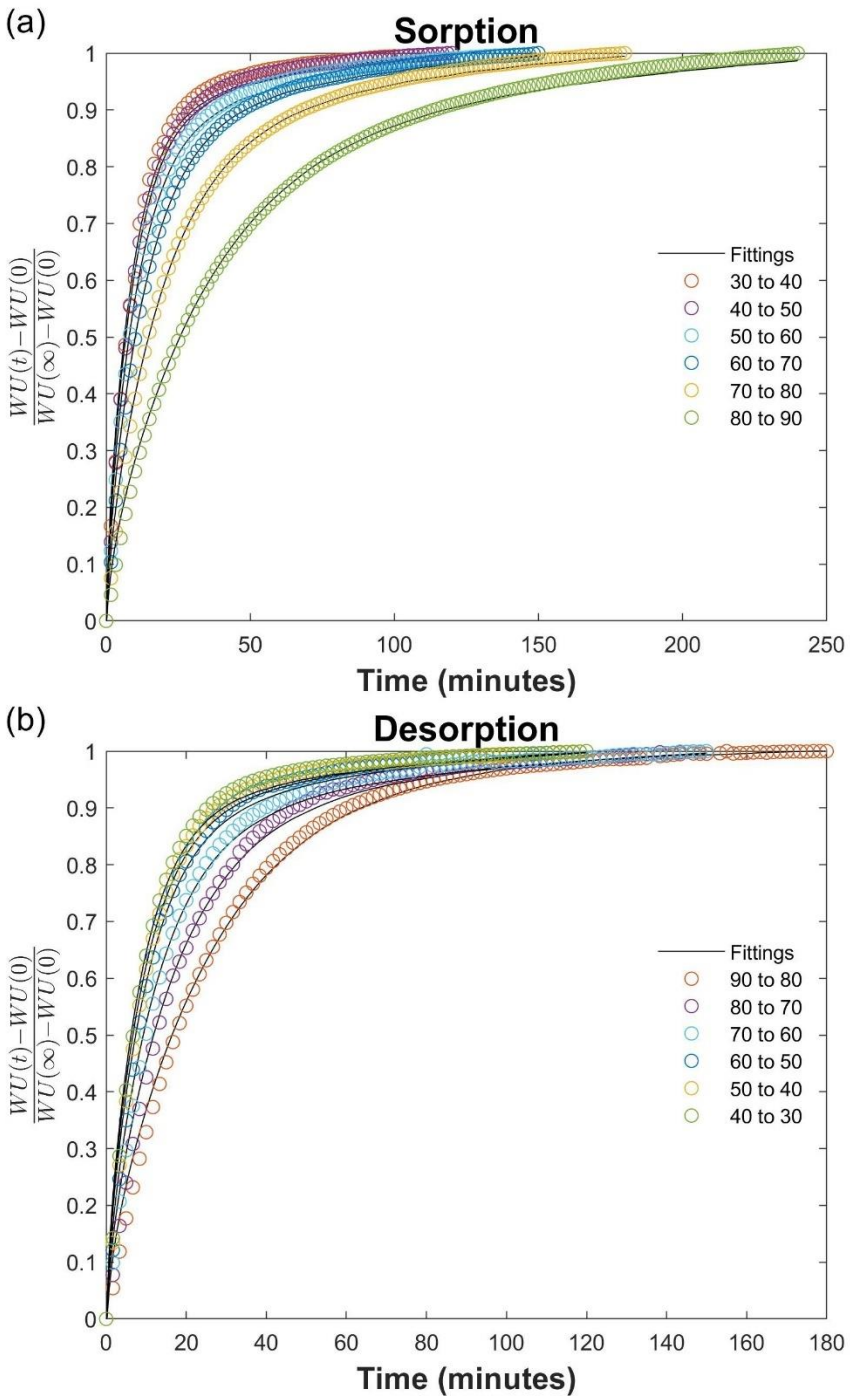

Figure 5.10 - Fittings of DVS (a) sorption and (b) desorption diffusion using finite element analysis.

When using finite element analysis, the spacial variation of water uptake can be extracted as shown in Figure 5.11. It should be noted that as this is based upon modelled data where only the average is compared to experimental data and RH data is used at the interface, the spacial water uptakes extracted are likely to contain some inaccuracies but do provide some insight

into water diffusion. The inaccuracies are particularly significant for the THz data where the RH data is less reliable due to the sensor response and hence has not been studied. As interfacial diffusion was not considered and the interface was assumed to be at equilibrium with its ambient humidity, the y-axis intercept demonstrates the change in relative humidity. As expected, water diffuses from the interface into the membrane and water uptake rapidly changes close to the interface, whereas a slower response can be seen as the distance from the interface increases and it can be seen that it takes over 1 minute for water to begin diffusing into the centre of the membrane.

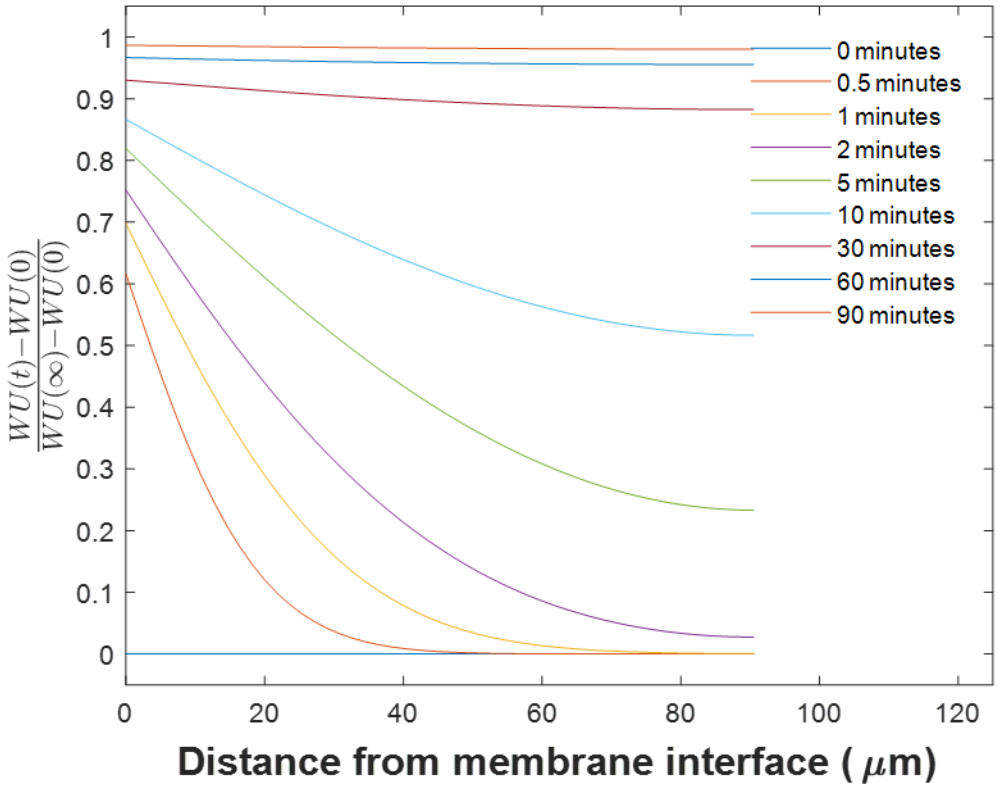

Figure 5.11 – Example of modelled water uptake profiles across the membrane from DVS measurement of Nafion 117 from 30 to 40% RH.

The fitted diffusion coefficients can be seen in Figure 5.12 for THz and DVS using finite element analysis both with and without RH inclusion. The data shows a decrease in diffusion coefficient with increased humidity and higher diffusivities for desorption which is consistent with prior transient studies [130–132]. The data also shows the expected increase in diffusion coefficient when including the RH response with the finite element model with the exception of the THz 80-90 desorption, this is likely due to the measurement having the highest overshoot in the RH response as previously seen in Figure 5.2. The fitted diffusivities help to demonstrate the impact of the humidity response, which is significant with an increase of 25±11% and

38±46% for the THz sorption and desorption respectively. As expected, the increase was higher for the DVS with 74±5% and 57±10% increase seen for sorption and desorption respectively, the deviation on these values is likely lower due to the more consistent RH response and reduced water uptake uncertainties. The diffusion coefficients of the THz data are generally higher than the DVS both with and without RH response, this is possibly due to a number of factors. The air flow rate in THz is higher and therefore any impact of interfacial resistance would be expected to be reduced. The slow response of the RH sensor used in the THz chamber would also be expected to result in a higher fitted diffusivity. The slower RH response of the DVS would also decrease the fitted diffusivity when not including the response in the model, this is consistent with the closer extracted diffusivities between THz and DVS when using the RH response with the exception of the THz desorption in the 30-60% RH range which is likely due to the need to reproduce the RH response for that data.

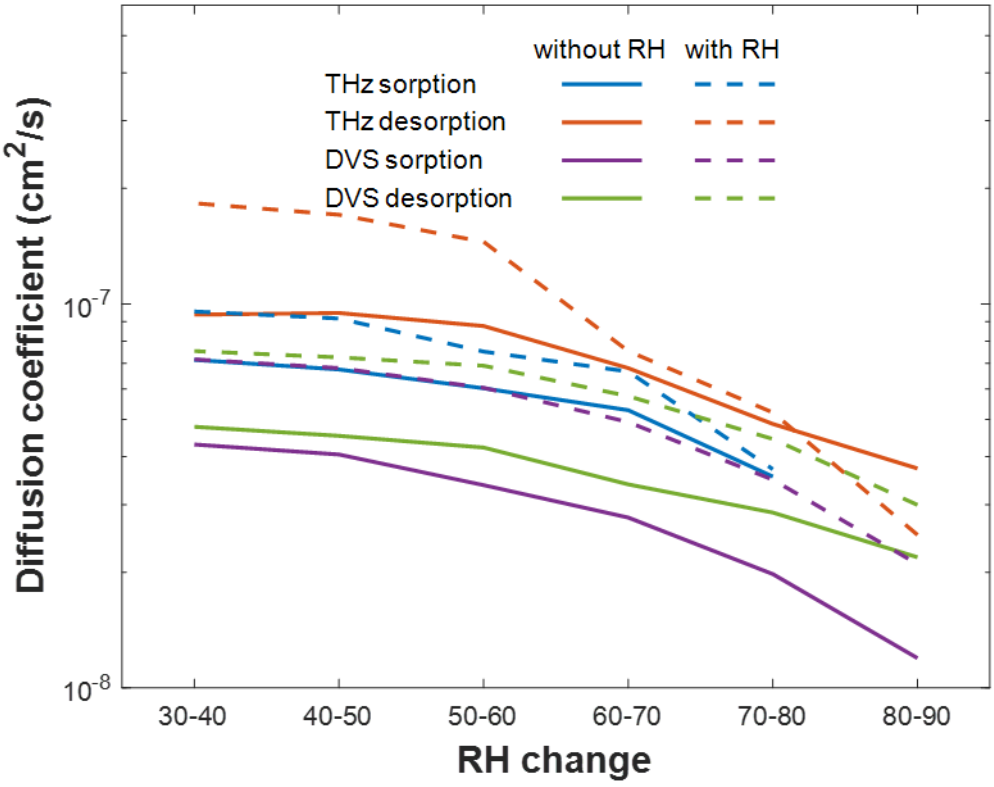

Figure 5.12 - Water diffusion coefficient in Nafion 117 membrane from finite element analysis.

The diffusivity coefficients from finite element analysis have also been compared to literature transient DVS diffusivity coefficients [130–132] as shown in Figure 5.13. An average of sorption and desorption was used and plotted using the higher humidity of the step change as found literature. In general, all data shows the same trend with a plateau at 30-50% RH and

decreasing diffusivity at lower and higher humidities. Whilst there is some spread in these values, the variations are within expectations based on literature values across all techniques as seen in Figure 2.7. The spread for transient studies is likely partly due to the different fitting methods used as this work and these literatures have all used different models. The temperature is also different with 25°C [130,132] and 30°C [131] used in literature whereas 20.5°C was used in the DVS data and the temperature uncontrolled at 19-25°C for the THz measurements. Diffusivity is known to increase with temperature [130,131,150] and the data appears to fit this trend making it a likely cause. It should also be noted that the spread in diffusivities is lower in Figure 5.13 than Figure 2.7 due to the use of RH for the x axis rather than water content. This is likely due to uncertainty in the water content as factors such as residual water and hysteresis can impact extracted water uptake.

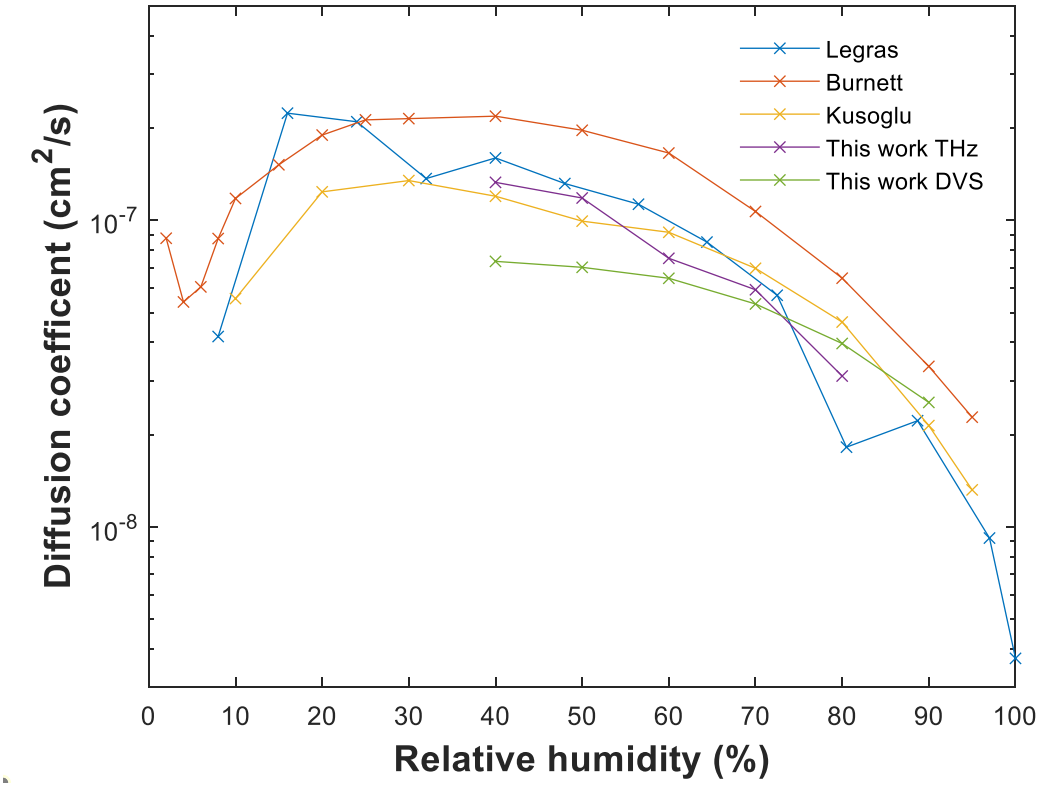

Figure 5.13 - Comparison of relative humidity diffusivity coefficient with transient DVS literature [130–132].

5.3 Swelling

Membrane thickness is a fitting parameter of the THz-TDS analysis, and the technique can therefore be used to understand the dynamics of membrane swelling and shrinking properties due to changes in hydration. However, as only relatively small changes in thickness are

expected, high accuracy of the acquired thicknesses are required and therefore the technique should be validated against complimentary techniques. Using a sample of Nafion 117, the thickness was also acquired independently using a LEXT OLS5000-SAF laser scanning confocal microscope which features a 405nm laser and was fitted with a 10x objective lens (MPLFLN10xLEXT). This microscope is capable of measuring the thickness of optically transparent materials without physical contact but does require the refractive index of the material which is 1.36 for Nafion [329]. This is close to the refractive index of water for this wavelength and 25°C at 1.342 [330] and therefore the refractive index of the membrane was assumed to be constant at 1.36 for all levels of hydration. The Nafion 117 membrane was hydrated to 90, 50 and 0% RH inside the RH chamber used for the THz measurements. The chamber was transported to the microscope and quickly removed to be measured with the confocal microscope, during analysis of this data 5 points were used. The thickness swellings from the confocal microscope have been plotted with swellings from the fittings of steady state THz measurements and literature values [114–117,119,121] as shown in Figure 5.14.

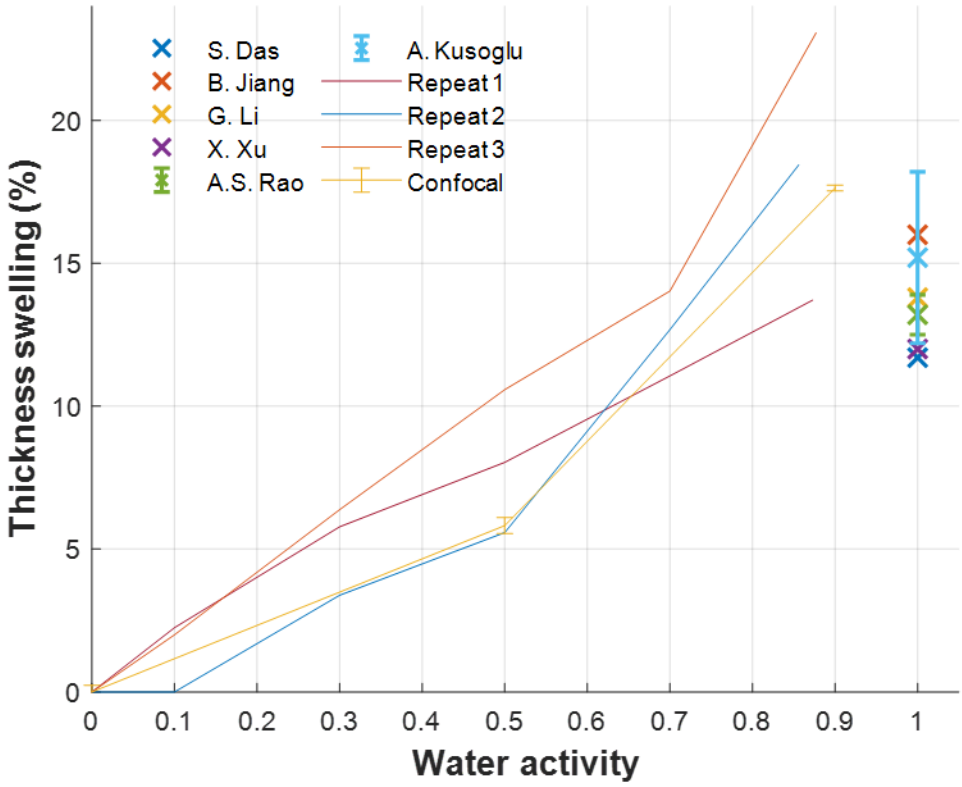

Figure 5.14 - Thickness swelling comparison of Nafion 117 against literature [114–117,119,121].

The results show that the relative increase in water thickness is consistent with the independent confocal micrometre results however, there is a lack in the consistency of the THz-TDS results

with a difference of 9.4% observed for the ~87% RH measurements between the 1st and 3rd repeats. As the samples were confined within a sample holder to try minimise in-plane shrinking, consistent shrinking was expected. However, it was observed that some slipping did occur which was likely inconsistent and resulted in different values and trends. The obtained values from THz-TDS and the confocal microscope also appear to be higher than literature values and this is due to the confinement of the samples. As in-plane shrinking is limited, the membrane is under in-plane tension causing the shrinking of the membrane thickness to increase accordingly.

As independent measurements yield differences in membrane thickness, a different approach was needed to validate THz membrane thicknesses. As the confocal measurements could take a few minutes and the microscope was not located in close proximity to the THz-TDS, the chamber had to sealed and then transported. As the humidity sensor and air delivery pipe had to be disconnected and the control program later restarted, additional time was also needed for the PID control to reach the setpoint. This was impractical for validating membrane thickness throughout the THz experiment and therefore measurements using a digital micrometre were obtained. The samples still had to be removed from the chamber to obtain the measurement, but the chamber could remain in place and so gas flow could remain with rapid recovery to the RH setpoint. Some difference in the measurements is expected due to a change in membrane water uptake under exposure to the ambient environment, although significantly reduced in comparison to the confocal microscope. Following a micrometre measurement, the sample was then returned to the chamber to equilibrate for the next measurement. The comparison of THz-TDS and micrometre thicknesses are shown in Figure 5.15 where it can be seen that THz-TDS thickness is close to the values from micrometre measurements which have a stated accuracy of ±2μm at 1μm resolution. With the exception of 30% RH which deviates from the trend in the micrometre measurements, all measurements are within 1μm of the THz-TDS fittings demonstrating the accuracy of THz-TDS thickness determination for these materials. The relative swellings from 0-90% RH are 16.2 and 16.7% from the THz-TDS and micrometre measurements respectively. These values are additionally consistent with relative swellings of the Nafion 117 which are shown in Figure 5.14.

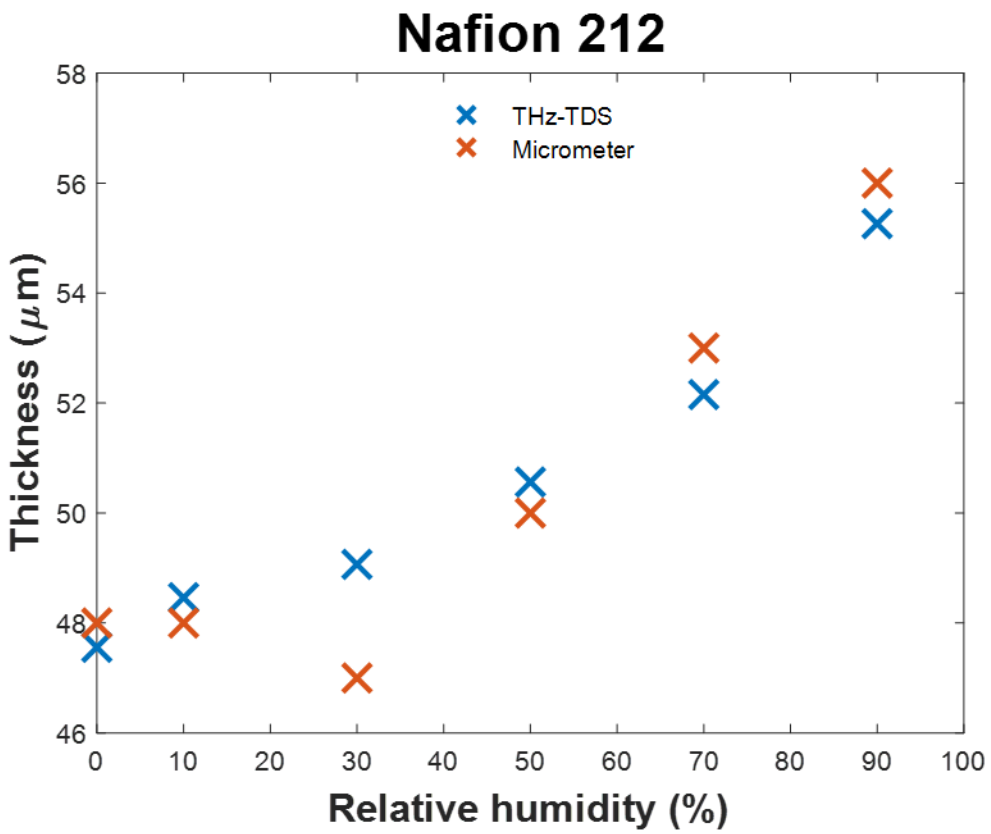

Figure 5.15 - Thickness comparison of Nafion 212 from THz-TDS fittings with complimentary micrometre measurements.

5.4 Dimensional stability

As the THz-TDS fitting algorithm can provide information on both dielectric properties and membrane thickness simultaneously, here the potential to resolve membrane's swelling and shrinkage behaviour over time is evaluated. In particular, RH inside the chamber was ramped up from 10% to 80% and dwelled for 90 minutes. This process is then ramped down from 80% to 10% RH followed by the same dwell time. Dehydration and hydration cycles were repeated 18 times with terahertz data being acquired in the beginning, middle and end of this cycling process. Five repeat measurements were acquired at the end of each 90 min dwell time for measurement repeatability. The results for Nafion 117 are shown in Figure 5.16 and the linear line of best fit shows some very small changes, however these changes are within the uncertainty of the measurement and suggests that negligible thickness change can be expected. This result is in agreement with an earlier study where non-reinforced membrane's physical dimensions were also observed to be unaffected by repeated hydration and dehydration cycles [110].

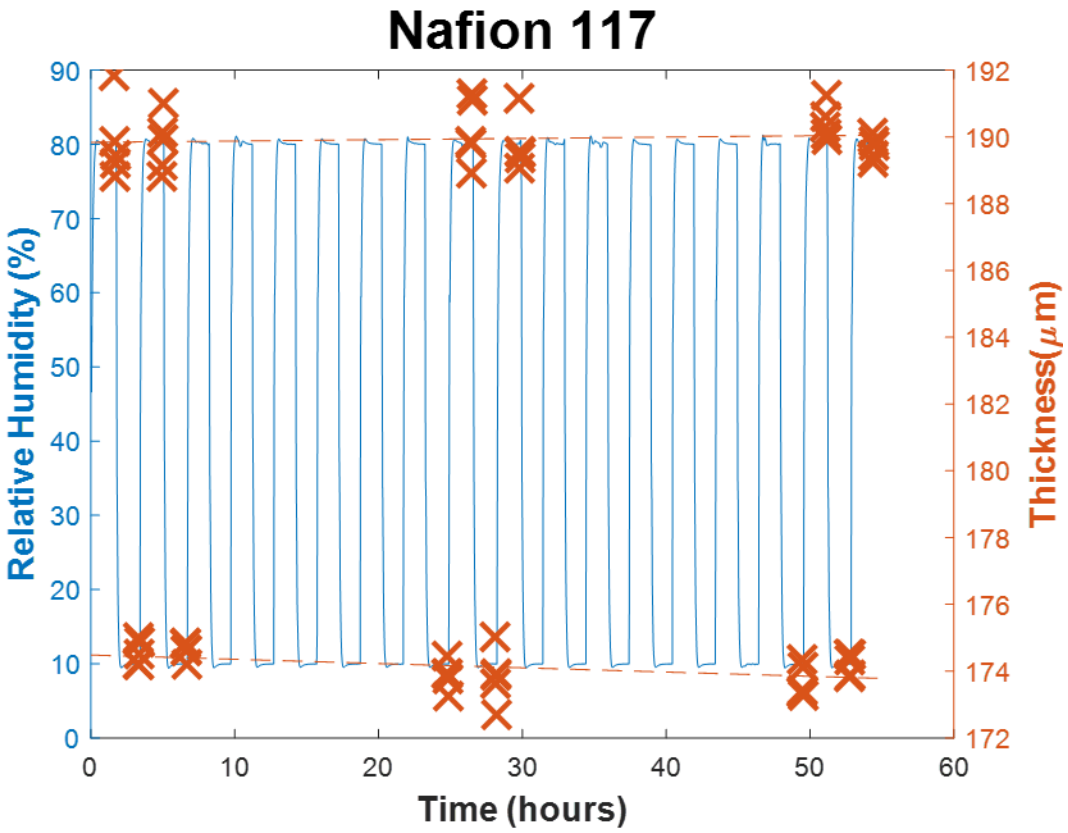

Figure 5.16 - Swelling and shrinkage cycling analysis of Nafion 117.

As ePTFE reinforced membranes have been shown to exhibit some dimensional instability under repeated hydration and dehydration cycles [110], a Fumasep F10120-PK reinforced membrane was selected for study. This membrane was selected as it is a thick (120-130µm) reinforced membrane. A relatively thick membrane was selected due to the uncertainty of the thickness obtained with THz-TDS as shown by the repeats in Figure 5.16. Unlike the ePTFE reinforced membranes previously studied [110], this membrane is reinforced with woven polyether ether ketone (PEEK) fibres as shown in Figure 3.1c. The cycling results for Fumasep F10120-PK are shown in Figure 5.17 where it can be seen that the humidity was not recorded during the first half of the experiment. The humidity was still cycling however and was monitored within the LabVIEW program.

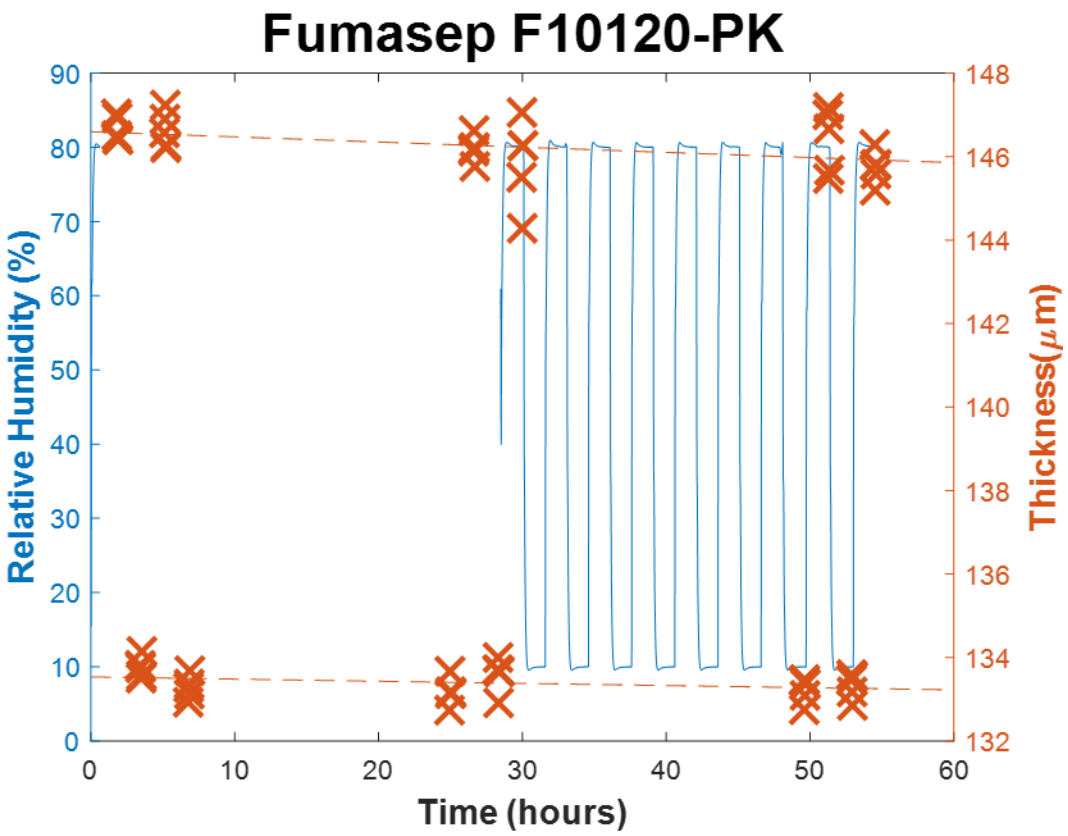

Figure 5.17 - Swelling and shrinkage cycling analysis of Fumasep F10120-PK.

As with the Nafion 117, a negligible change in thickness per cycle was observed within the measurement uncertainty. This membrane was expected to show some dimensionally instability however, there are many factors which may have contributed to this outcome. Firstly, the fibre reinforcement is different to the ePTFE reinforcement which has shown dimensional instability [110]. Some of the PFSA ionomer within an ePTFE reinforced membrane is contained within the pores of the reinforcement's microstructure. Expansion of the ionomer within these pores will impart some additional stress to the reinforcement whereas no ionomer is constrained within the reinforcement of a fibre reinforced membrane. Only small changes were previously observed in repeated cycling [110] and therefore these measurements may not have had the sensitivity to detect the changes. The thickness uncertainty may be due to laser jittering as no phase corrections were made and have been observed to impact membrane thickness. Therefore, reducing or eliminating the effects of laser jittering may lead to an improved accuracy and results may then show small signs of dimensional instability. Additionally, whilst all reinforced membranes tested previously exhibited dimensional instability, one of the membranes only exhibited this behaviour at 80°C and not 25°C [110], therefore the Fumasep may also only exhibit dimensional instability at higher temperatures. This work has studied the stability of membrane thickness rather than the in-plane stability of

the previous study [110] and this is may to lead to some additional differences of the acquired results. To observe instability, clamping the samples from an initially hydrated state may also yield more significant results as this is known to increase membrane stress due to additional in-plane tension during shrinking [86,110], although care would need to taken to ensure to slipping occurred.

5.5 Summary

In general, this work has demonstrated the ability of THz-TDS with an RH controlled environment to extract the transient water diffusivity coefficient inside hydrophilic membranes at different humidities. Values are in agreement with complimentary literature DVS values [130–132] and our own DVS measurement although closer values are expected with improvements to the THz system. Whilst this work demonstrated the applicability of THz to diffusion studies, significant improvements can be made to the experimental methodology such as improved RH sensor response, optimisation of PID control and mitigation of heating effects due to the motorised stage, which could be improved through chamber temperature control which would also reduce uncertainty of the results and improved comparability. A repeat of THz desorption measurements in the range of 30-60% RH would also beneficial. A Nafion 117 membrane was chosen due to its thickness and whilst the water uptake of thinner more industrially relevant membranes such as Nafion 211 can be determined, the water uptake response of these thinner membranes is much quicker. This is shown by equation 3.28 where the exponential rate of response is proportional to $1/l^2$ and therefore a 25µm 211 membrane with the same diffusivity would respond over 50 times as fast as the 183µm 117. This model assumes an instant RH change and no interfacial resistance which are significant factors which will mean that obtaining diffusivities of thin membranes using this method are likely impossible. This is due to the time resolution and need to deconvolute the diffusivity from RH response and interfacial resistance. Therefore, transient diffusivity's measurements can only be recommended for thick membranes and steady state diffusivity measurements should therefore be used for thin membranes.

The impact of hygral swelling has also been studied, firstly thicknesses obtained at steady state with THz-TDS were compared to complimentary confocal microscopy and micrometre measurements. Results were in agreement although inconsistencies were observed between samples, likely due to the clamping and later slipping of the samples within sample holders. Based on these results, the dimensional stability of Nafion 117 and Fumasep F10120-PK

membranes under humidity cycling between 10 and 80% RH was studied, in this case the samples were not clamped to obtain consistent results. The results show that the membranes are both dimensionally stable in the thicknesses direction for this temperature (20-25°C) when not clamped. Clamping the samples would increase the induced strain upon the membranes potentially leading to dimensional instability. Additionally, increasing the temperature has been shown to reduce membrane dimensional stability [110]. Therefore, to observe dimensional stability with these membranes, higher temperatures and/or reliable clamping may be needed.

6 Conclusions and further work

This chapter aims to summarise the research described throughout this dissertation including the objectives and results. In addition, this chapter aims to address any practical limitations of the developed techniques and provide suggestions to improve the quality, capability and scope of the work.

6.1 Results

A selection PFSA membranes has beenstudied using a THz-TDS spectrometer in the range of 0.2-1.05 THz and the acquired data was used to determine the water uptake and molecular water states within the PFSA membranes. Steady state measurements using a relative humidity-controlled chamber at 0, 10, 30, 50, 70 and 90% RH were obtained for all membranes studied. Acquired water uptakes were determined using effective medium theory and a linear mixing model relating. Acquired water uptakes followed a nonlinear uptake profile as expected, and values were in agreement with dynamic vapor sorption literature and a measurement. Some differences were observed between values obtained from THz-TDS and DVS particularly related to the quantity of residual water present at 0% RH which resulted in an WU offset as values are determined by the difference between the measurements and 0% RH. These differences were also observed between different DVS measurements of the same membranes. All membranes had similar water uptakes with a small reduction observed for Nafion XL and Fuamsep due to them containing hydrophobic reinforcements.

THz-TDS is sensitive to the reorientation dynamics of water and can characterise water as bulk, bound and free states using the dielectric strengths of bulk and free relaxations. Bound water can then be determined based on the total water content. It was found that all of these states are present at all humidities studied. Little change to proportion of free water was observed but the proportion of bulk water was very small at 0% RH but the proportion increased with increasing humidity whereas the proportion of bound water decreased. The trend was similar for all membranes studied and only small differences were observed between Nafion membranes which are all manufactured from the same PFSA ionomer. More significant differences were observed for Aquivion and Fumasep membranes which are made from different PFSA ionomers with different chemical structure and ion exchange capacities.

Obtained water states were compared with other techniques. Firstly bulk water was compared with freezable water and bound water as compared to non-freezable water obtained from water fusion enthalpies using differential scanning calorimetry. Literature values were compared in addition to measurements of Nafion 117 prehydrated to 85 and 100% RH A similarity in the observed trends could be seen however the quantity of bulk water was higher than freezable water and no freezable water was observed until ~80% RH [211]. There are a number of reasons for this such as the differences in the boundary between the water states being probed resulting in some of the non-freezable water being incorrectly categorised as bulk water by the terahertz

measurement. This difference arises from different physical parameters being measured e.g. water fusion enthalpy by DSC as opposed to bulk water dielectric strengths by terahertz. Changes in temperature will also have an effect on the THz water states as the reorientation dynamics of water are impacted shown by changes to the dielectric strength and relaxation times of bulk water with temperature [200,264,287–296]. Therefore, it is possible that some bulk water can become loosely bound as temperature decreases.

Bulk water was also compared with FTIR, specifically the band located at 1630 cm^{-1} which is assigned to the HOH bending vibration of water molecules associated with SO_3^- groups. This band had been shown to be correlated with the membrane proton conductivity [202] and was therefore of great interest. Unfortunately, no RH dependant FTIR data was available and therefore a desorption from a hydrated state with a dry air purge was used to replicate the available FTIR literature. Both techniques showed as sharp decrease in their respective parameters (dielectric strength and band peak area) at a similar rate and reaching an equilibrium close to 0. Although promising there is difficulty comparing due to the lack of points of known water uptakes or humidity. No fractions can be obtained with TFIR for comparison as band area is not proportional to species population and therefore values cannot be compared. Additionally, many factors such as water uptake will also show the same trend under rapid desorption.

Using a motorised stage to more rapidly obtain THz sample and reference measurements every 2 minutes, the water uptake of Nafion 117 was studied in response to 10% RH changes in humidity from 30-80% RH in sorption and 90-30% RH in desorption for 90 minutes per RH step. These experiments were then replicated with dynamic vapor sorption although longer measurements were required due to the slower change in humidity. These experiments were designed to study the mass transfer of water within the membrane through diffusion. As only the average water uptake could be obtained, water diffusion had to be modelled. The water follows Fickian diffusion where diffusive flux is proportional to the concentration gradient. However, there are a number of Fickian diffusion models which can be used and are derived based upon different assumptions. For this work, water was initially assumed to be evenly distributed throughout the membrane prior to the change in humidity (steady state) and diffusion was only considered in the thickness direction due to the relatively thin nature of the membrane. An empirical exponential was first used however a number of theoretical models were considered which generally differ based upon the boundary conditions at the air-membrane interface upon the change in RH. This included an instantaneous change to the

steady state equilibrium corresponding to the new RH setpoint, interfacial resistance and an exponential change corresponding to the rate of changing humidity. Interfacial resistance was thought to be insignificant due to the thickness of Nafion 117 and the humidity change of both THz and DVS did not follow an exponential response. Therefore, the model using an instantaneous change was used and was applied to the THz data. When applied to the DVS data the fittings were not sufficient as the RH was slow and even after 4 hours a small increase could still be seen to reach 90% RH. Therefore, a different approach was needed and finite element analysis was selected as the RH data could be inserted into the model however, this method is much more computationally intensive and unstable if too large step sizes are used.. Using the RH data to determine concentration at the membrane boundary resulted in improved fittings and higher diffusivities were aquired. This was then applied to the THz data however, due to the slow response of the RH sensor and some heating caused by the motorised stage, the fittings were less satisfactory. Desorption was found to be faster than sorption and in the 30-70% RH range and diffusivity decreased with humidity for both sorption and desorption. The extracted diffusivities obtained with fittings using finite element analysis were found to be in general agreement with literature DVS values [130–132]. Some spread was observed between values which is possibly due to differences in RH response and the different diffusion models used. Additionally, the values of diffusivity do appear to follow a trend due to temperature which was 19-30°C across these measurements and literature values with diffusivity increase with temperature. This is agreement with literature where both sorption and desorption increase with temperature [130,131,150] and can be represented by an Arrhenius equation [130], although the range is small, so no comparison was made.

DVS provides better time resolution, reduced data analysis and improved measurement uncertainty when compared to THz-TDS. However, as THz-TDS is contact free this opens this technique up to simultaneous study using additional techniques in addition to acquiring both membrane thickness and water state information.

Membrane swelling was also studied as the THz-TDS analysis can be used to extract membrane thickness. Steady state measurements were first compared to complimentary confocal laser microscopy and micrometre measurements for validation. Results were in agreement although inconsistencies were observed between samples, this was likely due to insufficient membrane clamping within sample holders and therefore samples may have slipped within the frames. Based upon these results the dimensional stability of the membranes thickness was studied under repeated cycling between 10 and 80% RH. The samples were not clamped due to the

slipping issues. Nafion 117 and Fumasep F10120-PK were studied due to their greater thickness and the reinforcement of the Fumasep for comparison. Neither membrane exhibited any significant change in thickness across the experiment and only minor changes were observed which were within uncertainty. In order to see any dimensional instability, it is likely that a higher temperature is required and possibly membrane clamping, although slipping would need to be eliminated.

6.2 Practical Limitations

In spite of the challenges associated with comparing techniques that probe different parameters, a general agreement has been observed between the presented terahertz results against literature DVS, DSC, FTIR, confocal laser microscopy and micrometre data. These complimentary techniques all have their limitations and challenges which must be considered. However, it is also important to highlight some associated practical challenges with humidity-controlled THz-TDS. For the terahertz measurements presented here, a number of limitations should be considered.

- The steady state terahertz measurements performed using the controlled humidity chamber are desorption data only, thus results will differ from sorption due to membrane hysteresis.
- No temperature control has been implemented, thus variations will exist in the quantified water states due to small temperature variations. Particularly for water fractions as the bulk relaxation time is temperature dependant. Additionally, the lack of temperature control has caused some issues for studying diffusion due to heat generated by the motorised stage, which also impact the response of the humidity control and the capability to reach high humidities which was limited to 80% RH in sorption for the diffusion study.
- There are practical challenges in reaching and maintaining high humidities (i.e. $\geq 90\%$) inside the humidity chamber and this is the range particularly relevant to observe the steep WU increase. These factors are inevitably affected by sensor uncertainties as some deviations from actual humidities can be expected. This is especially the case at 0% RH where some moisture is expected to remain.
- The current humidity sensor has a relatively slow response which has had satisfactory performance for steady state and swelling experiments. However, as the data has been used in the finite element analysis of diffusion data, the quality of fittings has reduced

and places some uncertainty in the acquired diffusivity values despite the close match with literature values.

- To analyse thin membranes phase correction was required to account for small differences in timing of the THz spectrometer (<15 fs). Extracted parameters and phase information can be compared with known values, complimentary measurements and known trends from thicker membranes. However, this process inevitably leads to an increase in measurement uncertainty.
- Transient diffusion of Nafion 117 has been shown however it is important to note that this should not be recommended for thin membranes due to the relationship between thickness and rate of WU change due to diffusion. In the case of thin membranes, the effects of interfacial resistance, and humidity response become much more significant, whereas interfacial resistance has been considered insignificant in this work. Therefore, care must be taken to separate the effects of interfacial resistance and humidity response. The time resolution of the terahertz measurements was 2 minutes and while this could be reduced with improvements, particularly to the motorised stage. The rate of change is rapid as shown by previous work where a new equilibrium was reached in approximately 3 minutes for 15μm membranes [283]. This rapid rate of change presents a significant challenge due to the limited time resolution and the humidity response which is significantly slower than diffusion.

6.3 Improvements and further work

Improvements to the work presented can be made, some of which have already been discussed. Additionally, the scope of this technique can be expanded to extract additional information, facilitate simultaneous complimentary measurements and provide a different experimental configuration as listed:

- The current sensor response is slow for diffusion studies and a sensor with faster response is recommended. A faster sensor response would also provide a faster and more accurate humidity response with increased stability due to reduced delay to the PID control.
- The lack of temperature control has been a significant source of experimental inconsistency, as experiments were susceptible to temperature variations in the ambient environment. Implementing temperature control would reduce uncertainty and increase the accuracy of the results whilst providing additional benefits. Temperature control

would improve the humidity response during diffusion and allow measurements up to 90% RH in sorption diffusion measurements. The ability to perform measurements at higher temperatures would also be of benefit as membranes operate at higher temperatures which are typically 50-100°C for polymer-based membranes. Many studies are conducted at these operating conditions and therefore temperature-controlled measurements could be compared to a greater number of measurements and literature studies. Higher temperatures may also allow this technique to study the dimensional instability of membrane thicknesses which were not observed at room temperature.

- The spot size of the THz beam is only a few millimetres in diameter and can therefore be used to study different areas of the membranes unlike gravimetric techniques. The membranes studied in this work were uniform and therefore the point of sample measurement was not of significant concern. However, approaches such as raster scanning can be used to study samples with special variations such as membranes of non-uniform thickness or possibly capture information such as the distribution of terahertz absorbing additives or coatings.
- Gravimetric techniques such as DVS require physical contact and are susceptible to any external change in weight, but THz-TDS can perform contact free water uptake measurements regardless. This allows for other simultaneous measurements requiring physical contact to be performed such as conductivity which would otherwise need to be determined independently. These measurements would not be able to interfere with the THz beam or stop air reaching the membrane. In regard to conductivity this means that in plane measurements would be required rather than through plane due to terahertz absorption by conductive materials needed to perform the measurements.
- While this work has focused on PFSA membranes the technique could also be applied to other polymer membranes such as anion exchange membranes or hydrocarbon membranes such as sPEEK.
- With the current system, terahertz data is acquired manually in the software provided and the humidity and motorised stage are controlled separately. Software can be used to capture the terahertz data and control both the humidity and motorised stage. Integrating all control and data acquisition into one software would allow for measurements to be acquired without an operator, allowing overnight measurements and increase the rate of acquiring measurements which have significantly decreased

compared with desorption measurements from a hydrated state in the ambient environment as used previously.

7 References

[1] J. Diab, L. Fulcheri, V. Hessel, V. Rohani, M. Frenklach, Why turquoise hydrogen will Be a game changer for the energy transition, Int J Hydrogen Energy 47 (2022). https://doi.org/10.1016/j.ijhydene.2022.05.299.

[2] P. Bains, S. Bennett, L. Collina, E. Connelly, C. Delmastro, S. Evangelopoulou, M. Fajardy, A. Gouy, M. Kotani, J.-B. Le Marois, P. Levi, R.M. Gordon, S. McDonagh, F. Pavan, A. Pizarro, N. Sloots, C. Winkler, Global Hydrogen Review 2023 – Analysis - IEA, 2023.

[3] M. Shahabuddin, G. Brooks, M.A. Rhamdhani, Decarbonisation and hydrogen integration of steel industries: Recent development, challenges and technoeconomic analysis, J Clean Prod 395 (2023). https://doi.org/10.1016/j.jclepro.2023.136391.

[4] M. Alsunousi, E. Kayabasi, The role of hydrogen in synthetic fuel production strategies, Int J Hydrogen Energy 54 (2024). https://doi.org/10.1016/j.ijhydene.2023.11.359.

[5] M.A. Pellow, C.J.M. Emmott, C.J. Barnhart, S.M. Benson, Hydrogen or batteries for grid storage? A net energy analysis, Energy Environ Sci 8 (2015). https://doi.org/10.1039/c4ee04041d.

[6] Y. Zhang, P.E. Campana, A. Lundblad, J. Yan, Comparative study of hydrogen storage and battery storage in grid connected photovoltaic system: Storage sizing and rule-based operation, Appl Energy 201 (2017). https://doi.org/10.1016/j.apenergy.2017.03.123.

[7] M. Voldsund, A. Reyes-Lúa, C. Fu, M. Ditaranto, P. Nekså, M.J. Mazzetti, O. Brekke, A.U. Bindingsbø, D. Grainger, J. Pettersen, Low carbon power generation for offshore oil and gas production, Energy Conversion and Management: X 17 (2023). https://doi.org/10.1016/j.ecmx.2023.100347.

[8] S. Rehman, L.M. Al-Hadhrami, M.M. Alam, Pumped hydro energy storage system: A technological review, Renewable and Sustainable Energy Reviews 44 (2015). https://doi.org/10.1016/j.rser.2014.12.040.

[9] A. Blakers, M. Stocks, B. Lu, C. Cheng, A review of pumped hydro energy storage, Progress in Energy 3 (2021). https://doi.org/10.1088/2516-1083/abeb5b.

[10] O. Karaduman, Economics of Grid-Scale Energy Storage, 2020.

[11] T.A. Faunce, J. Prest, D. Su, S.J. Hearne, F. Iacopi, On-grid batteries for large-scale energy storage: Challenges and opportunities for policy and technology, MRS Energy and Sustainability 5 (2018). https://doi.org/10.1557/mre.2018.11.

[12] H.S. Hirsh, Y. Li, D.H.S. Tan, M. Zhang, E. Zhao, Y.S. Meng, Sodium-Ion Batteries Paving the Way for Grid Energy Storage, Adv Energy Mater 10 (2020). https://doi.org/10.1002/aenm.202001274.

[13] N. Chawla, M. Safa, Sodium batteries: A review on sodium-sulfur and sodium-air batteries, Electronics (Switzerland) 8 (2019). https://doi.org/10.3390/electronics8101201.

[14] D. Landi, M. Marconi, G. Pietroni, Comparative life cycle assessment of two different battery technologies: Lithium iron phosphate and sodium-sulfur, in: Procedia CIRP, 2022. https://doi.org/10.1016/j.procir.2022.02.080.

[15] A.I. Ikeuba, P.C. Iwuji, I.-I.E. Nabuk, O.E. Obono, D. Charlie, A.A. Etim, B.I. Nwabueze, J. Amajama, Advances on lithium, magnesium, zinc, and iron-air batteries as energy delivery devices—a critical review, Journal of Solid State Electrochemistry 28 (2024) 2999–3025. https://doi.org/10.1007/s10008-024-05866-x.

[16] A.Z. Weber, M.M. Mench, J.P. Meyers, P.N. Ross, J.T. Gostick, Q. Liu, Redox flow batteries: A review, J Appl Electrochem 41 (2011). https://doi.org/10.1007/s10800-011-0348-2.

[17] A. Franco, C. Giovannini, Hydrogen Gas Compression for Efficient Storage: Balancing Energy and Increasing Density, Hydrogen 5 (2024) 293–311. https://doi.org/10.3390/hydrogen5020017.

[18] V.Yu. Plaksin, I.A. Kirillov, Hydrogen flammability and explosion concentration limits for a wide temperature range, J Loss Prev Process Ind 94 (2025) 105554. https://doi.org/10.1016/j.jlp.2025.105554.

[19] N. Armaroli, V. Balzani, The Hydrogen Issue, ChemSusChem 4 (2011) 21–36. https://doi.org/10.1002/cssc.201000182.

[20] J.B. Vorderbrueggen, Imperial sugar refinery combustible dust explosion investigation, Process Safety Progress 30 (2011). https://doi.org/10.1002/prs.10445.

[21] R. Hannah, What are the safest and cleanest sources of energy?, Our World in Data (2020). https://ourworldindata.org/safest-sources-of-energy.

[22] S. Jonathan, Characterization and Science of an Aluminum Fuel Treatment Process, Massachusetts Institute of Technology, 2017.

[23] J. Kurtz, S. Sprik, T.H. Bradley, Review of transportation hydrogen infrastructure performance and reliability, Int J Hydrogen Energy 44 (2019). https://doi.org/10.1016/j.ijhydene.2019.03.027.

[24] Alison Cowley, PGM market report, 2024. https://matthey.com/products-and-markets/pgms-and-circularity/pgm-markets/pgm-market-reports.

[25] L. Osmieri, Q. Meyer, Recent advances in integrating platinum group metal-free catalysts in proton exchange membrane fuel cells, Curr Opin Electrochem 31 (2022). https://doi.org/10.1016/j.coelec.2021.100847.

[26] E. Alonso, F.R. Field, R.E. Kirchain, Platinum availability for future automotive technologies, Environ Sci Technol 46 (2012). https://doi.org/10.1021/es301110e.

[27] M. Simas, F. Aponte, K. Wiebe, The Future is Circular Circular Economy and Critical Minerals for the Green Transition, 2022. https://wwfint.awsassets.panda.org/downloads/the_future_is_circular___sintefminerals finalreport_nov_2022__1__1.pdf.

[28] Y. Sun, M. Delucchi, J. Ogden, The impact of widespread deployment of fuel cell vehicles on platinum demand and price, Int J Hydrogen Energy 36 (2011). https://doi.org/10.1016/j.ijhydene.2011.05.157.

[29] E. Miller, N. Fitzgerald, D. Peterson, N. Stetson, D. Papageorgopoulos, J. Adams, N. Rustagi, J. Stanford, Hydrogen and Fuel Cell Technologies Office Multi-Year Program Plan, 2024. https://www.energy.gov/eere/fuelcells/hydrogen-and-fuel-cell-technologies-office-multi-year-program-plan.

[30] G. HINDS, Performance and Durability of PEM Fuel Cells: A Review, 2004. https://eprintspublications.npl.co.uk/3056/1/DEPC_MPE2.pdf.

[31] G. Kakoulaki, I. Kougias, N. Taylor, F. Dolci, J. Moya, A. Jäger-Waldau, Green hydrogen in Europe – A regional assessment: Substituting existing production with electrolysis powered by renewables, Energy Convers Manag 228 (2021). https://doi.org/10.1016/j.enconman.2020.113649.

[32] F. Spyrakis, T.A. Dragani, The EU's Per- and Polyfluoroalkyl Substances (PFAS) Ban: A Case of Policy over Science, Toxics 11 (2023). https://doi.org/10.3390/toxics11090721.

[33] D.R. Dekel, Review of cell performance in anion exchange membrane fuel cells, J Power Sources 375 (2018). https://doi.org/10.1016/j.jpowsour.2017.07.117.

[34] R.G. Lemus, J.M. Martínez Duart, Updated hydrogen production costs and parities for conventional and renewable technologies, Int J Hydrogen Energy 35 (2010). https://doi.org/10.1016/j.ijhydene.2010.02.034.

[35] W. Schmittinger, A. Vahidi, A review of the main parameters influencing long-term performance and durability of PEM fuel cells, J Power Sources 180 (2008). https://doi.org/10.1016/j.jpowsour.2008.01.070.

[36] J.J. Purcell, New components boost range of microwave systems, Electronics and Power 26 (1980). https://doi.org/10.1049/ep.1980.0006.

[37] X. Li, X. Huang, X. Hu, X. Guo, Y. Han, Recent progress on mid-infrared pulsed fiber lasers and the applications, Opt Laser Technol 158 (2023). https://doi.org/10.1016/j.optlastec.2022.108898.

[38] G. Davies, E. Linfield, Bridging the terahertz gap, Physics World 17 (2004). https://doi.org/10.1088/2058-7058/17/4/34.

[39] A. Redo-Sanchez, N. Laman, B. Schulkin, T. Tongue, Review of terahertz technology readiness assessment and applications, J Infrared Millim Terahertz Waves 34 (2013). https://doi.org/10.1007/s10762-013-9998-y.

[40] Office of Energy Efficiency and Renewable Energy, Comparison of Fuel Cell Technologies | Department of Energy, Hydrogen and Fuel Cell Technologies Office (2021). https://www.energy.gov/eere/fuelcells/comparison-fuel-cell-technologies.

[41] K. Yassin, I.G. Rasin, S. Willdorf-Cohen, C.E. Diesendruck, S. Brandon, D.R. Dekel, A surprising relation between operating temperature and stability of anion exchange membrane fuel cells, Journal of Power Sources Advances 11 (2021). https://doi.org/10.1016/j.powera.2021.100066.

[42] J.H. Wee, Applications of proton exchange membrane fuel cell systems, Renewable and Sustainable Energy Reviews (2007). https://doi.org/10.1016/j.rser.2006.01.005.

[43] U.S. Selamoğullari, T.R. Willemain, D.A. Torrey, A systems approach for sizing a stand-alone residential PEMFC power system, J Power Sources 171 (2007). https://doi.org/10.1016/j.jpowsour.2007.06.024.

[44] M. Aysla Costa De Oliveira, A. D'Epifanio, H. Ohnuki, B. Mecheri, Platinum group metal-free catalysts for oxygen reduction reaction: Applications in microbial fuel cells, Catalysts 10 (2020). https://doi.org/10.3390/catal10050475.

[45] S. Zaman, L. Huang, A.I. Douka, H. Yang, B. You, B.Y. Xia, Oxygen Reduction Electrocatalysts toward Practical Fuel Cells: Progress and Perspectives, Angewandte Chemie - International Edition 60 (2021). https://doi.org/10.1002/anie.202016977.

[46] Y.-H. Lai, Shorting in Polymer Electrolyte Fuel Cells: Aspects of Material Testing and Operating Conditions, ECS Meeting Abstracts MA2016-02 (2016). https://doi.org/10.1149/ma2016-02/38/2456.

[47] M. Inaba, T. Kinumoto, M. Kiriake, R. Umebayashi, A. Tasaka, Z. Ogumi, Gas crossover and membrane degradation in polymer electrolyte fuel cells, Electrochim Acta 51 (2006). https://doi.org/10.1016/j.electacta.2006.03.008.

[48] R. Sgarbi, W. Ait Idir, Q. Labarde, M. Mermoux, P. Wu, J. Mainka, J. Dillet, C. Marty, F. Micoud, O. Lottin, M. Chatenet, Does the platinum-loading in proton-exchange membrane fuel cell cathodes influence the durability of the membrane-electrode assembly?, Industrial Chemistry & Materials 1 (2023). https://doi.org/10.1039/d3im00059a.

[49] P. Schneider, M. Batool, A.O. Godoy, R. Singh, D. Gerteisen, J. Jankovic, N. Zamel, Impact of Platinum Loading and Layer Thickness on Cathode Catalyst Degradation in PEM Fuel Cells, J Electrochem Soc 170 (2023). https://doi.org/10.1149/1945-7111/acb8df.

[50] A. Kongkanand, M.F. Mathias, The Priority and Challenge of High-Power Performance of Low-Platinum Proton-Exchange Membrane Fuel Cells, Journal of Physical Chemistry Letters 7 (2016). https://doi.org/10.1021/acs.jpclett.6b00216.

[51] Y.X. Xiao, J. Ying, H.W. Liu, X.Y. Yang, Pt–C interactions in carbon-supported Pt-based electrocatalysts, Front Chem Sci Eng 17 (2023). https://doi.org/10.1007/s11705-023-2300-5.

[52] M.A. Uddin, A.I. Rais, Platinum group metal-free catalysts for fuel cells: status and prospects, in: Fuel Cells for Transportation: Fundamental Principles and Applications, 2023. https://doi.org/10.1016/B978-0-323-99485-9.00007-1.

[53] V.K. Mathur, J. Crawford, Fundamentals of gas diffusion layers in PEM fuel cells, in: Recent Trends in Fuel Cell Science and Technology, 2007. https://doi.org/10.1007/978-0-387-68815-2_4.

[54] L. Xia, M. Ni, Q. He, Q. Xu, C. Cheng, Optimization of gas diffusion layer in high temperature PEMFC with the focuses on thickness and porosity, Appl Energy 300 (2021). https://doi.org/10.1016/j.apenergy.2021.117357.

[55] W. Zhang, F. Guo, Y. Zhou, S. Yu, A. Chen, H. Jiang, H. Jiang, C. Li, Gas Diffusion Layer with a Regular Hydrophilic Structure Boosts the Power Density of Proton Exchange Membrane Fuel Cells via the Construction of Water Highways, ACS Appl Mater Interfaces 14 (2022). https://doi.org/10.1021/acsami.2c03388.

[56] S. Park, J.W. Lee, B.N. Popov, A review of gas diffusion layer in PEM fuel cells: Materials and designs, Int J Hydrogen Energy 37 (2012). https://doi.org/10.1016/j.ijhydene.2011.12.148.

[57] X. Li, Bipolar plates and flow field design, in: Fuel Cells for Transportation: Fundamental Principles and Applications, 2023. https://doi.org/10.1016/B978-0-323-99485-9.00003-4.

[58] C.T.A. Sarjuni, A.A.D. Shahril, H.C. Low, B.H. Lim, Bipolar Plate Design Assessment: Proton Exchange Membrane Fuel Cell and Water Electrolyzer, Fuel Cells 24 (2024). https://doi.org/10.1002/fuce.202300196.

[59] S. Zhang, H. Xu, Z. Qu, S. Liu, F.K. Talkhoncheh, Bio-inspired flow channel designs for proton exchange membrane fuel cells: A review, J Power Sources 522 (2022). https://doi.org/10.1016/j.jpowsour.2022.231003.

[60] T. Wilberforce, A.G. Olabi, D. Monopoli, M. Dassisti, E.T. Sayed, M.A. Abdelkareem, Design optimization of proton exchange membrane fuel cell bipolar plate, Energy Convers Manag 277 (2023). https://doi.org/10.1016/j.enconman.2022.116586.

[61] B. Abderezzak, Introduction to Hydrogen Technology, in: Introduction to Transfer Phenomena in PEM Fuel Cell, 2018. https://doi.org/10.1016/b978-1-78548-291-5.50001-9.

[62] J. Wang, H. Wang, Flow-field designs of bipolar plates in PEM fuel cells: Theory and applications, Fuel Cells 12 (2012). https://doi.org/10.1002/fuce.201200074.

[63] T. Wilberforce, A. Amiri, Comparative study on bipolar plate geometry designs on the performance of proton exchange membrane fuel cells, Fuel 346 (2023). https://doi.org/10.1016/j.fuel.2023.128389.

[64] F. Barbir, Chapter Six - Stack Design, in: PEM Fuel Cells (Second Edition), Academic Press, 2013. https://doi.org/10.1016/B978-0-12-387710-9.00006-0.

[65] L. Vichard, N.Y. Steiner, N. Zerhouni, D. Hissel, Hybrid fuel cell system degradation modeling methods: A comprehensive review, J Power Sources 506 (2021). https://doi.org/10.1016/j.jpowsour.2021.230071.

[66] C. Hochgraf, Applications - Transportation | Electric Vehicles: Fuel Cells, in: Encyclopedia of Electrochemical Power Sources, 2009. https://doi.org/10.1016/B978-044452745-5.00863-7.

[67] J.J. Giner-Sanz, E.M. Ortega, V. Pérez-Herranz, Hydrogen crossover and internal short-circuit currents experimental characterization and modelling in a proton exchange membrane fuel cell, in: Int J Hydrogen Energy, 2014. https://doi.org/10.1016/j.ijhydene.2014.06.157.

[68] Z. Kang, M. Pak, G. Bender, Introducing a novel technique for measuring hydrogen crossover in membrane-based electrochemical cells, Int J Hydrogen Energy (2021). https://doi.org/10.1016/j.ijhydene.2021.02.054.

[69] F. Ding, X. Zhan, T. Wei, J. Sun, H. Huang, Y. Cui, Z. Shao, Similarities and differences between internal short-circuit current and hydrogen crossover current in a proton exchange membrane fuel cell, Chemical Engineering Journal 494 (2024) 153091. https://doi.org/10.1016/j.cej.2024.153091.

[70] F. Mazzeo, L. Di Napoli, M. Carello, Assessing Open Circuit Voltage Losses in PEMFCs: A New Methodological Approach, Energies (Basel) 17 (2024) 2785. https://doi.org/10.3390/en17112785.

[71] L. Khotseng, Oxygen Reduction Reaction, in: Electrocatalysts for Fuel Cells and Hydrogen Evolution - Theory to Design, IntechOpen, 2018. https://doi.org/10.5772/intechopen.79098.

[72] H. Abdi, R. Rasouli Nezhad, M. Salehimaleh, Chapter 5 - Fuel cells, in: Distributed Generation Systems: Design, Operation and Grid Integration, Butterworth-Heinemann, 2017. https://doi.org/10.1016/B978-0-12-804208-3.00005-4.

[73] T. Mennola, M. Mikkola, M. Noponen, T. Hottinen, P. Lund, Measurement of ohmic voltage losses in individual cells of a PEMFC stack, J Power Sources 112 (2002). https://doi.org/10.1016/S0378-7753(02)00391-9.

[74] K. Priya, K. Sathishkumar, N. Rajasekar, A comprehensive review on parameter estimation techniques for Proton Exchange Membrane fuel cell modelling, Renewable and Sustainable Energy Reviews 93 (2018). https://doi.org/10.1016/j.rser.2018.05.017.

[75] U. Mitra, A. Arya, S. Gupta, A comprehensive and comparative review on parameter estimation methods for modelling proton exchange membrane fuel cell, Fuel 335 (2023). https://doi.org/10.1016/j.fuel.2022.127080.

[76] R.P. O'Hayre, S.-W. Cha, W.G. Colella, F.B. Prinz, Fuel cell fundamentals , Fuel Cell Fundamentals (2016). https://app.knovel.com/hotlink/toc/id:kpFCFE0004/fuel-cell-fundamentals/fuel-cell-fundamentals.

[77] S. Wang, Y. Liang, D. Li, Z. Zhang, J. Zhang, Analysis and proposition of limiting current density measurement protocol, Int J Hydrogen Energy 47 (2022). https://doi.org/10.1016/j.ijhydene.2022.05.144.

[78] J. Marcinkoski, R. Vijayagopal, J. Adams, B. James, J. Kopasz, R. Ahluwalia, Hydrogen Class 8 Long Haul Truck Targets. Subsection of the Electrified Powertrain Roadmap. Technical Targets for Hydrogen-Fueled Long-Haul Tractor-Trailer Trucks, 2019. https://www.hydrogen.energy.gov/docs/hydrogenprogramlibraries/pdfs/19006_hydrogen_class8_long_haul_truck_targets.pdf?Status=Master.

[79] Z. Hua, Z. Zheng, E. Pahon, M.C. Péra, F. Gao, A review on lifetime prediction of proton exchange membrane fuel cells system, J Power Sources 529 (2022). https://doi.org/10.1016/j.jpowsour.2022.231256.

[80] E. Wallnöfer-Ogris, F. Poimer, R. Köll, M.G. Macherhammer, A. Trattner, Main degradation mechanisms of polymer electrolyte membrane fuel cell stacks – Mechanisms, influencing factors, consequences, and mitigation strategies, Int J Hydrogen Energy 50 (2024). https://doi.org/10.1016/j.ijhydene.2023.06.215.

[81] L.W. McKeen, Polyolefins, Polyvinyls, and Acrylics, in: Permeability Properties of Plastics and Elastomers, 2017. https://doi.org/10.1016/b978-0-323-50859-9.00009-9.

[82] M. Martín, X. Centelles, A. Solé, C. Barreneche, A.I. Fernández, L.F. Cabeza, Polymeric interlayer materials for laminated glass: A review, Constr Build Mater 230 (2020). https://doi.org/10.1016/j.conbuildmat.2019.116897.

[83] W. Mabrouk, L. Ogier, S. Vidal, C. Sollogoub, F. Matoussi, J.F. Fauvarque, Ion exchange membranes based upon crosslinked sulfonated polyethersulfone for electrochemical applications, J Memb Sci 452 (2014). https://doi.org/10.1016/j.memsci.2013.10.006.

[84] E.B. Çelebi, F. Hacıvelioğlu, Improving the mechanical and methanol crossover properties of fluorinated sulfonic acid functional polyphosphazenes by blending with polyvinylidene difluoride for fuel cell applications, Polymer (Guildf) 255 (2022). https://doi.org/10.1016/j.polymer.2022.125175.

[85] J.S. Park, M.S. Shin, C.S. Kim, Proton exchange membranes for fuel cell operation at low relative humidity and intermediate temperature: An updated review, Curr Opin Electrochem 5 (2017). https://doi.org/10.1016/j.coelec.2017.10.020.

[86] A. Kusoglu, A.Z. Weber, New Insights into Perfluorinated Sulfonic-Acid Ionomers, Chem Rev 117 (2017) 987–1104. https://doi.org/10.1021/acs.chemrev.6b00159.

[87] V. Mehta, J.S. Cooper, Review and analysis of PEM fuel cell design and manufacturing, J Power Sources 114 (2003). https://doi.org/10.1016/S0378-7753(02)00542-6.

[88] H. Kahraman, Y. Akın, Recent studies on proton exchange membrane fuel cell components, review of the literature, Energy Convers Manag 304 (2024). https://doi.org/10.1016/j.enconman.2024.118244.

[89] T. Jahnke, G. Futter, A. Latz, T. Malkow, G. Papakonstantinou, G. Tsotridis, P. Schott, M. Gérard, M. Quinaud, M. Quiroga, A.A. Franco, K. Malek, F. Calle-Vallejo, R. Ferreira De Morais, T. Kerber, P. Sautet, D. Loffreda, S. Strahl, M. Serra, P. Polverino, C. Pianese, M. Mayur, W.G. Bessler, C. Kompis, Performance and degradation of Proton Exchange Membrane Fuel Cells: State of the art in modeling from atomistic to system scale, J Power Sources 304 (2016). https://doi.org/10.1016/j.jpowsour.2015.11.041.

[90] T. Ishimoto, T. Ogura, M. Koyama, Theoretical Study on Chemical Degradation Mechanism of Nafion Side Chain by the Attack of OH Radical in Polymer Electrolyte Fuel Cell, ECS Trans 35 (2011). https://doi.org/10.1149/1.3643346.

[91] J.M. Fenton, M.P. Rodgers, D.K. Slattery, X. Huang, L. Bonville, H.R. Kunz, Membrane Degradation Mechanisms and Accelerated Durability Testing of Proton Exchange Membrane Fuel Cells, ECS Meeting Abstracts MA2009-02 (2009). https://doi.org/10.1149/ma2009-02/10/812.

[92] T. Ishimoto, R. Nagumo, T. Ogura, T. Ishihara, B. Kim, A. Miyamoto, M. Koyama, Chemical Degradation Mechanism of Model Compound, CF[sub 3](CF[sub 2])[sub 3]O(CF[sub 2])[sub 2]OCF[sub 2]SO[sub 3]H, of PFSA Polymer by Attack of Hydroxyl Radical in PEMFCs, J Electrochem Soc 157 (2010). https://doi.org/10.1149/1.3462970.

[93] C. Chen, T.F. Fuller, The effect of humidity on the degradation of Nafion® membrane, Polym Degrad Stab 94 (2009). https://doi.org/10.1016/j.polymdegradstab.2009.05.016.

[94] M. Yamaguchi, DFT Study on Side Chain Detachment of Perfluorosulfonic Acid Ionomers by Radical-Assisted Nucleophilic Attack of Water, Polym Degrad Stab 196 (2022). https://doi.org/10.1016/j.polymdegradstab.2022.109832.

[95] L. Merlo, A. Ghielmi, V. Arcella, Fuel Cells - Proton-Exchange Membrane Fuel Cells | Membranes: Advanced Fluorinated, in: Encyclopedia of Electrochemical Power Sources, 2009. https://doi.org/10.1016/B978-044452745-5.00930-8.

[96] E.Y. Safronova, A.K. Osipov, A.B. Yaroslavtsev, Short Side Chain Aquivion Perfluorinated Sulfonated Proton-Conductive Membranes: Transport and Mechanical Properties, Petroleum Chemistry 58 (2018). https://doi.org/10.1134/S0965544118020044.

[97] S.H. Kwon, H. Kang, Y.J. Sohn, J. Lee, S. Shim, S.G. Lee, Molecular dynamics simulation study on the effect of perfluorosulfonic acid side chains on oxygen permeation in hydrated ionomers of PEMFCs, Sci Rep 11 (2021). https://doi.org/10.1038/s41598-021-87570-8.

[98] S.Y. Choi, M.M. Ikhsan, K.S. Jin, D. Henkensmeier, Nanostructure-property relationship of two perfluorinated sulfonic acid (PFSA) membranes, Int J Energy Res 46 (2022). https://doi.org/10.1002/er.7926.

[99] S.H. Shin, P.J. Nur, A. Kodir, D.H. Kwak, H. Lee, D. Shin, B. Bae, Improving the Mechanical Durability of Short-Side-Chain Perfluorinated Polymer Electrolyte Membranes by Annealing and Physical Reinforcement, ACS Omega (2019). https://doi.org/10.1021/acsomega.9b02436.

[100] L. Ghassemzadeh, K.D. Kreuer, J. Maier, K. Müller, Evaluating chemical degradation of proton conducting perfluorosulfonic acid ionomers in a Fenton test by solid-state 19F NMR spectroscopy, J Power Sources 196 (2011). https://doi.org/10.1016/j.jpowsour.2010.11.053.

[101] D. Wu, S.J. Paddison, J.A. Elliott, A comparative study of the hydrated morphologies of perfluorosulfonic acid fuel cell membranes with mesoscopic simulations, Energy Environ Sci 1 (2008). https://doi.org/10.1039/b809600g.

[102] R. Devanathan, M. Dupuis, Insight from molecular modelling: Does the polymer side chain length matter for transport properties of perfluorosulfonic acid membranes?, Physical Chemistry Chemical Physics 14 (2012). https://doi.org/10.1039/c2cp24132c.

[103] S. Cui, J. Liu, M.E. Selvan, S.J. Paddison, D.J. Keffer, B.J. Edwards, Comparison of the hydration and diffusion of protons in perfluorosulfonic acid membranes with molecular dynamics simulations, Journal of Physical Chemistry B 112 (2008). https://doi.org/10.1021/jp8039803.

[104] J. Karo, A. Aabloo, J.O. Thomas, D. Brandell, Molecular dynamics modeling of proton transport in nafion and hyflon nanostructures, Journal of Physical Chemistry B 114 (2010). https://doi.org/10.1021/jp903288y.

[105] W.Y. Hsu, T.D. Gierke, Ion transport and clustering in nafion perfluorinated membranes, J Memb Sci 13 (1983). https://doi.org/10.1016/S0376-7388(00)81563-X.

[106] T.D. Gierke, G.E. Munn, F.C. Wilson, MORPHOLOGY IN NAFION PERFLUORINATED MEMBRANE PRODUCTS, AS DETERMINED BY WIDE- AND SMALL-ANGLE X-RAY STUDIES., Journal of Polymer Science. Part A-2, Polymer Physics 19 (1981). https://doi.org/10.1002/pol.1981.180191103.

[107] D. Wu, S.J. Paddison, J.A. Elliott, S.J. Hamrock, Mesoscale modeling of hydrated morphologies of 3m perfluorosulfonic acid-based fuel cell electrolytes, Langmuir 26 (2010). https://doi.org/10.1021/la102358y.

[108] D. Wu, S.J. Paddison, J.A. Elliott, Effect of molecular weight on hydrated morphologies of the short-side-chain perfluorosulfonic acid membrane, Macromolecules 42 (2009). https://doi.org/10.1021/ma900016w.

[109] Y. Xing, H. Li, G. Avgouropoulos, Research progress of proton exchange membrane failure and mitigation strategies, Materials 14 (2021). https://doi.org/10.3390/ma14102591.

[110] A. Sadeghi Alavijeh, S. Bhattacharya, O. Thomas, C. Chuy, Y. Yang, H. Zhang, E. Kjeang, Effect of hygral swelling and shrinkage on mechanical durability of fuel cell membranes, J Power Sources 427 (2019). https://doi.org/10.1016/j.jpowsour.2019.04.081.

[111] S. Shi, A.Z. Weber, A. Kusoglu, Structure/property relationship of Nafion XL composite membranes, J Memb Sci 516 (2016). https://doi.org/10.1016/j.memsci.2016.06.004.

[112] A. Selim, G.P. Szijjártó, A. Tompos, Insights into the Influence of Different Pre-Treatments on Physicochemical Properties of Nafion XL Membrane and Fuel Cell Performance, Polymers (Basel) 14 (2022). https://doi.org/10.3390/polym14163385.

[113] Z. Lu, M. Lugo, M.H. Santare, A.M. Karlsson, F.C. Busby, P. Walsh, An experimental investigation of strain rate, temperature and humidity effects on the mechanical behavior of a perfluorosulfonic acid membrane, J Power Sources 214 (2012). https://doi.org/10.1016/j.jpowsour.2012.04.094.

[114] A. Kusoglu, Y. Tang, M. Lugo, A.M. Karlsson, M.H. Santare, S. Cleghorn, W.B. Johnson, Constitutive response and mechanical properties of PFSA membranes in liquid water, J Power Sources 195 (2010). https://doi.org/10.1016/j.jpowsour.2009.08.010.

[115] A.S. Rao, K.R. Rashmi, D. V. Manjunatha, A. Jayarama, S. Prabhu, R. Pinto, Pore size tuning of Nafion membranes by UV irradiation for enhanced proton conductivity for fuel cell applications, Int J Hydrogen Energy 44 (2019). https://doi.org/10.1016/j.ijhydene.2019.07.084.

[116] X. Xu, L. Li, H. Wang, X. Li, X. Zhuang, Solution blown sulfonated poly(ether ether ketone) nanofiber-Nafion composite membranes for proton exchange membrane fuel cells, RSC Adv 5 (2015). https://doi.org/10.1039/c4ra10898a.

[117] G. Li, C. Zhao, X. Li, D. Qi, C. Liu, F. Bu, H. Na, Novel side-chain-type sulfonated diphenyl-based poly(arylene ether sulfone)s with a hydrogen-bonded network as proton exchange membranes, Polym Chem 6 (2015). https://doi.org/10.1039/c5py00700c.

[118] Y.S. Sedesheva, V.S. Ivanov, A.I. Wozniak, A.S. Yegorov, Proton-exchange membranes based on sulfonated polymers, Oriental Journal of Chemistry 32 (2016). https://doi.org/10.13005/ojc/320501.

[119] B. Jiang, L. Yu, L. Wu, D. Mu, L. Liu, J. Xi, X. Qiu, Insights into the Impact of the Nafion Membrane Pretreatment Process on Vanadium Flow Battery Performance, ACS Appl Mater Interfaces 8 (2016). https://doi.org/10.1021/acsami.6b03529.

[120] M. Helen, B. Viswanathan, S. Srinivasa Murthy, Poly(vinyl alcohol)-polyacrylamide blends with cesium salts of heteropolyacid as a polymer electrolyte for direct methanol fuel cell applications, J Appl Polym Sci 116 (2010). https://doi.org/10.1002/app.31940.

[121] S. Das, K. Dutta, S. Hazra, P.P. Kundu, Partially Sulfonated Poly(vinylidene fluoride) Induced Enhancements of Properties and DMFC Performance of Nafion Electrolyte Membrane, Fuel Cells 15 (2015). https://doi.org/10.1002/fuce.201500018.

[122] R. Devanathan, N. Idupulapati, M.D. Baer, C.J. Mundy, M. Dupuis, Ab initio molecular dynamics simulation of proton hopping in a model polymer membrane, Journal of Physical Chemistry B 117 (2013). https://doi.org/10.1021/jp410229u.

[123] A.M.I. Trefilov, A. Balan, I. Stamatin, Hybrid proton-exchange membrane based on perfluorosulfonated polymers and resorcinol– formaldehyde hydrogel, Polymers (Basel) 13 (2021). https://doi.org/10.3390/polym13234123.

[124] T. Shimoaka, C. Wakai, T. Sakabe, S. Yamazaki, T. Hasegawa, Hydration structure of strongly bound water on the sulfonic acid group in a Nafion membrane studied by infrared spectroscopy and quantum chemical calculation, Physical Chemistry Chemical Physics 17 (2015). https://doi.org/10.1039/c5cp00567a.

[125] R. Devanathan, A. Venkatnathan, R. Rousseau, M. Dupuis, T. Frigato, W. Gu, V. Helms, Atomistic simulation of water percolation and proton hopping in Nafion fuel cell membrane, Journal of Physical Chemistry B 114 (2010). https://doi.org/10.1021/jp103398b.

[126] A. Luzar, D. Chandler, Effect of environment on hydrogen bond dynamics in liquid water, Phys Rev Lett 76 (1996). https://doi.org/10.1103/PhysRevLett.76.928.

[127] F.W. Starr, ohannes K. Nielsen, H.E. Stanley, Fast and slow dynamics of hydrogen bonds in liquid water, Phys Rev Lett 82 (1999). https://doi.org/10.1103/PhysRevLett.82.2294.

[128] T. by Cecilie Rønne, Intermolecular Liquid Dynamics Studied by THz-Spectroscopy, Aarhus University, 2000.

[129] T. Berning, On the nature of electro-osmotic drag, Energies (Basel) 13 (2020). https://doi.org/10.3390/en13184726.

[130] A. Kusoglu, A.Z. Weber, Water transport and sorption in nafion membrane, in: ACS Symposium Series, 2012. https://doi.org/10.1021/bk-2012-1096.ch011.

[131] D.J. Burnett, A.R. Garcia, F. Thielmann, Measuring moisture sorption and diffusion kinetics on proton exchange membranes using a gravimetric vapor sorption apparatus, J Power Sources 160 (2006). https://doi.org/10.1016/j.jpowsour.2005.12.096.

[132] M. Legras, Y. Hirata, Q.T. Nguyen, D. Langevin, M. Métayer, Sorption and diffusion behaviors of water in Nafion 117 membranes with different counter ions, Desalination 147 (2002). https://doi.org/10.1016/S0011-9164(02)00608-2.

[133] K.S. Han, J.D. Bazak, Y. Chen, T.R. Graham, N.M. Washton, J.Z. Hu, V. Murugesan, K.T. Mueller, Pulsed Field Gradient Nuclear Magnetic Resonance and Diffusion Analysis in Battery Research, Chemistry of Materials 33 (2021). https://doi.org/10.1021/acs.chemmater.1c02891.

[134] K. Kidena, T. Ohkubo, N. Takimoto, A. Ohira, PFG-NMR approach to determining the water transport mechanism in polymer electrolyte membranes conditioned at different temperatures, Eur Polym J 46 (2010). https://doi.org/10.1016/j.eurpolymj.2009.12.012.

[135] Z. Ma, R. Jiang, M.E. Myers, E.L. Thompson, C.S. Gittleman, NMR studies of proton transport in fuel cell membranes at sub-freezing conditions, J Mater Chem (2011). https://doi.org/10.1039/c1jm10097a.

[136] Q. Zhao, P. Majsztrik, J. Benziger, Diffusion and interfacial transport of water in Nafion, Journal of Physical Chemistry B (2011). https://doi.org/10.1021/jp1112125.

[137] J.C. Perrin, S. Lyonnard, F. Volino, Quasielastic Neutron Scattering Study of Water Dynamics in Hydrated Nafion Membranes, Journal of Physical Chemistry C 111 (2007) 3393–3404. https://doi.org/10.1021/JP065039Q.

[138] A.M. Pivovar, B.S. Pivovar, Dynamic behavior of water within a polymer electrolyte fuel cell membrane at low hydration levels, Journal of Physical Chemistry B 109 (2005). https://doi.org/10.1021/jp046029x.

[139] H. Nishiyama, A. Iiyama, J. Inukai, The distribution and diffusion coefficient of water inside a Nafion® membrane in a running fuel cell under transient conditions analyzed by operando time-resolved CARS spectroscopy, Journal of Power Sources Advances 13 (2022). https://doi.org/10.1016/j.powera.2021.100080.

[140] T.F. Fuller, Solid-polymer-electrolyte fuel cells, Lawrence Berkeley National Laboratory (LBNL), 1992. https://doi.org/10.2172/7001224.

[141] S. Tsushima, K. Teranishi, S. Hirai, Water diffusion measurement in fuel-cell SPE membrane by NMR, in: Energy, 2005. https://doi.org/10.1016/j.energy.2004.04.013.

[142] M.B. Satterfleld, J.B. Benziger, Non-Fickian water vapor sorption dynamics by nafion membranes, Journal of Physical Chemistry B 112 (2008). https://doi.org/10.1021/jp7103243.

[143] A.L. Rangel-Cárdenas, S.J. Picken, G.J.M. Koper, Anomalous water sorption kinetics in supported Nafion thin-films as membrane-electrode assemblies, J Memb Sci 650 (2022). https://doi.org/10.1016/j.memsci.2022.120368.

[144] P.W. Majsztrik, M.B. Satterfield, A.B. Bocarsly, J.B. Benziger, Water sorption, desorption and transport in Nafion membranes, J Memb Sci 301 (2007) 93–106. https://doi.org/10.1016/j.memsci.2007.06.022.

[145] D. Rivin, C.E. Kendrick, P.W. Gibson, N.S. Schneider, Solubility and transport behavior of water and alcohols in Nafion™, Polymer (Guildf) 42 (2001). https://doi.org/10.1016/S0032-3861(00)00350-5.

[146] J. Crank, The mathematics of diffusion, Second Edition, Oxford University Press (1975).

[147] L. Onishi, Equilibrium and transport properties of a proton-exchange membrane for fuel cells, PhD dissertation, University of California, 2009.

[148] T.E. Springer, T.A. Zawodzinski, S. Gottesfeld, Polymer Electrolyte Fuel Cell Model, J Electrochem Soc 138 (1991). https://doi.org/10.1149/1.2085971.

[149] X. Ye, M.D. LeVan, Water transport properties of Nafion membranes: Part I. Single-tube membrane module for air drying, J Memb Sci 221 (2003). https://doi.org/10.1016/S0376-7388(03)00255-2.

[150] S. Ge, X. Li, B. Yi, I.-M. Hsing, Absorption, Desorption, and Transport of Water in Polymer Electrolyte Membranes for Fuel Cells, J Electrochem Soc 152 (2005). https://doi.org/10.1149/1.1899263.

[151] H.R. Zelsmann, M. Pineri, M. Thomas, M. Escoubes, Water self-diffusion coefficient determination in an ion exchange membrane by optical measurement, J Appl Polym Sci 41 (1990). https://doi.org/10.1002/app.1990.070410726.

[152] D.R. Morris, X. Sun, Water-sorption and transport properties of Nafion 117 H, J Appl Polym Sci 50 (1993). https://doi.org/10.1002/app.1993.070500816.

[153] C.A. Edmondson, J.J. Fontanella, Free volume and percolation in S-SEBS and fluorocarbon proton conducting membranes, in: Solid State Ion, 2002. https://doi.org/10.1016/S0167-2738(02)00336-3.

[154] T.A. Zawodzinski, C. Derouin, S. Radzinski, R.J. Sherman, V.T. Smith, T.E. Springer, S. Gottesfeld, Water Uptake by and Transport Through Nafion® 117 Membranes, J Electrochem Soc 140 (1993). https://doi.org/10.1149/1.2056194.

[155] S. Ochi, O. Kamishima, J. Mizusaki, J. Kawamura, Investigation of proton diffusion in Nafion®117 membrane by electrical conductivity and NMR, Solid State Ion 180 (2009). https://doi.org/10.1016/j.ssi.2008.12.035.

[156] X. Gong, A. Bandis, A. Tao, G. Meresi, Y. Wang, P.T. Inglefield, A.A. Jones, W.Y. Wen, Self-diffusion of water, ethanol and decafluropentane in perfluorosulfonate ionomer by pulse field gradient NMR, Polymer (Guildf) 42 (2001). https://doi.org/10.1016/S0032-3861(01)00119-7.

[157] S. Engelbrecht, V. Pichot, T. Goepfert, H. Lin, B.M. Fischer, Extraction of Fickian water diffusion in polymers using terahertz time-domain spectroscopy, Polymer (Guildf) 257 (2022). https://doi.org/10.1016/j.polymer.2022.125285.

[158] K.D. Kreuer, M. Schuster, B. Obliers, O. Diat, U. Traub, A. Fuchs, U. Klock, S.J. Paddison, J. Maier, Short-side-chain proton conducting perfluorosulfonic acid ionomers: Why they perform better in PEM fuel cells, J Power Sources 178 (2008). https://doi.org/10.1016/j.jpowsour.2007.11.011.

[159] J. Wang, M. Yang, P. Dou, X. Wang, H. Zhang, Influences of annealing on the perfluorosulfonate ion-exchanged membranes prepared by melt extrusion, Ind Eng Chem Res 53 (2014). https://doi.org/10.1021/ie502037p.

[160] S. Shi, T.J. Dursch, C. Blake, R. Mukundan, R.L. Borup, A.Z. Weber, A. Kusoglu, Impact of hygrothermal aging on structure/function relationship of perfluorosulfonic-acid membrane, J Polym Sci B Polym Phys 54 (2016). https://doi.org/10.1002/polb.23946.

[161] A. Kusoglu, S. Savagatrup, K.T. Clark, A.Z. Weber, Role of Mechanical Factors in Controlling the Structure–Function Relationship of PFSA Ionomers, Macromolecules 45 (2012) 7467–7476. https://doi.org/10.1021/MA301419S.

[162] L. Maldonado, J.C. Perrin, J. Dillet, O. Lottin, Characterization of polymer electrolyte Nafion membranes: Influence of temperature, heat treatment and drying protocol on sorption and transport properties, J Memb Sci 389 (2012) 43–56. https://doi.org/10.1016/J.MEMSCI.2011.10.014.

[163] R. Narducci, P. Knauth, J.F. Chailan, M.L. Di Vona, How to improve Nafion with tailor made annealing, RSC Adv 8 (2018). https://doi.org/10.1039/c8ra04808h.

[164] O. Kwon, S. Wu, D.M. Zhu, Configuration changes of conducting channel network in nafion membranes due to thermal annealing, Journal of Physical Chemistry B 114 (2010). https://doi.org/10.1021/jp108163a.

[165] N.J. Economou, J.R. O'Dea, T.B. McConnaughy, S.K. Buratto, Morphological differences in short side chain and long side chain perfluorosulfonic acid proton exchange membranes at low and high water contents, RSC Adv 3 (2013). https://doi.org/10.1039/c3ra41976b.

[166] K. Feng, L. Hou, B. Tang, P. Wu, Does thermal treatment merely make a H2O-saturated Nafion membrane lose its absorbed water at high temperature?, Physical Chemistry Chemical Physics 17 (2015). https://doi.org/10.1039/c5cp00203f.

[167] G. Gebel, P. Aldebert, M. Pineri, Structure and Related Properties of Solution-Cast Perfluorosulfonated Ionomer Films, Macromolecules 20 (1987). https://doi.org/10.1021/ma00172a049.

[168] T. Takamatsu, A. Eisenberg, Densities and expansion coefficients of nafion polymers, J Appl Polym Sci 24 (1979). https://doi.org/10.1002/app.1979.070241102.

[169] C.E. Evans, R.D. Noble, S. Nazeri-Thompson, B. Nazeri, C.A. Koval, Role of conditioning on water uptake and hydraulic permeability of Nafion® membranes, J Memb Sci 279 (2006). https://doi.org/10.1016/j.memsci.2005.12.046.

[170] Y. Luan, Y. Zhang, H. Zhang, L. Li, H. Li, Y. Liu, Annealing effect of perfluorosulfonated ionomer membranes on proton conductivity and methanol permeability, J Appl Polym Sci 107 (2008). https://doi.org/10.1002/app.27070.

[171] S. Mbarek, N. El Kissi, Z. Baccouch, C. Iojoiu, Extrusion of Nafion and Aquivion membranes: environmentally friendly procedure and good conductivities, Polymer Bulletin 76 (2019). https://doi.org/10.1007/s00289-018-2427-6.

[172] S. Siracusano, C. Oldani, M.A. Navarra, S. Tonella, L. Mazzapioda, N. Briguglio, A.S. Aricò, Chemically stabilised extruded and recast short side chain Aquivion® proton exchange membranes for high current density operation in water electrolysis, J Memb Sci 578 (2019). https://doi.org/10.1016/j.memsci.2019.02.021.

[173] Y.S. Kim, C.F. Welch, R.P. Hjelm, N.H. Mack, A. Labouriau, E.B. Orler, Origin of toughness in dispersion-cast Nafion membranes, Macromolecules 48 (2015). https://doi.org/10.1021/ma502538k.

[174] Z. Wang, H. Tang, J. Li, Y. Zeng, L. Chen, M. Pan, Insight into the structural construction of a perfluorosulfonic acid membrane derived from a polymeric dispersion, J Power Sources 256 (2014). https://doi.org/10.1016/j.jpowsour.2014.01.096.

[175] D.C. Seo, I. Jeon, E.S. Jeong, J.Y. Jho, Mechanical properties and chemical durability of nafion/sulfonated graphene oxide/cerium oxide composite membranes for fuel-cell applications, Polymers (Basel) 12 (2020). https://doi.org/10.3390/POLYM12061375.

[176] P.L. Antonucci, A.S. Aricò, P. Cretì, E. Ramunni, V. Antonucci, Investigation of a direct methanol fuel cell based on a composite Nafion-silica electrolyte for high temperature operation, Solid State Ion (1999). https://doi.org/10.1016/S0167-2738(99)00206-4.

[177] V. Baglio, A. di Blasi, A.S. Aricò, V. Antonucci, P.L. Antonucci, F.S. Fiory, S. Licoccia, E. Traversa, Influence of TiO2 nanometric filler on the behaviour of a composite membrane for applications in direct methanol fuel cells, Journal of New Materials for Electrochemical Systems (2004).

[178] K.T. Park, U.H. Jung, D.W. Choi, K. Chun, H.M. Lee, S.H. Kim, ZrO2-SiO2/Nafion® composite membrane for polymer electrolyte membrane fuel cells operation at high temperature and low humidity, J Power Sources (2008). https://doi.org/10.1016/j.jpowsour.2007.11.081.

[179] D.H. Jung, S.Y. Cho, D.H. Peck, D.R. Shin, J.S. Kim, Preparation and performance of a Nafion®/montmorillonite nanocomposite membrane for direct methanol fuel cell, in: J Power Sources, 2003. https://doi.org/10.1016/S0378-7753(03)00095-8.

[180] Y.L. Liu, Y.H. Su, C.M. Chang, Suryani, D.M. Wang, J.Y. Lai, Preparation and applications of Nafion-functionalized multiwalled carbon nanotubes for proton exchange membrane fuel cells, J Mater Chem 20 (2010). https://doi.org/10.1039/c000099j.

[181] T. Sancho, J. Soler, M.P. Pina, Conductivity in zeolite-polymer composite membranes for PEMFCs, J Power Sources (2007). https://doi.org/10.1016/j.jpowsour.2007.01.079.

[182] C. Yang, X. Xing, Z. Li, S. Zhang, A comprehensive review on water diffusion in polymers focusing on the polymer-metal interface combination, Polymers (Basel) 12 (2020). https://doi.org/10.3390/polym12010138.

[183] P.M. Mangiagli, C.S. Ewing, K. Xu, Q. Wang, M.A. Hickner, Dynamic water uptake of flexible polymer networks ion-containing polymer networks, in: Fuel Cells, 2009. https://doi.org/10.1002/fuce.200800157.

[184] S.C. Yeo, A. Eisenberg, Physical properties and supermolecular structure of perfluorinated ion-containing (nafion) polymers, J Appl Polym Sci 21 (1977). https://doi.org/10.1002/app.1977.070210401.

[185] T. Takamatsu, M. Hashiyama, A. Eisenberg, Sorption phenomena in nafion membranes, J Appl Polym Sci 24 (1979). https://doi.org/10.1002/app.1979.070241101.

[186] M. Saito, K. Hayamizu, T. Okada, Temperature dependence of ion and water transport in perfluorinated ionomer membranes for fuel cells, Journal of Physical Chemistry B 109 (2005). https://doi.org/10.1021/jp045624w.

[187] E. Galitskaya, A.F. Privalov, M. Weigler, M. Vogel, A. Kashin, M. Ryzhkin, V. Sinitsyn, NMR diffusion studies of proton-exchange membranes in wide temperature range, J Memb Sci 596 (2020). https://doi.org/10.1016/j.memsci.2019.117691.

[188] S. Motupally, A.J. Becker, J.W. Weidner, Diffusion of Water in Nafion 115 Membranes, J Electrochem Soc 147 (2000). https://doi.org/10.1149/1.1393879.

[189] J.R.P. Jayakody, P.E. Stallworth, E.S. Mananga, J. Farrington-Zapata, S.G. Greenbaum, High Pressure NMR Study of Water Self-Diffusion in NAFION-117 Membrane, Journal of Physical Chemistry B 108 (2004). https://doi.org/10.1021/jp037621+.

[190] P.J. James, J.A. Elliott, J. McMaster, J.M. Newton, A.M.S. Elliott, S. Hanna, M.J. Miles, Hydration of Nafion® studied by AFM and X-ray scattering, Journal of Materials Science 2000 35:20 35 (2000) 5111–5119. https://doi.org/10.1023/A:1004891917643.

[191] C. Yin, Z. Wang, Y. Luo, J. Li, Y. Zhou, X. Zhang, H. Zhang, P. Fang, C. He, Thermal annealing on free volumes, crystallinity and proton conductivity of Nafion membranes, Journal of Physics and Chemistry of Solids 120 (2018) 71–78. https://doi.org/10.1016/j.jpcs.2018.04.028.

[192] P. Boillat, D. Kramer, B.C. Seyfang, G. Frei, E. Lehmann, G.G. Scherer, A. Wokaun, Y. Ichikawa, Y. Tasaki, K. Shinohara, In situ observation of the water distribution across a PEFC using high resolution neutron radiography, Electrochem Commun 10 (2008). https://doi.org/10.1016/j.elecom.2008.01.018.

[193] M. Nasu, H. Yanai, N. Hirayama, H. Adachi, Y. Kakizawa, Y. Shirase, H. Nishiyama, T. Kawamoto, J. Inukai, T. Shinohara, H. Hayashida, M. Watanabe, Neutron imaging of generated water inside polymer electrolyte fuel cell using newly-developed gas diffusion layer with gas flow channels during power generation, J Power Sources 530 (2022). https://doi.org/10.1016/j.jpowsour.2022.231251.

[194] N. Martinez, L. Porcar, S. Escribano, F. Micoud, S. Rosini, A. Tengattini, D. Atkins, G. Gebel, S. Lyonnard, A. Morin, Combined Operando High Resolution SANS and Neutron Imaging Reveals in-Situ Local Water Distribution in an Operating Fuel Cell, ACS Appl Energy Mater 2 (2019). https://doi.org/10.1021/acsaem.9b01266.

[195] Y. Higuchi, D. Setoyama, K. Isegawa, Y. Tsuchikawa, Y. Matsumoto, J.D. Parker, T. Shinohara, Y. Nagai, Pulsed neutron imaging for differentiation of ice and liquid water towards fuel cell vehicle applications, Physical Chemistry Chemical Physics 23 (2021). https://doi.org/10.1039/d0cp03887c.

[196] S. Ueda, S. Koizumi, Y. Tsutsumi, Initial conditioning of a polymer electrolyte fuel cells: The relationship between microstructure development and cell performance, investigated by small-angle neutron scattering, Results Phys 12 (2019). https://doi.org/10.1016/j.rinp.2019.01.066.

[197] K. Teranishi, S. Tsushima, S. Hirai, Analysis of Water Transport in PEFCs by Magnetic Resonance Imaging Measurement, J Electrochem Soc 153 (2006). https://doi.org/10.1149/1.2167954.

[198] F. Xu, S. Leclerc, D. Canet, NMR relaxometry study of the interaction of water with a nafion membrane under acid, sodium, and potassium forms. Evidence of two types of bound water, Journal of Physical Chemistry B 117 (2013). https://doi.org/10.1021/jp311062h.

[199] C. Wakai, T. Shimoaka, T. Hasegawa, 1H NMR analysis of water freezing in nanospace involved in a nafion membrane, Journal of Physical Chemistry B 119 (2015). https://doi.org/10.1021/acs.jpcb.5b03568.

[200] Z. Lu, G. Polizos, D.D. Macdonald, E. Manias, State of Water in Perfluorosulfonic Ionomer (Nafion 117) Proton Exchange Membranes, J Electrochem Soc (2008). https://doi.org/10.1149/1.2815444.

[201] S.J. Paddison, D.W. Reagor, T.A. Zawodzinski, High frequency dielectric studies of hydrated Nafion ®, Journal of Electroanalytical Chemistry 459 (1998). https://doi.org/10.1016/S0022-0728(98)00321-0.

[202] K. Kunimatsu, B. Bae, K. Miyatake, H. Uchida, M. Watanabe, ATR-FTIR study of water in nafion membrane combined with proton conductivity measurements during hydration/dehydration cycle, Journal of Physical Chemistry B (2011). https://doi.org/10.1021/jp112300c.

[203] S.F. Parker, S. Shah, Characterisation of hydration water in Nafion membrane, RSC Adv 11 (2021) 9381–9385. https://doi.org/10.1039/D1RA00791B.

[204] M. Falk, An infrared study of water in perfluorosulfonate (Nafion) membranes, Can J Chem 58 (1980). https://doi.org/10.1139/v80-237.

[205] M. Laporta, M. Pegoraro, L. Zanderighi, Perfluorosulfonated membrane (Nafion): FT-IR study of the state of water with increasing humidity, Physical Chemistry Chemical Physics 1 (1999). https://doi.org/10.1039/a904460d.

[206] M. Ludvigsson, J. Lindgren, J. Tegenfeldt, FTIR study of water in cast Nafion films, Electrochim Acta 45 (2000). https://doi.org/10.1016/S0013-4686(99)00438-7.

[207] B. Mecheri, V. Felice, Z. Zhang, A. D'Epifanio, S. Licoccia, A.C. Tavares, DSC and DVS investigation of water mobility in Nafion/zeolite composite membranes for fuel cell applications, Journal of Physical Chemistry C 116 (2012). https://doi.org/10.1021/jp301762h.

[208] Y. Wu, M. Adamski, H.F. Lee, S. Holdcroft, Water transport through hydrocarbon-based proton exchange membranes, J Memb Sci 610 (2020). https://doi.org/10.1016/j.memsci.2020.118276.

[209] S.J. Lue, S.J. Shieh, Water states in perfluorosulfonic acid membranes using differential scanning calorimetry, Journal of Macromolecular Science, Part B: Physics 48 (2009). https://doi.org/10.1080/00222340802561649.

[210] E.L. Thompson, T.W. Capehart, T.J. Fuller, J. Jorne, Investigation of Low-Temperature Proton Transport in Nafion Using Direct Current Conductivity and Differential Scanning Calorimetry, J Electrochem Soc 153 (2006). https://doi.org/10.1149/1.2359699.

[211] A. Siu, J. Schmeisser, S. Holdcroft, Effect of water on the low temperature conductivity of polymer electrolytes, Journal of Physical Chemistry B 110 (2006) 6072–6080. https://doi.org/10.1021/JP0531208.

[212] Y. Álvarez-Gallego, M.P. De Heer, Sub-freezing conductivity of PFSA membranes, Fuel Cells 9 (2009) 421–431. https://doi.org/10.1002/FUCE.200800177.

[213] J. Lin, P.H. Wu, R. Wycisk, P.N. Pintauro, Z. Shi, Properties of water in prestretched recast nafion, Macromolecules 41 (2008). https://doi.org/10.1021/ma800194z.

[214] A. Roy, M.A. Hickner, H.S. Lee, T. Glass, M. Paul, A. Badami, J.S. Riffle, J.E. McGrath, States of water in proton exchange membranes: Part A - Influence of chemical structure and composition, Polymer (Guildf) 111 (2017). https://doi.org/10.1016/j.polymer.2017.01.021.

[215] A. Roy, H.S. Lee, J.E. McGrath, Hydrophilic-hydrophobic multiblock copolymers based on poly(arylene ether sulfone)s as novel proton exchange membranes - Part B, Polymer (Guildf) 49 (2008). https://doi.org/10.1016/j.polymer.2008.08.046.

[216] Y.S. Kim, L. Dong, M.A. Hickner, T.E. Glass, V. Webb, J.E. McGrath, State of water in disulfonated poly(arylene ether sulfone) copolymers and a perfluorosulfonic acid copolymer (nafion) and its effect on physical and electrochemical properties, Macromolecules 36 (2003). https://doi.org/10.1021/ma0301451.

[217] Y. Tabuchi, R. Ito, S. Tsushima, S. Hirai, Analysis of in situ water transport in Nafion® by confocal micro-Raman spectroscopy, J Power Sources (2011). https://doi.org/10.1016/j.jpowsour.2010.07.078.

[218] A. Syouji, M. Sakai, M. Hara, H. Matsushima, Drying process of water in a Nafion membrane embedded in the fuel cell analyzed by coherent anti-Stokes Raman scattering spectroscopy, Jpn J Appl Phys 57 (2018). https://doi.org/10.7567/JJAP.57.117101.

[219] M. Hara, J. Inukai, B. Bae, T. Hoshi, K. Miyatake, M. Uchida, H. Uchida, M. Watanabe, Micro-Raman study on water distribution inside a Nafion membrane during operation of polymer electrolyte fuel cell, in: Electrochim Acta, 2012. https://doi.org/10.1016/j.electacta.2012.04.099.

[220] D.I. Ostrovskii, A.M. Brodin, L.M. Torell, Raman study of water in Nafion-117 membranes, Solid State Ion 85 (1996). https://doi.org/10.1016/0167-2738(96)00084-7.

[221] R. Hiesgen, E. Aleksandrova, G. Meichsner, I. Wehl, E. Roduner, K.A. Friedrich, High-resolution imaging of ion conductivity of Nafion® membranes with electrochemical atomic force microscopy, Electrochim Acta 55 (2009). https://doi.org/10.1016/j.electacta.2009.05.049.

[222] S. Sengupta, A. V. Lyulin, Molecular Modeling of Structure and Dynamics of Nafion Protonation States, Journal of Physical Chemistry B 123 (2019). https://doi.org/10.1021/acs.jpcb.9b04534.

[223] K.B. Daly, J.B. Benziger, A.Z. Panagiotopoulos, P.G. Debenedetti, Molecular dynamics simulations of water permeation across nafion membrane interfaces, Journal of Physical Chemistry B 118 (2014). https://doi.org/10.1021/jp5024718.

[224] G. Zhang, G. Yang, S. Li, Q. Shen, H. Wang, Z. Li, Y. Zhou, W. Ye, Effects of hydration and temperature on the microstructure and transport properties of nafion polyelectrolyte membrane: A molecular dynamics simulation, Membranes (Basel) 11 (2021). https://doi.org/10.3390/membranes11090695.

[225] H. Cavaye, R.J.L. Welbourn, J.G. Gluschke, P. Hughes, K. V. Nguyen, A.P. Micolich, P. Meredith, A.B. Mostert, Systematic in situ hydration neutron reflectometry study on Nafion thin films, Physical Chemistry Chemical Physics 24 (2022). https://doi.org/10.1039/d2cp03067e.

[226] Y. Li, Q.T. Nguyen, C.L. Buquet, D. Langevin, M. Legras, S. Marais, Water sorption in Nafion® membranes analyzed with an improved dual-mode sorption model-Structure/property relationships, J Memb Sci 439 (2013). https://doi.org/10.1016/j.memsci.2013.03.040.

[227] M.A. Barique, E. Tsuchida, A. Ohira, K. Tashiro, Effect of Elevated Temperatures on the States of Water and Their Correlation with the Proton Conductivity of Nafion, ACS Omega (2017). https://doi.org/10.1021/acsomega.7b01765.

[228] T. Agarwal, A.K. Prasad, S.G. Advani, S.K. Babu, R.L. Borup, Infrared spectroscopy for understanding the structure of Nafion and its associated properties, J Mater Chem A Mater 12 (2024) 14229–14244. https://doi.org/10.1039/D3TA05653H.

[229] K.D. Kreuer, S.J. Paddison, E. Spohr, M. Schuster, Transport in proton conductors for fuel-cell applications: Simulations, elementary reactions, and phenomenology, Chem Rev 104 (2004). https://doi.org/10.1021/cr020715f.

[230] K. Tajiri, U. Shrivastava, S. Verma, Measurement of Proton Conductivity and Water Diffusivity of Nafion Membrane at Subzero Temperatures, ECS Trans 98 (2020). https://doi.org/10.1149/09809.0427ecst.

[231] J. Jia, K. Liu, T. Zuo, D. Song, N. Wang, S. Hu, X. Wei, Q. Che, Enhancing proton conductivity at subzero temperature through constructing the well-ordered structure based on carbon dots, J Memb Sci 653 (2022). https://doi.org/10.1016/j.memsci.2022.120536.

[232] D. Koo, The characterization of states of water in Nafion and the relationship between states of water and Nafion properties, Ph.D. Thesis, University of Connecticut, 2008.

[233] K.J. Tielrooij, D. Paparo, L. Piatkowski, H.J. Bakker, M. Bonn, Dielectric relaxation dynamics of water in model membranes probed by terahertz spectroscopy, Biophys J (2009). https://doi.org/10.1016/j.bpj.2009.08.024.

[234] N. Devi, S. Ray, A. Shukla, S.D. Bhat, B. Pesala, Non-invasive macroscopic and molecular quantification of water in Nafion® and SPEEK Proton Exchange Membranes using terahertz spectroscopy, J Memb Sci 588 (2019). https://doi.org/10.1016/j.memsci.2019.117183.

[235] W.J. Choi, M.R. Armstrong, J.H. Yoo, T. Lee, Toward high-power terahertz radiation sources based on ultrafast lasers, J Mater Chem C Mater 12 (2024) 9002–9011. https://doi.org/10.1039/D4TC01502A.

[236] A.A. Gowen, C. O'Sullivan, C.P. O'Donnell, Terahertz time domain spectroscopy and imaging: Emerging techniques for food process monitoring and quality control, Trends Food Sci Technol 25 (2012). https://doi.org/10.1016/j.tifs.2011.12.006.

[237] M. Naftaly, N. Vieweg, A. Deninger, Industrial applications of terahertz sensing: State of play, Sensors 19 (2019). https://doi.org/10.3390/s19194203.

[238] J. Neu, C.A. Schmuttenmaer, Tutorial: An introduction to terahertz time domain spectroscopy (THz-TDS), J Appl Phys 124 (2018). https://doi.org/10.1063/1.5047659.

[239] Naftaly, Terahertz Metrology, Artech House, Boston, MA, 2014.

[240] D. Liu, J. Qin, Carrier dynamics of terahertz emission from low-temperature-grown GaAs, Appl Opt 42 (2003). https://doi.org/10.1364/ao.42.003678.

[241] A. Takazato, M. Kamakura, T. Matsui, J. Kitagawa, Y. Kadoya, Terahertz wave emission and detection using photoconductive antennas made on low-temperature-grown InGaAs with 1.56 μm pulse excitation, Appl Phys Lett 91 (2007). https://doi.org/10.1063/1.2754370.

[242] B.M. Fischer, M. Hoffmann, P.U. Jepsen, Dynamic range and numerical error propagation in terahertz time-domain spectroscopy, in: Optics InfoBase Conference Papers, 2005. https://doi.org/10.1364/otst.2005.tud1.

[243] G.P. Kniffin, Model-Based Material Parameter Estimation for Terahertz Reflection Spectroscopy, Master Thesis, Portland State University, 2011.

[244] L. Duvillaret, F. Garet, J.L. Coutaz, A reliable method for extraction of material parameters in terahertz time-domain spectroscopy, IEEE Journal on Selected Topics in Quantum Electronics (1996). https://doi.org/10.1109/2944.571775.

[245] T.D. Dorney, R.G. Baraniuk, D.M. Mittleman, Material parameter estimation with terahertz time-domain spectroscopy, Journal of the Optical Society of America A (2001). https://doi.org/10.1364/josaa.18.001562.

[246] R. Wilk, I. Pupeza, R. Cernat, M. Koch, Highly accurate THz time-domain spectroscopy of multilayer structures, IEEE Journal on Selected Topics in Quantum Electronics (2008). https://doi.org/10.1109/JSTQE.2007.910981.

[247] M. Scheller, Data extraction from terahertz time domain spectroscopy measurements, J Infrared Millim Terahertz Waves 35 (2014) 638–648. https://doi.org/10.1007/s10762-014-0053-4.

[248] I. Pupeza, R. Wilk, M. Koch, Highly accurate optical material parameter determination with THz time-domain spectroscopy, Opt Express 15 (2007). https://doi.org/10.1364/oe.15.004335.

[249] J.A. Hejase, E.J. Rothwell, P. Chahal, A multiple angle method for THz time-domain material characterization, IEEE Trans Terahertz Sci Technol 3 (2013). https://doi.org/10.1109/TTHZ.2013.2278460.

[250] X. Li, Z. Hong, J. He, Y. Chen, Precisely optical material parameter determination by time domain waveform rebuilding with THz time-domain spectroscopy, Opt Commun (2010). https://doi.org/10.1016/j.optcom.2010.06.088.

[251] J. Liu, L. Mao, J. Ku, J. He, L. Fan, THz spectroscopy detection method for GMOs based on adaptive particle swarm optimization, Opt Quantum Electron 48 (2016). https://doi.org/10.1007/s11082-015-0259-2.

[252] N. Chopra, N. Shaw, L. Lotkowska, C. Sui, M. Navarro-Cia, J. Lloyd-Hughes, Temperature-Dependent Dielectric Properties of Human Bone Constituents at THz Frequencies: Contrast Mechanisms and Bound Water Dynamics, in: International Conference on Infrared, Millimeter, and Terahertz Waves, IRMMW-THz, 2022. https://doi.org/10.1109/IRMMW-THz50927.2022.9896085.

[253] J.-L. Coutaz, F. Garet, V.P. Wallace, Principles of Terahertz Time-Domain Spectroscopy, 2018. https://doi.org/10.1201/b22478.

[254] D. Dragoman, M. Dragoman, Terahertz fields and applications, Prog Quantum Electron 28 (2004). https://doi.org/10.1016/S0079-6727(03)00058-2.

[255] L. Yang, T. Guo, X. Zhang, S. Cao, X. Ding, Toxic chemical compound detection by terahertz spectroscopy: A review, Rev Anal Chem 37 (2018). https://doi.org/10.1515/revac-2017-0021.

[256] H. Altan, B.L. Yu, S.A. Alfano, R.R. Alfano, Terahertz (THz) spectroscopy of Freon-11 (CCl3F, CFC-11) at room temperature, Chem Phys Lett 427 (2006). https://doi.org/10.1016/j.cplett.2006.06.064.

[257] W.C. Chen, R.A. Marcus, The Drude-Smith Equation and Related Equations for the Frequency-Dependent Electrical Conductivity of Materials: Insight from a Memory Function Formalism, ChemPhysChem 22 (2021). https://doi.org/10.1002/cphc.202100299.

[258] U. Strom, P.C. Taylor, Temperature and frequency dependences of the far-infrared and microwave optical absorption in amorphous materials, Phys Rev B 16 (1977). https://doi.org/10.1103/PhysRevB.16.5512.

[259] Z. Zang, Z. Li, X. Lu, J. Liang, J. Wang, H.L. Cui, S. Yan, Terahertz spectroscopy for quantification of free water and bound water in leaf, Comput Electron Agric 191 (2021) 106515. https://doi.org/10.1016/J.COMPAG.2021.106515.

[260] H. Lin, B.P. Russell, P. Bawuah, J.A. Zeitler, Sensing Water Absorption in Hygrothermally Aged Epoxies with Terahertz Time-Domain Spectroscopy, Anal Chem (2021). https://doi.org/10.1021/acs.analchem.0c04453.

[261] D. Paparo, K.J. Tielrooij, H. Bakker, M. Bonn, TeraHertz dielectric relaxation of biological water confined in model membranes made of lyotropic phospholipids, in: Molecular Crystals and Liquid Crystals, 2009. https://doi.org/10.1080/15421400802713769.

[262] D. Y.S. Chau, A. R Dennis, H. Lin, J. Axel Zeitler, A. Tunnacliffe, Determination of Water Content in Dehydrated Mammalian Cells Using Terahertz Pulsed Imaging: A Feasibility Study, Curr Pharm Biotechnol 17 (2015). https://doi.org/10.2174/1389201017666151029105941.

[263] H. Hoshina, Y. Iwasaki, E. Katahira, M. Okamoto, C. Otani, Structure and dynamics of bound water in poly(ethylene-vinylalcohol) copolymers studied by terahertz spectroscopy, Polymer (Guildf) 148 (2018). https://doi.org/10.1016/j.polymer.2018.06.020.

[264] H.J. Liebe, G.A. Hufford, T. Manabe, A model for the complex permittivity of water at frequencies below 1 THz, Int J Infrared Millimeter Waves 12 (1991). https://doi.org/10.1007/BF01008897.

[265] H. Ge, Z. Sun, Y. Jiang, X. Wu, Z. Jia, G. Cui, Y. Zhang, Recent Advances in THz Detection of Water, Int J Mol Sci 24 (2023). https://doi.org/10.3390/ijms241310936.

[266] Z. Lu, G. Polizos, D.D. Macdonald, E. Manias, State of Water in Perfluorosulfonic Ionomer (Nafion 117) Proton Exchange Membranes, J Electrochem Soc 155 (2008). https://doi.org/10.1149/1.2815444.

[267] S. Aparicio, R. Alcalde, B. García, J.M. Leal, Microwave dielectric spectroscopy of 2-pyrrolidone + water mixtures, Chem Phys Lett 444 (2007). https://doi.org/10.1016/j.cplett.2007.07.033.

[268] S.O. Yurchenko, K.I. Zaytsev, Spectroscopy of nafion in terahertz frequency range, J Appl Phys 116 (2014). https://doi.org/10.1063/1.4896194.

[269] H. Yada, M. Nagai, K. Tanaka, Origin of the fast relaxation component of water and heavy water revealed by terahertz time-domain attenuated total reflection spectroscopy, Chem Phys Lett 464 (2008). https://doi.org/10.1016/j.cplett.2008.09.015.

[270] W.H.H. Woodward, Broadband Dielectric Spectroscopy - A Practical Guide, in: ACS Symposium Series, 2021. https://doi.org/10.1021/bk-2021-1375.ch001.

[271] H. Wang, Y. Zhai, Y. Li, Y. Cao, B. Shi, R. Li, Z. Zhu, H. Jiang, Z. Guo, M. Wang, L. Chen, Y. Liu, K.G. Zhou, F. Pan, Z. Jiang, Covalent organic framework membranes for efficient separation of monovalent cations, Nat Commun 13 (2022). https://doi.org/10.1038/s41467-022-34849-7.

[272] W. Ensing, Protons and Sodium Ions Interacting With Nafion Confined Water, Master Thesis, Utrecht University, 2012. https://studenttheses.uu.nl/handle/20.500.12932/13056 (accessed January 3, 2024).

[273] J.K. Vij, D.R.J. Simpson, O.E. Panarina, Far infrared spectroscopy of water at different temperatures: GHz to THz dielectric spectroscopy of water, J Mol Liq 112 (2004). https://doi.org/10.1016/j.molliq.2003.12.014.

[274] H. Wang, J.Q. Guo, Y.S. Zhou, Understanding terahertz optical properties of amorphous carbon thin films, Carbon N Y 64 (2013). https://doi.org/10.1016/j.carbon.2013.07.028.

[275] Z. Lu, State of water in perfluorosulfonic acid membranes studied by microwave dielectric relaxation spectroscopy, Penn State University, 2005. https://etda.libraries.psu.edu/catalog/6867.

[276] N. Ottosson, J. Hunger, H.J. Bakker, Effect of cations on the hydrated proton, J Am Chem Soc 136 (2014). https://doi.org/10.1021/ja503635j.

[277] E.A.S. Cavell, P.C. Knight, M.A. Sheikh, Dielectric relaxation in non aqueous solutions. Part 2. - Solutions of tri(n-butyl)ammonium picrate and iodide in polar solvents, Transactions of the Faraday Society 67 (1971). https://doi.org/10.1039/TF9716702225.

[278] M. Scheller, C. Jansen, and M. Koch, M. Scheller, C. Jansen, and M. Koch, Applications of Effective Medium Theories in the Terahertz Regime, Recent Optical and Photonic Technologies (2010). https://doi.org/10.5772/6915.

[279] M. Scheller, S. Wietzke, C. Jansen, M. Koch, Modelling heterogeneous dielectric mixtures in the terahertz regime: A quasi-static effective medium theory, J Phys D Appl Phys 42 (2009). https://doi.org/10.1088/0022-3727/42/6/065415.

[280] G. Bánhegyi, Comparison of electrical mixture rules for composites, Colloid Polym Sci 264 (1986). https://doi.org/10.1007/BF01410321.

[281] J.F. Federici, Review of Moisture and Liquid Detection and Mapping using Terahertz Imaging, J Infrared Millim Terahertz Waves 33 (2012) 97–126. https://doi.org/10.1007/s10762-011-9865-7.

[282] E. Moukheiber, G. De Moor, L. Flandin, C. Bas, Investigation of ionomer structure through its dependence on ion exchange capacity (IEC), J Memb Sci 389 (2012). https://doi.org/10.1016/j.memsci.2011.10.041.

[283] D.F. Alves-Lima, X. Li, B. Coulson, E. Nesling, G.A.H. Ludlam, R. Degl'Innocenti, R. Dawson, M. Peruffo, H. Lin, Evaluation of water states in thin proton exchange membrane manufacturing using terahertz time-domain spectroscopy, J Memb Sci 647 (2022). https://doi.org/10.1016/j.memsci.2022.120329.

[284] Q. Li, J. Kolbel, T. Threlfall, J.A. Zeitler, Flow Cell to Study Crystallization Processes In Situ Using Terahertz Time-Domain Spectroscopy, IEEE Trans Terahertz Sci Technol 12 (2022). https://doi.org/10.1109/TTHZ.2021.3132800.

[285] Y.C. Huang, H.F. Lee, Y.C. Tseng, C.C. Lee, M.Y. Chang, W.Y. Huang, Synthesis of novel sulfonated poly(arylene ether)s containing a tetra-trifluoromethyl side chain and multi-phenyl for proton exchange membrane fuel cell application, RSC Adv 7 (2017). https://doi.org/10.1039/c7ra04731b.

[286] X. Xin, H. Altan, A. Saint, D. Matten, R.R. Alfano, Terahertz absorption spectrum of para and ortho water vapors at different humidities at room temperature, J Appl Phys 100 (2006). https://doi.org/10.1063/1.2357412.

[287] C. Rønne, L. Thrane, P.O. Åstrand, A. Wallqvist, K. V. Mikkelsen, S.R. Keiding, Investigation of the temperature dependence of dielectric relaxation in liquid water by

THz reflection spectroscopy and molecular dynamics simulation, Journal of Chemical Physics 107 (1997). https://doi.org/10.1063/1.474242.

[288] J. Zhou, X. Rao, X. Liu, T. Li, L. Zhou, Y. Zheng, Z. Zhu, Temperature dependent optical and dielectric properties of liquid water studied by terahertz time-domain spectroscopy, AIP Adv 9 (2019). https://doi.org/10.1063/1.5082841.

[289] A.J. Fitzgerald, E. Pickwell-MacPherson, V.P. Wallace, Use of Finite Difference Time Domain Simulations and Debye Theory for Modelling the Terahertz Reflection Response of Normal and Tumour Breast Tissue, PLoS One 9 (2014) e99291. https://doi.org/10.1371/JOURNAL.PONE.0099291.

[290] E. Pickwell, B.E. Cole, A.J. Fitzgerald, V.P. Wallace, M. Pepper, Simulation of terahertz pulse propagation in biological systems, Appl Phys Lett 84 (2004). https://doi.org/10.1063/1.1688448.

[291] T. Sato, R. Buchner, Dielectric relaxation processes in ethanol/water mixtures, Journal of Physical Chemistry A 108 (2004). https://doi.org/10.1021/jp035255o.

[292] J. Barthel, K. Bachhuber, R. Buchner, H. Hetzenauer, Dielectric spectra of some common solvents in the microwave region. Water and lower alcohols, Chem Phys Lett 165 (1990). https://doi.org/10.1016/0009-2614(90)87204-5.

[293] U. Kaatze, Complex Permittivity of Water as a Function of Frequency and Temperature, J Chem Eng Data 34 (1989). https://doi.org/10.1021/je00058a001.

[294] W.J. Ellison, Permittivity of pure water, at standard atmospheric pressure, over the frequency range 0-25 THz and the temperature range 0-100 °C, J Phys Chem Ref Data 36 (2007). https://doi.org/10.1063/1.2360986.

[295] R. Buchner, J. Barthel, J. Stauber, The dielectric relaxation of water between 0 ° C and 35 ° C, Chem Phys Lett 306 (1999). https://doi.org/10.1016/S0009-2614(99)00455-8.

[296] V.A. Rana, T.R. Pandit, Microwave dielectric relaxation spectroscopy of paracetamol and its aqueous solutions, J Mol Liq 314 (2020). https://doi.org/10.1016/j.molliq.2020.113673.

[297] H. Lin, O.J. Burton, S. Engelbrecht, K.H. Tybussek, B.M. Fischer, S. Hofmann, Through-substrate terahertz time-domain reflection spectroscopy for environmental graphene conductivity mapping, Appl Phys Lett 116 (2020). https://doi.org/10.1063/1.5135644.

[298] T. Fukasawa, T. Sato, J. Watanabe, Y. Hama, W. Kunz, R. Buchner, Relation between dielectric and low-frequency Raman spectra of hydrogen-bond liquids, Phys Rev Lett 95 (2005). https://doi.org/10.1103/PhysRevLett.95.197802.

[299] W.M. Haynes, CRC Handbook of Chemistry and Physics, 95th Edition, CRC Press, 2014. https://doi.org/10.1201/B17118.

[300] G.S. Park, Transport Principles—Solution, Diffusion and Permeation in Polymer Membranes, in: Synthetic Membranes: Science, Engineering and Applications, 1986. https://doi.org/10.1007/978-94-009-4712-2_3.

[301] D. Stoica, F. Alloin, S. Marais, D. Langevin, C. Chappey, P. Judeinstein, Polyepichlorhydrin membranes for alkaline fuel cells: Sorption and conduction properties, Journal of Physical Chemistry B 112 (2008). https://doi.org/10.1021/jp804787x.

[302] K. Fatyeyeva, C. Chappey, F. Poncin-Epaillard, D. Langevin, J.M. Valleton, S. Marais, Composite membranes based on Nafion® and plasma treated clay charges: Elaboration and water sorption investigations, J Memb Sci 369 (2011). https://doi.org/10.1016/j.memsci.2010.11.062.

[303] T. Van Nguyen, N. Vanderborgh, The rate of isothermal hydration of polyperfluorosulfonic acid membranes, J Memb Sci 143 (1998). https://doi.org/10.1016/S0376-7388(98)00030-1.

[304] S.K. Burgess, D.S. Mikkilineni, D.B. Yu, D.J. Kim, C.R. Mubarak, R.M. Kriegel, W.J. Koros, Water sorption in poly(ethylene furanoate) compared to poly(ethylene terephthalate). Part 2: Kinetic sorption, Polymer (Guildf) 55 (2014). https://doi.org/10.1016/j.polymer.2014.10.065.

[305] G.A.H. France, M. Mohammadpour, R. Degl'Innocenti, M. Peruffo, H. Lin, Probing Water Properties of Perfluorinated Sulfonic-Acid Membranes With Humidity-Controlled Terahertz Time-Domain Spectroscopy, IEEE Trans Terahertz Sci Technol 15 (2025) 743–750. https://doi.org/10.1109/TTHZ.2025.3594070.

[306] G.A.H. Ludlam, S.J.P. Gnaniah, R. Degl'Innocenti, G. Gupta, A.J. Wain, H. Lin, Measurement of Water Uptake and States in Nafion Membranes Using Humidity-Controlled Terahertz Time-Domain Spectroscopy, ACS Sustain Chem Eng 12 (2024) 7924–7934. https://doi.org/10.1021/acssuschemeng.4c01820.

[307] J.T. Kindt, C.A. Schmuttenmaer, Far-infrared dielectric properties of polar liquids probed by femtosecond terahertz pulse spectroscopy, Journal of Physical Chemistry 100 (1996). https://doi.org/10.1021/jp960141g.

[308] W. Ensing, J. Hunger, N. Ottosson, H.J. Bakker, On the orientational mobility of water molecules in proton and sodium terminated nafion membranes, Journal of Physical Chemistry C 117 (2013). https://doi.org/10.1021/jp312623p.

[309] P. Choi, N.H. Jalani, R. Datta, Thermodynamics and proton transport in Nafion I. Membrane swelling, sorption, and ion-exchange equilibrium, J Electrochem Soc 152 (2005). https://doi.org/10.1149/1.1855872.

[310] J. Peron, A. Mani, X. Zhao, D. Edwards, M. Adachi, T. Soboleva, Z. Shi, Z. Xie, T. Navessin, S. Holdcroft, Properties of Nafion® NR-211 membranes for PEMFCs, J Memb Sci 356 (2010). https://doi.org/10.1016/j.memsci.2010.03.025.

[311] M. Robert, A. El Kaddouri, J.-C. Perrin, S. Leclerc, O. Lottin, Towards a NMR-Based Method for Characterizing the Degradation of Nafion XL Membranes for PEMFC, J Electrochem Soc 165 (2018). https://doi.org/10.1149/2.0231806jes.

[312] A. Grimaldi, A. Baricci, S. De Antonellis, C. Oldani, A. Casalegno, Experimental study and modeling of water transport through short-side-chain perfluorosulfonic acid membranes, J Power Sources 558 (2023). https://doi.org/10.1016/j.jpowsour.2022.232556.

[313] A.J.K. Leoga, S. Roualdès, V. Rouessac, N. Follain, S. Marais, Sorption and permeation of water through Plasma Enhanced Chemical Vapour Deposited phosphonic acid-based membranes, Thin Solid Films 700 (2020). https://doi.org/10.1016/j.tsf.2020.137918.

[314] L. Wadsö, P. Jannasch, Water vapor sorption thermodynamics of the nafion ionomer membrane, Journal of Physical Chemistry B 117 (2013) 8561–8570. https://doi.org/10.1021/jp3089319.

[315] Z. Dai, L. Ansaloni, J.J. Ryan, R.J. Spontak, L. Deng, Nafion/IL hybrid membranes with tuned nanostructure for enhanced CO2 separation: Effects of ionic liquid and water vapor, Green Chemistry 20 (2018). https://doi.org/10.1039/c7gc03727a.

[316] V.I. Volkov, A. V. Chernyak, O.I. Gnezdilov, V.D. Skirda, Hydration, self-diffusion and ionic conductivity of Li+, Na+ and Cs+ cations in Nafion membrane studied by NMR, Solid State Ion 364 (2021). https://doi.org/10.1016/j.ssi.2021.115627.

[317] A. Ghielmi, P. Vaccarono, C. Troglia, V. Arcella, Proton exchange membranes based on the short-side-chain perfluorinated ionomer, J Power Sources 145 (2005). https://doi.org/10.1016/j.jpowsour.2004.12.068.

[318] N. Ramaswamy, S. Kumaraguru, R. Koestner, T. Fuller, W. Gu, N. Kariuki, D. Myers, P.J. Dudenas, A. Kusoglu, Editors' Choice—Ionomer Side Chain Length and Equivalent Weight Impact on High Current Density Transport Resistances in PEMFC Cathodes, J Electrochem Soc 168 (2021). https://doi.org/10.1149/1945-7111/abe5eb.

[319] S. Shi, X. Sun, Q. Lin, J. Chen, Y. Fu, X. Hong, C. Li, X. Guo, G. Chen, X. Chen, Fatigue crack propagation behavior of fuel cell membranes after chemical degradation, Int J Hydrogen Energy 45 (2020). https://doi.org/10.1016/j.ijhydene.2020.07.113.

[320] T. Böhm, R. Moroni, M. Breitwieser, S. Thiele, S. Vierrath, Spatially Resolved Quantification of Ionomer Degradation in Fuel Cells by Confocal Raman Microscopy, J Electrochem Soc 166 (2019). https://doi.org/10.1149/2.0051907jes.

[321] E. Moukheiber, G. De Moor, L. Flandin, C. Bas, Investigation of ionomer structure through its dependence on ion exchange capacity (IEC), J Memb Sci 389 (2012). https://doi.org/10.1016/j.memsci.2011.10.041.

[322] L. Yu, F. Lin, L. Xu, J. Xi, Structure-property relationship study of Nafion XL membrane for high-rate, long-lifespan, and all-climate vanadium flow batteries, RSC Adv 7 (2017). https://doi.org/10.1039/c7ra04996j.

[323] O. Fernihough, M.S. Ismail, A. El-kharouf, Intermediate Temperature PEFC's with Nafion® 211 Membrane Electrolytes: An Experimental and Numerical Study, Membranes (Basel) 12 (2022). https://doi.org/10.3390/membranes12040430.

[324] R. Sigwadi, M.S. Dhlamini, T. Mokrani, F. Ṋemavhola, P.F. Nonjola, P.F. Msomi, The proton conductivity and mechanical properties of Nafion®/ ZrP nanocomposite membrane, Heliyon 5 (2019). https://doi.org/10.1016/j.heliyon.2019.e02240.

[325] X. Zhu, H. Zhang, Y. Liang, Y. Zhang, Q. Luo, C. Bi, B. Yi, Challenging reinforced composite polymer electrolyte membranes based on disulfonated poly(arylene ether sulfone)-impregnated expanded PTFE for fuel cell applications, J Mater Chem 17 (2007) 386–397. https://doi.org/10.1039/B611690F.

[326] P. Talik, U. Hubicka, The DSC approach to study non-freezing water contents of hydrated hydroxypropylcellulose (HPC), J Therm Anal Calorim 132 (2018). https://doi.org/10.1007/s10973-017-6889-9.

[327] A.Y. Tolbin, V.E. Pushkarev, L.G. Tomilova, N.S. Zefirov, Threshold concentration in the nonlinear absorbance law, Physical Chemistry Chemical Physics 19 (2017). https://doi.org/10.1039/c7cp01514c.

[328] T.R. Willson, C.A. Giron Rodriguez, Q. Xu, J. Frow, F. Foglia, K. Smith, R. Ravikumar, M. Vinothkannan, N. Mahmoudi, I. Salam, A.P. Periasamy, D.K. Whelligan, M. Mamlouk, H. Lin, B. Seger, J.R. Varcoe, G. Rodriguez, Radiation-grafted anion-exchange membranes for CO 2 electroreduction cells: an unexpected effect of using a lower excess of N-methylpiperidine in their fabrication †, (2023). https://doi.org/10.1039/d3ta04915a.

[329] B. NF, I. PS, K. VA, S. AV, Z. SD, Z. AA, Study of the Phase States of Water Close to Nafion Interface, WATER Journal 4 (2013).

[330] R.W. Austin, G. Halikas, The index of refraction of seawater, SIO Ref. 76-1 (1976).

[331] L.W. McKeen, The effect of creep and other time related factors on plastics and elastomers, 2014. https://doi.org/10.1016/B978-0-323-35313-7.00013-4.

[332] L.W. McKeen, The effect of UV light and weather on plastics and elastomers, 2013. https://doi.org/10.1016/C2011-0-07329-5.

[333] K.J. Kim, S.B. Lee, N.W. Han, Effects of the degree of crosslinking on properties of poly(vinyl alcohol) membranes, Polym J 25 (1993). https://doi.org/10.1295/polymj.25.1295.

[334] Post-polymerization modification of monomer units - Matyjaszewski Polymer Group - Carnegie Mellon University, (2008). https://www.cmu.edu/maty/materials/Incorporation-of-functional-groups-into-polymers/post-polymerization-modification-of-monomer-units.html (accessed September 10, 2021).

[335] L. Wang, S.G. Advani, A.K. Prasad, Self-Healing Composite Membrane for Proton Exchange Membrane Fuel Cell Applications, ECS Trans 80 (2017). https://doi.org/10.1149/08008.0545ecst.

[336] X. Chen, M.A. Dam, K. Ono, A. Mal, H. Shen, S.R. Nutt, K. Sheran, F. Wudl, A thermally re-mendable cross-linked polymeric material, Science (1979) 295 (2002). https://doi.org/10.1126/science.1065879.

[337] Y. Li, L. Liang, C. Liu, Y. Li, W. Xing, J. Sun, Self-Healing Proton-Exchange Membranes Composed of Nafion–Poly(vinyl alcohol) Complexes for Durable Direct Methanol Fuel Cells, Advanced Materials 30 (2018). https://doi.org/10.1002/adma.201707146.

[338] Y. Li, Z. Li, W. Wang, J. Sun, Self-healing and highly elastic fluorine-free proton exchange membranes comprised of poly(vinyl alcohol) derivative and phytic acid for durable fuel cells, Sci China Mater 63 (2020). https://doi.org/10.1007/s40843-020-1308-y.

[339] D. Korkmaz, Determination of Chloride Ion Concentration by Titration (Mohr's Method), University of Cantearbury (2011).

[340] H.L. Nguyen, J. Han, X.L. Nguyen, S. Yu, Y.M. Goo, D.D. Le, Review of the durability of polymer electrolyte membrane fuel cell in long-term operation: Main influencing parameters and testing protocols, Energies (Basel) 14 (2021). https://doi.org/10.3390/en14134048.

[341] Appendix A: FCTT AST and Polarization Curve Protocols for PEMFCs U.S. DRIVE Fuel Cell Tech Team Cell Component Accelerated Stress Test and Polarization Curve Protocols for PEM Fuel Cells, (2013). http://web.anl.gov/PCS/acsfuel/preprint%20archive/Files/49_2_Philadelphia_10 (accessed September 28, 2021).

[342] Degradation Study of MEA for PEMFCs under Low Humidity Conditions, (2004). https://doi.org/10.1149/1.1739314.

[343] Glass Transition Temperature (Tg) of Plastics - Definition & Values, (2021). https://omnexus.specialchem.com/polymer-properties/properties/glass-transition-temperature (accessed July 7, 2021).

[344] K. Balani, V. Verma, A. Agarwal, R. Narayan, Physical, Thermal, and Mechanical Properties of Polymers, Biosurfaces (2015) 329–344. https://doi.org/10.1002/9781118950623.APP1.

[345] K. Broka, P. Ekdunge, Oxygen and hydrogen permeation properties and water uptake of Nafion® 117 membrane and recast film for PEM fuel cell, J Appl Electrochem 27 (1997). https://doi.org/10.1023/a:1018469520562.

[346] Differential Scanning Calorimetry; First and Second OrderTransitions in PETE, (2019). https://www.scribd.com/document/233940171/Dsc-Pete (accessed September 20, 2021).

[347] N. Devi, S. Ray, A. Shukla, S.D. Bhat, B. Pesala, Non-invasive macroscopic and molecular quantification of water in Nafion® and SPEEK Proton Exchange Membranes using terahertz spectroscopy, J Memb Sci 588 (2019). https://doi.org/10.1016/j.memsci.2019.117183.

[348] N. Penkov, N. Shvirst, V. Yashin, E. Fesenko, Terahertz Spectroscopy Applied for Investigation of Water Structure, Journal of Physical Chemistry B 119 (2015). https://doi.org/10.1021/acs.jpcb.5b06622.

[349] K. Kunimatsu, B. Bae, K. Miyatake, H. Uchida, M. Watanabe, ATR-FTIR study of water in nafion membrane combined with proton conductivity measurements during hydration/dehydration cycle, Journal of Physical Chemistry B 115 (2011). https://doi.org/10.1021/jp112300c.

[350] A.D. Squires, R.A. Lewis, Feasibility and Characterization of Common and Exotic Filaments for Use in 3D Printed Terahertz Devices, J Infrared Millim Terahertz Waves 39 (2018). https://doi.org/10.1007/s10762-018-0498-y.

[351] U. Møller, D.G. Cooke, K. Tanaka, P.U. Jepsen, Terahertz reflection spectroscopy of Debye relaxation in polar liquids [Invited], Journal of the Optical Society of America B 26 (2009). https://doi.org/10.1364/josab.26.00a113.

[352] Permittivity, (2021). https://www.chemeurope.com/en/encyclopedia/Permittivity.html (accessed September 20, 2021).

[353] T. Xue, J.S. Trent, K. Osseo-Asare, Characterization of nafion® membranes by transmission electron microscopy, J Memb Sci 45 (1989). https://doi.org/10.1016/S0376-7388(00)80518-9.

[354] B. Gill Choi, J. Hong, Y. Chul Park, D. Hwan Jung, W. Hi Hong, P.T. Hammond, H. Park, Innovative Polymer Nanocomposite Electrolytes: Nanoscale Manipulation of Ion Channels by Functionalized Graphenes, (2011). https://doi.org/10.1021/nn2013113.

[355] Polyvinyl Alcohol - an overview | ScienceDirect Topics, (2021). https://www.sciencedirect.com/topics/nursing-and-health-professions/polyvinyl-alcohol (accessed July 8, 2021).

[356] Phase transition diagram showing lower critical solution temperature... | Download Scientific Diagram, (2019). https://www.researchgate.net/figure/Phase-transition-diagram-showing-lower-critical-solution-temperature-and-upper-critical_fig3_323732681 (accessed July 8, 2021).

[357] C. Yin, Z. Wang, Y. Luo, J. Li, Y. Zhou, X. Zhang, H. Zhang, P. Fang, C. He, Thermal annealing on free volumes, crystallinity and proton conductivity of Nafion membranes, Journal of Physics and Chemistry of Solids 120 (2018). https://doi.org/10.1016/j.jpcs.2018.04.028.

[358] Poly(vinyl alcohol), (2020). https://polymerdatabase.com/polymers/polyvinylalcohol.html (accessed July 7, 2021).

8 Appendix - Self-healing membranes

Initially the focus of this thesis was dedicated to the synthesis and characterisation of intrinsic self-healing membranes and these membranes were manufactured and shown to be capable of healing fabricated holes. Unfortunately, it was difficult to manufacture membranes with consistent and even thickness using the available equipment, and although healing was demonstrated it was found that healing was inconsistent, and membranes were more susceptible to damage. This is due to the need for polymer chain mobility above the glass transition temperature at the high temperatures and hydration in which healing was conducted. As fuel cell and electrolyser membranes also operate at these conditions and any significant increase in temperature or humidity is not possible, any membranes with significant chain mobility would always be susceptible to damage. PFSA membranes operate below the glass transition temperature for these reasons. Therefore, the focus of this thesis was dedicated to THz-TDS studies. This chapter presents some of the early work dedicated to self-healing membranes.

8.1 Creating and modifying polymeric materials

Polymers can be created and modified in several ways to produce materials with more desirable properties. Copolymers are polymers made from more than one monomer and are copolymerised to create a polymer consisting of multiple monomer units [331]. This occurs through several methods but the two most common methods are condensation polymerisation and addition polymerisation which is the addition of monomers through double or triple bonds [332], this is the method used to create PTFE. Condensation polymerisation is where the reaction between monomers releases a small molecule such as water in the formation of a polyester. The monomer units can be arranged randomly, or they can be ordered such as with an alternating polymer [331], Nafion is an example of a copolymer as it consists of two monomer units.

Polymer blending is a process of combining at least two polymers to create a new material. These are different to copolymers as the polymers chains are not modified and instead the chains interact through intermolecular forces and sometimes temporary crosslinking. Cross linking is a process of forming one or a small sequence of covalent or ionic bonds between different chains, this can occur naturally, or it can be induced by changing the ambient conditions or through the use of a crosslinking agent. Crosslinking can strengthen polymers and reduce the swelling characteristics [333].

Post-polymerisation functionalisation is a process of modifying the functional groups of a polymer, this can be through the removal of protecting groups or addition to the polymer by grafting desired functional groups onto other functional groups. This has the advantage of incorporating functional groups which are incompatible with the polymerisation process [334],. An example is the sulfonation of sPEEK where the sulfonate group is grafted onto the PEEK polymer.

8.2 Self-healing membranes and mechanisms

The first publication of self-healing fuel cell membranes was in January of 2016 and employed the use of microcapsules, since then 2 more publications have been made all using different materials. Different mechanisms have been used to create materials which can heal mechanical damage such as microcapsules [335] reversible covalent bonding such as the reversible Diels-Alder reactions [336] and intermolecular forces such as reversible hydrogen bonds [337,338]. Microcapsules can heal mechanical damage effectively however, as a reagent is consumed in

the repair of damage this method is limited to the capacity of the reagents. The microcapsules do not conduct protons and so reduced proton conductivity is also observed [335]. Reversable Diels-Alder reactions have been shown to produce self-healing polymers by crosslinking with strong covalent bonds [336] however, this requires high temperature heating cycles to repair damage and has not been demonstrated for a fuel cell membrane. Reversable hydrogen bonding can provide intrinsic self-healing which is not limited by the capacity of any reagents. It has been shown that a self-healing membrane can be produced from a Nafion/Polyvinyl alcohol polymer blend, postmodified with 4-carboxybenzaldehyde [337]. The publication states that the PVA is modified by the addition of benzoic acid groups through the formation of acetal groups between the hydroxyl groups of the PVA and the aldehyde group of the 4-carboxybenzaldehyde. Self-healing is thought to occur through hydrogen bonding between the sulfonate group of the Nafion and the etherized PVA's hydroxyl and benzoic acid groups [337], the structure of this membrane material is shown in **Error! Reference source not found.**. There is little evidence to support this structure and hydrogen bonding as such there may also be other functional groups formed by side reactions during etherisation and/or crosslinking between the polymer chains, therefore further investigation is required. These membranes have been shown to have satisfactory mechanical strength, self-healing and can exhibit enhanced proton conductivity when applied to a direct methanol fuel cell but nothing has been reported for PEM fuel cells.

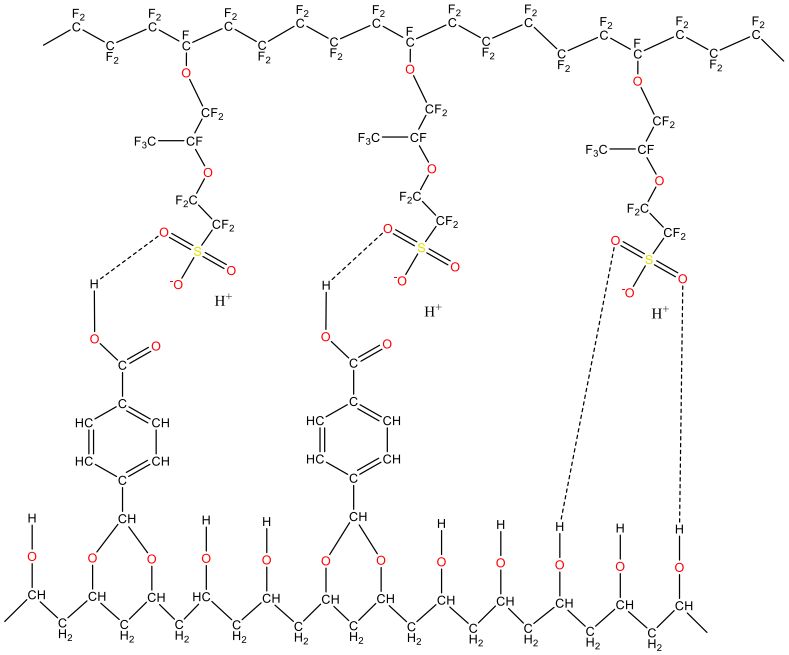

Figure 8.1 - Hydrogen bonding between the etherised PVA and Nafion blend

8.3 Membrane testing

In order to determine membrane performance and understand the material behaviour such as the mechanisms behind the self-healing, a number of experiments need to be conducted to characterise the various properties of the membrane. There are many well documented characterisation techniques for fuel cell membranes however, there are few documented methods to test the self-healing of polymers, particularly for fuel cell applications and so this is an area where new tests were conceived.

8.3.1 Electrochemical performance testing

Electrochemical performance determines the efficiency of a cell and therefore is a very import factor. As membranes have a significant contribution to the loss in efficiency, determination of their performance is necessary. This can include polarisation and power density curves, electrochemical impedance spectroscopy, gas crossover tests and electrochemical surface area. These can allow the determination of losses due to activation polarisation, ohmic polarisation, limited mass transport, gas crossover and catalyst degradation.

8.3.2 Self-healing tests

In order to determine if a membrane self-heals it must be damaged so that the degree to which it can recover its original properties can be determined. This can be done by physically damaging membranes which can be done with a needle/pin to create a hole or a blade to create a cut. Once the membrane has been exposed to conditions that should facilitate self-healing, the material must be characterised to determine if any self-healing has occurred.

Visual

One method to determine if self-healing has occurred is to visually check the site of the damage and see if the hole or cut has been filled over by the surrounding material. As the size of holes is very small (100-300μm) this has been done with a scanning electron microscope or an optical microscope [335,337,338]. This is a very basic determination and gives no quantitative information other than an approximate healing time and hole diameter.

Stress-strain

Stress-strain tests can be used to test the recovery of the tensile strength of the material by measuring different samples when they are in different states such as original material,

damaged material, partially healed and fully healed material. This allows a rate of self-healing to be determined and the loss in strength between original and healed membranes. The main problem with this method is the consistency of the results as each test is destructive and so many different samples are required. This means that samples and the damage done to them must be very uniform.

Ion crossover during healing

Another method to show self-healing using the crossover of negative ions could also be used, this would be done with a H-cell containing a solution with a negative ion such as chloride ions on one side and a chlorine free solution on the other. The membrane should act as a barrier for the negative ions however, holes would allow them to pass over the membrane. Detecting the concentration of negative ions would allow the diffusion across the membrane to be calculated, this could be done with an ion- selective electrode or through a titration method such as Mohr's method [339]. This technique could be used to show the restoration of the membrane as a barrier to the negative ions however, the rate of diffusion is unknown, and it may be difficult to obtain accurate results. This method would also test the membrane as a barrier for negative ions and not the gases that the membrane is required to block.

Electrochemical measurements during membrane healing

Visual and stress-strain tests have so far been done with membranes submerged in liquid for a period of time at elevated temperatures however, self-healing has not been demonstrated inside a fuel cell where the self-healing would have to occur in a commercial system. Membranes could be healed in a fuel cell and visual tests could be used to determine is self-healing has occurred however, for each measurement the membrane would have to be removed and dried in order to be tested, when placing the membranes back in the fuel cell the membrane hydration would change each time and may need to be hydrated beforehand. The proposed method is to test the membrane using electrochemical techniques to determine the self-healing. Gas crossover tests can be used to determine if the barrier for electrons and gases is being restored and recording the cell potential can be used to determine if electrochemical performance is recovering. This method would provide quantitative determination of self-healing with fuel cell conditions, using more relevant performance characteristics. The test could also be done at different current densities to determine its effect and determine if low current cycles would be needed to repair damage. As this method has not been reported in literature, this method may require many experiments to obtain satisfactory results.

8.3.3 Durability tests

A membrane that can heal damage provides an advantage in fuel cell durability however it must also be able to resist damage and therefore tests which damage membranes must be conducted to determine if any improved durability can be observed.

Mechanical resistance tests

Mechanical durability can be probed with stress-strain tests which have been used to determine the recovery of membranes to repeated tensile stresses [338]. The reported method applies a strain of 50% through repeated cycles and a reduction in stress can be observed between cycles. Introducing recovery times was also used in-between cycles which resulted in an improvement in recovery for both the self-healing and Nafion membranes tested.

The mechanical resistance can also be tested with an accelerated durability test and has been demonstrated for a microcapsule self-healing Nafion membrane [335]. This test is conducted inside the fuel cell at a high temperature and involves monitoring the cell potential with periodic cycling of dry and hydrated gases in order to dry and hydrate the membrane which causes it to swell and contract. This method uses the same damage mechanisms experienced by the membrane in a normal fuel cell operating conditions however, the rate of damage is significantly faster. This method can also be combined with gas crossover tests and EIS to obtain more information as other degradation can also occur for example catalyst degradation. One issue with this test is the time taken even though the rate of damage has been accelerated. This was shown by the microcapsules self-healing membrane test which took 220 hours.

Chemical resistance tests

The chemical resistance can be tested using Fenton's reagent (3% H_2O_2 with 2ppm $FeSO_4$). The Fe2+ ions in the solution catalyse the decomposition of the hydrogen peroxide into the reactive hydroxyl (HO•) and hydroperoxyl (HOO•) radicals [340]. These are the same radicals formed at the cathode and submersion of membranes in this solution chemically degrades membranes. The chemical degradation can then be measured by a change in membrane mass or a gas crossover test.

An in situ chemical stability test can also be used to characterise the chemical resistance. This test is conducted inside the fuel cell and involves monitoring the open circuit voltage. The cell is operated at low humidity's of 30% and a high temperature of up to 90°C [341] which is favourable for the formation of hydrogen peroxide and its radicals at the cathode [342]. The

advantage of this test over the Fenton's test is the improved characterisation and fuel cell operating conditions however, the test has to be run for long periods of time (>100 hours) and degradation of other components can occur for example catalyst degradation which can affect the results.

8.3.4 Glass transition temperature

An important part of intrinsic self-healing is the mobility of the polymer chains. As the material is an amorphous polymer, the structure can change meaning that the membrane can transform from a stiff polymer (glassy state) into a viscous liquid with the properties of rubber (rubbery state). The temperature at which this transition occurs is known as the glass transition temperature (T_g) although, this is a midpoint as the process occurs over a temperature range. The glass transition temperature is typically in the range of 170-500K for synthetic polymers [343]. The factors affecting this temperature are the molecular weight of the polymer chains, molecular structure (bulky and inflexible side groups increase the glass transition temperature due to decreased mobility), chemical cross linking and polar groups which increase the intermolecular forces [344]. Plasticisers can also decrease the glass transition temperature; water is a plasticiser [345] as hydrogen bonds are formed between the water and the polymer chains which increases the distance between the chains and decreases intermolecular cohesive forces therefore increasing their mobility [344].

Thermo-gravimetric analysis with differential scanning calorimetry (TGA/DSC) is a combination of two simultaneous methods, the method is destructive but only requires approximately 20mg of sample. TGA heats up and/or cools down the samples and measures the mass, when a fraction of the sample such as water evaporates, a change in mass is observed. As such it can be used to determine the content of these fractions although the identity of the different fractions needs to be known. DSC measures the energy required to increase or decrease the temperature at the set rate and as such can determine if a process is endothermic or exothermic such as the evaporation of a component of a sample. The TGA technique can be used to determine the water content of a membrane hydrated by atmospheric water vapour. For hydrated membranes it is unlikely that the surface water can be sufficiently removed as the membrane needs to be cut into very small pieces to obtain good results and therefore the result will have a high level of uncertainty. DSC can be used to determine the glass transition temperature of the membrane as the process is endothermic and shows itself as an S-shape transition in the DSC plot [346]. Melting and other transitions are also endothermic processes

and so careful analysis of the results is important. Glass transition temperature cannot be measured using TGA/DSC if there is a fraction evaporating and therefore a heating cycle is required to remove water before taking the measurement. The primary heating cycle can be used to determine water content, but the secondary heating cycle can be used to determine glass transition temperature. If a mass changed is observed during the second cycle, the DSC results can no longer be used as the heat flow cannot be attributed to just the glass transition temperature.

8.4 Analysis of membrane hydration and water retention with terahertz time domain spectroscopy

The physical and electrochemical properties of Nafion and other polymer electrolyte membranes depend upon the nature of water present within the membrane. This water can be strongly hydrogen bonded and predominately bound to the hydrophilic domain of polymers such as the sulfonate groups [200],[233] (bound water). The water can also be located in the centre of the pores and exhibit co-operative reorganization of hydrogen bonds (bulk water) [234],[233], this water contributes to maximum proton conductivity at high hydrations through proton hopping (Grotthuss mechanism) [347]. The water can also have little/no interaction with the polymer through hydrogen bonds (free water) [348],[287], this water does not significantly contribute to proton conductivity. Some techniques have been used to detect the different water fractions of water such as FTIR [349] , quasielastic neutron scattering [138] and dielectric spectroscopy [266] however these have not been used to quantify the amount of these water fractions. Low temperature differential scanning calorimetry has been shown to provide quantification of the bound fraction [209] as this is considered unfreezable however, this method is destructive, not continuous and cannot be used to study the free or bulk water. As terahertz is sensitive to both bulk and free water, it is possible to determine the nature of water within membranes using terahertz spectroscopy [347].

Polyvinyl alcohol is a very polar polymer and as such it has a higher refractive index and absorption coefficient than many other polymers [350]. On the other hand, terahertz has strong interactions with the hydrogen bond network in aqueous liquids [351] and so water with its high polarity and strong hydrogen bonding is strongly absorbed [237]. This means it can be used to quantify the water content in hydrated polymers as demonstrated by Devi [347]. This

is a fast and non-destructive method and as such was selected to study the water uptake and retention properties of the self-healing membranes.

A hydrated material with a randomly distributed water content throughout can be considered as two separate layers of dry membrane and water with an effective water thickness (l_{eff_w}). The exponential loss of amplitude with increasing effective water thickness can be modelled with Beer Lambert's law and rearranged to calculate the effective water thickness using the FFT amplitude of the dry and hydrated sample (E_{ref} and E_{hyd}), dry thickness (l_d) and the frequency dependant absorption coefficient of both water and the dry membrane (α_w and α_d). As properties are frequency dependant this is done for each frequency as shown and an average is taken.

$$l_{eff\_w}(v) = \frac{1}{\alpha_w(v)}\left[2ln\left(\frac{E_{ref}(v)}{E_{hyd}(v)}\right) - \alpha_d(v)l_d\right]$$

The thickness and density of the two layers can then be used to calculate the water content of the hydrated membrane.

The standard analysis works for thicker membranes however, parameters become unattainable in thinner membranes due to internal reflections within the sample known as Fabry-Perot reflections. These reflections can affect the measurement through their difference in phase and amplitude which can cause constructive and destructive interference.

As the reflections are superimposed, the contribution of each cannot be determined. To remove the effects of the reflections, the behaviour of the pulse through the membrane must be modelled. The complex dielectric response of the dry membrane was modelled through the following Debye model equation:

$$\hat{\varepsilon}(\omega) = \varepsilon_\infty + \frac{\Delta\varepsilon}{1 + i\omega\tau}$$

Where $\hat{\varepsilon}(\omega)$ is the complex permittivity, ε_∞ is the permittivity at the high frequency limit, τ is the relaxation time of the medium, ω is the angular frequency. Permittivity is a measure of the electric polarizability of a dielectric material such as a polymer meaning that materials with high permittivity polarizes more in response to an applied electric field than materials with lower permittivity. Complex permittivity introduces the phase of the response due to the fact that application of the electric field and polarization are not simultaneous [352] and varys with frequency. The permittivity is therefore treated as a complex function of the angular frequency of the applied electric field (Terahertz pulse)

Modelling the Fabry-Perot reflections can allow material quantification even when the effect of the reflections is significant. To do this the propagation of the pulse through the membrane must be modelled, this includes the reflections at the membrane/air interface and attenuation of the beam through the material. The modelled reflections can then fit to the measurement through an iterative method. One variable for the modelling of the reflections is the material thickness as it affects the phase and intensity of reflections, this can be measured for dry membranes. However, as membrane materials swell due to hydration, the thickness increases and therefore this cannot be considered constant when drying. As such the modelling of the reflections can also determine the material thickness through the iterative method of fitting to the measurement. The Double Debye model was then used to the model the dielectric response of the hydrated membrane and water fractions as shown in section 3.4

8.5 Molecular analysis

Determining the chemical structure and intermolecular interactions of the membrane materials is necessary to understanding their behaviour, there are a number of unknowns in this area such as whether any side reactions occur during etherisation or whether any polymer crosslinking is occurring. A number of methods can be used to determine these factors in particular Fourier transform infrared (FTIR), nuclear magnetic resonance (NMR) and x-ray photoelectron spectroscopy (XPS). Access to these techniques has been difficult and so far, no measurements have been made.

8.6 TEM for ionic channel size determination

Ionic channels are difficult to characterise due to their size. Transmission electron microscopes have been shown to be able to observe the ionic channels and determine their size by staining the ionic clusters using RuO_4 [353]. This method has been demonstrated in literature for the material being studied and has shown a reduction in the size of the ionic channels [337], it has been shown that this can strongly influence the proton conductivity [354].

8.7 Experimental results

The first step in the project was to produce self-healing membranes, the quality of these membranes has improved as the methods have slowly developed. In general, the cast membranes being produced have also become thinner, the driving processes for this has been

problems with the THZ-TDS measurements but also to produce membranes closer to the thickness typically used in fuel cells.

The self-healing of the membranes has been tested in order to determine if the membranes can heal in deionised water and the suitable temperature range for this instead of the methanol used in the previous study [337].

A large focus has been on obtaining the water fractions from the THz-TDS, a number of samples have been measured and repeats on samples have also been done. One issue which was not identified for a while was the issue of the sample thickness, the fitting of the transfer function appeared to be working, but the parameters obtained did not. Measurements have also been done with a number of repeats for commercial Nafion 211, 212 and 117.

TGA-DSC has been used to try and determine the glass transition temperature of PVA, Nafion, Nafion/PVA blend and the finished self-heling membranes. Unfortunately, there was an issue with the results obtained and so little information could be determined.

8.8 Membrane fabrication

A number of membranes have been produced all of which have been 50% Nafion and 50% PVA by mass which has then been postmodified for 8 hours in 10% 4-carboxybenzaldehyde, the degree of etherisation and Nafion content has a large effect of the material properties however, before any changes can be made the material needs to be characterised to understand the material properties and as a benchmark for comparison to any new compositions created.

5wt% Nafion® D-521 dispersion in water and propan-1-ol with an exchange capacity of ≥0.92 meq/g was purchased from Alfa Aesar. 98-99% hydrolysed polyvinyl alcohol (PVA) with high molecular weight, 98% 4-carboxybenzaldehyde and 99% N,N-Dimethylformamide were also purchased from Alfa Aesar. 37% Hydrochloric acid was purchased from Fisher Scientific and diluted to 1M. As the PVA is not 100% hydrolysed the polymer chain has acetate groups from the polyvinyl acetate that the PVA is produced from as shown in **Error! Reference source not found.**. This is common and PVA usually has a degree of hydrolysis of 85-99% [355].

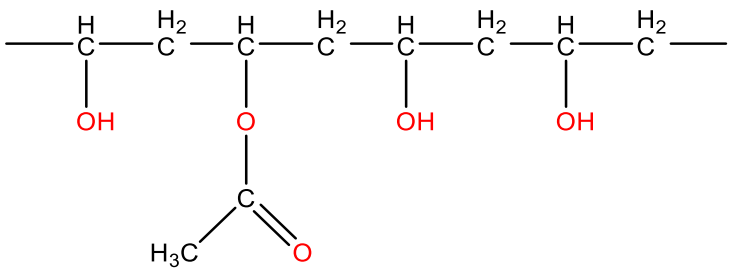

Figure 8.2 - Section of partially hydrolysed PVA

A 5wt% dispersion of Nafion in water and propan-1-ol was mixed with a 10wt% aqueous solution of polyvinyl alcohol in a 1:1 ratio of Nafion:PVA by mass and heated at 70°C under continuous stirring to increase the polymer concentration to 10wt%. Once at this concentration the stirrer was turned off to allow for the bubbles formed from stirring the solution to dissipate. The solution was poured into a silicone mould and dried at room temperature for 40 hours. Nafion-PVA membranes were easily removed from the silicone due to the hydrophobic surface. The hydroxyl groups of the PVA were then partially etherised with 4-carboxybenzaldehyde at a concentration of 10% in dimethyl formamide for 8 hours, this grafts benzoic acid groups onto the PVA chain. To remove the remaining 4-carboxybenzaldehyde, the membranes were thoroughly washed in excess dimethyl formamide (DMF) and left at room temperature for the DMF to evaporate. Thorough washing with DMF is required as number of membranes could not be used as CBA was not sufficiently removed this can be seen as small amounts of CBA crystalised onto the membrane surface. The membranes were then activated in a 1M aqueous solution of hydrochloric acid for 5 hours at 60°C. The membranes were then washed multiple times with deionised water in order to remove any residual acid.

There were a number of issues encountered whilst producing the membranes. The PVA is soluble in water however it exhibits an upper and lower critical solution temperature as shown in **Error! Reference source not found.** and the dissolution process is very slow which means that the temperature needs to be increased slowly under continuous mixing in order to achieve a homogeneous solution. This has been successful by increasing the hotplate temperature by 15°C per hour up to 130°C, attempts to speed this up resulted in a heterogeneous mixture.

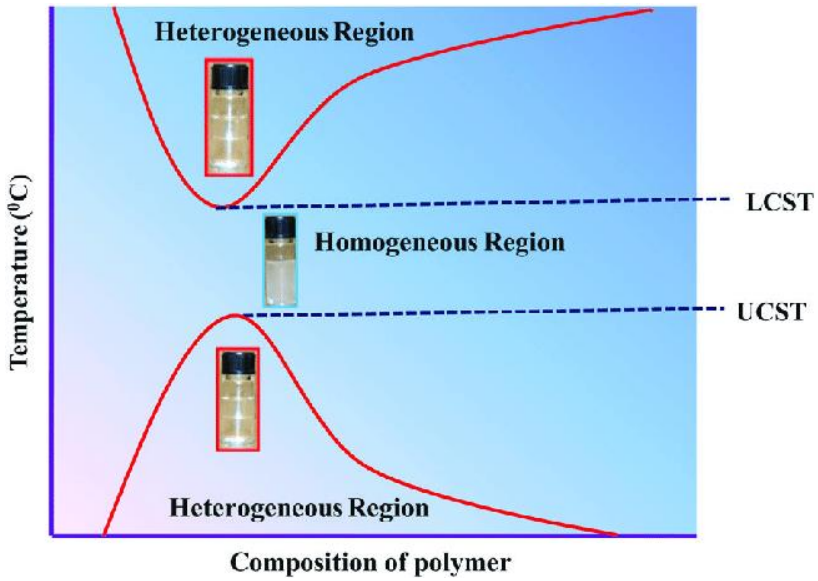

Figure 8.3 – Upper and lower critical solution temperature [356]

Another issue faced has been the agglomeration of the PVA/Nafion blend when increasing the concentration for casting, this has meant that the solvents need to be evaporated slowly under continuous stirring. Due to the viscosity of the solution, the stirring creates small bubbles which are undesirable and increase agglomeration, so the stirrer was set as slow as possible.

Silicone has been used as the mould material for casting the PVA/Nafion blend however, the moulds bend whilst drying meaning that the membranes do not have a uniform thickness. Glass and PTFE were tried as alternatives, the glass is very rigid and has a smooth surface however, the membranes stuck to the surface and could not be removed. The membranes do not stick when cast onto PTFE and the moulds remain flat however the surface is not as smooth and so marks can be seen on the bottom of cast membranes, this is not a significant problem as the membrane surface changes when etherised and so membranes can be produced with a more consistent thickness and a smooth finish

Drying of membranes at room temperature in a fume cupboard can take a few days for thick membranes and therefore experiments were done to try optimise the drying of solution cast membranes and improve the drying time. This was done by casting membranes and drying them in a vacuum oven at 30,35,40,45, and 50°C under atmospheric pressure and also in a vacuum at 30,40 and 50°C. Three membranes were cast for each from 4g of solution which produced membranes of approximately 120µm although this did vary across membranes due to some their uneven thicknesses. The drying time was determined by weighing the samples, the weight could not be gathered continuously inside the oven and so intermittent measurements were taken as seen in **Error! Reference source not found.**. A vacuum oven was used due to the fluctuating temperature in the other ovens available which are designed to work at higher temperatures

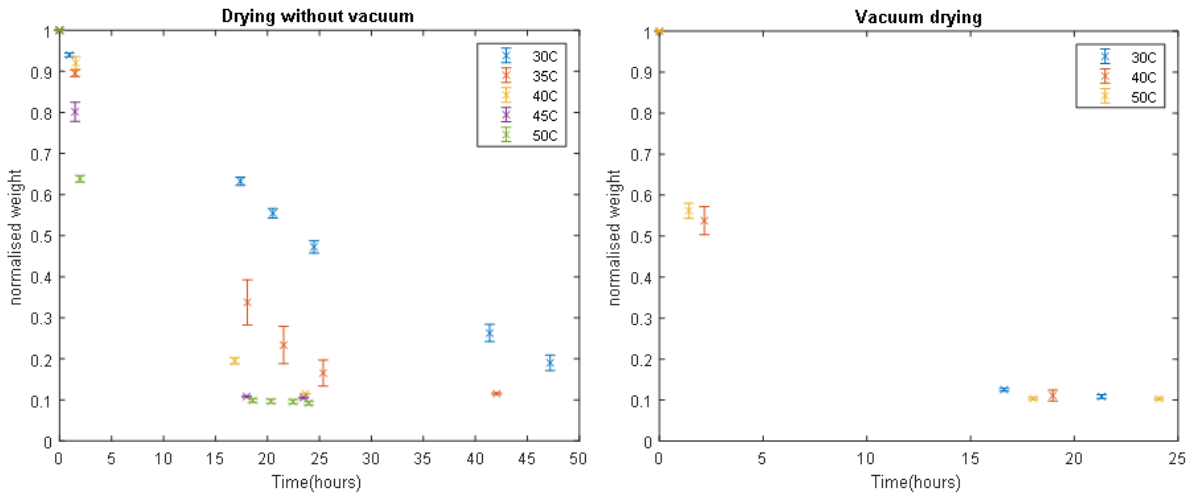

Figure 8.4 - Drying time of Nafion/PVA membranes, Weight has been normalised due to the variation of the initial weight of approximately 4g.

As expected, the drying time decreased with increasing temperature with 45 and 50°C samples drying overnight and vacuum drying significantly reducing drying time. However, the membranes at 30 and 35°C took longer than room temperature outside the oven. As a vacuum oven was being used the oven was air tight and therefore the air could not escape and it became saturated with the solvents being evaporated. The saturated air reduced the mass transport of the solvents and therefore increased the drying time compared to the membranes dried in the fume cupboard. This was observed through condensation of solvents on the sides of the oven for both atmospheric and vacuum pressure, an increase in the drying rate can also be seen after the oven was opened to weigh the samples as the saturated air could escape.

The quality of these membranes was poor due to the formation of bubbles in all samples. Images of some of these membranes are shown in **Error! Reference source not found.**. It can be seen that large bubbles are formed during the drying under a vacuum whereas a few smaller bubbles are formed at atmospheric pressure. The effect of membrane thickness was also tested with two thinner membranes at 50°C, this did not result in a reduction in the number of bubbles as hoped but reduced their size.

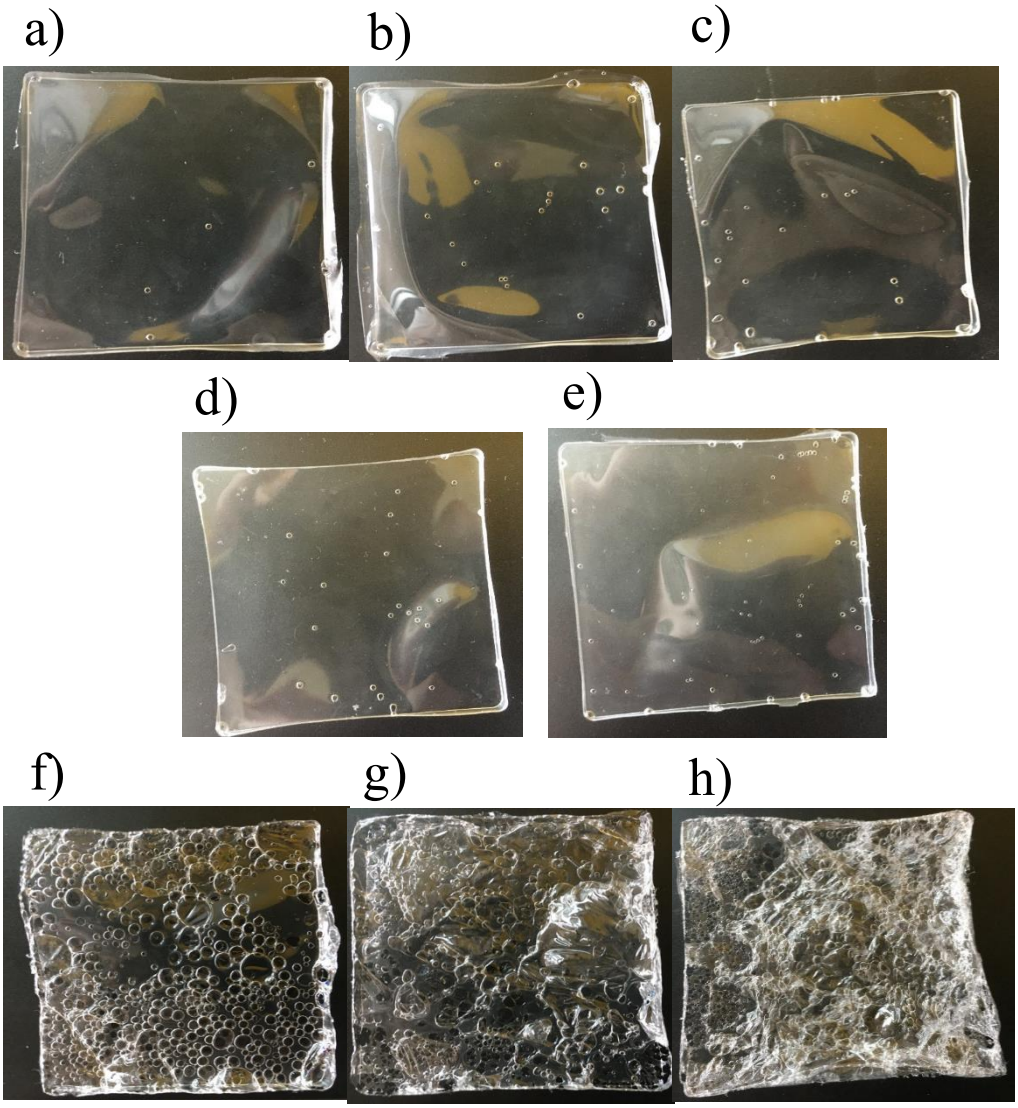

Figure 8.5 - Images of cast membranes dried at different temperatures and pressures. a) 30°C, 1atm, 4g. b) 40°C, 1atm, 4g. c) 50°C, 1atm, 4g. d) 50°C, 1atm, 3g. e) 50°C, 1atm, 2g. f) 30°C, vacuum, 4g. g) 40°C, vacuum, 4g. h) 50°C, vacuum, 4g.

Therefore, drying at room temperature in a fume cupboard was been identified as the best drying condition to obtain defect free membranes.

8.9 Self-healing

Membranes were damaged using a 250µm needle which created ~280µm holes, some of which had an opening which was wider. A confocal 3D microscope was used to image the holes and measure their diameter, the thickness was also measured using the film thickness technique of the microscope. Membranes were then submerged in deionised water and heated using a hot plate for 5 hours. Analysis using the 3D microscope was then used to determine if self-healing

had occurred. One membrane was cut into pieces and used for all experiments to obtain more consistent results however, the thickness variation of the sample varied from 242-373µm.

Error! Reference source not found. shows that the hole did not heal during its submersion in DI water for 5 hours at 60°C. The hole diameter is the same however, the surface has changed, this is due to drying the membrane on PTFE which transfers the lines to the membrane, the material is also more reflective due to the membrane being slightly hydrated.

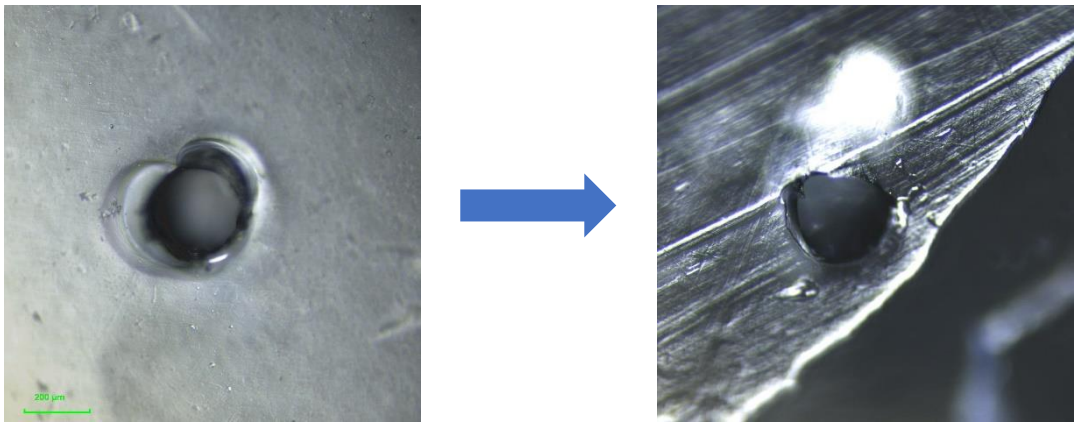

Figure 8.6 - Hole before and after submersion in water for 5 hours at 60°C

Error! Reference source not found. shows that the hole did not heal during its submersion in DI water for 5 hours at 70°C. Unlike the attempt to heal the membrane at 60°C, the hole diameter has reduced meaning that the membrane may heal at this temperature given more time. The surface has again changed due to drying the membrane on PTFE.

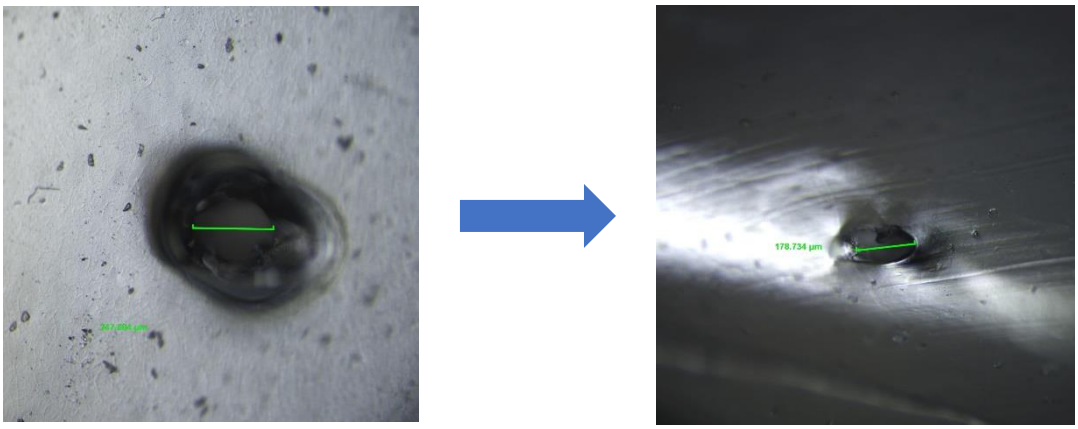

Figure 8.7 - Hole before and after submersion in water for 5 hours at 70°C

Error! Reference source not found. shows that the membrane can heal at 75°C when submerged in DI water, the hole has been closed however, a scar on the membrane surface is still remaining, the surface is more similar to the other non-healed images as the membrane was drier and was not touching the PTFE as it dried. **Error! Reference source not found.**

shows the measurement of the membrane thickness and this also shows the healing of the hole. Analysis showed the thickness near the hole reduced from 276-279µm to 91-111µm, the thickness of the healed section was thinner than the rest of the material at 60-68µm. A reduction in thickness around the hole was observed for all the membranes tested, this was due to the membranes slightly sticking to the PTFE which restricted their contraction in the horizontal plane.

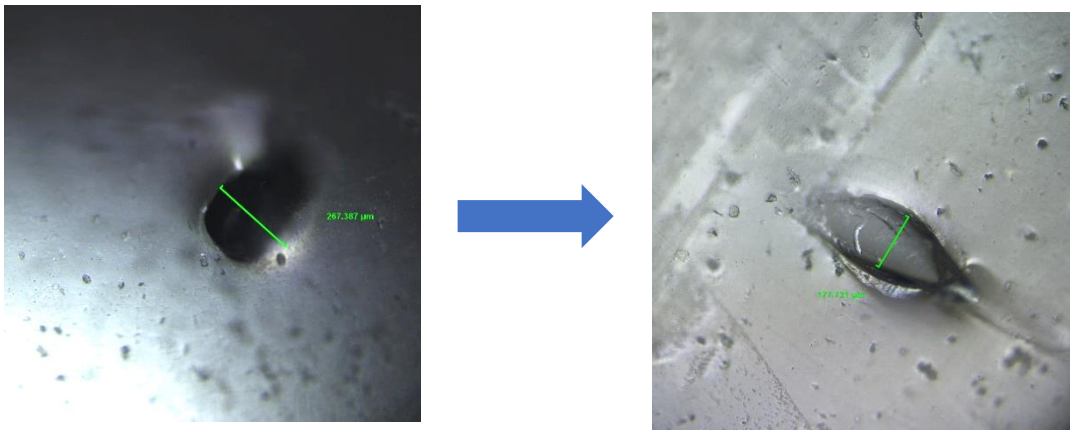

Figure 8.8 - Hole before and after submersion in water for 5 hours at 75°C

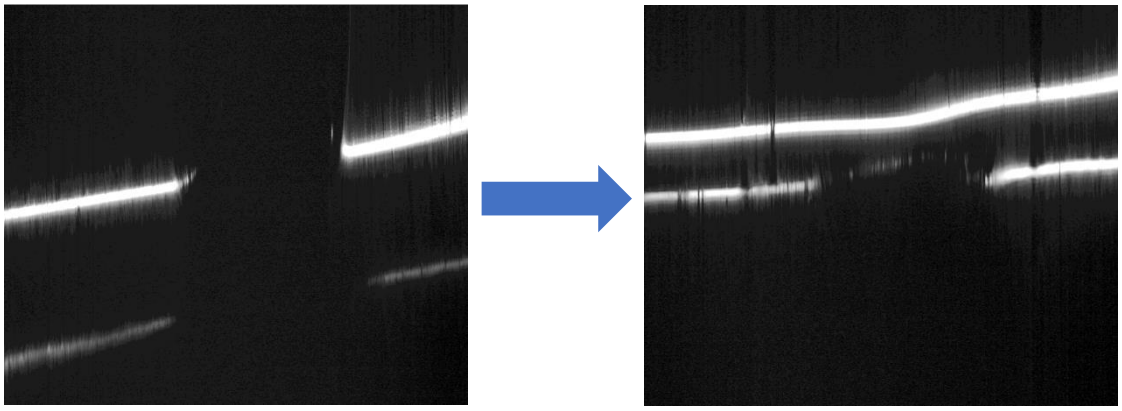

Figure 8.9 - Thickness measurement across hole before and after submersion in water for 5 hours at 75°C

Error! Reference source not found. shows that the membrane can heal at 80°C. The thickness around the hole decreased from 360-366µm to 115-127µm and the healed area had a thickness of 47-56µm.

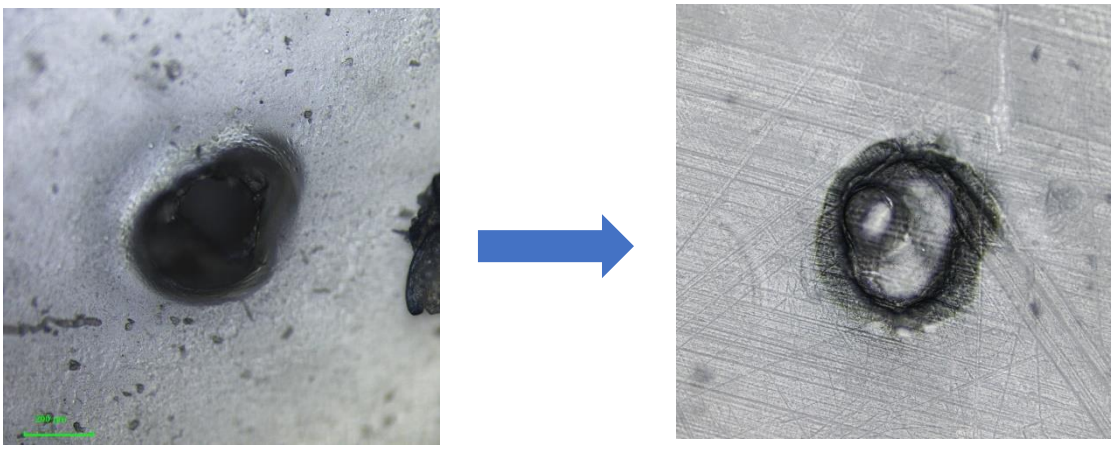

Figure 8.10 - Hole before and after submersion in water for 5 hours at 80°C

Error! Reference source not found. shows the hole of the membrane healed at 85°C, unfortunately the location of the hole was lost, and the material became very fragile causing it to break when being removed from the water. This means this temperature is unsuitable for self-healing while submerged although it may heal at this temperature under high humidity and retain more mechanical strength.

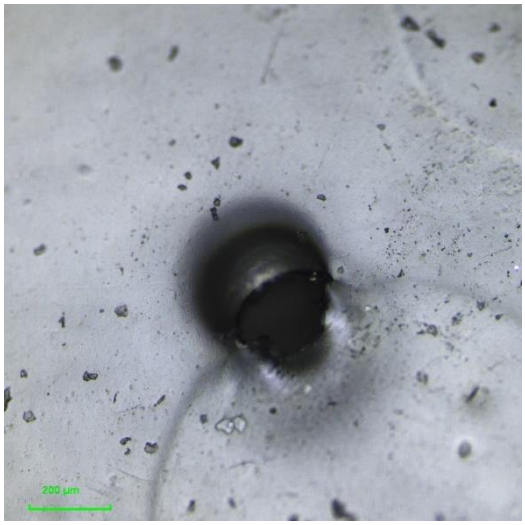

Figure 8.11 - Hole for 85°C healing

The results show that the material can self-heal in deionised water. In 5 hours, the membrane hole was healed for 75 and 80°C, at 70°C the hole diameter reduced suggesting that the hole would heal given more time. The healed sections of the membranes had a reduced thickness compared to the surrounding material. At 85°C the material began to lose too much of its mechanical strength and therefore this temperature cannot be used to heal membranes when submersed in water. All the membranes reduced in thickness during the experiment, this was due to the expansion of the material as it hydrated and the limitation on shrinking caused by the membrane sticking to the PTFE.

To improve these results, frames have been made to stop the restriction of membrane shrinking. A more extensive self-healing study is being conducted which also looks into the effect on hole size, membrane thickness, healing time and application of water through 100% humidity as well as submersion. A design of experiments has been done to reduce the number of experiments required.

8.10 THz-TDS of self-healing membranes

The terahertz measurements were made on a TERA K15 THz Time domain Spectrometer (THz-TDS) from Menlo Systems GmbH and has been configured as shown in Figure 3.13. This setup gives a point measurement rather than a columnated beam over an area of the membrane such as the one used by Devi [347], this is advantageous for these measurements as the thickness of the samples being tested are not uniform across the whole membrane.

The hydrated membranes were prepared by soaking them in deionized water for 24 hours at room temperature and the surface water was removed by pat drying with paper towels just before measuring to ensure the beam is only attenuated by the polymer sample. Dry membranes were prepared in a vacuum oven at 40°C for 18 hours. The membranes were then placed in a sample frame within the beam path in order to gather the data. For dry and reference measurements 500 averages were taken and 50 were taken for hydrated measurements. Hydrated samples were measured every minute in order to monitor the changes in hydration as they dried.

Error! Reference source not found. shows the waveforms of a dry 660µm membrane, in the time domain the absorption and delay of the waveform can be seen from the reduction in intensity and the time shift. Analysis of the waveform has been cut at -200ps before the FFT was calculated in order to remove the reflections from the TPX lenses observed at -195ps and -160ps. Absorption peaks can be observed in the FFT spectrum at frequencies greater than 1THz, these are caused by water vapor in the beam path and can be reduced by purging with an inert gas such as nitrogen however, as the effect on the results is insignificant and this would affect the drying of the samples it has not been done.

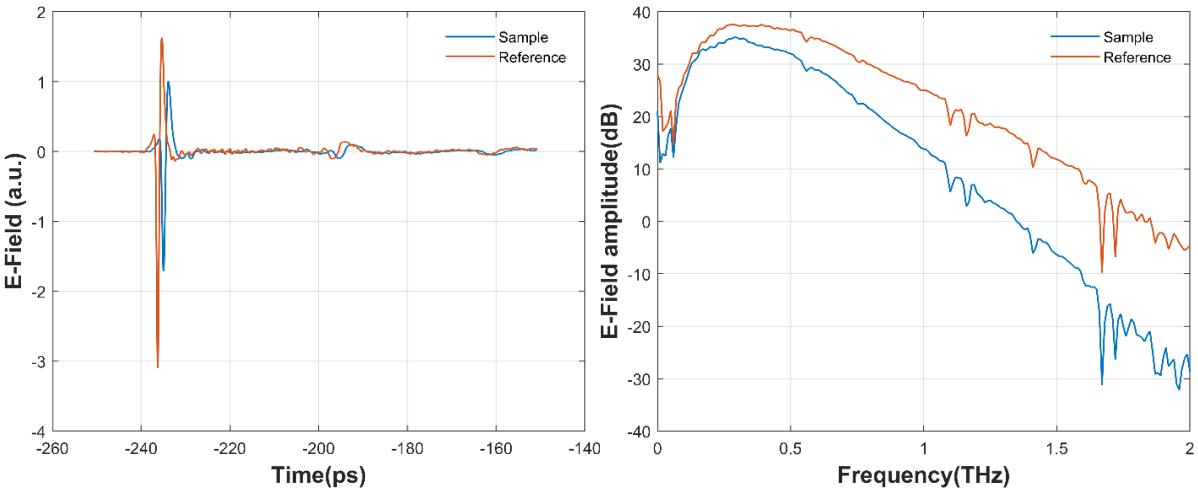

Figure 8.12 - Waveforms in the time and frequency domains for dry 660µm sample

8.10.1 Debye fit

In order to use the Debye model for thin samples it must be shown that the material behaves according to the Debye model, as such the model must be compared to the measurements for a thick sample where Fabry-Perot reflections do not affect the measurement. **Error! Reference source not found.** shows that permittivity of the 660 µm sample can be fit to the Deybe model and as such the model can be used to analyse the measurements for thinner samples.

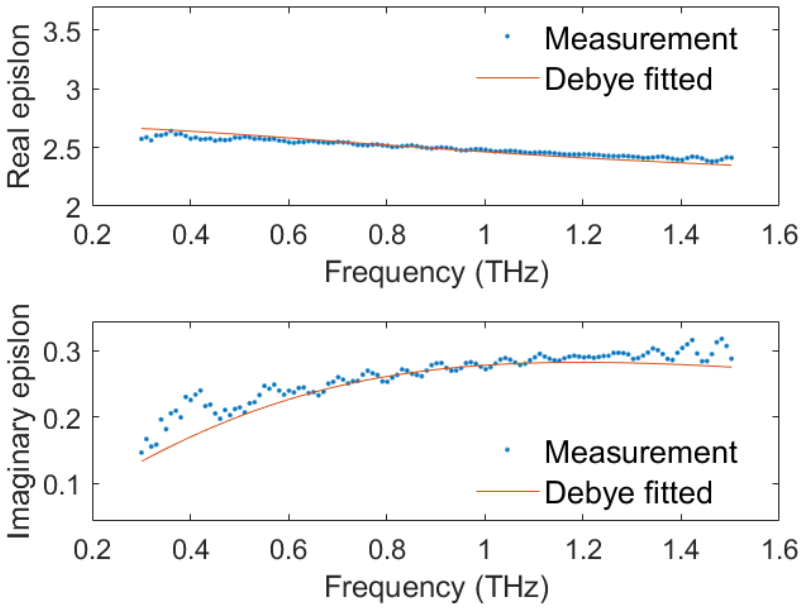

Figure 8.13- Real and imaginary permittivity obtained from the measurement and the Debye fit

The optical parameters of thinner samples can be extracted using the Debye model and **Error! Reference source not found.** shows that samples have similar refractive index and absorption coefficient regardless of the thickness.

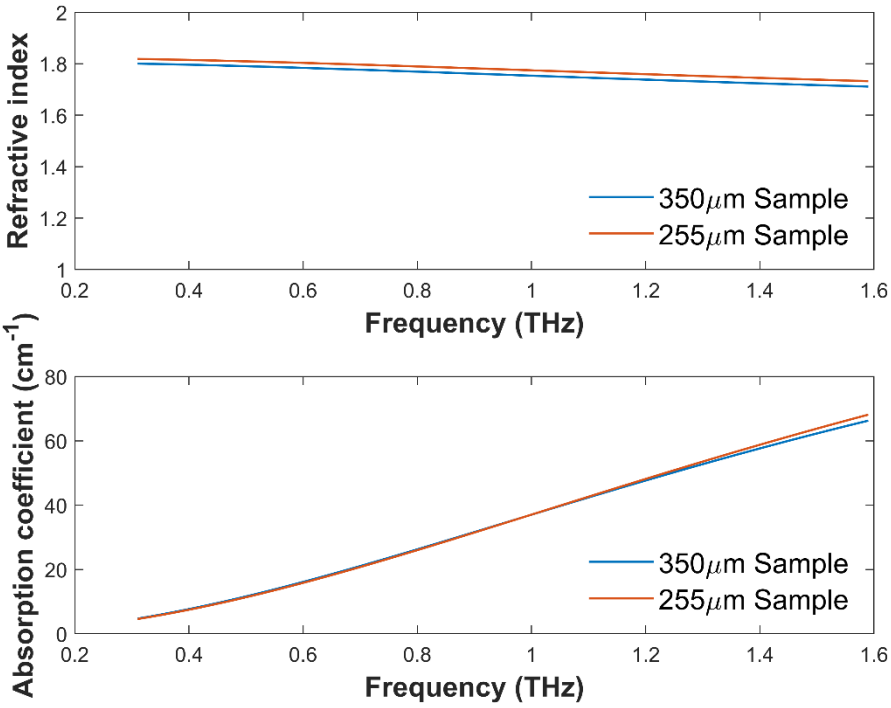

Figure 8.14 - Refractive index and absorption coefficient of 255 and 350μm samples by fitting the measurements to the Debye model

8.10.2 Water Content

The water content was determined by analysis of the terahertz measurements which were taken as the membrane dried at 32-34% humidity and 21.1-21.7°C, the effective water thickness obtained from beer lamberts law is shown in **Error! Reference source not found.**. The effective water thickness is larger for the thicker sample as expected and are therefore difficult to compare however, the initial effective water thickness is 71% and 67% of the dry material thickness for the 255μm and 350μm membranes respectively. This significant water thickness was observed when hydrating and drying the membranes as the membranes exhibited significant swelling.

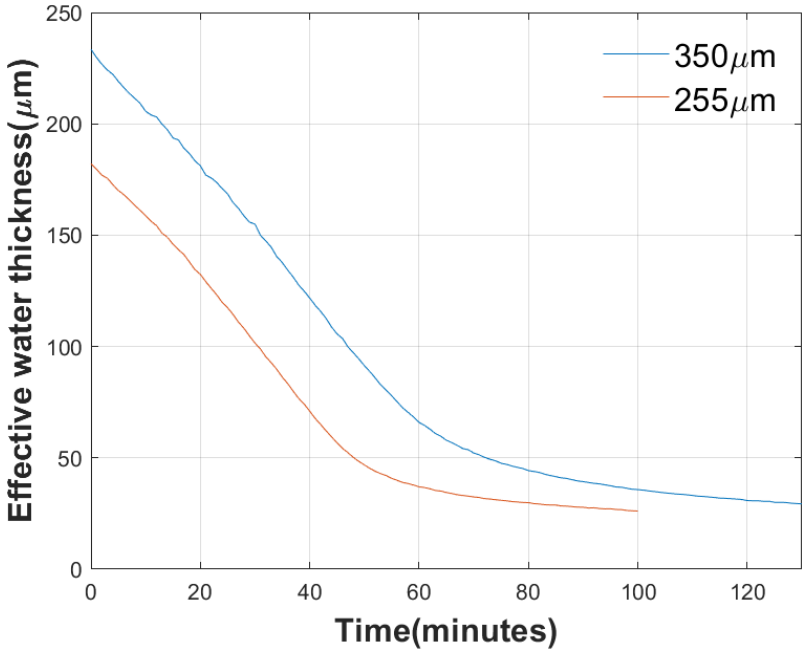

Figure 8.15 - Effective water thickness of 350 and 255μm hydrated membranes as they dry

The water content was then calculated using the effective water thickness, material density and thickness, the results are shown in **Error! Reference source not found.**. The maximum water content at the start of the test matches the reported water content [337] for 7 hours of etherisation at 37.2%. Repeating the measurement increased the water retention of the membranes, the membranes were only dried under a vacuum at 40°C and then hydrated in deionised water at room temperature between measurements. The vacuum drying may be thermally annealing the membranes as it is well known that thermally annealing of Nafion membranes changes a number properties including water retention [357]. Crosslinking may also be occurring which is supported by the small reduction in initial water content [333] although this may be down to the removal of surface water. Another reason could be that either process is removing a component of the membrane, this could be a part of the membrane or a species remaining from the production process such as DMF, CBA, Cl^- or propanol. Alternatively, it could also be due to the rearrangement of the polymer chains as significant structural rearrangement occurs which has been observed in Nafion at high water contents [165].

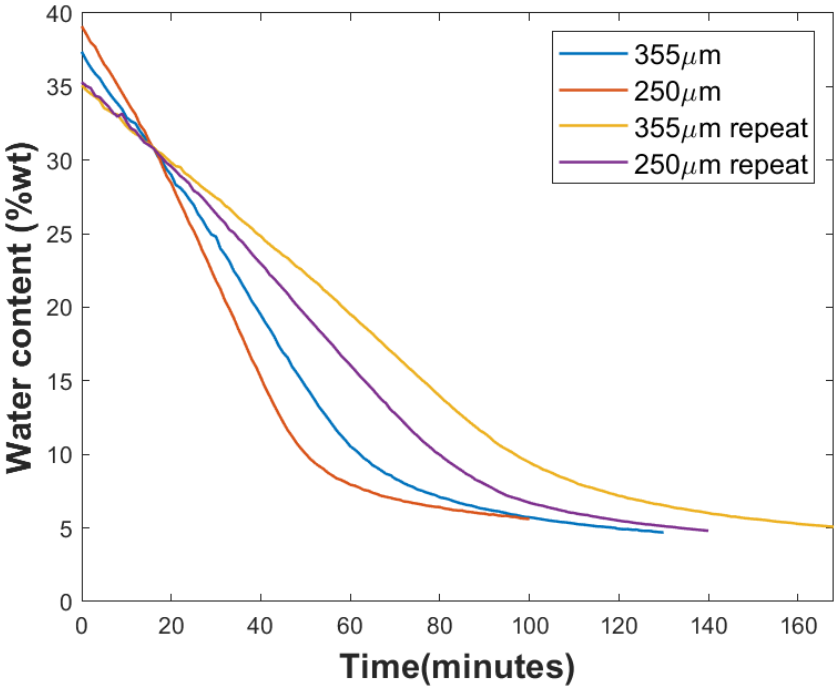

Figure 8.16 - Water content of hydrated membranes as they dry

8.10.3 Double Debye fitting

The fitting of the double Debye model could not determine the thickness for the hydrated membrane. This was due to the high-water content and the relatively thick membrane. The amplitude of the Fabry-Perot reflections in the measurements of the significantly hydrated membrane were too small. As the reflections and main pulse cannot be separated the optimiser fits both contributions together and therefore the reflection was too small to distinguish them from the noise of the main pulse.

8.11 TGA/DSC

Thermo-gravimetric analysis (TGA) analysis was done on samples in a Nitrogen atmosphere to try and determine the glass transition temperature of the material, this was also done on PVA, Nafion and non-etherised samples in order to compare and try and understand the possible effects of changing the material composition and degree of etherisation. The TGA was also able to give the water content of the membranes hydrated by air moisture due to the mass change seen during the drying stage of the test. After a number of tests to find good heating cycle parameters, results were obtained. The tests identified that Nafion blended with PVA had a higher water content at atmospheric conditions than both Nafion and PVA, it also showed that etherisation reduced water content. Unfortunately, during the tests a mass loss occurred for all samples as shown from **Error! Reference source not found.** and **Error! Reference source**

not found.. This affected the results of the DSC and therefore the measurements could not be used to determine the glass transition temperatures, other than for the PVA as this had a low glass transition temperature of approximately 95°C which was well below the mass change which began at approximately 200°C. Experimental values from the literature place the glass transition temperature of PVA in the range of 68-99°C [358]. This range is due to differences in polyvinyl alcohol such as molecular weight and the degree of hydrolysis from the polyvinyl acetate that the PVA is produced from as shown in **Error! Reference source not found.**. As the polyvinyl alcohol used was high molecular weight the glass transition temperature was expected to be high in this range. In order to get good results and determine if the loss in mass is due to a change in hydration or a loss of a component of the membrane, the experiments need to be repeated with the primary heating cycle under vacuum conditions which requires new parts.

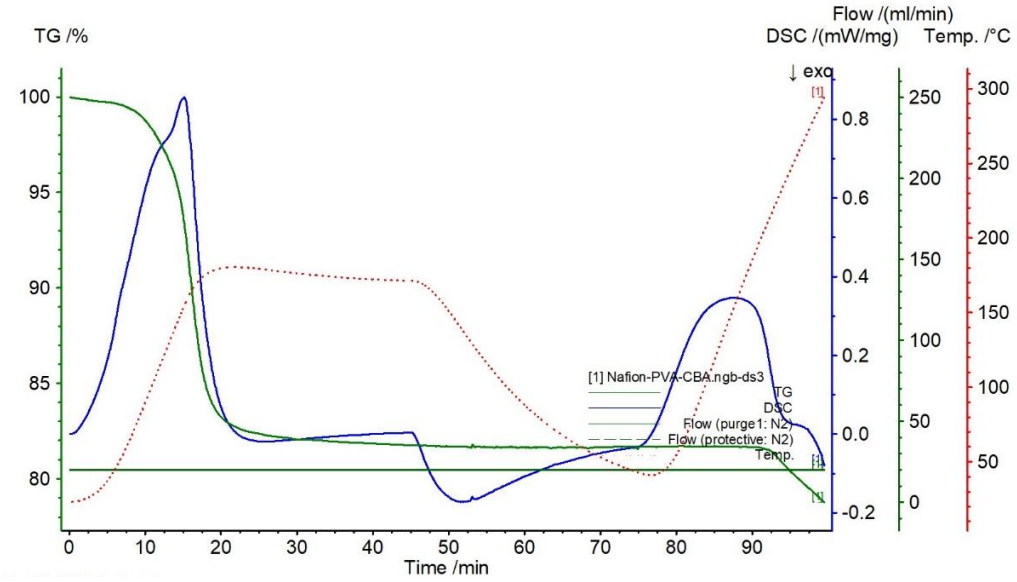

Figure 8.17 - TGA/DSC of Nafion and etherised PVA blend

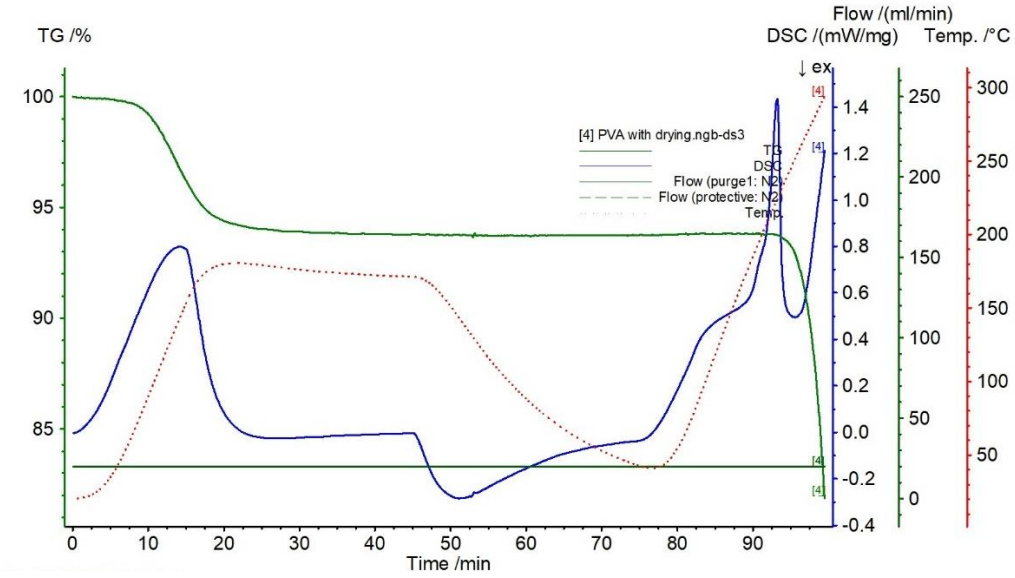

Figure 8.18 - TGA/DSC of PVA